Inaugural dissertation

for

obtaining the doctoral degree

of the

Combined Faculty of Mathematics, Engineering and Natural Sciences

of the

Ruprecht - Karls – University

Heidelberg

Presented by

M.Sc. Clarissa Feuerstein-Akgöz

born in Engen, Germany

Oral examination: 25.04.2022

Integrated multi-omic dynamics of human adipocyte differentiation with focus on DNA hydroxymethylation and epigenomic effects of long-term docosahexaenoic acid treatment

Referees:

PD Dr. Odilia Popanda
Prof. Dr. med. Achim Bub

Contributions

Sections of this thesis, including material and methods part and results from part 1 (Fig. 8) are based on a manuscript in preparation entitled “Integrated multi-ome dynamics of human adipocyte differentiation with focus on DNA hydroxymethylation”. The draft was written by me as first author but contains suggestions and corrections from co-authors.

I performed all downstream bioinformatic data processing described in this thesis, including integration of published data and data visualization, mainly in R language, and in selected cases also in bash and python, using the indicated packages or own functions.

Experimentally, in thesis part 1, I performed the adipocyte differentiation of experiment 1, using the Simpson-Golabi-Behmel syndrome (SGBS) cell line, generated the images, and performed the nucleic acids extractions and qPCR experiments (Fig. 8).

SGBS adipocyte differentiation, as well as nucleic acids extraction of experiment 2 were performed by Linda Kessler under my co-supervision. Whole-genome bisulfite (WGBS) and oxidative bisulfite (WGoxBS) sequencing library preparation for this experiment were generated by myself (Fig. 8).

hMeSeal library preparation for hydroxymethylation analysis and sequencing alignment was done by Florian Janke (Division Cancer Genome Research, German Cancer Research Center (DKFZ)) (Fig. 8 + 10).

White adipose tissue samples were collected by collaboration partners of the PATHWAY-27 consortium, Silvia Garelli, Marianna Farnè, Giampaolo Ugolini, Giancarlo Rosati, and Luigi Ricciardiello from the Department of Medical and Surgical Sciences, University of Bologna, Italy. The collection was coordinated by Alessandra Bordoni from the Department of Agricultural and Food Sciences, University of Bologna, Italy. Pulverization and nucleic acid extraction of the adipose tissue biopsies were performed by Annette Weninger and Karin Klimo. For ACT-seq analysis, Dieter Weichenhan purified the pA-Tn5ase protein, and Jessica Heilmann and Karin Klimo prepared the libraries for sequencing (Fig. 10).

In thesis part 2, I performed the docosahexaenoic acid (DHA) complexation, the cytotoxicity experiments, DHA long-term cultivation experiments (experiment 5), as well as the nucleic acids extractions (Fig. 9).

Methylation and RNA-seq data for cultured untreated SGBS cells from Lisa Demoen (Student 2, experiment 6) and Linda Kessler (Student 3, experiment 7) were included in this thesis to compare cell culture effects with experiment 5 (Fig. 9).

Methylation analysis using 450k and EPIC arrays, RNA-seq library preparation, sequencing of all RNA-seq, hMeSeal, and WGBS/oxBS libraries were performed by the Genomics and Proteomics Core Facility of the DKFZ. Storage of sequencing data and alignment of RNA and WGBS/oxBS sequencing data were performed by the DKFZ Omics IT and Data Management Core Facility (Fig. 8 - 10).

To indicate the contributions in each figure legend, I used the following abbreviations for each contributor (Table 1):

Table 1| Abbreviations of contributors to this thesis.

Contributor	Abbreviation
Alessandra Bordoni	AB
Annette Weninger	AW
Clarissa Feuerstein-Akgöz (Student 1)	CFA
Dieter Weichenhan	DW
Florian Janke	FJ
Giancarlo Rosati	GR
Giampaolo Ugolini	GU
Jessica Heilmann	JH
Karin Klimo	KK
Lisa Demoen (Student 2)	LD
Linda Kessler (Student 3)	LK
Luigi Ricciardiello	LR
Marianna Farnè	MF
Silvia Garelli	SG

Contents

Contributions vii

Contents ix

Summary xiii

Zusammenfassung xv

List of Figures xix

List of Supplementary Figures xxi

List of Tables xxi

List of Abbreviations xxiii

PATHWAY-27 project xxvii

1 Introduction 1

1.1 A definition of the metabolic syndrome 1

1.2 Pathophysiology of the metabolic syndrome 2
1.2.1 Adipocyte cell types and their functions 4
1.2.2 White adipose tissue dysfunction in metabolic syndrome 5
1.2.3 Adipose tissue depots and their associated risks 7

1.3 Adipogenesis 7
1.3.1 Transcriptional networks controlling white adipogenesis 8
1.3.2 SGBS cells as an in vitro model of human adipogenesis 9

1.4 Epigenetic gene regulation 10
1.4.1 Chromatin organization 11
1.4.2 Histone modifications 11
1.4.3 DNA methylation and demethylation 12
1.4.4 Interplay of cell metabolism and epigenetics 14
1.4.5 Analysis of DNA hydroxymethylation 15
1.4.6 Epigenetics of adipogenesis 17
1.4.7 NEIL1, a potential hydroxymethylation reader 18

1.5 DHA and prevention of Metabolic Syndrome 19

2 Aims 21

3 Material and Methods 23

3.1 Materials 23
3.1.1 Instruments 23
3.1.2 Consumables 24

3.2 SGBS cells 26

3.3 SGBS adipocyte differentiation 26

3.4 Long-term cultivation of SGBS preadipocytes with bioactive substances 27
3.4.1 Complexation of DHA with BSA 27
3.4.2 Cytotoxicity experiments 28
3.4.3 Long-term cultivation experiments with DHA and nonDHA 28

3.5 WAT tissue biopsies 29

3.6 Images 30
3.7 Extraction of nucleic acids for epigenetic analyses 30
3.8 Base-resolution hydroxymethylation analysis 31
3.8.1 WGBS/oxBS followed by sequencing 31
3.8.2 BS/oxbBS followed by Illumina 450k array 32
3.9 Non-base resolution hydroxymethylation analysis by hMeSeal 33
3.10 Base resolution DNA methylation analysis by Illumina EPIC array 34
3.12 Gene expression analyses 35
3.12.1 mRNA expression analysis by reverse-transcription qPCR 35
3.12.2 Analyses of mRNA expression by RNA-seq 36
3.13 Proteome data 37
3.14 Metabolome data 37
3.14.1 Targeted metabolome data 37
3.14.2 Untargeted metabolome data 38
3.15 ACT-seq data of WAT tissue 38
3.16 Bioinformatic downstream analyses 41
3.16.1 PMD, LMR, UMR, FMR definitions 41
3.16.2 Mfuzz clustering 41
3.16.3 UCSC genome browser tracks 41
3.16.4 EnrichedHeatmaps and Heatmaps 42
3.16.5 EpiAnnotator enrichment analysis 42
3.16.6 TF motif enrichment analyses 42
3.16.7 hMeSeal cluster at gene expression cluster enrichment analysis 43
3.16.8 Pathway analyses 44
3.16.9 Correlation of hydroxymethylation, histone marks and ATAC 44
3.16.10 Gene body hydroxymethylation correlation analysis 44
3.16.11 Mitotic scores 45
3.17 Data access 45

4 Results Part 1 47

4.1 Global analysis of the methylome during SGBS differentiation 48
4.2 Gain in hydroxymethylation masks the loss of methylation in bisulfite converted data 49
4.3 DNA hydroxymethylation is a stable mark 52
4.4 Clustering of hydroxymethylation dynamics 56
4.5 Hydroxymethylation is enriched at adipocyte enhancer regions 58
4.5.1 5hmC at adipogenic TF binding 63
4.5.2 5hmC at CTCF binding 63
4.6 Transcriptome changes during SGBS differentiation 65
4.6.1 Global transcriptome changes 65
4.6.2 Transcriptome changes linked to hydroxymethylation 68
4.7 Metabolic changes 69
4.7.1 Integrated pathway analysis based on metabolites and associated proteins 69
4.7.2 TCA cycle and hydroxymethylation 72
4.8 Hydroxymethylation in white adipose tissue (WAT) – in vivo relevance 74
4.8.1 Hydroxymethylation at WAT enhancers 74
4.8.2 Hydroxymethylation in WAT highly expressed genes 78
4.9 Acetylated NEIL1 accumulates at adipogenic enhancers in white adipose tissue 79

5 Discussion Part 1 83

5.1 Hydroxymethylation at functional enhancer regions and gene body 83

5.2 Hydroxymethylation dynamics ... 84
5.3 Regulation of hydroxymethylation dynamics ... 85
5.3.1 Potential role of NEIL1 as 5hmC binding protein ... 86
5.3.2 Metabolism and TET activity ... 87
5.3.2.1 The role of αKG and other factors ... 87
5.3.2.2 Modulation of TET activity by posttranslational modifications ... 88
5.4 Function of hydroxymethylation as an epigenetic mark ... 89

6 Conclusion & Outlook Part 1 ... 90

7 Results Part 2 ... 93
7.1 Experimental design and treatment conditions ... 93
7.2 Characterization of the SGBS methylome represented on the EPIC array ... 95
7.3 Global methylation changes during SGBS cultivation confound DHA-induced methylation changes ... 96
7.4 Gain of methylation in gene regulatory regions ... 100
7.5 Epigenetic mitotic clocks in SGBS cells ... 103
7.6 DHA-induced gene expression changes ... 105
7.7 DHA affects TFs regulated in adipocyte differentiation ... 109

8 Discussion Part 2 ... 111
8.1 Cultivation-associated effect in SGBS preadipocytes ... 111
8.1.1 DNA methylation and demethylation machinery ... 112
8.1.2 Metabolism and epigenetic regulation ... 113
8.1.3 Signaling-induced cellular identity ... 114
8.1.4 Lessons learned from cultivating SGBS preadipocytes ... 115
8.2 DHA-associated effects in SGBS preadipocytes ... 116
8.2.1 DHA affects in vitro and in vivo adipocyte differentiation ... 116
8.2.2 Anti-inflammatory effect of DHA in preadipocytes ... 118
8.2.3 DHA-associated repression of SREBP signaling in preadipocytes ... 118

9 Conclusion & Outlook Part 2 ... 120

10 References ... 123

11 Appendix ... 145

12 Publications and Presentations ... 151
12.1 Publications ... 151
12.2 PATHWAY-27 Project Reports ... 151
12.3 Oral Presentations ... 152
12.4 Poster Presentations ... 152

13 Acknowledgements ... 153

Summary

Metabolic Syndrome is a multifactorial metabolic disorder characterized by obesity in association with altered lipid profiles, elevated glucose levels, and/or increased blood pressure, forming a cluster of risk factors for cardiovascular diseases and type 2 diabetes. Changes in lifestyle and diet are powerful strategies in preventing the development of the metabolic syndrome. An evolving research field linked with preventable diseases is the consumption of bioactive-enriched foods since for some bioactives the dose for health-promoting effects can only be achieved by enrichment. Docosahexaenoic acid (DHA) is an n-3 fatty acid displaying lipid-lowering activity. In the liver, DHA inhibits lipogenesis thereby promoting an improved lipid profile in the blood. However, the impact of DHA on preadipocytes, the source for new adipocytes generated during adipogenesis for additional lipid storage, remains insufficiently characterized.

Cell differentiation processes are controlled by epigenetic mechanisms including DNA hydroxymethylation and are associated with cell-type specific transcriptional regulation. To profile epigenetic gene regulation of our model system, I first characterized human adipocyte differentiation of Simpson-Golabi-Behmel Syndrome (SGBS) cells at the level of DNA hydroxymethylation (5hmC) using two whole-genome sequencing techniques. I observed gain in the 5hmC mark during adipocyte differentiation, particularly enriched at enhancer regions, around adipogenic transcription factor (TF) binding sites. Based on cluster analyses, I was able to describe clusters with different dynamics of hydroxymethylation associated with the binding of specific TFs. Early hydroxymethylation clusters were enriched with TF binding motifs involved, e.g., in clonal expansion at an early stage of adipogenesis. On the other hand, hydroxymethylation emerging during late adipogenesis was associated with TF binding in the second phase of chromatin remodeling, such as of the peroxisome proliferator-activated receptor gamma (PPARG) and of CCAAT/enhancer binding protein alpha (CEBPA). Integrated analysis of hydroxymethylation and gene expression recapitulated the involvement of hydroxymethylated enhancer regions in the regulation of gene expression programs characteristic of mature adipocytes. By maintaining mature adipocytes in culture for 14 days after completion of adipocyte differentiation, I could provide evidence for 5hmC as a stable epigenetic mark. *In vivo* relevance of these findings was confirmed by a high degree of overlap with hydroxymethylation in white adipose tissue (WAT). As 5hmC is often considered as an intermediated mark generated during DNA demethylation, I investigated potential mechanisms involved in 5hmC stabilization. I detected that acetylated nei like DNA glycosylase 1 (acNEIL1), reported previously as a hydroxymethylation binding protein, was enriched in WAT promoter and enhancer regions, but its binding was independent of the hydroxymethylation mark,

especially in promoter regions. Based on metabolome data, I rather hypothesize that declining α-ketoglutarate (αKG) levels during adipogenesis could compromise ten-eleven translocation (TET)-mediated demethylation and thereby contribute to stabilization of the 5hmC mark in non-proliferating mature adipocytes.

In the second part of my thesis, I investigated the effect of long-term cultivation (3 - 4 weeks) of SGBS in the presence of low-dose DHA on genome-wide DNA methylation (EPIC array) and gene expression levels (RNA-seq). DHA-treatment resulted in massive methylation differences. However, these methylation differences mainly overlapped with gradual culture-associated methylation changes. A subset of the differentially methylated CpGs was located in partially methylated domains (PMDs) associated with the nuclear lamina and characterized by late replication timing. These sites displayed gradual loss in methylation, correlating with a methylation-based mitotic score (EpiCMIT.hypo) and attributed to an impairment of DNA methylation maintenance during replication. At the gene expression level, I could separate effects directly attributable to DHA from culture-associated gene expression changes. Notably, I detected anti-inflammatory activity by reduction of tumor necrosis factor alpha (TNFα) signaling and repression of sterol regulatory element-binding protein 1/2 (SREBP1/2) signaling, possibly contributing to reduced lipogenesis and increased insulin sensitivity – two crucial mechanisms in the prevention of the metabolic syndrome.

To sum up, molecular understanding of the interplay of cellular metabolism and epigenetics in gene regulation of human adipocyte differentiation might be crucial for the deeper understanding of the development of metabolic syndrome – a disease with altered energy metabolism. Furthermore, deciphering the molecular mechanisms of DHA in human preadipocytes might help to understand how to reverse some of the adverse effects of obesity and its associated metabolic complications, showing us a path towards improved public health.

Zusammenfassung

Das metabolische Syndrom ist eine multifaktorielle Stoffwechselstörung, die durch Fettleibigkeit in Verbindung mit veränderten Lipidprofilen, erhöhten Glukosespiegeln und/oder erhöhtem Blutdruck gekennzeichnet ist und ein Cluster von Risikofaktoren für Herz-Kreislauf-Erkrankungen und Typ-2-Diabetes bildet. Änderungen des Lebensstils und der Ernährung sind wirksame Strategien, um die Entwicklung des metabolischen Syndroms zu verhindern. Ein sich entwickelnder Forschungsbereich im Zusammenhang mit vermeidbaren Krankheiten ist der Verzehr von mit Bioaktivstoffen angereicherten Lebensmittel, da bei einigen Bioaktivstoffen die Dosis für gesundheitsfördernde Wirkungen nur durch Anreicherung erreicht werden kann. Docosahexaensäure (DHA) ist eine n-3-Fettsäure mit lipidsenkender Wirkung. In der Leber hemmt DHA die Lipogenese, wodurch ein verbessertes Lipidprofil im Blut gefördert wird. Die Wirkung von DHA auf Präadipozyten, die sich während der Adipogenese zu neuen Adipozyten für zusätzliche Lipidspeicherung entwickeln können, ist jedoch noch unzureichend charakterisiert.

Zelldifferenzierungsprozesse werden durch epigenetische Mechanismen gesteuert, einschließlich DNA-Hydroxymethylierung, um die zelltypspezifische Genexpression zu regulieren. Um die epigenetische Genregulation unseres Modellsystems zu profilieren, habe ich zunächst die humane Adipozytendifferenzierung von Simpson-Golabi-Behmel Syndrom (SGBS) Zellen auf der Ebene der DNA-Hydroxymethylierung (5hmC) unter Verwendung von zwei Sequenzierungstechniken, die das gesamte Genom abdecken, charakterisiert. Ich beobachtete eine Zunahme von 5hmC während der Adipozytendifferenzierung, besonders an Enhancer-Regionen um die Bindungsstellen der adipogenen Transkriptionsfaktoren (TF) herum. Basierend auf Clusteranalysen konnte ich Cluster mit unterschiedlichen Dynamiken der Hydroxymethylierung beschreiben, die mit der Bindung spezifischer TFs assoziiert waren. Frühe Hydroxymethylierungscluster waren mit TF-Bindungsmotiven angereichert, die z. B. an der klonalen Expansion im frühen Stadium der Adipogenese beteiligt sind. Andererseits war eine spätere Anreicherung der Hydroxymethylierung mit Bindung von TFs in der zweiten Phase des Chromatin-Umbaus assoziiert, wie z. B. des Peroxisom-Proliferator-aktivierten Rezeptor Gamma (PPARG) und von CCAAT/Enhancer-Binding-Protein Alpha (CEBPA). Die integrierte Analyse von Hydroxymethylierung und Genexpression rekapitulierte die Beteiligung von hydroxymethylierten Enhancer-Regionen an der Regulierung von Genexpressionsprogrammen, die für reife Adipozyten charakteristisch sind. Beispielsweise waren spät induzierte Hydroxymethylierungscluster um Gene lokalisiert, die am

Lipidstoffwechsel beteiligt sind. Indem ich reife Adipozyten für 14 Tage nach Abschluss der Adipozytendifferenzierung in Kultur hielt, konnte ich Hinweise darauf geben, dass die beobachtete Hydroxymethylierung eine stabile epigenetische Modifizierung ist. Die *in vivo*-Relevanz dieser Befunde wurde durch einen hohen Grad an Überlappung mit der Hydroxymethylierung im weißen Fettgewebe (WAT) bestätigt. Da 5hmC oft als Zwischenprodukt der DNA-Demethylierung angesehen wird, habe ich mögliche Mechanismen untersucht, die an der 5hmC-Stabilisierung beteiligt sein könnten. Ich fand heraus, dass acetylierte nei-ähnliche DNA-Glykosylase 1 (acNEIL1), die zuvor als Hydroxymethylierungs-bindendes Protein beschrieben worden war, in WAT-Promotor- und Enhancer-Regionen angereichert war, aber die Bindung unabhängig von der Hydroxymethylierung war, insbesondere in Promotor-Regionen. Basierend auf Metabolomdaten stelle ich eher die Hypothese auf, dass sinkende α-Ketoglutarat (αKG)-Konzentrationen während der Adipogenese die Ten-Eleven-Translokation (TET)-vermittelte Demethylierung beeinträchtigen und somit zur Stabilisierung der 5hmC-Modifizierung in nicht proliferierenden reifen Adipozyten beitragen könnten.

Im zweiten Teil meiner Arbeit untersuchte ich die Wirkung einer Langzeitkultivierung (3 - 4 Wochen) von SGBS Präadipozyten in Gegenwart von niedrig dosiertem DHA auf die genomweite DNA-Methylierung (EPIC-Array) und Genexpressionsniveaus (RNA-Sequenzierung). DHA-behandelte Proben zeigten im Vergleich zu Kontrollproben massive Methylierungsunterschiede. Diese Methylierungsunterschiede überschnitten sich jedoch hauptsächlich mit graduellen Zellkultur-assoziierten Methylierungsänderungen. Ein Teil der differenziell methylierten CpGs befand sich in partiell methylierten Domänen (PMDs), die mit der Nuklearlamina assoziiert sind und durch ein spätes Replikationstiming gekennzeichnet sind. Diese Stellen zeigten einen allmählichen Methylierungsverlust, der mit einem methylierungsbasierten mitotischen Index (EpiCMIT.hypo) korreliert und auf eine Beeinträchtigung der DNA-Methylierung während der Replikation zurückzuführen ist. Auf der Ebene der Genexpression konnte ich Effekte, die direkt auf DHA zurückzuführen sind, von Zellkultur-assoziierten Veränderungen der Genexpression trennen. Ich beobachtete eine entzündungshemmende Aktivität durch die Verringerung der Signalübertragung des Tumornekrosefaktors alpha (TNFα) und die Unterdrückung der Signalübertragung des ‚Sterol regulatory element-binding protein 1/2' (SREBP1/2), was möglicherweise zu einer verringerten Lipogenese und einer erhöhten Insulinsensitivität beiträgt, zwei entscheidende Mechanismen zur Prävention des Metabolischen Syndroms.

Zusammenfassend lässt sich sagen, dass das molekulare Verständnis des Zusammenspiels von Zellstoffwechsel und Epigenetik bei der Genregulation der Adipozytendifferenzierung entscheidend für das tiefere Verständnis der Entwicklung des metabolischen Syndroms ist,

einer Krankheit mit verändertem Energiestoffwechsel. Darüber hinaus könnte die Aufklärung molekularer Mechanismen von DHA in menschlichen Präadipozyten helfen zu verstehen, wie einige der metabolischen Komplikationen, die mit Fettleibigkeit verbunden sind, rückgängig gemacht werden können, um uns einen Weg zu einer verbesserten Gesundheit der Bevölkerung aufzuzeigen.

List of Figures

Fig. 1| Development of the metabolic syndrome. 3
Fig. 2| The modes of expansion of white adipose tissue (WAT). 6
Fig. 3| Two waves of adipogenic transcription factor (TF) binding. 9
Fig. 4| DNA methylation and demethylation cycle. 13
Fig. 5| Metabolism regulating epigenetic remodeling. 15
Fig. 6| Hydroxymethylation sequencing methods. 16
Fig. 7| n-6 and n-3 fatty acid-derived lipid mediators involved in inflammation 20
Fig. 8| Overview of experiments related to multi-omic analyses during adipogenesis (thesis part 1). 27
Fig. 9| Overview of the DHA long-term treatment experiments and applied epigenetic methods (thesis part 2). 29
Fig. 10| Overview of WAT biopsies and applied epigenetic methods (thesis part 2) 30
Fig. 11| SGBS adipocyte differentiation. 47
Fig. 12| Genome-wide characterization of the SGBS methylome. 48
Fig. 13| Loss in DNA methylation during adipocyte differentiation. 50
Fig. 14| Gain in hydroxymethylation during adipocyte differentiation. 51
Fig. 15| Quality control of hMeSeal-based hydroxymethylation profiles during adipocyte differentiation. 52
Fig. 16| hMeSeal identifies regions with CpG sites gaining hydroxymethylation. 53
Fig. 17| Hydroxymethylation validation by WGBS/oxBS at individual loci. 55
Fig. 18| Mfuzz clustering of hydroxymethylation dynamics. 56
Fig. 19| Comparison of hydroxymethylation changes in hydroxymethylation clusters. 57
Fig. 20| Hydroxymethylation is enriched in enhancer regions. 58
Fig. 21| Hydroxymethylation in chromatin accessible regions. 59
Fig. 22| UCSC genome browser track of hMeSeal signal at the PLIN1 locus. 60
Fig. 23| Motifs of adipogenic transcription factors (TF) are enriched at hydroxymethylation clusters. 61
Fig. 24| Hydroxymethylation is enriched around the TF binding motifs. 62
Fig. 25| Hydroxymethylation is enriched around CEBPA and PPARG binding. 63
Fig. 26| Hydroxymethylation levels at CTCF binding sites. 64
Fig. 27| Mfuzz clustering of transcriptional changes. 65
Fig. 28| KEGG overrepresentation analysis of eCls. 66
Fig. 29| Validation of mRNA expression changes of eCl5 at the protein level. 68
Fig. 30| Transcriptional changes linked to hydroxymethylation changes. 69
Fig. 31| Mfuzz clustering of metabolites. 70
Fig. 32| Integrated KEGG pathway enrichment analysis of protein and metabolite dynamics. 71
Fig. 33| Proteins of the TCA cycle are upregulated, but metabolites have distinct dynamics. 72
Fig. 34| TCA cycle displayed at the level of gene expression and metabolites. 73
Fig. 35| UCSC track of hydroxymethylation and histone marks in WAT at the ADIPOQ locus. 75
Fig. 36| Hydroxymethylation at WAT enhancer 76

Fig. 37| Transcription factor motifs at WAT enhancer. 77
Fig. 38| Gene body hydroxymethylation in WAT enhances genes..... 78
Fig. 39| Transcriptional changes of NEIL1 and interaction partners in adipogenesis and adipose tissue. 79
Fig. 40| The hydroxymethylation reader NEIL1 accumulates at enhancer regions in white adipose tissue. 80
Fig. 41| UCSC brower track with NEIL1 binding at the PPARG locus. 81
Fig. 42| Cytotoxicity experiments of docosahexaenoic acid (DHA), propionate (PRO), and protocatechuic acid (PA) using SRB staining. 94
Fig. 43| Characterization of the SGBS methylome and its representation on the EPIC array. 95
Fig. 44| Partially methylated domains are marked by H3K9me3 and flanked by H3K27me3..... 96
Fig. 45| Tri-dimensional PCA of methylation changes during SGBS cultivation and DHA long-term treatment. 97
Fig. 46| Methylation changes associated with principal component 1. 98
Fig. 47| Methylation changes associated with principal component 2. 99
Fig. 48| Methylation changes associated with principal component 3. 100
Fig. 49| Enrichment analysis of ChromHMM states. 101
Fig. 50| Top10 enriched transcription factor motifs associates with Principal Component 2 (-). 102
Fig. 51| Principal component 2 correlates best with mitotic clock EpiCMIT.hypo. 103
Fig. 52| DHA treatment effects on methylation-based mitotic clocks. 104
Fig. 53| DHA-associated gene expression changes in cultivated SGBS preadipocytes. 105
Fig. 54| Heatmap of DHA-regulated genes. 106
Fig. 55| Pathway overrepresentation analysis of DHA-induced downregulated genes..... 106
Fig. 56| DHA downregulates genes associated with Cholesterol metabolism and the SREBP signaling pathway. 107
Fig. 57| Transcription factor activity associated with DHA treatment. 108
Fig. 58| DHA-associated TF in adipocyte differentiation. 110

List of Supplementary Figures

Supplementary Fig. 1| Validation of differentially methylated sites by 450k array. 145
Supplementary Fig. 2| PCA of WGBS/oxBS-derived hydroxymethylation levels..... 145
Supplementary Fig. 3| Heatmap of CpGs associated with PC1. 146
Supplementary Fig. 4| Heatmap of CpGs associated with PC2. 147
Supplementary Fig. 5| CpGs of PC2 (+ assoc.) are enriched for the largest PMDs with the strongest degree of demethylation. 148
Supplementary Fig. 6| Heatmap of CpGs associated with PC3. 149
Supplementary Fig. 7| Expression of epigenetic genes during long-term cultivation. 150

List of Tables

Table 1| Abbreviations of contributors to this thesis. viii
Table 2| International Diabetes Federation (IDF) definition of the metabolic syndrome. 2
Table 3| Histone marks and associated enzymes in the modulation of chromatin function 12
Table 4| Master mix for cDNA synthesis. 35
Table 5| RT-qPCR primers. 36
Table 6| Selected ion monitoring (SIM) values. 38
Table 7| List of antibodies against histone marks used for ACT-seq. 38

List of Abbreviations

5caC	5-carboxyl C
5fC	5-formyl C
5hmC	5-hydroxymethyl C
5mC	5-methylcytosine (C)
A	adenine
acetyl-CoA	acetyl-Coenzyme A
acNEIL1	acetylated nei-like DNA glycosylase 1
ACSL1	Acyl-CoA Synthetase Long Chain Family Member 1
ADIPOQ	adiponectin
ADS	adipose derived stem cells
ALA	alpha-linoleic acid
AMP	adenosine monophosphate
AMPK	AMP-activated protein kinase
ASF1A	anti-silencing function protein 1A
ATAC	assay for transposase-accessible chromatin
ATP	adenosine triphosphate
BER	base excision repair
bp	base pairs
BS	bisulfite
BSA	bovine serum albumin
C	cytosine
cAMP	cyclic adenosine monophosphate
cDNA	complementary deoxyribonucleic acid (DNA)
CEBPA/B/D/E	CCAAT enhancer binding protein alpha/beta/delta/epsilon
CFD	complement factor D
CHAF1A	chromatin assembly factor (CAF)-1 subunit A
ChIP-seq	chromatin immunoprecipitation sequencing
COX	cyclooxygenase
CpG	cytosine phosphate guanine
CPM	counts per million
CREB1	cAMP response element-binding protein 1
CTCF	CCCTC-binding factor
CYP	cytochrome P450
DEX	dexamethasone
DHA	docosahexaenoic acid
DhMS	differentially hydroxymethylated CpG site
DHS	DNAse I hypersensibility sites
DKFZ	Deutsches Krebsforschungszentrum (German Cancer Research Center)
DMS	differentially methylated CpG site
DMSO	dimethylsulfoxid
DNA	deoxyribonucleic acid
DNMT1/3a/3b	DNA (cytosine-5)-methyltransferase 1/3a/3b
dNTP	deoxynucleotide triphosphate
EBF1	EBF transcription factor 1
eCl	expression cluster
ECM	extracellular matrix

EHMT2	euchromatic histone lysine methyltransferase 2
EMT	epithelial-to-mesenchymal transition
EPA	eicosapentaenoic acid
EpiCMIT	epigenetically-determined cumulative mitoses
EU	European Union
EZH2	enhancer of zeste homolog 2
FABP4	fatty acid-binding protein 4
FAD	flavin adenine dinucleotide
FADH2	reduced flavin adenine dinucleotide (FAD)
FASN	fatty acid synthase
fdr	false discovery rate
FFA	free fatty acid
FFAR4	free fatty acid receptor 4
FGF1	fibroblast growth factor 1
FOSL1	FOS like 1
FOX	forkhead-box
G	guanine
GPC3	glypican 3
GR	glucocorticoid receptor
H3	histone H3
H3K27ac	histone H3 lysine 27 acetylation
H3K27me3	histone H3 lysine 27 tri-methylation
H3K4me1	histone H3 lysine 4 mono-methylation
H3K4me3	histone H3 lysine 4 tri-methylation
H3K9me2	histone H3 lysine 9 di-methylation
H3K9me3	histone H3 lysine 9 tri-methylation
HPRT1	hypoxanthine phosphoribosyltransferase 1
IBMX	1-methyl-3-isobutylxanthine
IC	inhibitory concentration
IDF	International Diabetes Federation
IDH1	Isocitrate dehydrogenase 1
IL-6	interleukin-6
IPA	ingenuity pathway analysis
ISMARA	Integrated System for Motif Activity Response analysis
KLF4/5	kruppel-like factor 4/5
L-2-HG	2-hydroxyglutarate
LA	linoleic acid
LDL	low density lipoprotein
LIS	large intervention study
LMR	lowly methylated region
log2CPM	log2 counts per million
LOX	lipoxygenase
LPS	lipopolysaccharide
MAFB	MAF BZIP transcription factor B
mCl	metabolite clusters
MCP-1	monocyte chemoattractant protein-1
MECP2	methyl-CpG binding protein 2
MED1	mediator complex subunit 1
mRNA	messenger ribonucleic acid

MS	mass spectrometry
MSC	mesenchymal stem cell
MSH6	mutS homolog 6
mTOR	mechanistic target of rapamycin
NAD+	nicotinamide adenine dinucleotide
NADH	reduced nicotinamide adenine dinucleotide
NADPH	reduced nicotinamide-adenine dinucleotide phosphate
NEIL1	nei like DNA glycosylase 1
NFIA/C	nuclear factor I A/C
NFκB	nuclear factor kappa B
oxBS	oxidative bisulfite
PA	protocatechuic acid
PBS	phosphate buffered saline
PC	principal component
PCA	principal component analysis
PCNA	proliferating cell nuclear antigen
PCR	polymerase chain reaction
PLIN1	perilipin 1
PMD	partially methylated domain
PPARG/G2	peroxisome proliferator activated receptor gamma/gamma transcript 2
Prdm16	PR/SET domain 16
PRO	propionate
PUFA	polyunsaturated fatty acid
qPCR	quantitative polymerase chain reaction
RNA	ribonucleic acid
RNA-seq	RNA sequencing
RT-qPCR	reverse-transcription quantitative polymerase chain reaction
RXR	retinoid X receptor
RXRA	retinoid X receptor alpha
SAM	S-adenosyl methionine
SAT	subcutaneous adipose tissue
SD	standard deviation
SDS	sodium dodecylsulfate
SFA	saturated fatty acid
SGBS	Simpson-Golabi-Behmel syndrome
SRB	sulforhodamin B
SREBF1/2	sterol regulatory element binding transcription factor 1/2
SREBP1a/1c/2	sterol regulatory element binding protein 1a/1c/2
STAT5A/B	signal transducer and activator of transcription 5A/B
T	thymine
TBP	TATA-box binding protein
TCA cycle	tricarboxylic acid cycle
TDG	thymine DNA glycosylase
TET	ten-eleven translocation
TF	transcription factor
TG	triglycerides
TGFB1	transforming growth factor beta 1
TGFβ	transforming growth factor beta
TNFα	tumor necrosis factor alpha

TSS	transcription start site
UCSC	University of Carlifornia, Santa Cruz
UHRF1/2	ubiquitin like with PHD and ring finger domains 1/2
UMR	unmethylated region
UPLC	ultra-performance liquid chromatography
VAT	visceral adipose tissue
VLDL	very low density lipoprotein
WAT	white adipose tissue
WGBS	whole-genome bisulfite sequecing
WGoxBS	whole-genome oxidative bisulfite sequencing
ZBTB7A	zinc finger and BTB domain containing 7a
αKG	α-ketoglutarate

PATHWAY-27 project

The work of this thesis was part of the EU-funded project PATHWAY-27, formed by an interdisciplinary team consisting of 25 partner institutions across Europe, including universities, research institutes, and SMEs (Small and Medium Enterprise). The aim of PATHWAY-27 was to develop and investigate the effect of three bioactives, namely docosahexaenoic acid (DHA), β-glucan, and anthocyanins, enriched in three different food matrices (egg-based-, dairy-, and bakery products)) in preventing the development of the metabolic syndrome (www.pathway27.eu).

DHA is an essential n-3 fatty acid produced by algae and found in sea fish and is known for its anti-inflammatory function and reducing triglycerides in the blood (Albracht-Schulte et al., 2018). β-glucan is a fiber found in oat or barley and is involved in improving cholesterol levels (Tiwari and Cummins, 2011). The third investigated group of bioactives are the anthocyanins, water-soluble pigments responsible for various fruits' blue or red color, which serve as powerful antioxidants (Yeung et al., 2019).

Several natural food compounds are known for their health-promoting activity. However, their concentrations found in foodstuff are often too low to achieve these effects through a regular diet. Therefore, health-promoting effects could be achieved by formulation of foods enriched in these bioactives. To commercialize and advertise the bioactive-enriched foods with health-promoting effects, health claims have to be approved by the European Food Safety Authority (EFSA), by presenting convincing evidence of the given health claims. Therefore, PATHWAY-27 served as an example of how to develop bioactive-enriched foods, test the stability of the bioactives in the food matrix, investigate the bioactive function *in vitro*, and finally *in vivo* in a large dietary intervention study (LIS). The overarching goal of PATHWAY-27 was to generate protocols, best practices, and guidelines for the food industry and research institutes for the future development of bioactive-enriched foods and the generation of health claims (Bordoni et al., 2019).

As a partner of PATHWAY-27, our group was to analyze the epigenetic influence of the three key compounds on adipocytes. Different from previous *in vitro* studies, I planned to use i) low physiologically relevant concentrations, ii) perform long-term chronic compound treatment for several weeks instead of short term exposure, iii) use physiologically relevant metabolites of the study compounds, i.e. beside DHA, protocatechuic acid (PA), one of the most abundant metabolites of anthocyanins, and propionate (PRO), a metabolite of β-glucan, and iv) use the compounds alone and in combination to mimic dietary exposure. Part 2 of this thesis introduces

the findings of low-dose, long-term DHA treatment in pre-adipocytes, which turned out to be the most effective compound.

As a model of human adipogenesis, I employed the preadipocyte cell line Simpson-Golabi-Behmel syndrome (SGBS). SGBS cells can be differentiated *in vitro* to mature adipocytes and seemed ideal for our epigenomics analyses. Since this cell strain had not been epigenetically characterized before, I initially analyzed the DNA methylome during adipogenesis without prior compound treatment. During these analyses, I realized that not only the DNA methylome, but especially the DNA hydroxymethylome changed during adipocyte differentiation. By collaborating with groups from Munich and Leipzig that were not part of PATHWAY-27, I also had the opportunity to compare our epigenetic results with proteome and metabolome changes during adipogenesis in the same SGBS cell line. These findings are presented in the first part of the thesis.

1 Introduction

1.1 A definition of the metabolic syndrome

Overweight and obesity describe the expansion of adipose tissue resulting from an imbalance of energy intake and expenditure and are defined by a body mass index (BMI) ≥ 25 and ≥ 30, respectively. In 2016, overweight affected about 35 % of the adult population worldwide, and obesity about 13 %. Although principally preventable, overweight and obesity have developed into a global pandemic. In addition, obesity poses a risk for developing metabolic disorders such as glucose intolerance, dyslipidemia, and cardiovascular diseases, being the most frequent cause of death worldwide (World Health Organization, 2021).

Metabolic disorders associated with obesity form a cluster of interrelated diseases, likely driven by common underlying causes and mechanisms, as all risk factors respond to diet and physical activity (Huang, 2009). Therefore, it is presumable that obesity itself is a central component driving the metabolic syndrome (Lemieux et al., 2000). To better identify the individuals with a high risk of developing obesity-related diseases, several groups and institutions introduced definitions of the metabolic syndrome. The International Diabetes Federation (IDF) definition focused on the worldwide practical usability to identify individuals at risk while allowing worldwide comparability of the identified prevalence. The main criterion of the metabolic syndrome is central obesity, defined by ethnic- and sex-specific waist circumference cut-offs (Table 2). In addition to central obesity, individuals must fulfill two of the four following metabolic complications: raised triglycerides, reduced high-density lipoprotein (HDL)-cholesterol, increased blood pressure (BP), and hyperglycemia identified by raised fasting plasma glucose (FPG) or previously diagnosed type 2 diabetes. The factors are determined by surpassing the clinical cut-offs or by specific treatment of the corresponding metabolic complication (Alberti et al., 2005). Although insulin resistance is a central part of the cluster of metabolic complications and highly correlates with waist circumference and triglycerides, the IDF did not include insulin resistance as a criterion for metabolic syndrome, as it is not easy to estimate (Lemieux et al., 2000).

Table 2| International Diabetes Federation (IDF) definition of the metabolic syndrome.

Criteria	Clinical cut-off
Central obesity	defined as waist circumference with ethnicity-specific values, Europids: ≥ 94 cm (male), ≥ 80 cm (female)
plus any two of the following four factors:	
Raised triglycerides	≥ 150 mg/dL (1.7 mmol/L) or specific treatment for this lipid abnormality
Reduced HDL cholesterol	< 40 mg/dL (1.03 mmol/L) in males < 50 mg/dL (1.29 mmol/L) in females or specific treatment for this lipid abnormality
Raised blood pressure (BP)	systolic BP ≥ 130 mm Hg or diastolic BP ≥ 85 mm Hg or treatment of previously diagnosed hypertension
Raised fasting plasma glucose (FPG)	FPG ≥ 100 mg/dL (5.6 mmol/L), or previously diagnosed type 2 diabetes.

HDL: high-density lipoprotein (Adapted from S. G. Alberti et al., 2006)

1.2 Pathophysiology of the metabolic syndrome

Obesity is a central component of the metabolic syndrome (Fig. 1). Obese adipose tissue fuels the development of metabolic syndrome by the secretion of free fatty acids (FFAs) and inflammatory cytokines, inducing systemic inflammation (Eckel et al., 2005; Miranda et al., 2005). When in adipose tissue lipid storage capacity has reached a limit, lipids accumulate ectopically, e.g., in muscle cells. There, FFAs inhibit intramuscular glycogen synthesis. Furthermore, FFAs and systemic inflammation result in muscular insulin resistance (Boden and Shulman, 2002). As insulin resistance leads to reduced glucose uptake into muscle cells and, therefore, a decreased glucose clearance in the bloodstream, β-cells secrete increased insulin levels as a compensation mechanism. However, this can cause ß-cell exhaustion, and the reduced insulin levels cannot sufficiently lower blood glucose levels (hyperglycemia) (Hudish et al., 2019). FFAs also accumulate in the liver and promote the development of fatty liver disease. In the liver, systemic inflammation and excess lipids can cause insulin resistance, resulting in uncontrolled glucose production (gluconeogenesis), further increasing blood glucose levels (hyperglycemia) (Eckel et al., 2005). To alleviate the high levels of lipids, the liver secretes triglycerides packed within very low density lipoprotein (VLDL) particles that, when depositing lipids in adipose or muscle tissue, are transformed to low density lipoprotein (LDL) particles.

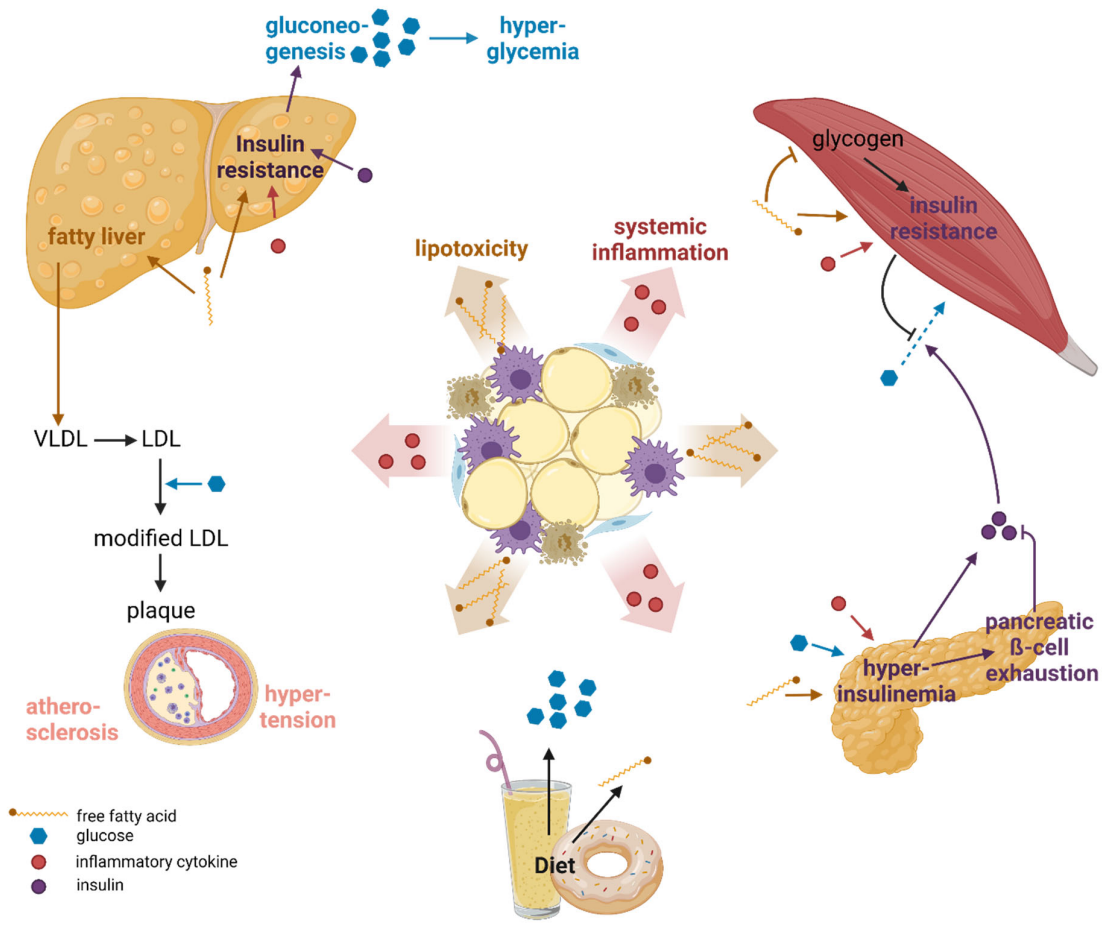

Fig. 1| Development of the metabolic syndrome. During the development of the metabolic syndrome, a high caloric diet promotes obese adipose tissue. The obese adipose tissue secretes pro-inflammatory cytokines and free fatty acids, promoting low-grade systemic inflammation, lipotoxicity, and insulin resistance in several organs. More detailed description in chapter 1.2. The figure was created with BioRender.com and adapted from (Eckel et al., 2005). VLDL: very low density lipoprotein; LDL: low density lipoprotein.

LDL particles can get oxidized or glycated in an environment of oxidative stress, inflammation, and high blood glucose levels. These modified LDL particles are no longer quickly cleared from the bloodstream. In the development of atherosclerosis, modified LDL particles pass the endothelial wall that has been damaged, e.g., by hypertension or smoking. The LDL particles get trapped around the endothelium and immune cells uptake these modified LDL particles in an uncontrolled way to form foam cells, creating plaque in the arteries (Linton et al., 2000).

Insulin resistance is considered a major metabolic complication that prevents glucose uptake by various organs. However, by reducing glucose uptake, insulin resistance also prevents excessive lipid accumulation (lipotoxicity) across multiple tissue types by stimulating fatty acid oxidation and preventing de novo lipogenesis. Further, in search of the origin of the metabolic syndrome, Unger suggested that insulin resistance might only result from leptin resistance.

Leptin is a hormone produced and secreted from adipocytes to regulate energy balance in the brain, by inhibiting hunger. However, during leptin resistance, leptin cannot successfully pass the blood-brain barrier and control food intake in the first place (Unger, 2003).

1.2.1 Adipocyte cell types and their functions

Adipose tissue comprises adipocytes, occupying most of its volume, with its central function in serving as a storage place for energy. Adipocytes are, however, not the most abundant cell type, as the adipose tissue represents a heterogeneous tissue, also containing adipocyte precursor cells, the preadipocytes, stem cells, macrophages, neutrophils, lymphocytes, and endothelial cells (Esteve Ràfols, 2014). Adipocytes store energy in the form of triglycerides, and in times of energy deprivation, they release energy by lipolysis (Birsoy et al., 2013). Over the past two decades, it became evident that adipose tissue also functions as an endocrine organ to control whole-body energy homeostasis. Adipocytes secrete adipose-derived cytokines, adipokines, and lipokines. Additional functions can be local energy supply to neighboring tissues such as lymph nodes or the heart by paracrine secretion of fatty acids (Ouwens et al., 2010), support of immune cells, and supply of mammary glands with fatty acids for lactation. Adipose tissue also acts as a thermal insulator or can generate heat by thermogenesis. It also can protect by absorbing shocks, e.g., in the heels and around inner organs and blood vessels (Zwick et al., 2018).

The body possesses different adipocytes organized in different tissue types and locations to fulfill their variety of functions. However, most adipose tissues contain white adipocytes forming white adipose tissue (WAT). WAT cells derive from perivascular cells of the mesenchymal lineage, located along the vasculature (Gupta et al., 2012; Tang et al., 2008; Tran et al., 2012). When differentiated to mature white adipocytes, they contain a large lipid droplet, while the cytoplasm and nucleus are densely packed at the cell periphery. Their principal role is the storage of excess energy. Upon glucose import, white adipocytes undergo de novo lipogenesis to form triglycerides (TGs) deposited in lipid droplets. White adipocytes also store circulating lipids which they take up as FFA or from lipid transport particles such as VLDL particles or chylomicrons. In energy deprivation, white adipocytes undergo lipolysis, where fatty acids stored as TGs are hydrolyzed to FFA and glycerol for delivery to the blood circulation. WAT can be found subcutaneously and is therefore also called subcutaneous adipose tissue (SAT) and around the inner organs, where it is called visceral adipose tissue (VAT) (Zwick et al., 2018).

In contrast to WAT, the primary function of brown adipose tissue is heat production. Brown adipose tissue is organized in islands between WAT, at the neck, armpits, next to the kidney,

along the large blood vessels and trachea, and in children between shoulder blades (Enerbäck, 2010). Morphologically, brown adipocytes are distinct from white as they contain several small lipid droplets (multilocular) and owe their brown color to a high number of mitochondria. Brown adipocytes can exploit fatty acids for heat production and weight control instead of ATP synthesis in exposure to an obesogenic diet or cold (Feldmann et al., 2009). The uncoupling protein 1 (UCP1) transmembrane protein generates a proton leak across the mitochondrial inner membrane. Therefore, through non-shivering thermogenesis, it uncouples respiration from ATP production, and instead of ATP, heat is generated (Nicholls and Locke, 1984). Brown preadipocytes also originate from mesenchymal stem cells (MSCs). However, they display a myogenic transcriptional signature and a distinct lineage development. In contrast, beige/bright adipocytes functionally and morphologically resemble brown adipocytes but transdifferentiate from white adipocytes upon cold exposure. Therefore they do not form their own depot but are interspersed within WAT (Berry et al., 2015). Recent research interest has focused on studying how to increase the differentiation rate of brown or beige adipocytes or to increase their activity in the hope of increasing energy expenditure in the prevention of metabolic syndrome (Enerbäck, 2010).

Bone marrow adipocytes have a characteristic yellow color owed to the intermediate levels of mitochondria and have been mostly ignored in the past. They are thought to have a function in the regulation of bone and energy homeostasis, but their exact function and lineage development are yet far from understood (Berry et al., 2015)

1.2.2 White adipose tissue dysfunction in metabolic syndrome

In functional adipose tissue, energy homeostasis upon excessive calorie intake is regained by extending the energy storage capacity in WAT. Another level of regulation is endocrine signaling, e.g., by secreting increased levels of leptin, controlling the food intake and energy expenditure in the brain. Healthy adipose tissue increases storage capacity by combining two mechanisms: adipocyte hypertrophy and hyperplasia (Fig. 2). First, existing mature adipocytes store the additional lipids while increasing their volume (hypertrophy). Next, hypertrophic adipocytes induce hyperplasia via paracrine signaling: The signaling molecules induce adipocyte precursor cell differentiation to mature adipocytes, providing additional storage capacity.

In unhealthy adipose tissue, paracrine signaling becomes deregulated and induces a shift towards hypertrophy while inhibiting hyperplasia. When adipocytes reach a critical size, mechanical stress and hypoxia increase, both resulting in adipose tissue inflammation.

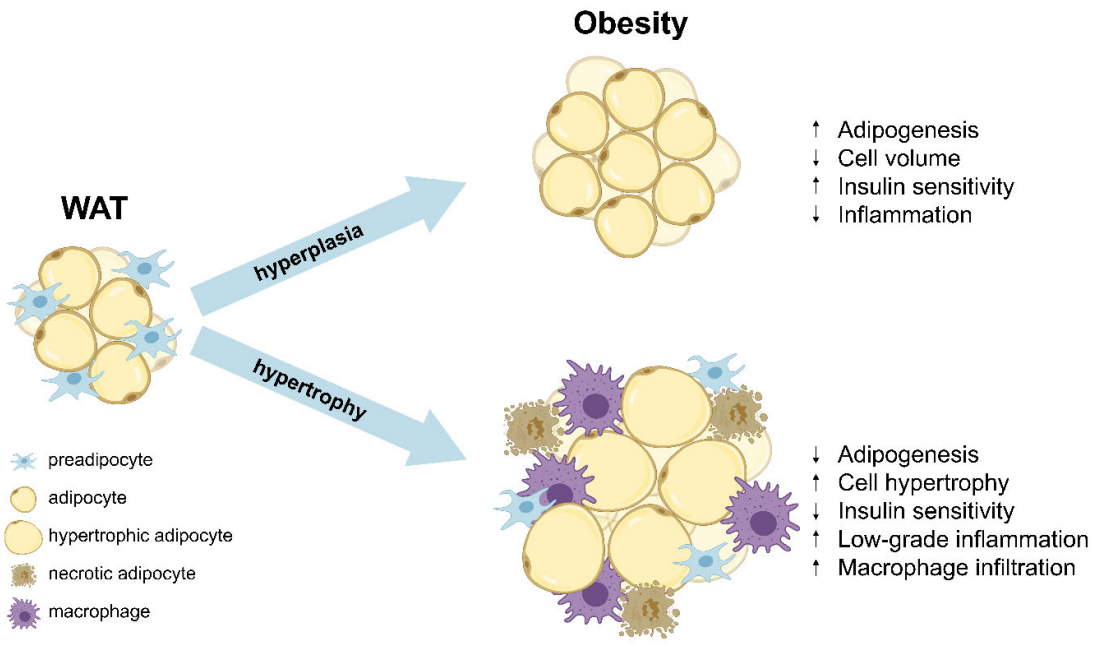

Fig. 2| The modes of expansion of white adipose tissue (WAT). In obesity, adipose tissue can handle excessive energy intake through two different mechanisms. Hyperplasia is a healthy adaptation process in preadipocytes that differentiate to mature adipocytes. With the additional adipocytes, energy can be stored without metabolic complications. On the other hand, hypertrophy is an unhealthy adaptation in which pre-existing adipocytes have to handle the excess energy intake and become enlarged, associated with adverse side effects. The figure was created with BioRender.com and adapted from Longo et al., 2019.

Hypertrophic adipocytes secrete several proinflammatory cytokines, including tumor necrosis factor alpha (TNFα), interleukin-6 (IL-6), interleukin-8 (IL-8), and monocyte chemoattractant protein-1 (MCP-1). Local inflammation decreases insulin sensitivity of adipocytes by phosphorylation of insulin receptor substrate 1 (IRS-1) and recruits immune cells. First T-cells, then pro-inflammatory M1 macrophages, instead of the tissue-resident anti-inflammatory M2 macrophages, are recruited. A typical feature of adipose tissue in obesity is macrophages forming crown-like structures around necrotic adipocytes. Accumulation of pro-inflammatory immune cells in adipose tissue finally advances systemic inflammation and contributes to insulin resistance (Ghaben and Scherer, 2019; Vegiopoulos et al., 2017). Inflammation further reduces the expression and secretion of the anti-inflammatory and energy homeostasis-controlling adipokine adiponectin. Finally, adipose tissue insulin resistance increases the rate of lipolysis and therefore promotes FFA secretion, resulting in ectopic lipid deposition and lipotoxicity (Morigny et al., 2016).

To sum up, when in obesity the storage capacity of adipocytes reaches its maximum, metabolic complications arise. The development of lipotoxicity and systemic inflammation initiated in obese adipose tissue are pivotal to developing insulin resistance in different organs and associated complications (Fig. 1 + 2) (Tan and Vidal-Puig, 2008).

1.2.3 Adipose tissue depots and their associated risks

During overfeeding, the most affected storage location is SAT (> 80 %) followed by VAT (10 % (female), 20 % (male)) (Walker et al., 2014). However, tissue expansion in these two locations is associated with different risks. In VAT, hypertrophy leads to inflammation associated with insulin resistance, which occurs only to a smaller extent in SAT (Verboven et al., 2018). In contrast, in SAT, preadipocytes maintain a higher proliferation rate which allows overall a higher lipid accumulation rate (Macotela et al., 2012; Tchkonia et al., 2006), while adipocytes in VAT display higher rates of lipolysis and apoptosis (Arner et al., 1990; Lafontan and Girard, 2008). It is, however, important to mention that the problematic circulating FFAs mainly are delivered from SAT. This suggests that hypertrophic SAT is the source of circulating FFAs and, therefore, the development of the metabolic syndrome. This results in lipotoxicity in various organs, including VAT, where adipocytes can cope worse with the excess lipids due to their metabolic differences. These findings have recently brought the spotlight onto SAT instead of VAT as the “real” culprit in the development of metabolic syndrome (Jensen, 2020).

1.3 Adipogenesis

Within eight years, 50 % of adipocytes in SAT are replaced (Spalding et al., 2008). This high turnover of adipocytes opens possibilities for interventions in obesity to promote the expansion of the adipose tissue via hyperplasia instead of hypertrophy. The adipocyte pool is renewed from undifferentiated progenitor cells or by dedifferentiation of mature adipocytes to preadipocytes, which proliferate and subsequently redifferentiate back to mature adipocytes (Symonds, 2017). Adipocyte development can be divided into two stages, the commitment of MSCs to the adipogenic lineage and the differentiation to mature adipocytes. With the study of *in vitro* models, we have learned that several signals, such as growth hormones, elevated cyclic adenosine monophosphate (cAMP), glucocorticoids, and changes in the extracellular matrix (ECM) induce adipocyte differentiation. When preadipocytes reach confluency, cells go into growth arrest. Upon stimulation, preadipocytes synchronously re-enter the cell cycle and after few rounds of mitotic clonal expansion, cells are able to enter terminal maturation (Farmer, 2006). During differentiation, the cell shape switches very early from fibroblastic to spherical shape, and during the end of the terminal maturation, the lipid accumulation in lipid droplets becomes visible (Gregoire et al., 1998).

1.3.1 Transcriptional networks controlling white adipogenesis

While little is known about the commitment of MSCs to preadipocytes, the network of regulatory transcription factors (TFs) controlling the differentiation of preadipocytes to adipocytes has been extensively studied. There are two waves of TF binding and chromatin remodeling (Fig. 3). After reaching confluency, stimulation with an adipogenic medium induces the first wave occurring in the first two days, during clonal expansion. cAMP elevating agents activate cAMP response element-binding protein 1 (CREB1), which induces in the first hour the mRNA expression of CEBPB (CCAAT enhancer binding protein beta). Furthermore, glucocorticoids bind to the glucocorticoid receptor (GR) and induce the expression of *CEBPB* and *D*. In the first wave CEBPB/D act together with other early TFs, such as GR, STAT5A/B (signal transducer and activator of transcription 5A/B), CREB1, KLF4/5 (kruppel-like factor 4/5) and EGR2 (early growth response 2). In this process, CEBPB can act as a pioneering factor binding to closed chromatin, where chromatin becomes remodeled to enhancer regions (with acetylation of histone H3 at lysine 27 (H3K27ac)) (see chapter 1.4.2). Then, additional TFs can bind and jointly induce the expression of the target genes. Two essential target genes induced within the first wave are the adipogenic master TFs PPARG (peroxisome proliferator activated receptor gamma) and CEBPA (CCAAT enhancer binding protein alpha). In the second wave, PPARG further induces the expression of *CEBPA,* and synergistically, they form with other TFs TF hotspots of the second wave, located at DNAse I hypersensibility sites (DHS) of the first wave (stable DHS) or at new genomic positions (*de novo* DHS). CEBPA also binds 90 % of PPARG binding sites, showing that TFs often collaborate in gene activation of downstream genes forming the phenotype of mature adipocytes, e.g., by the induction of the insulin receptor, fatty acid-binding protein 4 (FABP4), and adiponectin (ADIPOQ) (reviewed in Cristancho & Lazar, 2011; Siersbaek & Mandrup, 2011).

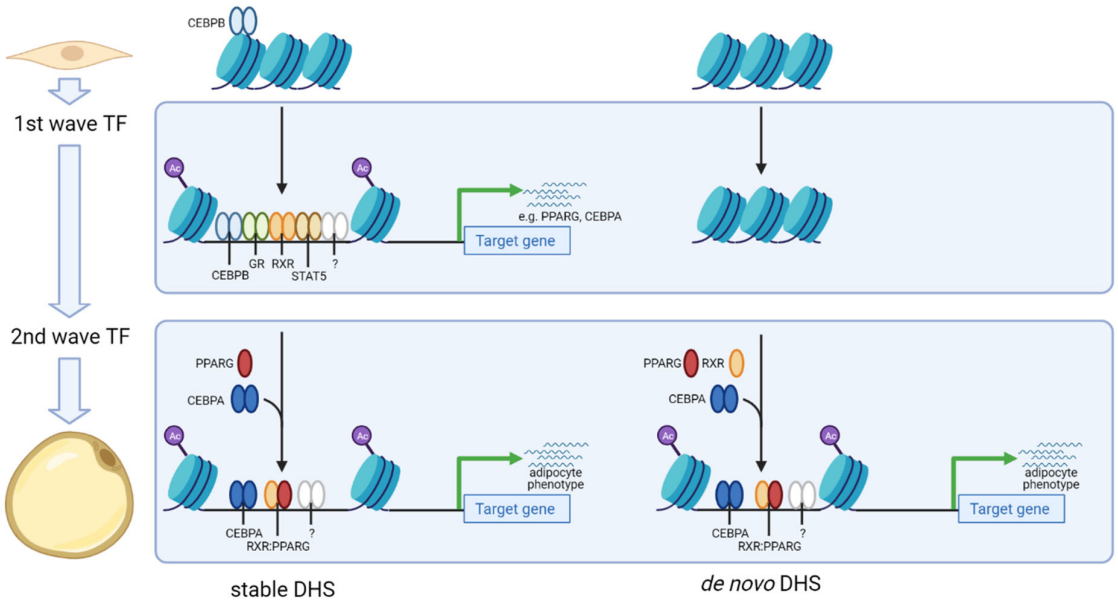

Fig. 3| Two waves of adipogenic transcription factor (TF) binding. The adipocyte differentiation is coordinated by two temporal waves of TF binding at hotspots where the signal of multiple TFs is integrated. In the first wave, pioneering factors such as CEBPB induce chromatin remodeling for binding of additional TFs of the first wave. These TF binding sites are characterized by accessible chromatin and histone H3 lysine 27 acetylation (H3K27ac). TF induced during the first wave, e.g., PPARG and CEBPA, are recruited during the second wave to the same TF hotspots (stable DHS) or to new TF hotspots (de novo DHS). Together with TFs of the first wave they induce the expression of genes forming the adipocyte phenotype. Transient DHS are TF hotspots only present at the first wave (not shown). The figure was created with BioRender.com and adapted from (Siersbaek and Mandrup, 2011; Steger and Lazar, 2011). CEBPA/B: CCAAT enhancer binding protein alpha/beta, GR: glucocorticoid receptor, RXR: retinoid X receptor, STAT5: signal transducer and activator of transcription 5. DHS: DNAse I hypersensibility sites.

1.3.2 SGBS cells as an *in vitro* model of human adipogenesis

Most knowledge on adipocyte differentiation has been generated with the murine transformed preadipocyte 3T3-L1 cell line. Studying the differentiation process in the Simpson-Golabi-Behmel syndrome (SGBS) preadipocyte cell strain should enhance the relevance of the acquired knowledge, as the cell strain is, in contrast to 3T3-L1, human and diploid with a stable genome (Fischer-Posovszky et al., 2008; Yuan and Zhao, 2011). The cell strain was generated from a SAT biopsy of a male infant with the Simpson-Golabi-Behmel syndrome. However, no mutation was identified at the *glypican 3 (GPC3)* gene commonly associated with SGBS.

Compared to primary cells, the cells retain their differentiation capacity up to 50 generations. A further advantage is the ability to study the synchronized differentiation under chemically defined conditions (serum-free). SGBS cells harbor a heterogeneous C risk allele rs1421085 at the *FTO alpha-ketoglutarate dependent dioxygenase (FTO)* gene that shifts the gene expression program towards a white - and not beige - adipocyte differentiation program.

However, dependent on the stimuli, both white and beige differentiation of SGBS cells can be accomplished, and therefore they serve as a model for both lineages (Klusóczki et al., 2019).

For white differentiation, first, confluency of SGBS cells is assured, as cell-cell contact affects adipogenesis via the Rho-family GTPases (Cristancho and Lazar, 2011). Three days post-confluency, synchronized differentiation with chemically defined conditions by delivery of serum-free differentiation medium is induced. The differentiation medium contains the synthetic glucocorticoid dexamethasone (DEX) and cortisol, activating the GR. Adding 1-methyl-3-isobutylxanthine (IBMX), an inhibitor of phosphodiesterases, increases cAMP levels. Further, the differentiation medium contains the potent PPARG agonist rosiglitazone. Triiodothyronine (T3) and insulin activate the thyroid hormone receptor and the insulin receptor, respectively. Differentiation is achieved in about two weeks with visible lipid accumulation.

1.4 Epigenetic gene regulation

The DNA carries the code for human life with the four DNA bases cytosine (C), guanine (G), thymine (T), and adenine (A). However, cell differentiation and the development of different organs cannot be explained by genetics, as all cells are genetically identical (Reik, 2007). In 1942, Conrad Waddington proposed the concept of epigenetics, introducing a new layer between genetics and phenotype, which would explain heritable changes in gene function that the DNA sequence does not encode for (Waddington, 1942). With the epigenome, we today classify modifications on top of (“epi”) the DNA, which control the accessibility of the DNA to regulate gene expression. These modifications include DNA methylation and hydroxymethylation, but also chemical modifications on histones, the protein scaffold, around which DNA is wrapped. Epigenetic layers also include non-coding RNAs such as enhancer RNA, microRNAs (miRNAs), and long non-coding RNAs, the purpose of which is not to encode for proteins (non-coding) but to regulate the expression of other genes (Deichmann, 2016).

1.4.1 Chromatin organization

The DNA of each human cell is around 2 m long and needs to be tightly organized and packed to fit into the nucleus, but in such a way that it can also be accessible at regions for cell type-specific gene activation. Chromosomal regions that are not transcribed are packed at the nuclear lamina (heterochromatin). In contrast, actively transcribed regions are more loosely organized in bundles towards the center of the nucleus (euchromatin). These bundles are regions of the DNA that are in close contact and are frequently interacting, such as promoter regions and their enhancer regions within so-called topologically associating domains (TADs) (Hansen et al., 2021). Such genomic domains are separated from other genomic regions by so-called membrane-less organelles by a process called liquid-liquid phase separation, allowing local control of the organization of the chromatin (Banani et al., 2017; Shin and Brangwynne, 2017).

1.4.2 Histone modifications

To achieve different levels of chromatin compaction, the DNA is organized in nucleosomes formed by a complex of DNA wrapped around eight histone proteins. The nucleosomes can slide aside or be removed by chromatin remodelers to enable chromatin accessibility, e.g., for TFs to bind the DNA (Markert and Luger, 2021). Modifications at the histone tails or at domains physically interacting with the DNA dictate how close the DNA is attached to the histones, e.g., by modifying the charge of the histone protein or marking histones for their recognition by so-called histone mark “readers”. The cell-type specific histone modifications are dynamically placed by “writers” and removed by “erasers” (Table 3). The repression of genes is accomplished by deposition of tri-methylation at lysine 27 (H3K27me3) or di-methylation at lysine 9 of histone H3 (H3K9me2). Active enhancer and promoter regions are marked by acetylation at H3K27 (H3K27ac) deposited by histone acetyltransferases (HAT) (Morgan and Shilatifard, 2020). While enhancers are primed H3K4me1, promoter regions are marked at the same lysine with trimethylation (H3K4me3). Whole genomes of different cell types have been screened for histone modifications to annotate the genome's genomic function systematically. With the use of a multivariate Hidden Markov Model (ChromHMM), the chromatin immunoprecipitation (ChIP)-sequencing data is integrated and can model the presence of certain chromatin states associated with different functional regions (Ernst and Kellis, 2012).

Table 3| Histone marks and associated enzymes in the modulation of chromatin function

Modification	Writer	Eraser	Location	Function
H3K27me3	PRC2	UTX1, JMJD3	CpG-rich promoters and intergenic regions	Silencing
H3K9me2	G9A and GLP	JMJD2A, JMJD2B, JMJD2C and JMJD2D; JMJD1A, JMJD1B and JMJD1C	Gene bodies, intergenic regions, and enhancers	Silencing
H3K4me3	COMPASS-like proteins (SET1, MLL1-MLL2)	JARID1A, JARID1B, JARID1C, and JARID1D; KDM2B	Mainly promoters	Possibly activating
H3K27ac	HATs (including CBP/p300, GNATs, and MYSTs)	HDACs and sirtuins	Promoters and enhancers	Activating
H3K4me1	COMPASS-like proteins (MLL3-MLL4)	LSD1 and LSD2	Promoters, enhancers, and intergenic regions	Priming and/ or activating

Modified from (Atlasi and Stunnenberg, 2017).

1.4.3 DNA methylation and demethylation

One of the most studied epigenetic marks is the methylation at the 5' carbon of cytosines (5mC) when guanine (G) follows the C. The so-called CpG dinucleotides are symmetrically methylated, and during DNA replication, the methylation on the nascent strand is maintained by DNA (cytosine-5)-methyltransferase 1 (DNMT1). DNMT3a/b are involved in *de novo* methylation (Li et al., 1992; Okano et al., 1999). The removal of the methylation mark is classified into passive and active demethylation: During replication, the infidelity of DNMT1 to remethylate the nascent strand will create passive demethylation, especially in late-replicating regions, resulting in partially methylated domains (PMDs) (Gaidatzis et al., 2014; Ginno et al., 2020). The active demethylation is accomplished by stepwise oxidation of the 5mC by ten-eleven translocation (TET) enzymes to 5-hydroxymethyl C (5hmC), 5-formyl C (5fC), and 5-carboxyl C (5caC) (Fig. 4). The unmethylated C can be reestablished by replication-dependent passive dilution of oxidized bases (oxi-mC: 5hmC, 5fC, 5caC) or by thymine DNA glycosylase (TDG)-mediated base excision repair (BER) of 5fC or 5caC (Ginno et al., 2020).

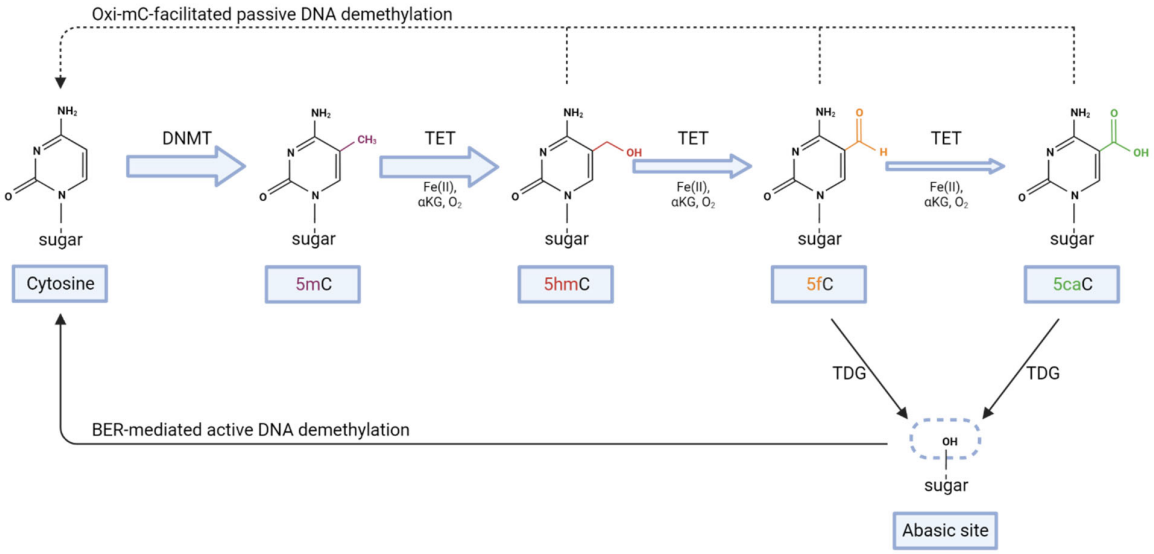

Fig. 4| DNA methylation and demethylation cycle. Cytosines (C) in the context of CpG dinucleotides are methylated by DNA (cytosine-5)-methyltransferases (DNMTs). The demethylation process can occur passively as a result of the infidelity of DNMT1 (not shown) or actively involving step-wise oxidation by ten-eleven translocation (TET) enzymes and TDG-mediated base excision repair (BER). During replication, oxidized bases (5hmC, 5fC, or 5caC) are not maintained (Oxi-mC-facilitated passive DNA demethylation). The figure was created with BioRender.com and adapted from (An et al., 2017). TDG: thymine DNA glycosylase. αKG: alpha-ketoglutarate.

Most of the methylated genome is associated with non-accessible chromatin and functions in, e.g., preventing the transcription of imprinted genes or mobile genetic elements. Promoter regions are generally unmethylated regions (UMR) with high CpG density, ensuring accessibility for the transcriptional machinery. Methylation in the gene body is thought to prevent alternative transcription start sites (TSS), speeding up transcription. The methylation status of most CpG sites is static. The interest of epigenetic studies is, however, to identify those regions which change the methylation status dependent on the cellular state, differentiation, or during carcinogenesis (Locke et al., 2019).

The hydroxymethylation mark (5hmC) as the first step of demethylation is found in higher proportions compared to 5fC and 5caC and is therefore considered as an independent epigenetic mark. 5hmC is found at low-to-intermediate CpG dense regions with intermediate methylation levels (lowly methylated regions (LMRs)), at promoters boundaries, bivalent promoters, and enhancer regions. Its function might be the prevention from remethylation by DNMTs. 5hmC is also found at the gene body of highly expressed genes and exon-intron boundaries, possibly marking splicing sites. It is highly discussed whether the 5hmC mark is just a step during demethylation or a stable mark with its own regulatory function. While the question has not been answered yet, it probably depends on the cellular system and the genomic position: 5hmC has been identified as a snapshot between dynamic cycling of

methylation and demethylation at promoter regions (Kangaspeska et al., 2008; Métivier et al., 2008a) and as a stable mark (Bachman et al., 2014).

The differences in 5hmC function might be dependent on how each cell type utilizes the regulatory mechanisms of demethylation to control the 5hmC state. The levels of regulation include the recruitment of TET enzymes by local chromatin environment, by TF, or through promoter-enhancer looping.

1.4.4 Interplay of cell metabolism and epigenetics

Epigenetic remodeling is directly regulated by cellular metabolism, as many metabolites are substrates or cofactors for epigenetic enzymes. For example, the availability of oxygen, Fe(II), and α-ketoglutarate (αKG) controls TET activity, while the inhibitory substrates L-2-hydroxyglutarate (L-2-HG), succinate, and fumarate decrease TET activity (Fig. 4 + 5) (Lu et al., 2015). Vitamin C is also known to efficiently increase the activity of TET enzymes by restoration of iron Fe(II) via the reduction of Fe(III) (Rose et al., 2011). Histone demethylases (HDM) are also αKG-dependent dioxygenases regulated by the same metabolites (Fig. 5). Histone and DNA methylation depends on S-adenosyl methionine (SAM) availability. In contrast, S-adenosyl homocysteine (SAH) inhibits histone and DNA methyltransferases (Miranda et al., 2009). Acetylation of histones is highly dependent on acetyl-Coenzyme A (acetyl-CoA), and for deacetylation, nicotinamide adenine dinucleotide (NAD^+) is used as a substrate. Apart from the “canonical” modifications (DNA methylation and histone methylation/acetylation), several additional emerging posttranslational modifications regulated by chromatin-modifying metabolites have been described (Fig. 5) (Dai et al., 2020; Sun et al., 2021). A few examples are, e.g., histone O-GlcNAcylation, lactylation, or citrullination, but not all of these emerging modifications are fully understood in their regulatory function. However, it has been shown that in several processes, such as differentiation, immune regulation, or tumor progression, changes in the metabolism that are regulated, e.g., by nutrient availability and growth factor signaling, are followed by changes in the epigenome (Dai et al., 2020). Therefore, the tightly controlled metabolism serves as an axis between the environment and epigenetic gene regulation. However, it remains unclear how local metabolite availability can be regulated at different genomic domains (Katada et al., 2012) and whether the liquid-liquid phase separation is involved in that process (Dai et al., 2020).

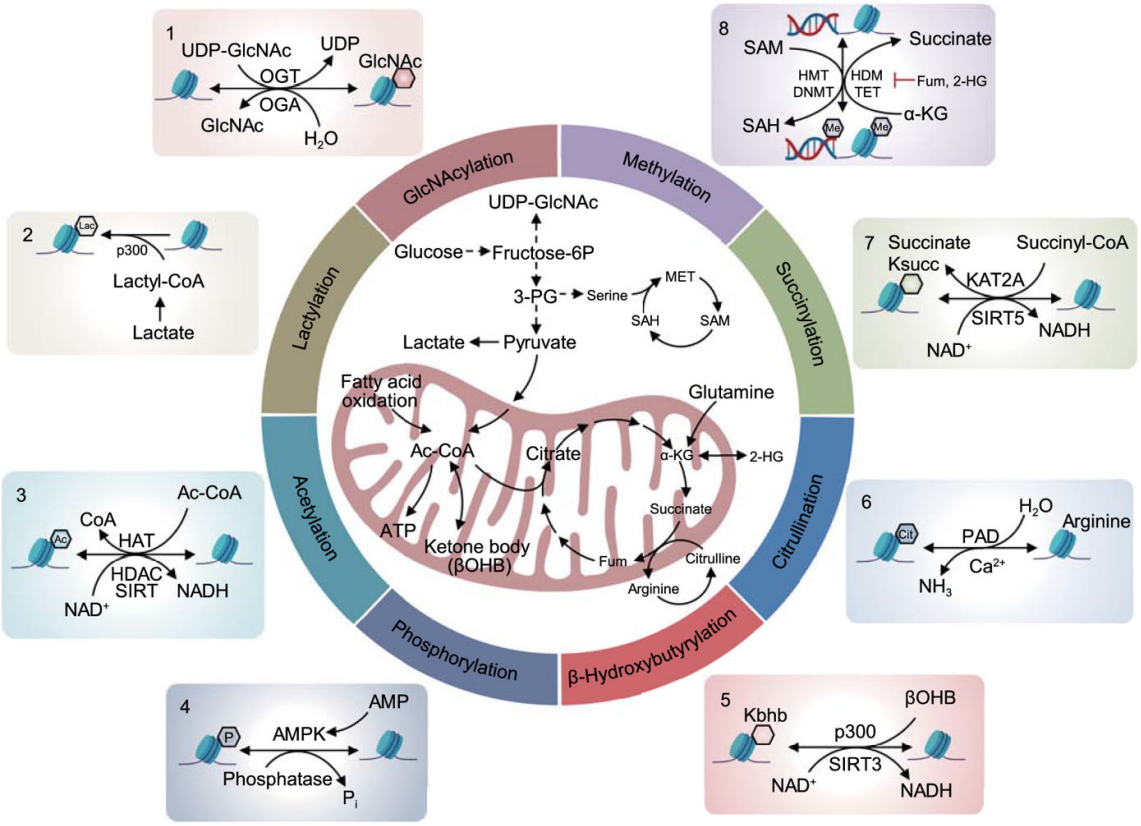

Fig. 5| Metabolism regulating epigenetic remodeling. Nutrients are metabolized in the cells and the generated metabolic intermediates can serve as epigenetic substrates or cofactors, such as acetyl-CoA, NAD+, SAM, and ATP. From (Sun et al., 2021). OGT: O-linked N-acetylglucosamine (GlcNAc) transferase, OGA: O-GlcNAcase, p300: E1A binding protein P300, HAT: histone acetyltransferase, HDAC: histone deacetylase, SIRT: Sirtuin, AMPK: AMP-activated protein kinase, PAD: peptidyl arginine deiminase, KAT2A: lysine acetyltransferase 2A, HMT: histone methyltransferase, DNMT: DNA methyltransferase, HDM: histone demethylase, TET: ten-eleven translocation.

1.4.5 Analysis of DNA hydroxymethylation

A variety of methods to detect hydroxymethylation have been developed in the past years, and they are grouped into base-resolution and non-base-resolution methods, reviewed by (Wu and Zhang, 2014, 2017). Base-resolution methods generally involve bisulfite (BS) sequencing (Fig. 6a). With this technique, unmodified cytosines (C) are chemically deaminated to uracil upon bisulfite treatment. During PCR amplification, uracil is converted to thymine. Consequently, unmethylated Cs are sequenced as T. At the same time, methylated cytosines are protected from bisulfite-induced deamination and sequenced as C. This method delivers absolute proportions and a genome-wide profile of methylated C. However, bisulfite sequencing cannot discriminate between 5mC and 5hmC. To do so, additional steps are required that depend on the differential behavior of the modified cytosines during bisulfite conversion, such as in oxidative bisulfite (oxBS) sequencing. During oxBS, 5hmC is first oxidized to 5fC, which can

then be bisulfite-converted and sequenced as T. Finally, 5hmC can be calculated by subtracting oxBS from BS proportions (Booth et al., 2012).

In contrast to BS, enrichment-based methods selectively enrich fragments with 5hmC, which are then sequenced (Fig. 6b). Enrichment can be achieved by 5hmC-specific antibodies or chemical modification of 5hmC. In hMeSeal, DNA is fragmented, and subsequently, ß-glucosyltransferase (β-GT) is used to glycosylate 5hmC. With the usage of click chemistry, glycosylated 5hmCs are labeled with biotin, and finally, biotinylated fragments are pulled down by streptavidin to sequence hydroxymethylated fragments. Enrichment-based methods cannot determine which CpG within a fragment is hydroxymethylated, and no absolute hydroxymethylation proportions can be estimated. However, the technique is very sensitive in detecting hydroxymethylated regions and is cost-effective in sequencing (Song et al., 2011).

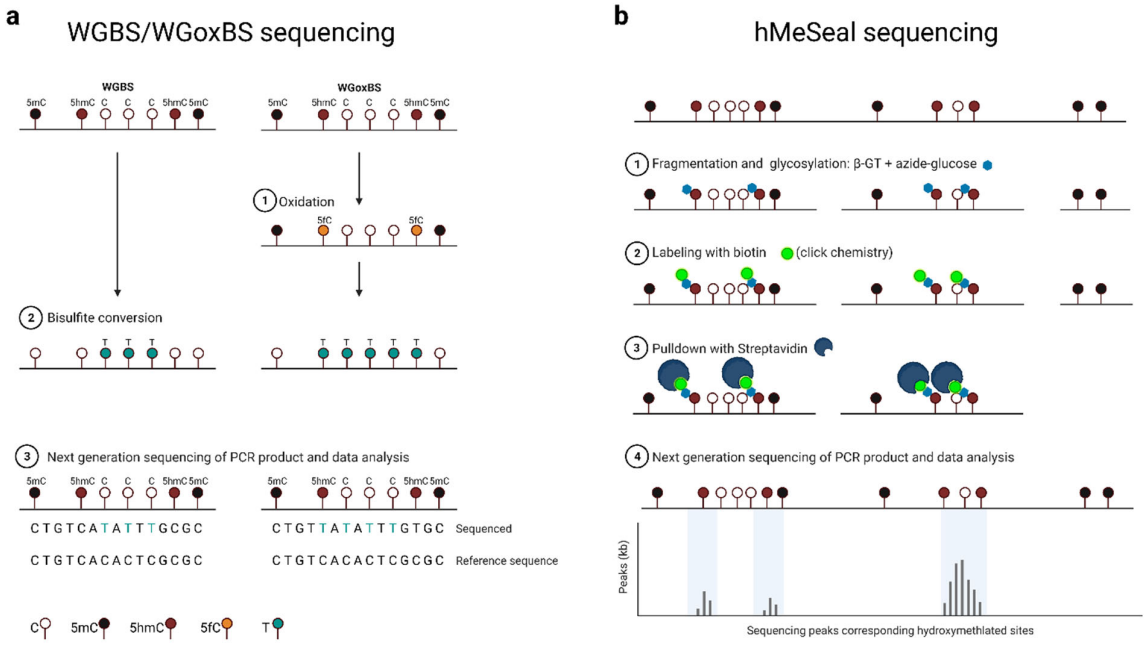

Fig. 6| Hydroxymethylation sequencing methods. a, Whole-genome bisulfite sequencing (WGBS-seq) in combination with oxidative bisulfite sequencing (WGoxBS-seq) is a base-resolution method to estimate hydroxymethylation proportion levels. With WGBS, unmodified cytosines (C) are bisulfite-converted (2) and sequenced as a T, while modified cytosines are sequenced as a C (3). With WGoxBS, during an additional oxidation step (1), 5hmC is oxidized to 5fC, which can then be bisulfite-converted and is sequenced as T (3) and thereby distinguished from 5mC, which is sequenced as a C. **b**, hMeSeal is an enrichment-based method, where DNA is fragmented, and 5hmC is glycosylated with ß-glucosyltransferase (β-GT) (1). With the usage of click chemistry, glycosylated 5hmC are labeled with biotin (2) and pulled down by streptavidin (3) to sequence hydroxymethylated fragments (4). The figure was created with BioRender.com.

1.4.6 Epigenetics of adipogenesis

In murine adipogenesis, the generation of new CTCF (CCCTC-binding factor) and PPARG binding sites were associated with hydroxymethylation (Dubois-Chevalier et al., 2014; Serandour et al., 2012). It was shown that CTCF (Dubois-Chevalier et al., 2014) and PPARG (Fujiki et al., 2013) recruit TET1 and thereby orchestrate site-specific hydroxymethylation necessary for enhancer progression. siRNA knockdown revealed that TET1 and TET2 are involved in lineage differentiation by enhancer activation through oxidation of 5mC to 5hmC (Cakouros et al., 2019). In contrast, TET1 can also act as a repressor of adipogenesis. It can recruit co-repressor proteins, such as SIN3A (SIN3 transcription regulator family member A) and EZH2 (enhancer of zeste homolog 2), and repress promoters. At the local level, it was shown that during clonal expansion, DNMT1 maintains the methylation at the *PPARG2* promoter. Afterwards, TET1/2 demethylate the *PPARG2* promoter and selected promoters of adipogenic genes (*leptin, FABP4*) (Noer et al., 2006; Teven et al., 2011; Yoo et al., 2017).

Rauch *et al.* provided a global view on adipogenesis at the levels of chromatin accessibility by comparing changes in ATAC-seq data observed during adipogenesis with those observed in osteogenesis. Epigenetically, osteoblasts are more closely related to MSCs than adipocytes, and therefore adipogenesis requires more dramatic chromatin remodeling than osteogenesis (Rauch et al., 2019). Mikkelsen *et al.* have characterized genome-wide changes in histone modifications, CTCF, and PPARG binding during murine and human adipogenesis. Although the critical adipogenic transcription factors are conserved, the genomic locations of enhancer regions (H3K27ac) with PPARG and CTCF binding seem to be different between species.

As PPARG and CEBPA drive adipocyte differentiation, many epigenetic studies have also studied the effect of epigenetic players on the expression of *CEBPB*, *PPARG*, and *CEBPA* (Ambele et al., 2020; Nanduri, 2021). Most of the studied epigenetic enzymes promote the differentiation process, but a few inhibit adipocyte differentiation. The histone deacetylase 9 (HDAC9) inhibits the expression of *CEBPB* by deacetylating H3K27ac, and sirtuin 1/2 (SIRT1/2) inhibit the expression of both *CEBPA* and PPARG by deacetylating H3K9ac. The euchromatic histone lysine methyltransferase 2 (EHMT2) generates the H3K9me2 mark and therefore inhibits the binding of CEBPB at the *PPARG* promoter. Finally, the lysine specific demethylase 1 (LSD1) functions both in the promotion and the repression of *CEBPA* expression by increasing H3K4me2 and H3K9me2, respectively. To induce the expression of the adipogenic regulators *CEBPA* and *PPARG*, the polycomb repressive complex 2 (PRC2) with its subunit enhancer of zeste (EZH2) deposits the repressive mark H3K27me3 and therefore indirectly promotes adipogenesis by repressing Wnt genes. The switch/sucrose non-fermentable (SWI/SNF) and the CREB-binding protein (CBP)/p300 protein complex display

direct effects on the promotion of *PPARG* expression with their function in chromatin remodeling and acetylation of H3K27 at the *PPARG2* promoter, respectively.

1.4.7 NEIL1, a potential hydroxymethylation reader

To study additional functions of the hydroxymethylation mark, pulldown experiments have been performed to identify proteins preferentially binding to 5hmC, compared to the other marks. Among them, UHRF1/2 (ubiquitin like with PHD and ring finger domains 1/2), MECP2 (methyl-CpG binding protein 2), MSH6 (mutS homolog 6), and NEIL1 (nei like DNA glycosylase 1) were identified as 5hmC binding proteins (Iurlaro et al., 2013; Spruijt et al., 2013).

NEIL1 is an enzyme with DNA glycosylase activity and can therefore excise oxidized bases. NEIL1 recognizes the oxidized base in replicating cells, preventing the nascent chain from growing. It then lets the fork regress the single-strand back to its double-strand position allowing safe BER (Hegde et al., 2013). NEIL1 is also involved in repairing oxidative stress-induced damage in non-proliferating cells. It is found in a complex with BER proteins and nucleosome remodeling proteins, the “BERosome”, constantly sitting on nucleosomes. When NEIL1 identifies oxidized bases, nucleosomes are remodeled so that DNA is accessible for repair. Then, inhibitors of NEIL1, CHAF1A (chromatin assembly factor (CAF)-1 subunit A), the p150 subunit of the histone H3/H4 chaperone, and its partner ASF1A (anti-silencing function protein 1A) are released from the complex, and NEIL1 becomes active and initiates BER (Yang et al., 2017).

However, NEIL1 might also have functions other than canonical repair, as there was no increased mutation rate by NEIL1 knockout. Vartanian *et al.* speculated a role in the regulation of transcription (Vartanian et al., 2006). Others describe a role in DNA demethylation, as NEIL1 overexpression can partially replace the function of TDG in excising 5fC and 5caC, but TDG is considered as the main glycosylase to accomplish this job (Müller et al., 2014). Regarding the possible function on 5hmC, it was described that purified human NEIL1 can cooperate with TDG to initiate BER on 5fC and 5caC, but was not able to excise 5hmC (Slyvka et al., 2017). Beside the ability of binding 5hmC, several *in vivo* knockout studies support a role of NEIL1 in maintaining adipose tissue. NEIL1 knockout in mice has shown that deficiencies in *Neil1*, but also in another repair enzyme, 8-oxoguanine DNA glycosylase (*Ogg1*), resulted in the development of severe obesity (Arai et al., 2006; Sampath et al., 2011; Vartanian et al., 2006), which might be due to defective adipogenesis (Longo et al., 2019).

1.5 DHA and prevention of Metabolic Syndrome

The most effective prevention of metabolic syndrome is achieved by weight loss through lifestyle changes, including diet and physical activity. Other possible treatments to reduce weight include surgery or the intake of pharmaceuticals or dietary supplements.

One way to reduce the risk of cardiovascular disease was to substitute saturated fatty acids (SFA) with polyunsaturated fatty acids (PUFAs), containing two or more double bonds; n-6 and n-3, indicating the position of the first double bond (Lenighan et al., 2019). Linoleic acid (LA) and alpha-linoleic acid (ALA) are the two essential fatty acids from which the other n-6 and n-3 fatty acids can be generated (Fig. 7). Later, it became apparent that the ratio between PUFAs and SFAs is critical, but the ratio of n-6 (mainly pro-inflammatory) to n-3 (rather anti-inflammatory) is to be considered, too. Eicosapentaenoic acid (EPA) and docosahexaenoic acid (DHA), e.g., are derived from ALA by desaturation and elongation, but as conversion rates are considered low, these fatty acids are suggested to be ingested directly by fish or algae oils (Brenna et al., 2009; Burdge, 2004; Plourde and Cunnane, 2007).

The PUFAs are part of membrane lipids. When lipases release these FAs from the membranes, the PUFAs compete for lipoxygenase (LOX), cyclooxygenase (COX), and cytochrome P450 (CYP), which metabolize them to the downstream effectors, the oxylipins (Fig. 7). From n-6 PUFAs mostly proinflammatory oxylipins, are generated, while from n-3 PUFAs, mainly pro-resolving and anti-inflammatory oxylipins (resolvins, protectins, and maresins) are produced (Duan et al., 2021; Liput et al., 2021).

EPA and DHA themselves affect cellular metabolism by integration into membranes, where they change the structure of lipid rafts and affect the function of membrane receptors. In addition, they can bind membrane receptors such as G protein-coupled receptors (GPCRs), inhibit the action of inflammasomes, activate intracellular receptors such as PPAR and retinoid X receptors (RXR), and inhibit the function of the transcription factors liver X receptor α (LXRA), sterol regulatory element binding protein 1c (SREBP1c), carbohydrate responsive element binding protein (ChREBP), and nuclear factor kappa B (NFκB) (Bordoni et al., 2006; Liput et al., 2021).

In humans, it has been shown that EPA and DHA have a protective function against cardiovascular diseases through their anti-inflammatory and hypotriglyceridemic action (Albracht-Schulte et al., 2018). Direct effects on the adipose tissue have been shown in mice, where supplementation with EPA and DHA has resulted in weight loss. In humans, at least a prevention of weight gain has been shown, and the action is discussed to be mainly *via* lipid mediators (oxylipins) by reducing the secretion of leptin and increasing the levels of

adiponectin (Rausch et al., 2021). Furthermore, they have been shown to reduce low-grade inflammation in the adipose tissue, promote insulin sensitivity, and increase the oxidation of FAs and their re-esterification in adipocytes. Finally, EPA and DHA also affect immune cells, e.g., supporting a switch from M1 to M2 macrophage phenotype (Kuda et al., 2018). Although the ingestion of n-3 FAs, specifically by EPA- and DHA-rich fish oil supplementation, is suggested, it is yet not clear what is the optimal ratio of n-6 to n-3 FA and which of the biological effects are accomplished by EPA and DHA themselves or by the downstream effectors, the oxylipins.

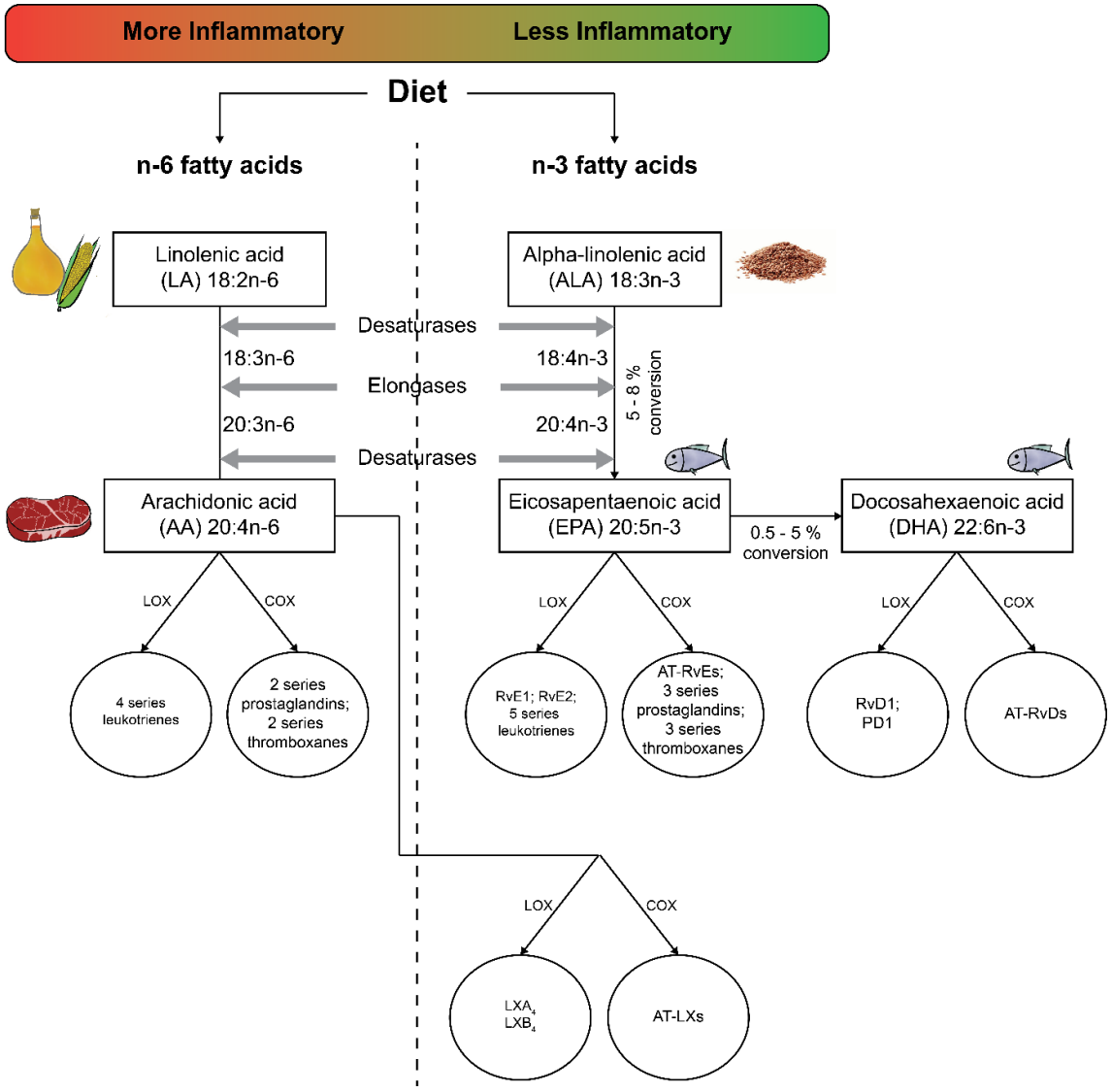

Fig. 7| n-6 and n-3 fatty acid-derived lipid mediators involved in inflammation. Linoleic acid (LA) and alpha-linoleic acid (ALA) are n - 6 and n - 3 essential fatty acids, respectively, categorized by the position of the first double bond. These fatty acids are the templates for the generation of other polyunsaturated fatty acids (PUFAs) with the help of desaturases and elongases. Oxylipins are downstream lipid mediators involved in inflammation that are generated by lipoxygenase (LOX), cyclooxygenase (COX), or cytochrome P450 (CYP) (not shown) enzymes. Adapted from McDaniel et al., 2013.

2 Aims

Metabolic syndrome is a multifactorial metabolic disorder with a pandemic expansion. As part of the PATHWAY-27 project (EU grant agreement n° 311876) aiming at prevention of the metabolic syndrome by dietary intervention with foods enriched for bioactive compounds, I planned first to characterize the SGBS *in vitro* model for human adipocyte differentiation at the epigenetic level (part 1). Second, I aimed to investigate the influence of chronic exposure to bioactive compounds on SGBS preadipocytes to study the effect of the bioactive compounds at the molecular level (part 2).

During early investigations of the SGBS cell differentiation model, I identified that not necessarily DNA methylation but hydroxymethylation levels were mainly altered. Therefore, the focus of the first part was to characterize hydroxymethylation changes during adipocyte differentiation and understand its molecular role in epigenetic gene regulation. To address this aim, the following objectives were devised throughout this thesis:

- To map DNA methylation and hydroxymethylation changes during adipocyte differentiation (day 0 – day 11) at the base-resolution (using a combination of WGBS and WGoxBS sequencing, and validated with the 450k array), as well as at non-base-resolution (hMeSeal sequencing).
- To investigate whether hydroxymethylation is a stable mark by maintaining mature adipocytes in culture for an extended time.
- To characterize the genomic location of hydroxymethylation sites using published chromatin states (ChromHMM) and data of adipogenic TF binding (ChIP-seq).
- To investigate the possible gene regulatory function of hydroxymethylation by its integration with gene expression (RNA-seq) and protein levels (untargeted proteome).
- To validate the *in vivo* relevance of hydroxymethylation sites, by comparing hydroxymethylation in mature SGBS cells with those in white adipose tissue (WAT).
- To investigate the involvement of the metabolome in the regulation of hydroxymethylation dynamics, using targeted and untargeted metabolome data of differentiating SGBS cells.
- To clarify the potential role of acNEIL1 as a hydroxymethylation binding protein in the regulation of hydroxymethylation. For that, acNEIL1 ChIP-seq binding was compared with hydroxymethylation in WAT to investigate its *in vivo* co-localization.

In the second part of this thesis, I aimed to investigate the function of the PATHWAY-27 bioactive compounds *in vitro* in SGBS preadipocytes to study their effect on the differentiation capacity necessary for adipose tissue hyperplasia (increase in cell number) instead of

hypertrophy (increase in adipocyte size). I also aimed to investigate the possible anti-inflammatory effects, as preadipocytes are more responsive to the proinflammatory signaling than mature adipocytes. The PATHWAY-27 consortium aimed to study the low-dose long-term effect of docosahexaenoic acid (DHA), protocatechuic acid (PA), one of the most abundant metabolites of anthocyanins and propionate (PRO), a metabolite of β-glucan and their combination treatments. As DHA displayed the strongest biological activity, while PA and PRO did not show any additive effects, I focused in this thesis on DHA treatment effects. To investigate the DHA-associated effects, I aimed:

- To test the cytotoxicity of the bioactive compounds in SGBS preadipocytes to select treatment concentrations.
- To map DHA-associated methylation changes (EPIC array) and gene expression changes (RNA-seq) in a long-term cultivation experiment in SGBS preadipocytes using low doses of DHA concentration
- To compare methylation changes with changes in independent cultivation experiments to separate cultivation-associated indirect DHA effects from direct DHA effects.
- To identify, based on gene expression data, DHA-associated signaling pathways and associated TF activities to understand the molecular mechanism of DHA in SGBS preadipocytes.
- To investigate the effect of DHA on SGBS differentiation capacity.

Overall, a better insight into human adipocyte differentiation and the effect of DHA on human preadipocytes will enhance our understanding of regulatory mechanisms for healthy adipocyte function and contribute to the improvement of metabolic syndrome in human adipose tissue.

3 Material and Methods

3.1 Materials

3.1.1 Instruments

Instruments	Manufacturer
5973N mass selective detector	Agilent, Waldbronn, Germany
6890N gas chromatograph	Agilent, Waldbronn, Germany
Bioanalyzer 2100	Agilent Technologies, Santa Clara, CA, USA
Biofuge fresco	Heraeus, Hanau, Germany
Biofuge pico	Heraeus, Hanau, Germany
CellXpert C170i	Eppendorf, Hamburg, Germany
Centrifuge 5415R	Eppendorf, Hamburg, Germany
Centrifuge 5424 R	Eppendorf, Hamburg, Germany
Covaris M220 Focused-ultrasonicator	Covaris, Woburn, Massachusetts, USA
DM IL light microscope	Leica, Wetzlar, Germany
E1-ClipTip Electronic Adjustable Tip Spacing Multichannel Equalizer Pipettes	Thermo Fisher Scientific, Waltham, MA, USA
Herasafe laminar Flow workbench	Heraeus Instruments
HiSeq X instrument	Illumina, San Diego, CA, USA
HP5-MS column	Agilent, Waldbronn, Germany
Illumina NextSeq 550 instrument	Illumina, San Diego, CA, USA
Illumina NovaSeq 6000 machine	Illumina, San Diego, CA, USA
Leica DFC300 FX digital color camera	Leica Microsystems, Wetzlar, Germany
M220 Focused-ultrasonicator	Covaris, Woburn, MA, USA
Mastercycler gradient 3	Eppendorf, Hamburg, Germany
Mastercycler nexus gradient	Eppendorf, Hamburg, Germany
Mettler AT 261 Deltarange microgram scale	Mettler Toledo, Zwingenberg, Germany
Micro-Dismembrator S	Sartorius, Göttingen, Germany
MSO Minishaker IKA	Laborgeräte München, Germany
Nanodrop spectrophotometer ND1000	Peqlab, Erlangen, Germany
QIAvac 24 Plus vacuum manifold, (19413)	Qiagen, Venlo, Netherlands
Qubit 3.0 Fluorometer	Invitrogen, Life Technologies, Darmstadt, Germany
Roche Light Cycler 480	Roche Diagnostics, Mannheim, Germany
SPECTRAmax M5 microplate reader	Molecular Devices, Sunnyvale, CA, USA
TapeStation 4150	Agilent Technologies, Santa Clara, CA, USA
Thermo Scientific Series 8000 WJ (Water Jacket) Incubator	Thermo Fisher Scientific, Waltham, MA, USA
Thermomixer Comfort	Eppendorf, Hamburg, Germany
Thermomixer Compact	Eppendorf, Hamburg, Germany
TissueLyser II	Qiagen, Venlo, Netherlands

3.1.2 Consumables

Consumables/Reagents	Manufacturer
1-methyl-3-isobutyl xanthine (IBMX), (I5879)	Sigma Aldrich, St. Louis, MO, USA
accutase solution, (A6964)	Sigma Aldrich, St. Louis, MO, USA
AMPure XP beads, (A63880)	Beckman Coulter, Brea, USA
biotin, (B4639)	Sigma Aldrich, St. Louis, MO, USA
bovine serum albumin (BSA), (A6003)	Sigma Aldrich, St. Louis, MO, USA
BRL49653 (Rosiglitazone), (350-125)	Enzo Life Sciences, Inc, Farmingdale, USA
chloroform, (22711.324)	VWR, Radnor, PA, USA
cOmplete, EDTA-free Protease Inhibitor Cocktail (11873580001)	Roche Diagnostics, Mannheim, Germany
cortisol, (H0888)	Sigma Aldrich, St. Louis, MO, USA
dexamethasone (DEX), (D1756)	Sigma Aldrich, St. Louis, MO, USA
dimethyl sulfoxide (DMSO), (20-139)	Merck, Darmstadt, Germany
DMEM/Nutrient Mixture F-12, containing 2.5 mM L-Glutamine, 15 mM Hepes, (11330)	Thermo Fisher Scientific, Waltham, MA, USA
dNTP Mix, (201900)	Qiagen, Venlo, Netherlands
docosahexaenoic acid (DHA), (D8768)	Sigma Aldrich, St. Louis, MO, USA
DPBS, (14190)	Thermo Fisher Scientific, Waltham, MA, USA
DTT, (92008)	Thermo Fisher Scientific, Waltham, MA, USA
ethanol 96%, (P075.1)	Carl Roth, Karlsruhe, Germany
E-Toxa-Clean, (E9029)	Sigma Aldrich, St. Louis, MO, USA
fetal bovine serum (FBS), (10270)	Thermo Fisher Scientific, Waltham, MA, USA
fibroblast growth factor 1 (FGF1), (F5542)	Sigma Aldrich, St. Louis, MO, USA
first-strand buffer, (1712020)	Thermo Fisher Scientific, Waltham, MA, USA
heparin, (H4784)	Sigma Aldrich, St. Louis, MO, USA
human transferrin, (T2252)	Sigma Aldrich, St. Louis, MO, USA
hydroxyethyl piperazine ethanesulfonic acid (HEPES), (H3375)	Sigma Aldrich, St. Louis, MO, USA
insulin, (I1507)	Sigma Aldrich, St. Louis, MO, USA
isopropanol (2-Propanol), (6752.3)	Carl Roth, Karlsruhe, Germany
Kaliumchlorid (KCl), (4936)	Merck, Darmstadt, Germany
NEBNext High-Fidelity 2x PCR master mix, (M0544)	New England BioLabs, Ipswich, MA, USA
pantothenate, (P5155)	Sigma Aldrich, St. Louis, MO, USA
penicillin/streptomycin, (P0781)	Thermo Fisher Scientific, Waltham, MA, USA
propionate (PRO), (P1880)	Sigma Aldrich, St. Louis, MO, USA
proteinase K, (158918)	Qiagen, Venlo, Netherlands
protocatechuic acid (PA), (03930590)	Sigma Aldrich, St. Louis, MO, USA
random hexamer oligonucleotides, (S0142)	Thermo Fisher Scientific, Waltham, MA, USA
RNase A, (1045699)	Qiagen, Venlo, Netherlands
RNaseOUT, (10777019)	Thermo Fisher Scientific, Waltham, MA, USA
Rotilabo-Gewindefläschchen ND8	Carl Roth, Karlsruhe, Germany

RWT buffer, (1067933)	Qiagen, Venlo, Netherlands
safe lock tubes (DNA LoBind Tube), (022431021)	Eppendorf, Hamburg, Germany
Schraubkappen geschl. PP, ND8	Carl Roth, Karlsruhe, Germany
sodium butyrate, (13121)	Cayman Chemical Company, Ann Arbor, MI, USA
sodium dodecyl sulfate (SDS), (L4509)	Sigma Aldrich, St. Louis, MO, USA
spermidine, (S2501)	Sigma Aldrich, St. Louis, MO, USA
sulforhodamin B (SRB), (230162)	Sigma Aldrich, St. Louis, MO, USA
SuperScript III RT, (18080093)	Thermo Fisher Scientific, Waltham, MA, USA
SybrGreen	Thermo Fisher Scientific, Waltham, MA, USA
T12.5 flask, with vented caps	Falcon, Corning Incorporated, Durham, USA
T25 fask, with vented caps	Greiner Bio-One, Kremsmünster, Austria
T75 fask, with vented caps	Greiner Bio-One, Kremsmünster, Austria
TRI Reagent, (T9424)	Sigma Aldrich, St. Louis, MO, USA
trichloroacetic acid, (15494749)	Thermo Fisher Scientific, Waltham, MA, USA
triiodothyronine (T3), (T6397)	Sigma Aldrich, St. Louis, MO, USA
Triton X-100	Gerbu, Gailberg, Germany
UltraPure Distilled Water, (10977)	Thermo Fisher Scientific, Waltham, MA, USA
β-mercaptoethanol, (M6250)	Sigma Aldrich, St. Louis, MO, USA

Kits	**Manufacturer**
AllPrep DNA/RNA Mini Kit, (80204)	Qiagen, Venlo, Netherlands
DNA BR Assay Kit	Thermo Fisher Scientific, Waltham, MA, USA
EZ DNA Methylation Kit 96-well kit	Zymo Research Europe GmbH, Freiburg, Germany
Illumina TrueSeq Stranded total RNA Library Prep Kit	Illumina, San Diego, CA, USA
Infinium Human Methylation 450k Bead Chip Illumina arrays	Illumina, San Diego, CA, USA
Infinium Methylation EPIC BeadChip Kit	Illumina, San Diego, CA, USA
MinElute Reaction Cleanup Kit	Qiagen, Venlo, Netherlands
Ovation Ultralow Methyl-Seq Library System	Tecan, Männedorf, Switzerland
Ovation Ultralow Methyl-Sey DR Mutliplex System 1-8	Nugen, San Carlos, CA, USA
RNA BR Assay Kit	Thermo Fisher Scientific, Waltham, MA, USA
RNase-Free DNase Set, (79251)	Qiagen, Venlo, Netherlands
Roche universal probe library (UPL) system	Roche, Mannheim, Germany

3.2 SGBS cells

Simpson-Golabi-Behmel Syndrome (SGBS) preadipocytes were kindly provided by Dr. Wabitsch (Ulm University, Germany) (Wabitsch et al., 2001) and were tested regularly negative for mycoplasm contamination at Multiplexion. The SGBS cell line is no commonly misidentified cell line (ICLAC register), and I confirmed its cell authenticity regularly by differentiation capacity.

3.3 SGBS adipocyte differentiation

For experiment 1 (Fig. 8), I have grown SGBS cells in growth medium (Dulbecco's Modified Eagle's Medium F12 (DMEM/Nutrient Mixture F-12)) supplemented with 10 % fetal bovine serum, 1 % penicillin/streptomycin, 33 µM biotin, 17 µM pantothenate, 90 µg/mL human heparin, and 1 ng/mL fibroblast growth factor 1 (FGF1)). Cells were seeded at a density of 2 – 3x10^5 cells/T75 flask and passaged twice weekly. Before induction of differentiation, cells were grown to confluency in T25 flasks. Three days after reaching confluency, I stimulated SGBS cells with a differentiation cocktail in serum-free medium containing 100 nM insulin, 200 pM triiodothyronine (T3), 1 µM cortisol, 2 µM BRL49653 (rosiglitazone), 0.115 mg/ml 1-methyl-3-isobutylxanthine (IBMX), 0.25 mmol/L dexamethasone (DEX), and 0.01 mg/ml human transferrin. SGBS cells were kept in full differentiation media until day 6 after induction. Then the medium was replaced with differentiation medium without FGF1, heparin, rosiglitazone, IBMX, and DEX. I harvested cells for epigenetic analyses at day 0, 1, 7, and 11 of differentiation. Differentiation was performed in three biological replicates. Linda Kessler (LK) repeated the adipocyte differentiation in experiment 2 in three biological replicates using the same protocol but kept mature SGBS cells in differentiation medium without FGF1, heparin, rosiglitazone, IBMX, and DEX until day 27 (Fig. 8).

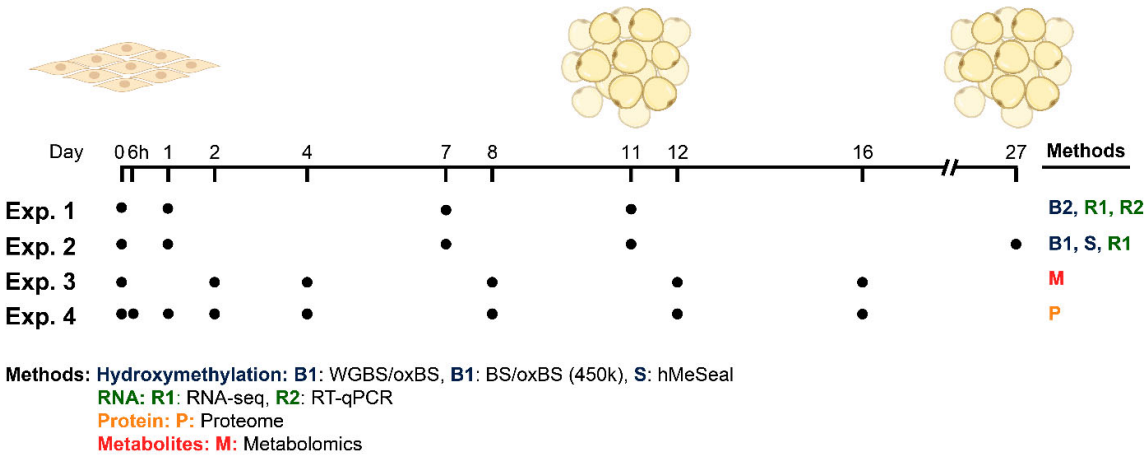

Fig. 8| Overview of experiments related to multi-omic analyses during adipogenesis (thesis part 1). SGBS preadipocytes were differentiated to mature adipocytes (day 11/12) or kept in culture up to day 27. SGBS differentiation of experiment 1 (n = 3) was performed by myself (CFA) for methylation and hydroxymethylation analysis using bisulfite (BS)/oxidative BS treatment analyzed by 450k array technology and for gene expression analysis by RNA-seq and RT-qPCR analysis. Differentiation of experiment 2 (n = 3) was performed by LK, I (CFA) performed WGBS/oxBS library preparation, and FJ performed hMeSeal library preparation for hydroxymethylation analysis. Metabolome analysis of differentiating SGBS cells (experiment 3, n = 5 - 6) were provided by (Miehle et al., 2020) and proteome analysis (experiment 4, n = 5) by (Schaffert et al., 2021). Downstream bioinformatic data processing was done by myself (CFA). Modified from (Feuerstein-Akgoz, C. et al., *in preparation*)

3.4 Long-term cultivation of SGBS preadipocytes with bioactive substances

3.4.1 Complexation of DHA with BSA

For delivery to SGBS cells, DHA was conjugated and solubilized with bovine serum albumin (BSA) in a DHA:BSA ratio of 4:1 with a concentration of 1 mM DHA according to protocol (SeahorseBioscience, n.d.) with minor modifications. To avoid lipopolysaccharide (LPS) contamination, all glassware and stir bars needed for complexation were soaked overnight in a 1 % solution of alkaline detergent (E-TOXA-CLEAN), washed 8 to 10 times with warm running tap water, five times with distilled water, and finally twice with endotoxin-free water. For the complexation procedure, BSA was dissolved in 150 mM NaCl solution to a concentration of 0.5 mM BSA by stirring in a 37 °C water bath. Similarly, DHA was dissolved in 150 mM NaCl solution at 2 mM concentration by stirring in a 37 °C water bath under a nitrogen atmosphere to avoid oxidation of DHA. Next, the BSA solution was slowly added to the DHA solution under a nitrogen atmosphere, creating a final concentration of 1 mM DHA, 0.25 mM BSA, 150 mM NaCl and stirred for another hour. BSA solution was diluted 1:1 in 150 mM NaCl solution as solvent control. pH was adjusted to 7.4 with NaOH and solutions

were sterile-filtered and aliquoted to clean brown glass flasks. Air in the flask was removed with nitrogen gas, and solutions were stored at -80 °C.

3.4.2 Cytotoxicity experiments

To determine cell growth inhibitory potential of compounds for SGBS preadipocytes, I seeded cells in a 96 well format with 500 cells/well; a cell number I had previously defined in a cell growth experiment. After 24 hours, I renewed growth medium (200 µl/well) and supplemented with a serial dilution of DHA with concentrations ranging between 0.02 µM – 45 µM, or supplemented with PA or PRO with concentrations between 0.78 µM – 100 µM. For cell growth experiments, PA and PRO were dissolved in DMSO, pH 2. Control samples for DHA were treated with a serial dilution of BSA in NaCl. In control samples for PA and PRO, DMSO concentration was adjusted to 0.5 %. Treatment was stopped after 0, 24, 48, and 72 h, respectively, by removal of the medium. Cells were fixed with 10 % trichloroacetic acid for 30 min at 4 °C and washed extensively with tap water to remove trichloroacetic acid and dried to avoid detachment of the cells. For quantification of cell growth and anti-proliferative or cytotoxic activities of the substances, I performed sulforhodamin B (SRB) staining as described by (Skehan et al., 1990a). I stained cells with 0.4 % SRB solution for exactly 30 min at room temperature. Afterwards, I removed the SRB solution and washed the plate several times with 1 % acetic acid. Finally, I added 200 µl 20 mM Tris base solution to each well and shook the plates until the dye was completely dissolved. For quantification of the staining, I measured the absorbance at 515 nm (for high cell concentrations at 490 nm). The absorbance ratio of treated cells to solvent control cells was taken as readout for anti-proliferative activities. To distinguish between cytostatic and cytotoxic effects, I subtracted the absorbance at day 0 from absorbance values at the respective time points. Thus, cytotoxic effects result in negative values, while positive values represent cytostatic effects. Solvent control values for each time point were used to calculate the relative percentage of cell growth inhibition. Half-maximal inhibitory concentration (IC_{50}) values were computed from the results of eight serial 2-fold dilutions of test compound tested in technical duplicates. Nonlinear fitting of the dose-response curve was performed using GraphPad Prism version 5.00 for Windows, GraphPad Software, La Jolla California USA, www.graphpad.com.

3.4.3 Long-term cultivation experiments with DHA and nonDHA

I cultivated SGBS cells in growth medium (see chapter 3.3) in T75 flasks at 37 °C and 5 % CO_2, while avoiding cells to grow confluent. I prepared 1 mM stock solution of DHA as described above, I dissolved PRO in ethanol at a concentration of 31.1 mM and PA in DMSO

at 20 mM concentration. To investigate bioactive-induced alterations in DNA methylation and gene expression, I cultivated SGBS preadipocytes (three biological replicates: I, III, IV) for 2.5 to 4 weeks with the bioactives at non-toxic concentrations: 5 µM DHA, 70 µM PRO and 20 µM PA, alone or in combinations (experiment 5, Fig. 9). Independent of the treatment, all treated samples and solvent controls received all three solvents at a final concentration of 0.1 % DMSO, 0.23 % ethanol, and 1.25 µM BSA. I passaged the cells twice a week and freshly supplemented with bioactives at each passage. Afterwards I isolated nucleic acids using the protocol described in chapter 3.7.

Untreated control samples of experiment 6 were passaged by Lisa Demoen (LD) for 29 days in three independent replicates. In experiment 7, Linda Kessler (LK) cultured SGBS cells for 14 days in three independent replicates. Then, the cells were seeded into T12.5 cm2 flasks and grown to confluency until day 21, using the same growth medium. Each student isolated nucleic acids using the protocol described in chapter 3.7.

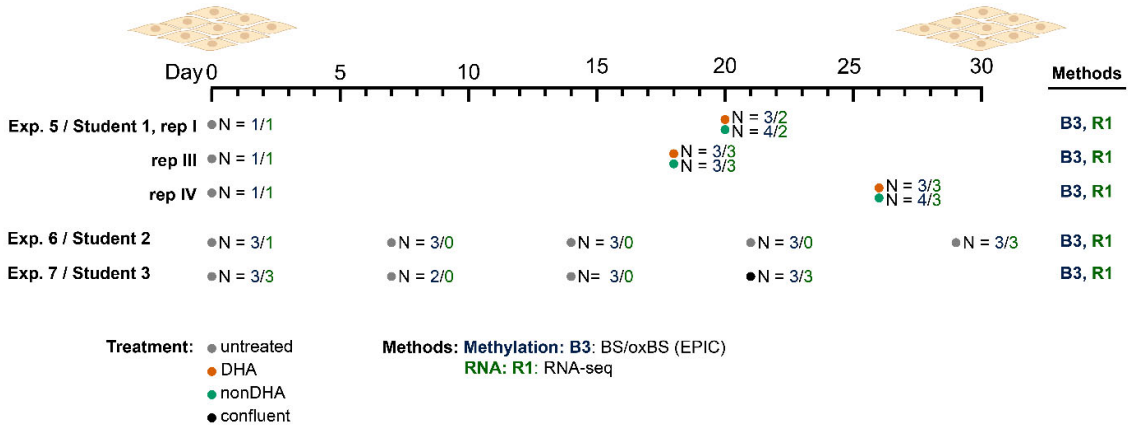

Fig. 9| Overview of the DHA long-term treatment experiments and applied epigenetic methods (thesis part 2). SGBS were cultivated for several passages with docosahexaenoic acid (**DHA**: DHA, DHA+PA or DHA+PRO) or without DHA (**nonDHA**: untreated, solvent, PA or PRO) in three independent replicates (experiment 5/Student 1: rep I, III, IV). Untreated control samples of SGBS cultivation by two other students were included to interpret changes occurring during cultivation (experiment 6/Student 2 and experiment 7/Student 3 in 3 replicates, each). Methylation was analyzed on EPIC arrays and gene expression by RNA-seq. The number of included replicates on the EPIC array and RNA-seq are indicated in blue or green, respectively. Experiments 5 - 6 were performed by myself (CFA), LD, and LK, respectively. DHA: docosahexaenoic acid, PA: protocatechuic acid, PRO: propionate.

3.5 WAT tissue biopsies

Subcutaneous white adipose tissue biopsies were taken from participants of the PATHWAY-27 human large intervention study (LIS) (NCT02702713, ClinicalTrials.gov). A subset of 5 biopsies of study participants recruited at the University of Bologna was used in this thesis (Fig. 10). Biopsies were collected from participants with or at risk of metabolic syndrome and

frozen at -80°C by collaboration partners of the PATHWAY-27 consortium, Silvia Garelli (SG), Marianna Farnè (MF), Giampaolo Ugolini (GU), Giancarlo Rosati (GR) and Luigi Ricciardiello (LR), from the Department of Medical and Surgical Sciences, University of Bologna, Italy and coordinated by Alessandra Bordoni (AB) from the Department of Agricultural and Food Sciences, University of Bologna, Italy. After shipment of frozen biopsies, Karin Klimo (KK) and Annette Weninger (AW) pulverized the biopsies under liquid nitrogen using the Micro-Dismembrator S for further downstream processing.

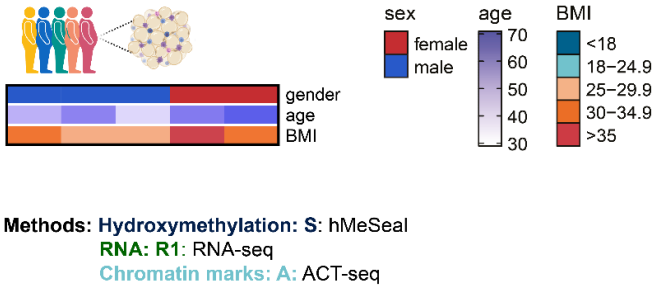

Fig. 10| Overview of WAT biopsies and applied epigenetic methods (thesis part 1). To investigate the *in vivo* relevance of the obtained *in vitro* findings, I included white adipose tissue (WAT) samples, characterized by gender, age, and body mass index (BMI). Biopsies were obtained by SG, MF, GU, GR, LR under the coordination of AB. Tissue was pulverized by KK and AW, ACT-seq, and hMeSeal libraries were prepared by JH and FJ, respectively. All downstream analyses were performed by myself (CFA). Modified from (Feuerstein-Akgoz, C. et al., *in preparation*)

3.6 Images

I took images of differentiating SGBS cells using the Leica DFC300 FX digital color camera with the software Leica Application Suite (LAS) Version 3.8.0.

3.7 Extraction of nucleic acids for epigenetic analyses

DNA and RNA of SGBS cells or WAT biopsies were isolated using the AllPrep DNA/RNA Mini Kit according to the manufacturer's instructions with modifications described below. Isolations were performed by myself or by the responsible experimenter, both mentioned in the chapter with the corresponding sample descriptions. Tissues were lysed in safe-lock tubes with lysis buffer of the kit (RLT Plus), supplemented with 1 % freshly added β-mercaptoethanol. Fat of the tissue lysates was removed as an upper layer after centrifugation. Cell lines were first washed with PBS and then lysed with the same lysis buffer directly in the plates. During lysis, cells were scraped from the flasks and transferred for completion of the lysis to safe-lock tubes.

DNA was collected on an AllPrep DNA spin column and flow-through was kept for RNA isolation, described below. DNA on the column was cleared from RNA contamination with RNase A digestion at 56 °C. Afterwards, Proteinase K digestion was performed and, after several washing steps on the column, DNA was eluted in H_2O and stored at 4 °C.

For RNA isolation, all centrifugation steps were performed at full speed and at 4 °C to avoid RNA degradation. 450 µl of the flow-through was vortexed thoroughly with 1 ml TRI reagent and incubated for 5 min. Next, 200 µl chloroform was added and again vortexed and incubated for 15 min at room temperature. Then samples were centrifuged for 15 min and the upper aqueous phase containing the RNA was transferred carefully to a fresh safe-lock tube to be mixed with 500 µl isopropanol. After 30 min incubation at room temperature, Proteinase K digestion (15 µl) was performed and RNA was collected on RNA spin columns using the QIAvac 24 Plus vacuum manifold. For that, lysates mixed with RWT washing buffer were transferred onto the columns, pre-equilibrized with RWT washing buffer. Afterwards, columns were washed with RWT washing buffer and on-column DNase I digest was performed using the RNase-Free DNase Set. Columns were then washed once with RWT buffer. The flow-through was retransferred onto the column and then washed three times with RPE buffer. The membranes were dried for 2 min and RNA on the column was eluted by adding RNase-free water followed by centrifugation. An aliquot of 5 µl was removed for quantification and quality check. The remainder of the RNA solution was subsequently directly stored at -80 °C to prevent degradation.

I quantified the extracted RNA and DNA by QuBit using the DNA BR Assay Kit and the RNA BR Assay Kit. For verifying the quality, I determined RNA integrity using the Agilent Bioanalyzer 2100 with the RNA 6000 Nano Kit, while DNA integrity was confirmed on a 0.5 % agarose gel.

3.8 Base-resolution hydroxymethylation analysis

3.8.1 WGBS/oxBS followed by sequencing

For hydroxymethylation analysis during adipocyte differentiation, I processed DNA of experiment 2, using the Ovation Ultralow Methyl-Seq Library System. For that I sheared 750 ng DNA in 10 % TE buffer on a M220 Focused-ultrasonicator with peak incident power of 50 W, duty factor of 15 %, 200 cycles per burst for 200 - 240 s at 6 °C to achieve an average peak size of 200 base pairs (bp). I performed library preparation according to the manufacturer's instructions with the sheared DNA. I submitted multiplexes of BS and oxBS libraries of the

same sample for sequencing on a HiSeq X instrument in a 150 bp paired-end setting on four lanes per multiplex at the DKFZ Genome and Proteome Core Facility. I analyzed samples that fulfilled the quality requirements (Q30 read 1/2 value ≥ 80 %) (n = 3 (day 0); n = 1 (day 7); n = 2 (day 11); n = 1 (day 27)). Of those samples, reads had an average median insert size of 156 bp (standard deviation 11 bp) and a median coverage of 63-fold in BS and 48-fold in oxBS libraries. Data preprocessing was performed by the One Touch Pipeline (OTP) for WGBS data (https://github.com/DKFZ-ODCF/AlignmentAndQCWorkflows) of the DKFZ Omics IT and Data Management Core Facility (Reisinger et al., 2017).

Calculation of methylation and hydroxymethylation values was performed using MLML2R maximum likelihood estimation of DNA methylation and hydroxymethylation proportions based on BS and oxBS data using the MLML2R package (Kiihl et al., 2019) implemented into the methrix package (https://github.com/CompEpigen/methrix) for fast and efficient summarization. This was performed on CpGs with coverage ≥ 15x, but omitting CpGs with extremely high coverage (0.99 quantile). To identify changes of methylation and hydroxymethylation proportions between day 11 and day 0, we applied the DMLtest function on unsmoothed proportions of 9,013,162 CpGs outside of common PMDs, identified in SGBS cells. Sites with mean proportion difference ≥ 0.25, *p* value < 0.005, and difference between each sample to mean of the other group > 0.15 were considered as significant. Genomic locations of CpGs are given according to human genome version hg19 (hg19/GRCh37).

3.8.2 BS/oxbBS followed by Illumina 450k array

For validation of the hydroxymethylation changes, I submitted DNA samples (0.7 – 1.5 µg) from differentiation experiment 1 to the DKFZ Genome and Proteome Core Facility for methylation/hydroxymethylation analyses on 450k arrays. BS- and oxBS-treatment was performed using the TrueMethyl Array Kit according to the manufacturer's instructions in the User Guide Version 2 (Feb 2015) as described by Gross *et al.* (Gross et al., 2017) and analyzed with the Infinium Human Methylation 450k Bead Chip Illumina arrays. During bisulfite conversion, methylated C is conserved as C, and unmethylated C is deaminated and replaced by a T. After hybridizing DNA to bead-bound probes on the array, dependent on the artificially generated genetic difference (C/T), green or red will be detected by binding of the corresponding color-labeled base. In a simplified manner, the ratio of red and green signals, the so-called β-value reflects DNA methylation values between 0 and 1 (Bibikova et al., 2011).

Quality control, data pre-processing, and normalization were done using the RnBeads R package (Assenov et al., 2014). Briefly, raw IDAT files were used as input and preprocessed separately for BS and oxBS data. Probes were filtered for a detection *p* value threshold of 0.01,

cross-reactive probes were removed (Chen et al., 2013), and remaining data was normalized using the beta-mixture quantile normalization (BMIQ) method (Teschendorff et al., 2013). The normalized BS and oxBS beta values were multiplied with the sum of total signal intensity (methylated + unmethylated) for maximum likelihood estimation of DNA methylation and hydroxymethylation proportions using the MLML2R package (Kiihl et al., 2019). Data of experiment 1 (day 0, 1, 7, and 11) represented 450,395 CpG sites after preprocessing. Changes between methylation and hydroxymethylation proportions between day 0 & 1 (n = 5) and day 11 were identified by Mann-Whitney U (MWU)-test (Supplementary Data 1). Sites with mean proportion difference > 0.1 and *p* value < 0.05 were defined as significantly differentially methylated (BS or oxBS). Genomic locations of CpGs are given according to human genome version hg19 (hg19/GRCh37).

3.9 Non-base resolution hydroxymethylation analysis by hMeSeal

For non-base resolution hydroxymethylation analysis during adipocyte differentiation, Florian Janke (FJ) used DNA of experiment 2 to generate hMeSeal sequencing libraries according to (Song et al., 2017) with minor modifications as described in (Janke, 2021). In short, fragmented DNA and spike-ins were ligated with sequencing adapters. Then, hydroxymethylated sites were conjugated to an azide-containing sugar using a T4 phage β-glucosyltransferase and afterwards labeled with a biotin group using click-chemistry. Finally, biotin-tagged DNA fragments were pulled down using streptavidin-coupled magnetic beads. For sequencing, fragments enriched for hydroxymethylation, and background libraries were amplified using 14 and 11 PCR cycles, respectively. Libraries were multiplexed and submitted to the Genome and Proteome Core Facility of the DKFZ for paired-end 75 bp sequencing on the Illumina NextSeq 550 instrument. After sequencing, data preprocessing was performed by Florian Janke as described in (Janke, 2021), aligning to the human reference genome hg19/GRCh37.

For downstream analyses, I first removed sequencing reads overlapping with the ENCODE blacklist (Amemiya et al., 2019). After downsampling reads of sample “day11, replicate 3” to a comparable library size of other day 11 samples, I merged reads of each day for peak calling. I called narrow peaks with MACS2 using the q-value cutoff 10^{-6} and the option --nomodel –format BAMPE on merged bam files (Zhang et al., 2008). Finally, I prepared a count matrix of reads for each peak, filtered for peaks with an average log2CPM > 2 in at least on time point, and corrected for library size within the csaw framework (Lun and Smyth, 2016). To analyze hydroxymethylation dynamics, I clustered scaled log2CPM values into 6 clusters with Mfuzz clustering using minimum membership of 0.3 (Kumar and E. Futschik M, 2007). For the

generation of bigWig files for visualization using the UCSC browser (Kent et al., 2002), I performed normalization of 'reads per genome coverage' with the deeptools function bamCoverage using the options -bs 20 –smoothLength 40 --normalizeUsing RPGC (Ramirez et al., 2016). For circos plots I used the circlize package in R (Gu et al., 2014). To perform a genome-wide correlation of hMeSeal peaks in SGBS cells of day 27 and in WAT samples, I binned the genome to 4 kb by setting the bamCoverage option to -bs 4000 (Ramirez et al., 2016). Afterwards, I performed spearman correlation on averaged hMeSeal scores of replicates over 4 kb bins.

3.10 Base resolution DNA methylation analysis by Illumina EPIC array

For methylation analyses of experiments 5, 6, and 7, 500 ng DNA were submitted for Infinium Methylation EPIC beadchip array analyses to the Genomics and Proteomics Core Facility (GPCF) of the DKFZ. In short, DNA was first bisulfite-converted using the EZ DNA Methylation Kit 96-well kit. I performed data pre-processing and normalization using the RnBeads package in R (Assenov et al., 2014). Briefly, I used IDAT files as input. Probes were filtered for a detection *p* value threshold of 0.01 and cross-reactive probes were removed (Chen et al., 2013). On the remaining 726,333 CpG sites, I applied SeSAMe's "noobsb" method for background subtraction and performed a dye bias correction using the linear scaling method "dyeBiasCorr" (Zhou et al., 2018).

To identify cell culture or DHA treatment-associated methylation changes during long-term cultivation in experiments 5, 6, and 7, I performed a principal component analysis (PCA) on methylation values. To filter for CpGs associated with the first three principal components (PCs), I applied a linear model and identified CpGs of which the methylation variability displayed a significant linear association (positive or negative) with the corresponding PC coordinates of each sample (FDR adj. *p* value < 0.005) and a methylation range > 0.2.

3.12 Gene expression analyses

3.12.1 mRNA expression analysis by reverse-transcription qPCR

For cDNA synthesis of experiment 1, I used 1 – 1.5 µg of RNA in 10 µl RNase free water for reverse transcription. I added 2 µl of random hexamer oligonucleotides (50 ng/µl) and 1 µl dNTPs (10 mM) to RNA and incubated at 65 °C for 5 min. I immediately cooled the samples on ice and then added 7 µl of a master mix prepared as following (Table 4):

Table 4| Master mix for cDNA synthesis.

Master mix	Amount [µl]
5x first-strand buffer	4
0.1 M DTT	1
RNaseOUT	1
SuperScript III RT (200 units/µl)	1

For reverse transcription, I incubated the reaction mix for 5 min at 25 °C, for 60 min at 50 °C, and for 15 min at 70 °C. cDNA was afterwards stored at -20°C. Not all primers could be designed as intron spanning, so I generated a negative control for the non-intron spanning primers by repeating the same reverse transcription reaction but substituting SuperScript III RT with RNAse-free water.

I performed real-time qPCR analysis of 1:10 diluted cDNA samples on the Roche Light Cycler 480 in 384 well plates using the Roche universal probe library (UPL) system with a program of 10 min at 95 °C followed by 45 cycles of 10 s at 95 °C, 20 s at 55 °C and 1 s at 72 °C on a Lightcycler480 RealTime PCR System. I designed the primers whenever possible as intron spanning by using the UPL Assay Design Center to avoid amplifying genomic DNA. I tested primary efficiency by calculating the amplification curve of a serial 1:10 dilution and considered an > 1.8-fold increase per cycle as acceptable. Expression levels of target genes in experiment 1 were normalized to the housekeeping genes *HPRT1 (hypoxanthine phosphoribosyltransferase 1)* and *TBP (TATA-box binding protein)* according to the Livak method (Livak and Schmittgen, 2001). Primers and respective probe numbers are listed in For statistical analysis, I performed one-way ANOVA with post hoc Dunnett's analysis for pairwise comparisons between different time points of SGBS differentiation (day 1, day 7, day 11) and day 0. Statistical tests were done using GraphPad Prism version 5.03 for Windows, GraphPad Software, San Diego California USA, www.graphpad.com.

Table 5. For statistical analysis, I performed one-way ANOVA with post hoc Dunnett's analysis for pairwise comparisons between different time points of SGBS differentiation (day 1, day 7, day 11) and day 0. Statistical tests were done using GraphPad Prism version 5.03 for Windows, GraphPad Software, San Diego California USA, www.graphpad.com.

Table 5| RT-qPCR primers.

Target gene	UPL probe	Forward primer	Reverse primer	Relative expression to HKG at day0
PPARGt2	7	gacaggaaagacaacagacaaatc	ggggtgatgtgtttgaacttg	0.776
*CEBPA**	28	ggagctgagatcccgaca	ttctaaggacaggcgtggag	0.016
CFD	18	tccaagcgcctgtacgac	gtgtggccttctccgaca	0.022
PLIN1	64	ggacacagtggtgcattacg	gtcccggaattcgctctc	< 0.001
HPRT1	73	tgaccttgatttattttgcatacc	cgagcaagacgttcagtcct	1.068 – 1.302
TBP	51	cccatgactcccatgacc	tttacaaccaagattcactgtgg	0.547 – 0.936

HKG: housekeeping genes (HPRT1, TBP). *non-intron spanning

3.12.2 Analyses of mRNA expression by RNA-seq.

“Sequencing libraries were prepared by the Genomics and Proteomics Core Facility (DKFZ, Heidelberg) from total RNA using the Illumina TrueSeq Stranded total RNA Library Prep Kit according to the manufacturer’s instructions. RNA isolated from SGBS cells was sequenced in multiplexes of 13 samples in a paired-end setting (100 bp) on an Illumina NovaSeq 6000 machine. WAT-isolated RNA was sequenced in multiplexes of 5 - 6 samples in a paired-end setting (100 bp) on an Illumina Hiseq 4000 machine. Data were processed with the nf-core rnaseq pipeline (Ewels et al., 2020). Default parameters were used unless mentioned otherwise. Sequences were aligned to the human reference genome (hg19/GRCh37) by application of the software HISAT2, --unstranded option. Transcripts were assembled using StringTie and GENCODE gene annotation v.29 lift 37. Gene counts were generated with the Stringties prepDE.py script (setting: -eb). Normalized counts per million (CPM) were used for statistical analyses performed by edgeR (Robinson et al., 2010).” (Feuerstein-Akgoz, C. et al., *in preparation*).

To identify DHA-associated gene expression differences in experiment 5, I performed a principal component analysis on log2CPM values of genes with log2CPM > 1 in at least 2 replicates. To filter for genes with differential expression in DHA- vs nonDHA-treated samples separated in PC3, I applied a linear model to identify those genes whose expression variability displayed a significant linear association with the PC3 coordinates of each sample (p value < 0.05) and log2CPM range > 1.

3.13 Proteome data

To generate protein expression data from differentiating SGBS cells (details in (Schaffert et al., 2021)), protein separation was performed by sodium dodecylsulfate (SDS) polyacrylamide gel electrophoresis. Gels were stained with Coomassie Brilliant Blue R-250 dye, and proteins were in-gel proteolytically digested with trypsin. Untargeted proteomics data were generated by nano ultra-performance liquid chromatography (UPLC) followed by mass spectrometry (Schaffert et al., 2021) and were kindly provided for integrated analysis. Changes in protein levels were estimated for proteins detected in at least three of five replicates. Average fold change of corrected signal intensities of five replicates was used for visualizations as described in (Schaffert et al., 2021).

3.14 Metabolome data

Targeted and untargeted metabolome data of the SGBS differentiation experiment 3 were provided by and partially published by collaboration partners (Miehle et al., 2020). SGBS differentiation, sample extraction, and sample homogenate were prepared as described in the publication.

3.14.1 Targeted metabolome data

“For targeted analysis, 400 µl homogenated cell sample solution was spiked with internal standards (ISTD) and subsequently evaporated to complete dryness. Afterwards, derivatization was performed using 50 µl of 20 mg/ml methoxyamine hydrochloride in pyridine for 1 h at 60 °C and 50 µl MSTFA for another 1 h at 60 °C. For analysis, 1.5 µl of derivatized sample solution was automatically injected into the 6890N gas chromatograph. Separation was performed on a HP5-MS column (30 m x 0.25 mm, 0.25 µM) with 8:1 split mode. Helium was used as carrier gas with a flow of 1.0 ml/min. A temperature gradient with following conditions was used: 1 min hold time at 50 °C, temperature increase of 8 °C/min to 175 °C, 5 min hold time at 175 °C, temperature increase of 8 °C/min to 200 °C, temperature increase of 50 °C/min to 300 °C, and post run at 300 °C for 5 min. The GC was coupled with a transfer line, heated at 310 °C, to a 5973N mass selective detector. Detection was performed in the EI mode (70 eV) using selected ion monitoring (SIM) and matching the retention time. The used SIM values were as listed in Table 6. For quantification, seven calibration levels were used. The ion source temperature was set to 240 °C and the single quadrupole temperature to 150 °C. Metabolites were completely excluded from the data set if concentration values were

missing (NA) in more than 33.3 % of the samples within a harvesting time point. Missing values were replaced by the respective minimal metabolites concentration measured, divided by 2 and multiplied by a randomly chosen factor between 0.75 and 1.25." (Feuerstein-Akgoz, C. et al., *in preparation*)

Table 6| Selected ion monitoring (SIM) values.

Metabolites	m/z	Corresponding ISTD	m/z
2-hydroxyglutaric acid	247.1	D3-2-hydroxyglutaric acid	250.2
α-ketoglutaric acid	198.1	13C4-α-ketoglutaric acid	308.1
isocitric acid	245.1	D3-2-hydroxyglutaric acid	250.2
citric acid	273.1	D4-citric acid	276.1

ISTD: internal standard

3.14.2 Untargeted metabolome data

For the untargeted metabolome data, cell homogenates were centrifuged for 5 min at 5,500 x g and applied to ultra-high-performance liquid chromatography-tandem mass spectrometry (UPLC-MS/MS) in electrospray positive ionization mode. One analysis was performed by UPLC-MS/MS in negative ionization mode, one by UPLC-MS/MS in negative ionization mode for polar compounds as recently published (Moellmann et al., 2020).

3.15 ACT-seq data of WAT tissue

ACT-seq of histone marks and acNEIL1 binding was performed on pulverized WAT samples. First, the pA-Tn5ase protein was purified from E.coli by Dieter Weichenhan (DW), as described in (Liu et al., 2021). Afterwards, Karin Klimo (KK) performed ACT-seq experiments for histone marks and Jessica Heilmann (JH) for acNEIL1 on pulverized tissues. For that, pA-transposome-antibody (pA-TnpOme-Ab) complex was prepared using the antibodies against the following histone marks: H3K27ac, H3K27me3, H3K4me1, H3K4me3 (overview in Table 7), and Anti-acetylated NEIL1 (Sengupta et al., 2018) (AcNL1, generously provided by Muralidhar Hegde and Sankar Mitra, Houston Methodist Research Institute).

Table 7| List of antibodies against histone marks used for ACT-seq.

Antibody	Manufacturer
Anti-H3K27ac, (#4729)	Abcam, Cambridge, UK
Anti-H3K27me3, (#9733)	Cell Signaling Technology, Denver, MA, USA
Anti-H3K4me, (#8895)	Abcam, Cambridge, UK
Anti-H3K4me3, (#C15410003)	Diagenode, Denville, NJ, USA

The tissue permeabilization process was adapted from the CUT&Tag protocol (Kaya-Okur et al., 2020). Approximately 25 mg of each pulverized adipose tissue biopsy was lysed by gentle pipetting in 0.6 ml ice-cold nuclear extraction buffer (20 µM HEPES-KOH, pH 7.9, 10 µM KCl, 0.5 µM spermidine, 0.1 % Triton X-100), kept on ice for 3 min and homogenized for 30 s using the TissueLyser II. Next, samples were centrifuged at 4 °C and 4,000 rpm for 15 s to remove the top layer of fat. The remaining nuclei suspensions were centrifuged again at 4 °C and 5,000 rpm for 10 min. Nuclei pellets were washed first with 0.8 ml PBS (supplemented with 1x cOmplete, EDTA-free Protease Inhibitor Cocktail and 15 mM sodium butyrate) and then twice with 0.8 ml PBS. Finally, PBS was removed by pipetting while leaving ~ 25 µl to avoid loss of nuclei and resuspended with additional 25 µl 2x complex formation buffer (CB) (1 x CB: 100 mM Tris, pH 8, 0.3 M NaCl, 0.1 % Triton X-100, 25 % glycerol) and incubated on ice for 10 min.

To tag the DNA associated with the protein of interest, the antibody-complexed was allowed to enter the nucleus and bind to the protein of interest. For that 2.6 µl pA-TnpOme-Ab complex was added to 50 µl sample and incubated for 1 h at room temperature. Next, nuclei were washed twice with 350 µl wash buffer (WB, 50 mM Tris, pH 8.0, 150 mM NaCl, 0.05 % Triton X-100) and centrifuged at 4 °C and 5,000 rpm for 5 min. Afterward, supernatants were discarded, and 100 µl WB was added. The tagmentation reaction was initiated by the addition of 1 µl 1 M $MgCl_2$ sustained at 37 °C. After 60 min the reaction was stopped with 4 µl 0.5 M EDTA, pH 8.0, 2 µl 10 % SDS and 1 µl proteinase K solution (20 mg/ml) by incubation for 60 min at 55 °C. Finally, the DNA fragments generated by the tagmentation reaction were purified using a MinElute Reaction Cleanup Kit and eluted in 25 µl 37 °C-warm elution buffer (EB).

For library preparation, 25 µl of the eluted DNA were amplified with 2.5 µl custom nextera PCR primers 1 and 2, each, and 25 µl NEBNext High-Fidelity 2x PCR master mix. First, a PCR preamplification was performed using the following program: 72 °C for 5 min, 98 °C for 30 s; 5 cycles of [98 °C for 10 s, 63 °C for 10 s, 72 °C for 10 s] and a final 72 °C for 1 min. Then with an aliquot of 5 µl preamplified PCR product, the optimal number of cycles for amplification was determined according to (Buenrostro et al., 2015). For that the qPCR reaction was performed in a 384-well format with a Lightcycler480 Real-Time PCR System. 1 µl 10x SybrGreen was added to 5 µl PCR product and further amplified using the following program: 98 °C for 30 s; 20 cycles of [98 °C for 10 s, 63 °C for 10 s, 72 °C for 10 s] and a final 72 °C for 1 min. After estimating the optimal number of additional cycles, the remaining 20 µl of preamplified PCR product was amplified in a second round using the same cycle conditions as in the preamplification protocol. Finally, the amplified libraries were purified using magnetic AMPure XP beads in a two-sided reaction with 0.5x and 1.3x volumes of beads, and eluted in 15 µl EB.

For sequencing (paired-end, 75 bp) with mid-output on the NextSeq 550 system, six to eight samples were multiplexed and submitted to the Genome and Proteome Core Facility of the DKFZ.

Data preprocessing was performed by a fully dockerized workflow using the Common Workflow Language v. 1.0 (Amstutz et al., 2016) which is publicly available (Breuer et al., 2020). In short, quality control of the sequencing reads and adapter trimming was performed with Trim Galore v. 0.4.4 (https://www.bioinformatics.babraham.ac.uk/projects/trim_galore/) in combination with Cutadapt v. 1.14 (Martin, 2011) with the non-default parameters "--paired", "--nextera", "--length_1 35", "--length_2 35". Alignment was performed against the human reference genome hg19/GRCh37 using Bowtie2 v. 2.2.6 (Langmead and Salzberg, 2012) with the "--very-sensitive" flag enabled. Aligned reads of the same sample, but sequenced on different lanes were merged using SAMtools merge v. 1.5 (Li et al., 2009). Reads with mapping quality below 20 on the Phred scale or not mapping with a pair were filtered out with SAMtools view. As each Tn5 transposase homodimer binds a DNA stretch of 9 bp central region, where the transposition occurs, as well as two 10 bp flanking regions, the calculated minimal fragment size in a tagmentation reaction is 38 bp (Adey et al., 2010). Therefore, we removed all read pairs displaying size < 38 bp. To accurately estimate the center of the transposition events, reads centers were shifted by +4 bp when aligned to the + strand and read centers were shifted by -5 bp when aligned to the – strand, as described by (Buenrostro et al., 2013). All downstream analyses were based on these adjusted read coordinates.

"Broad peaks were called with MACS2 (Zhang et al., 2008) on merged bam files using the option –nomodel and setting the q-value to q = 0.05 for histone marks (loose cutoff) or q = 1e-5 (if stringent peak calling is specified). Within the csaw framework (Lun and Smyth, 2016), normalization of the reads was performed by TMM normalization within peaks. BigWigs were normalized with the deeptools function bamCoverage (Ramirez et al., 2016) by removing reads overlapping with the ENCODE blacklist (Amemiya et al., 2019) and using the options -p max -bs 20 --smoothLength 40 –e --normalizeUsing RPGC." (Feuerstein-Akgoz, C. et al., *in preparation*)

3.16 Bioinformatic downstream analyses

3.16.1 PMD, LMR, UMR, FMR definitions

To determine partially methylated domains (PMDs), we applied the MethylSeekR package (Burger et al., 2013) on each sample using raw BS data with coverage ≥ 10x, while omitting CpGs with extremely high coverage (0.99 quantile) of experiment 2. I defined common PMDs for intervals where at least 4 of 7 samples displayed PMD characteristics. Further, I defined common unmethylated regions (UMRs) according to default settings and lowly methylated regions (LMRs) using a modified cutoff of at least 3 CpGs with a methylation level below 0.7. Common UMRs needed to be overlapping in all samples, and common LMRs were defined as overlapping in more than four samples. Fully methylated regions (FMRs) were defined as the genomic regions not defined as PMDs, UMRs, or LMRs.

3.16.2 Mfuzz clustering

I performed Mfuzz clustering with several datasets using the published Mfuzz package (Kumar and E. Futschik M, 2007) and applying method specific parameters, to identify dynamic changes during adipocyte differentiation. For hydroxymethylation data, I used scaled log2CPM in hMeSeal peaks for generating 6 Mfuzz clusters using minimum membership of 0.3 (experiment 2, Fig. 18). For gene expression data, I preselected the 75 % most variable genes (based on standard deviation (SD)), expressed in at least two samples with log2CPM > 1. Then I applied Mfuzz clustering on scaled mean log2CPM of all time points using minimum membership of 0.5 to generate 5 clusters (experiment 2, Fig. 27). For metabolome data, I performed Mfuzz clustering using metabolites with a Human Metabolome Database ID (HMDB, https://hmdb.ca) (experiment 3, Fig. 31). I clustered mean signal intensities of all time points of the untargeted metabolome analysis applying a minimum membership of 0 to generate 3 clusters.

3.16.3 UCSC genome browser tracks

To generate genome visualizations in Fig. 12, 22, 35 and 44, bedgraph or bigWig files of analyzed data (individual replicates or merged data files as indicated) were uploaded to the UCSC genome browser with the human genome version hg19 (hg19/GRCh37) (Kent et al., 2002).

3.16.4 EnrichedHeatmaps and Heatmaps

I generated heatmaps using the R package ComplexHeatmap (Gu et al., 2016) or EnrichedHeatmap (Gu et al., 2018).

In the enriched heatmaps, I displayed hydroxymethylation values based on WGBS/oxBS, as well as hMeSeal, ACT-seq, DHS, mediator complex subunit 1 (MED1) normalized reads and/or ATAC enrichment bigwigs, representing fold change over background (Fig. 14, 15, 19 - 21, 36, 37 and 40). I displayed regions of ± 1, 2.5, or 5 kb around the site of interest and quantified the signal intensity in a window size of 50 bp in each row, respectively. In Fig. 19 and 20, mean values of several sites of interest were plotted. For display, I used the mean_mode = “w0” and the smooth = F option. I smoothed hydroxymethylation data (based on WGBS/oxBS) in a window size of 50 bp and displayed using the mean_mode = “absolute” option. The upper line plots in Fig. 14, 36, and 40 display average intensity curves as indicated. As site of interest and heatmap centers served hMeSeal peak, centers of LMRs, or centers of enhancers defined by centers of H3K27ac peaks overlapping with H3K4me1 and absence of stringent H3K4me3 peaks.

3.16.5 EpiAnnotator enrichment analysis

I performed enrichment analysis of hMeSeal peaks or CpG sites of interest in chromatin states with the EpiAnnotator tool (Pageaud et al., 2018).

For hMeSeal peak enrichment during adipogenesis (Fig. 20), ChromHMM states of *in vitro* differentiated mature adipocytes (Adipocytes, E023, (Roadmap Epigenomics et al., 2015)) were used, defined by the ChromHMM algorithm (Ernst and Kellis, 2012). As background, I used ~ 40,000 randomly generated regions of the same interval size as peaks in clusters.

For enrichment analysis of CpGs with methylation variability associated with cultivation effects of SGBS preadipocytes (Fig. 49), I used ChromHMM states of adipose-derived stem cells (ADS, E025, (Roadmap Epigenomics et al., 2015)). In addition, I used as target sites CpGs significantly positively or negatively associated with PC1 - 3 (see chapter 3.10) and as background the remaining CpGs (after preprocessing and filtering) on the EPIC array.

3.16.6 TF motif enrichment analyses

I performed TF motif enrichment analysis using the GimmeMotifs gimme motif function on hMeSeal peaks in clusters and on WAT enhancer (Bruse and Heeringen, 2018). WAT

enhancers were defined by H3K27ac peaks overlapping with H3K4me peaks and not overlapping with stringent H3K4me3 peaks. Background regions were corrected for CG content. Hocomoco v11 motifs were clustered based on motif similarity by RSAT matrix-clustering software using standard settings (http://rsat.sb-roscoff.fr/matrix-clustering_form.cgi) (Castro-Mondragon et al., 2017).

In Fig. 23, I displayed the top 5 enriched motif cluster. Of each enriched cluster, I show a representation of the binding motif, the enrichment *p* value and highlight the name of the best enriched motif. In the last column, all enriched (*p* value < 1e-2, with > 2 % matches in input) and expressed motifs of the cluster are listed. In Fig. 37 displaying enriched TF motifs in WAT enhancers, I display the top 10 enriched TF motif clusters with a significant enrichment (P-value < 1e-2, with > 1 % matches in input) and expression in WAT samples. Finally, in Fig. 50 I displayed the top 10 enriched TF motif clusters enriched in LMRs with a CpG negatively associated with PC2 (see chapter 3.10) with a significant enrichment (*p* value < 0.05, with > 1 % matches in input). As background served all CpGs on the EPIC array not negatively associated with PC2. I displayed in the heatmap the enrichment ratio and at the right side I listed all significantly enriched motifs associated with the motif cluster and expressed in SGBS cells. The correlation plot at the right, displays the Pearson's r correlation coefficient between methylation at CpGs negatively associated with PC2 and gene expression of the identified TFs.

To find the exact motif position within the peaks, I used the function gimme scan. These positions were used to draw a density plot of hydroxymethylated CpGs using WGBS/oxBS data around the identified binding motif in an interval of ± 200 bp (Fig. 24+26).

3.16.7 hMeSeal cluster at gene expression cluster enrichment analysis

To investigate the role of different hydroxymethylation dynamics (six hydroxymethylation clusters) at enhancer regions in the regulation of gene programs (5 gene clusters), I performed a distance-based enrichment analysis on data of experiment 2 (Fig. 30). "I mapped to each hMeSeal peak all genes with a distance of the TSS to the peak center ≤ 100 kb. Then I performed for each hMeSeal cluster an enrichment analysis at the five gene clusters that were mapped by distance to the specific hMeSeal clusters. As background served random intervals to which genes of the five gene clusters were mapped likewise. Fisher's exact test was performed to define significant enrichment (Bonferroni-adjusted *p* value ≤ 0.05)." (Feuerstein-Akgoz, C. et al., *in preparation*)

3.16.8 Pathway analyses

Pathway overrepresentation analysis was performed with the WebGestaltR package (Liao et al., 2019). For gene expression clusters (eCl) I used genes of the cluster for KEGG pathway analysis and displayed all significantly enriched pathways (FDR adj. *p* value < 1e-5) (Fig. 28). For genes with expression changes significantly associated with DHA treatment (PC3) (see chapter 3.12.2), I performed KEGG and Wikipathway overrepresentation analysis, and displayed top ten significantly (FDR adj. *p* value < 0.05) enriched pathways (Fig. 55). For all analyses, I used all transcripts of the genome as background and default settings.

For genes with expression changes significantly associated with DHA treatment, I also performed Ingenuity Pathway Analysis (IPA) on the log2 fold change between DHA vs nonDHA samples (Fig. 56), using replicates as a covariate in the edgeR robust function for differential gene expression analysis (Zhou et al., 2014)

To identify KEGG pathways associated with the protein-metabolite clusters (Fig. 32), I used the MetaboAnalyst 5.0 Joint Pathway Analysis tool for Metabolic pathways (integrated) using the default settings (Xia et al., 2009). I displayed pathways with an FDR adj. *p* value < 1e-5.

3.16.9 Correlation of hydroxymethylation, histone marks and ATAC

For the correlation of hydroxymethylation (hMeSeal), histone marks, and ATAC signal in WAT at enhancer regions, I selected a range of ± 5 kb around the center of enhancer regions defined by H3K27ac binding (n = 3) overlapping with H3K4me1 (n = 3) and absence of stringent H3K4me3 (n = 4) binding. I performed a Spearman correlation analysis of 1 kb binned normalized mean signal intensities.

3.16.10 Gene body hydroxymethylation correlation analysis

“Gene body correlation analysis was performed at WAT enhanced genes. I identified enhanced genes using the definition of “tissue enhanced” expression of the Protein atlas (Uhlen et al., 2015) and applied it on GTEx expression data of all available tissues (GTEx Consortium, 2020). First genes were filtered for an average expression of TPM > 5 in subcutaneous tissue. Further, the average expression in subcutaneous tissue was selected for > 4 compared to the average expression in the other tissues. To calculate the average expression of other tissues, mean expression levels of each tissue type, or median of means of tissue subtypes was taken, excluding visceral adipose tissue and mammary tissue due to their high content in adipocytes.

As background genes served non-WAT enhanced genes with same average expression distribution as WAT enhanced genes in the WAT samples. At WAT enhanced genes or background genes, Pearson and Spearman correlation was performed on five samples between hMeSeal reads mapped to the gene body (log2CPM) and gene expression (log2CPM).” (Feuerstein-Akgoz, C. et al., *in preparation*)

3.16.11 Mitotic scores

EpiCMIT.hyper and EpiCMIT.hypo mitotic scores were calculated using the epiCMIT mitotic clock calculator for methylation data (https://github.com/Duran-FerrerM/Pan-B-cell-methylome) (Duran-Ferrer et al., 2020). I displayed 1-EpiCMIT.hypo to display a decrease of the score in line with the loss in methylation (Fig. 51 + 52).

3.17 Data access

(Hydroxy-)methylation and RNA-seq data generated from SGBS cells in experiment 2 and ACT-seq data of histone marks of WAT have been submitted to the NCBI Gene expression omnibus (GEO, http://www.ncbi.nlm.nih.gov/geo/) under accession number GSE131318. ChromHMM data with the sample numbers E025 (ChromHMM ADS), E023 (ChromHMM Adipocytes), and E063 (ChromHMM Adipose tissue) used for EpiAnnotator enrichment analysis and displayed in UCSC genome browser tracks were obtained from Epigenomics Roadmap (Roadmap Epigenomics et al., 2015). DHS and MED1 ChIP-seq data of SGBS cells at day 10 of differentiation were retrieved from GSE64233 for visualization in the UCSC genome browser tracks and EnrichedHeatmaps (Schmidt et al., 2015). PPARG and CEBPA ChIP-seq tracks of SGBS cells at day 10 of differentiation, used for enrichment analyses and display in the UCSC genome browser tracks, were accessed from GSE27450 (Schmidt et al., 2011). CTCF binding in adipogenesis was accessed from GSE21366 (Mikkelsen et al., 2010) and CTCF ChIP-seq clusters were downloaded from the ENCODE portal (Gerstein et al., 2012; Wang et al., 2012b, 2013). ATAC-seq data of SGBS cells at day 14 of differentiation and of adipose tissue were taken from GSE110734 (Cannon et al., 2019). The following datasets were retrieved directly from the UCSC browser for visualization (Kent et al., 2002): WGBS data of adipose-derived stem cells (ADS) were published by (Lister et al., 2011). WGBS, PMDs, H3K27me3, and H3K9me3 of the ADS (E025) were published by (Roadmap Epigenomics et al., 2015). ChIP-seq data for H3K27me3 and H3K9me3 of ADS (92) are from REMC/Broad/Roadmap. Tissue-specific gene expression to identify WAT-enhanced genes was retrieved from GTEx Portal.

4 Results Part 1
DNA hydroxymethylation dynamics during adipogenesis

To characterize epigenetic changes during human adipogenesis, I established the differentiation of the SGBS preadipocyte cell line to mature adipocytes as a model (Fig. 8 + 11). Fig. 8 (chapter 3.3) summarizes the experimental design and gives an overview of the differentiation experiments analyzed with various –omics technologies as indicated.

To accomplish SGBS differentiation, the cells were grown to confluency, which induces a commitment stage. Then, the growth medium was changed to differentiation medium at day 0 of the differentiation protocol to initiate the differentiation program synchronously. Cells underwent a round of mitotic clonal expansion, and the cellular morphology switched from a spindle-shaped to a round cell structure (day 1). I confirmed adipocyte differentiation by lipid droplet accumulation starting from day 7, which was completed on day 11 (Fig. 11a). At the mRNA expression level, I was able to confirm the upregulation of PPARG and CEBPA in

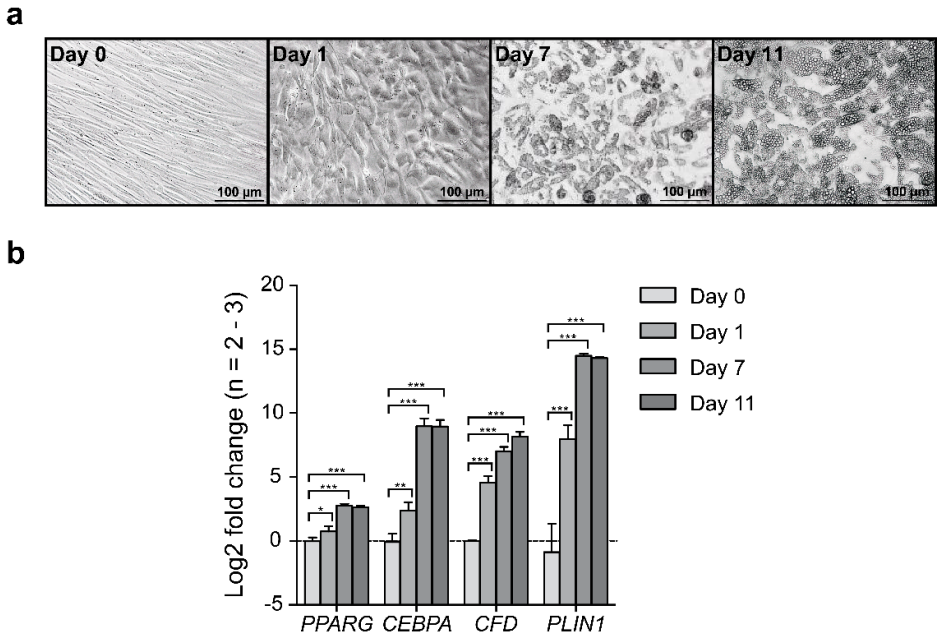

Fig. 11| SGBS adipocyte differentiation. a, Differentiation of SGBS preadipocytes to mature adipocyte at day 0, 1, 7, and 11. Multilocular lipid accumulation is visible on days 7 and 11. **b**, mRNA expression changes of adipocyte-specific marker genes depicted as log2 fold change (RT-qPCR) relative to day 0 (day 0, 1, 7, 11) with n = 3, except day 0 with n=2. As housekeeping genes served *TBP* and *HPRT1*. *P* values were estimated by parametric one-way ANOVA with Bonferroni's post hoc test for multiple comparisons. * p value < 0.05, ** p value < 0.01, *** p value < 0.001, **** p value < 0.0001. Overall p value for each gene < 0.0001. Bars indicate mean + standard deviation. Data in this figure are derived from experiment 1, performed by myself (CFA). See Fig. 8 for the experimental design. Modified from (Feuerstein-Akgoz, C. et al., *in preparation*).

mature adipocytes, which are induced in the first wave of TFs. PPARG and CEBPA are adipocyte-specific TFs which then, in turn, induce multiple metabolic genes contributing to the function of mature adipocytes. One example is the induction of the adipokine complement factor D (CFD), which displays the binding of both TFs at its promoter region (not shown). Perilipin 1 (PLIN1) is another upregulated marker gene that coats lipid storage droplets (Fig. 11b).

4.1 Global analysis of the methylome during SGBS differentiation

To characterize the DNA methylation landscape, I generated base-pair resolution methylomes performing whole-genome bisulfite sequencing (WGBS) from differentiating adipocytes (experimental summary in Fig. 8). Unexpectedly in the not-immortalized SGBS strain, I identified pronounced manifestations of partially methylated domains (PMDs) with reduced average DNA methylation (Fig. 12). PMDs are associated with gene-poor, heterochromatic areas in the nuclear periphery (Lister et al., 2009), and are likely not strongly related to epigenetic gene regulation or the differentiation process itself. The overall level of PMD

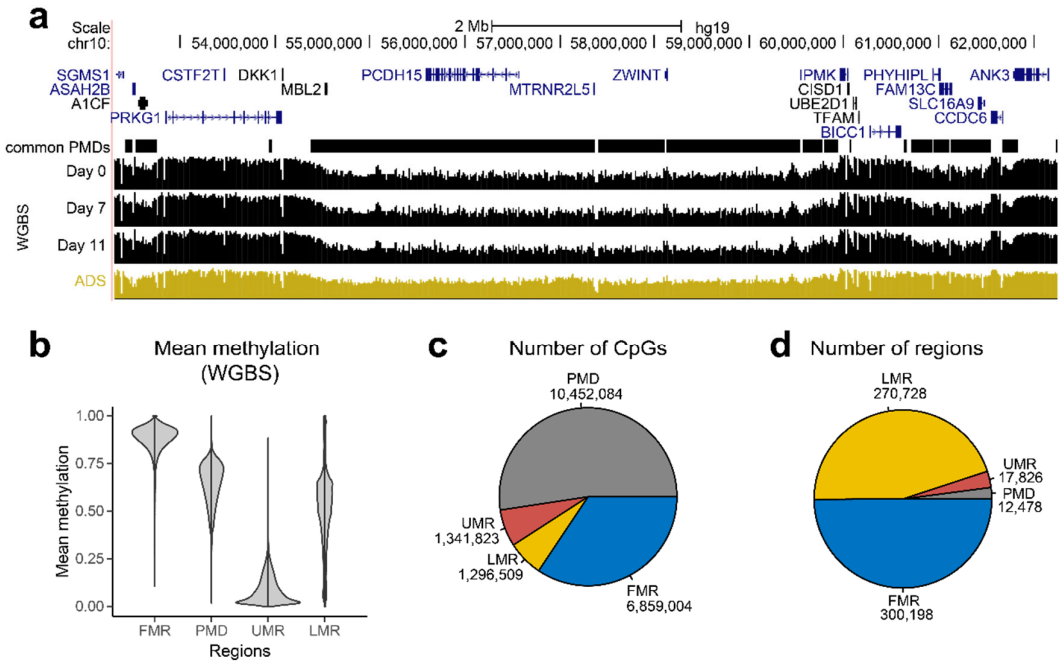

Fig. 12| Genome-wide characterization of the SGBS methylome. **a**, UCSC browser track depicting a partially methylated domain (PMD) on chromosome 10 at different time points of adipocyte differentiation (experiment 2) and of adipose-derived stem cells (ADS) (Lister et al., 2011). **b**, Violin plots of mean methylation levels within fully methylated regions (FMR), PMDs, unmethylated (UMR), and lowly methylated regions (LMR) defined using bisulfite (BS) data of experiment 2. **c**, Pie chart depicting the number of CpGs from WGBS-seq data (coverage ≥ 10x) within PMD, UMR, LMR, and FMR. **d**, Pie chart depicting the number of PMDs, FMRs, LMRs, and UMRs within the genome of SGBS cells. Experiment 2 was performed by LK. WGBS library generation and data analysis performed by myself (CFA). See Fig. 8 for experimental design. WGBS: whole-genome bisulfite.

methylation did not change over time (Fig. 12a). Therefore, I excluded ~ 10 million CpG sites located in PMDs from further analyses and focused on fully methylated (FMRs), unmethylated (UMRs), and lowly-methylated regions (LMRs) (Fig. 12b-c). While ~ 1.3 million CpGs in UMRs are highly condensed in only ~ 18,000 regions with high CpG density (CpG islands) representing mostly promoter regions, further 1.3 million CpGs located in LMRs were distributed in ~ 271,000 regions with lower CpG density, representing enhancer regions (Burger et al., 2013).

4.2 Gain in hydroxymethylation masks the loss of methylation in bisulfite converted data

Using the “gold standard” method whole-genome bisulfite sequencing (WGBS) for methylation analysis, I defined significantly differentially methylated CpG sites (DMS) by a mean methylation difference > 0.25 (which corresponds to ~ 3 SD), *p* value < 0.005, and difference between each sample to means of the other groups > 0.15. In total, I identified 1,812 DMS between preadipocytes (day 0, n = 3) and mature adipocytes (day 11, n = 2) (Fig. 13a, left). During the differentiation process, most DMS became hypomethylated. By including an additional oxidation step to discriminate methylated and hydroxymethylated CpG sites (oxBS), I detected over four times more DMS than after BS treatment (Fig. 13a, right), and the degree of hypomethylation at day 11 was more pronounced (Fig. 13c). I used Illumina 450k array-based BS/oxBS analysis to confirm the loss of methylation, with the disadvantage of covering only about 450,000 predefined CpG sites, however profiting in comparison to WGBS from high coverage. Among the covered CpG sites, loss of methylation was reproduced from the WGBS analysis to > 89 %, while I was not able to validate the few examples of gain in methylation, which might represent technical artifacts due to low coverage in WGBS (Supplementary Fig. 1).

Higher numbers of DMS after oxBS suggested that in conventional methylation analyses with BS treatment, loss of methylation might be masked by an increase in hydroxymethylation, as BS cannot distinguish these two epigenetic marks (Fig. 6a + 13b). Therefore, I applied a maximum likelihood-based analysis of BS and oxBS data to estimate hydroxymethylation levels (Kiihl et al., 2019). I identified 4,927 significantly differentially hydroxymethylated CpG sites (DhMS) between preadipocytes and mature adipocytes with gain in hydroxymethylation, which overlapped to 41 % with the hypomethylated DMS in the oxBS analysis.

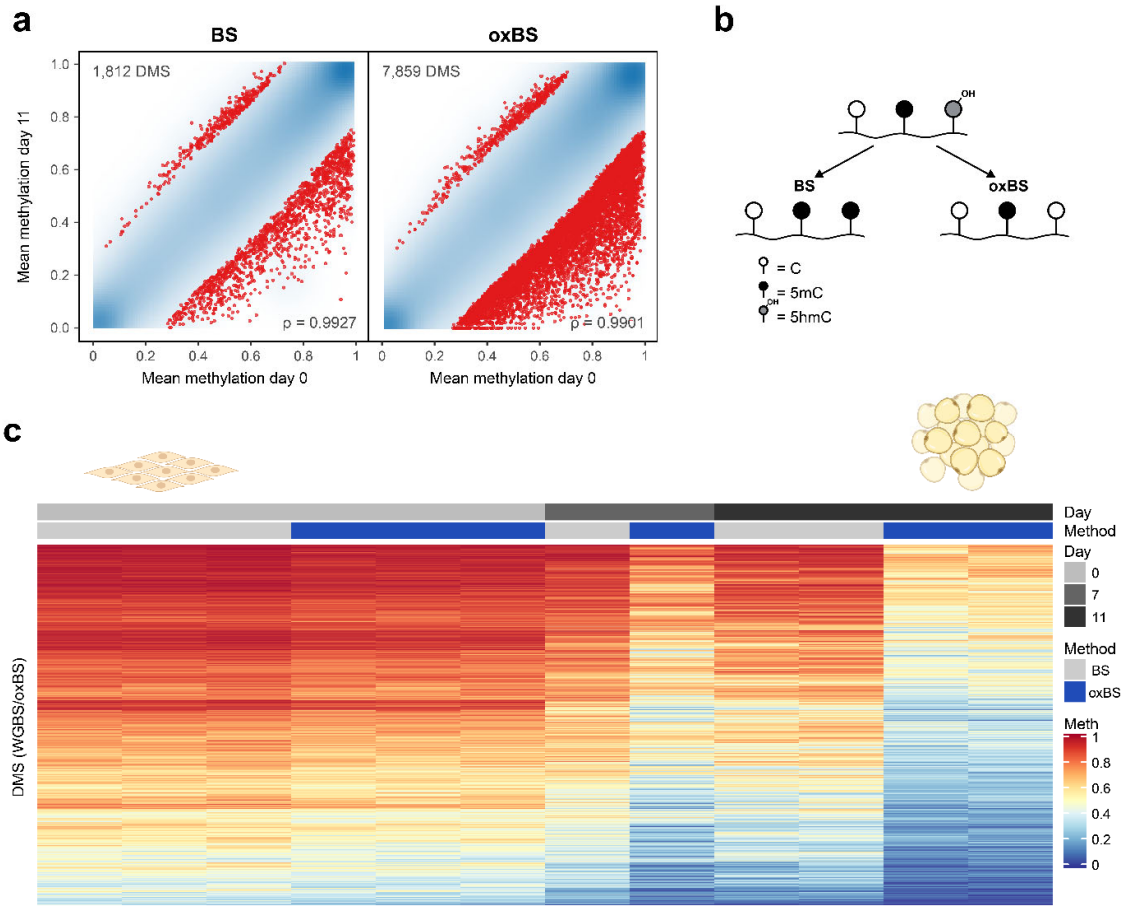

Fig. 13| Loss in DNA methylation during adipocyte differentiation. a, Scatter plot of mean methylation of CpG dinucleotides located outside of partially methylated domains (PMDs) after BS and oxBS treatment followed by sequencing. Differentially methylated sites (DMS) between mature adipocytes (day 11, n = 2) and preadipocytes (day 0, n = 3) are plotted in red. **b**, Schematic diagram depicting differences in methylation detection: Bisulfite (BS) treatment of DNA discriminates unmethylated C from modified C; oxidative bisulfite (oxBS) conversion differentiates 5mC from all other modifications. **c,** Heatmap depicting methylation levels of DMS at day 0, 7, and 11 detected by the BS (grey) and oxBS (blue) method. Methylation levels (Meth: range of 0 – 1) are shown in a color gradient between blue and red. DMS: mean methylation difference > 0.25, *p* value < 0.005, and the difference between each sample to mean of the other group > 0.15. Experiment 2 was performed by LK. WGBS/oxBS library generation and data analysis performed by myself (CFA). See Fig. 8 for experimental design.

DhMS were enriched in LMRs, which were characterized by intermediate methylation levels and a mean size of about 1,000 bp (31 - 7,537 bp) (Fig. 14a). I visualized hydroxymethylation levels at LMRs overlapping with DhMS in a range of 5 kb around the center of the LMR. I observed a sharp increase of hydroxymethylation at the LMR boundaries (Fig. 14b). Hydroxymethylation levels at the 2,157 DhMS located in LMRs gradually increased during adipogenesis. In contrast, the concomitant gradual loss in methylation was only detectable after oxBS treatment, indicating stalling of the demethylation process at the 5hmC mark (Fig. 14c).

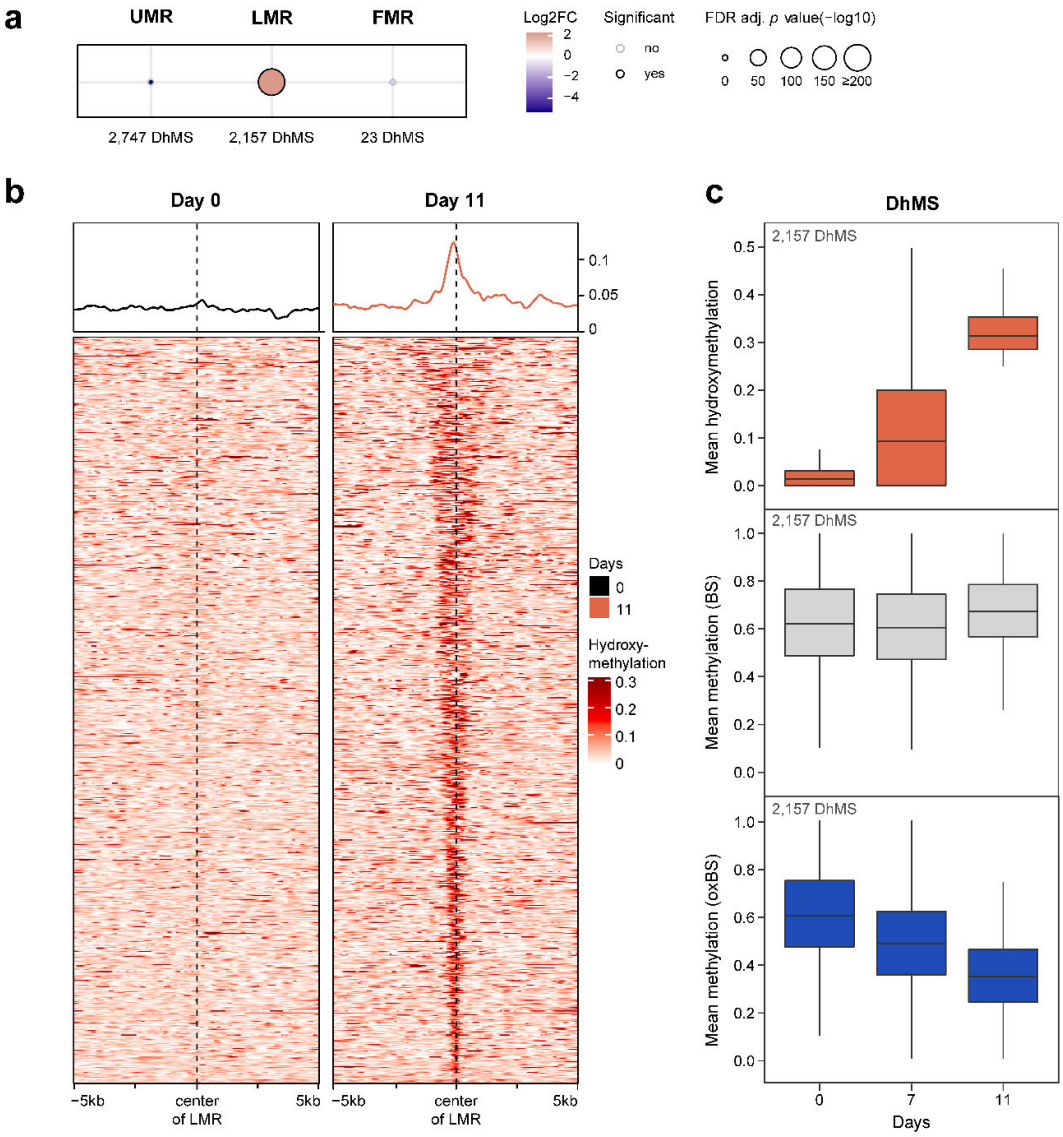

Fig. 14| Gain in hydroxymethylation during adipocyte differentiation. a, Enrichment analysis for unmethylated (UMR), lowly methylated (LMR), and fully methylated (FMR) regions was performed on 4,927 differentially hydroxymethylated sites (DhMS) with a significant increase in 5hmC at day 11 vs day 0 using. WGBS/oxBS data. Fisher's exact test was performed to define significant enrichment (Bonferroni-adjusted *p* value ≤ 0.05). **b**, Smoothed average intensity curves (upper panel) and heatmaps (lower panel) of hydroxymethylation (5hmC) levels of 2,157 DhMS located in LMRs in a range of ± 5 kb from the center of the LMR are displayed at days 0 and 11 of differentiation. **c**, Box plots depicting mean hydroxymethylation levels (upper panel), methylation levels after BS (middle panel), and methylation levels after oxBS (lower panel) at 2,157 DhMS located in LMRs at day 0 (n =3), 7 (n = 1), and 11 (n = 2) of differentiation. Boxplots show median (horizontal line), upper, and lower quartiles (boxes), and vertical lines extending to the 1.5× interquartile range. DhMS: mean 5hmC difference > 0.25, *p* value < 0.005, and difference between each sample to mean of the other group > 0.15. Data in this figure are derived from experiment 2, performed by LK, library generation and data analysis by myself (CFA). See Fig. 8 for the experimental design. WGBS/oxBS: whole-genome bisulfite/oxidative bisulfite.

4.3 DNA hydroxymethylation is a stable mark

Hydroxymethylation is generally discussed as an intermediate step in DNA demethylation (Ito et al., 2011; Tahiliani et al., 2009). To explore the fate of hydroxymethylation during adipogenesis, mature SGBS adipocytes were maintained in culture until day 27 post-induction of differentiation. We extended the detection of 5hmC during adipogenesis using the enrichment-based method hMeSeal, specifically capturing DNA fragments harboring at least one chemically labeled 5hmC. This method requires only minute amounts of DNA and allows a more detailed analysis of hydroxymethylation dynamics due to its sensitivity. By mapping hydroxymethylated DNA fragments, I identified peaks with a median width of ~ 582 bp and a median number of 9 CpG sites (Fig. 15a). Enrichment methods do not precisely determine the hydroxymethylated CpG site within a DNA fragment. However, a principal component analysis of hMeSeal peaks showed that the hydroxymethylation data was highly reproducible due to the method's high sensitivity. In contrast, hydroxymethylation data estimated from WGBS displayed higher within time point variability, possibly resulting from low coverage and that the method in general is more error-prone (Supplementary Fig. 2).

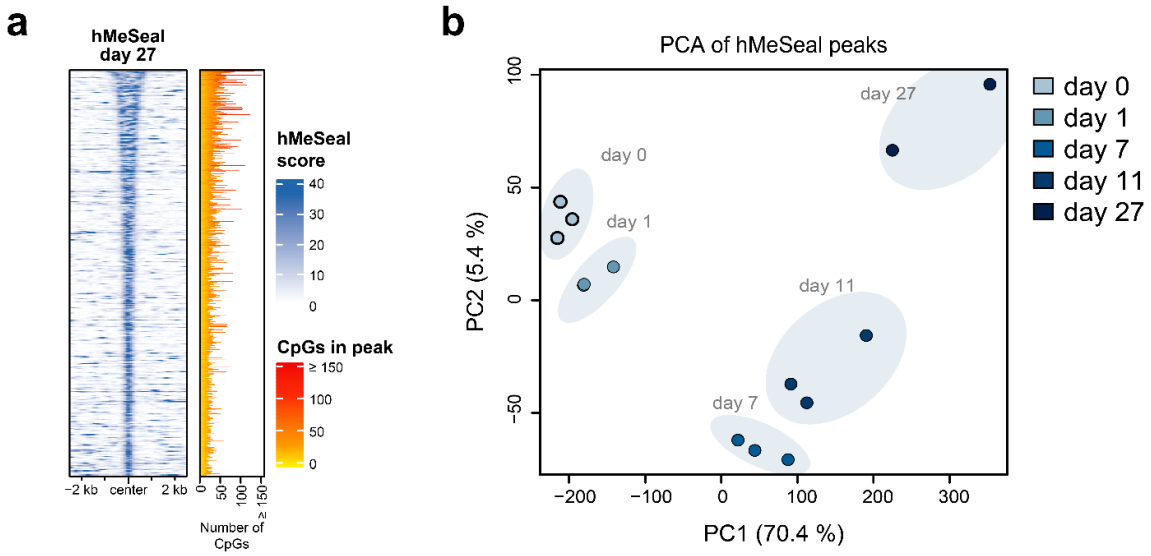

Fig. 15| Quality control of hMeSeal-based hydroxymethylation profiles during adipocyte differentiation. a, Heatmap depicting hMeSeal scores at peaks detected at day 27 post-induction of SGBS differentiation. hMeSeal reads are depicted in an interval ± 2.5 kb around the peak center and sorted by descending peak size. At the right side, a bar plot depicts the corresponding number of CpGs within each hMeSeal peak. **b**, Principal component analysis (PCA) based on hydroxymethylation scores in hMeSeal peaks detected at a genome-wide scale at days 0 to 27 of SGBS differentiation. Individual biological replicates are depicted by circles. Time points are color-coded by a gradient from light to dark blue. Data in this figure are derived from experiment 2, performed by LK, hMeSeal library generation and data alignment by FJ, and downstream data analysis by myself (CFA). See Fig. 8 for the experimental design. Modified from (Feuerstein-Akgoz, C. et al., *in preparation*).

The principal component analysis (PCA) of hMeSeal peaks separated biological replicates of SGBS differentiation by time point at the first principal component, representing more than 70 % of the total variance (Fig. 15b). During the differentiation process, the total number of hydroxymethylation peaks continuously increased from day 0 (2,874 hMeSeal peaks) to day 27 (83,980 hMeSeal peaks) (Fig. 16a). This first analysis at the genome-wide level already confirmed the accumulation of hydroxymethylation and stalling of the demethylation process at the hydroxymethylation stage. When mature adipocytes were kept in culture until day 27 post-induction of differentiation, I detected almost 24 % more hMeSeal peaks than at day 11, and the level of hMeSeal scores also increased on average from 2.18 to 2.43. I could show the *in vivo* relevance of hydroxymethylation in mature adipocytes by a significant correlation between hMeSeal peaks detected at day 27 and in subcutaneous WAT of five human volunteers (Fig. 10b), with a Spearman correlation coefficient rho of 0.722. These data collectively suggested that hydroxymethylation is a stable DNA modification in mature adipocytes and WAT.

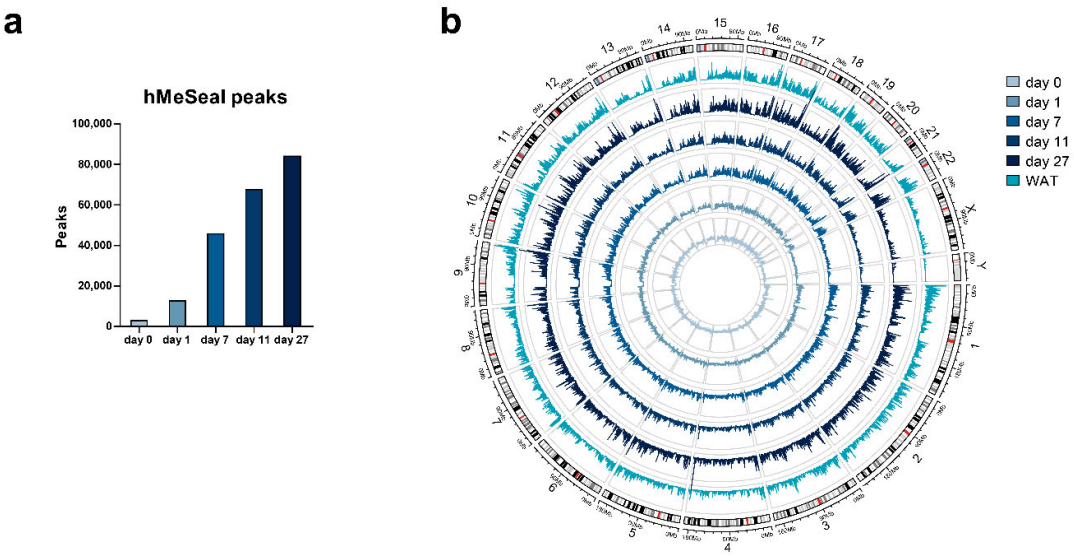

Fig. 16| hMeSeal identifies regions with CpG sites gaining hydroxymethylation. **a**, Bar plot depicts the number of hMeSeal peaks identified at day 0, 1, 7, 11, and 27 of SGBS adipogenesis, representing regions with hydroxymethylated CpGs (experiment 2). **b**, Circos plot displays mean normalized hMeSeal reads (hydroxymethylation) along the genome in SGBS differentiation (n = 2 - 3, experiment 2) and human white adipose tissue (WAT) samples (n = 5, PATHWAY-27 LIS). Experiment 2 was performed by LK, WAT samples were collected by SG, MF, GU, GR, LR under coordination of AB, WAT tissue was pulverized by KK and AW, hMeSeal library generation and data alignment by FJ, and downstream data analysis by myself (CFA). See Fig. 8 + 10 for the experimental design. Modified from (Feuerstein-Akgoz, C. et al., *in preparation*). LIS: large intervention study.

After detecting the global increase in hydroxymethylation, I displayed the hydroxymethylation levels also at individual loci (Fig. 17). In the three examples, I identified hydroxymethylation at enhancer regions defined in adipose-derived stem cells (ADS) (Roadmap Epigenomics et al., 2015) at and around the gene loci of *ACSL1* (Acyl-CoA Synthetase Long Chain Family Member 1), *ELOVL3* (Fatty Acid Elongase 3), and *IDH1* (Isocitrate dehydrogenase 1). The hMeSeal peaks overlap in all examples with an increased density of hydroxymethylated CpG sites shown in the WGBS/oxBS tracks. The hydroxymethylated enhancers overlapped with published data of DHS and MED1, CEBPB, and/or PPARG binding in mature SGBS cells (Schmidt et al., 2011). ACSL1 and ELOVL3 are two enzymes involved in cholesterol metabolism, while ACSL1 has an additional role in lipid biosynthesis and PPAR signaling (Slenter et al., 2018). IDH1 is an enzyme that converts isocitrate to α-ketoglutarate (αKG). This metabolite is the co-factor of TET methylcytosine dioxygenases to oxidize 5mC to 5hmC (Wu and Zhang, 2017) and, therefore, potentially is involved in stabilizing the hydroxymethylation mark.

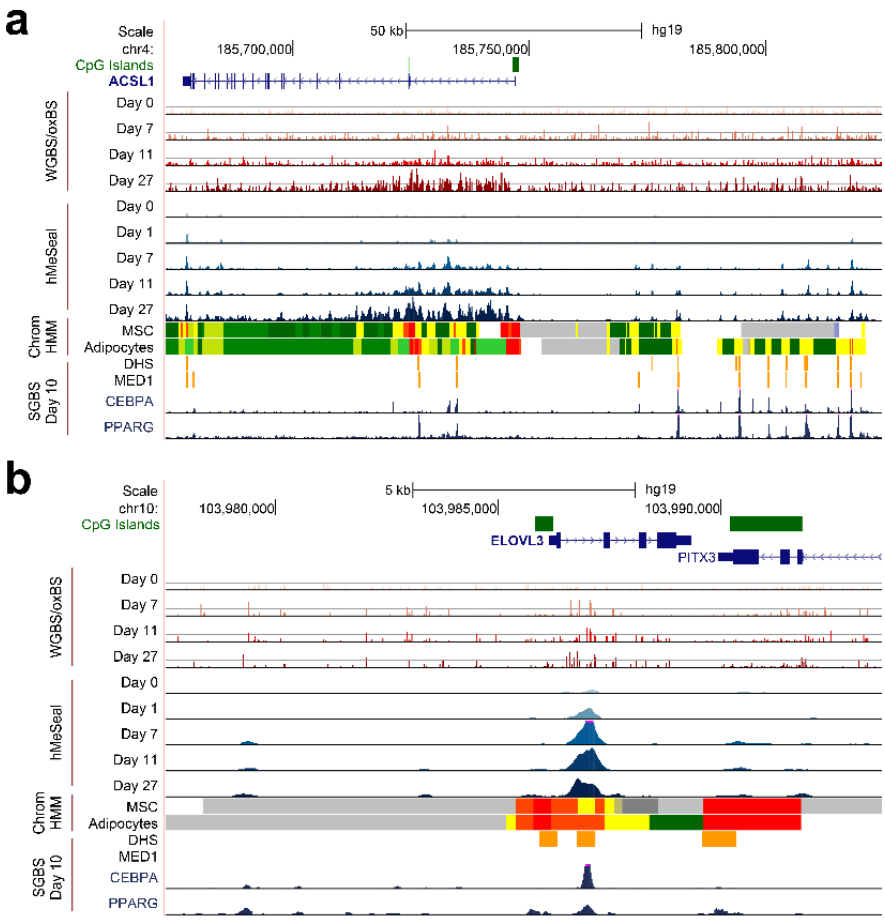

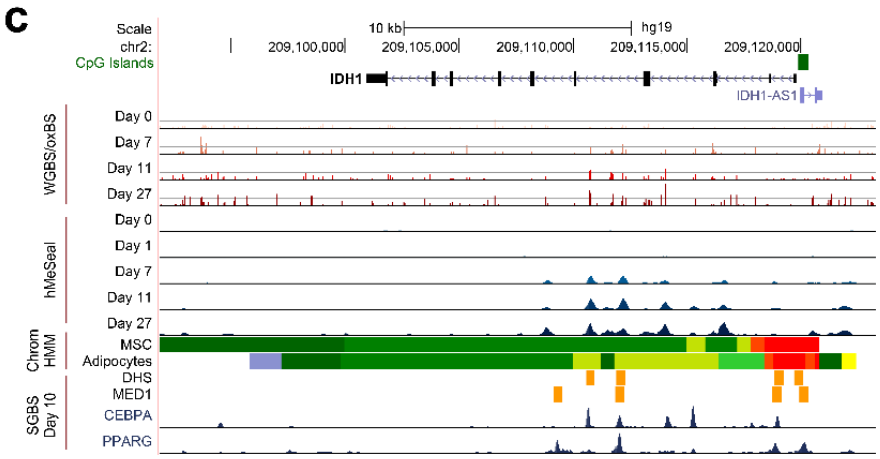

Fig. 17| Hydroxymethylation validation by WGBS/oxBS at individual loci. a-c, UCSC browser tracks displaying hydroxymethylation data at the *ACSL1* (Acyl-CoA Synthetase Long Chain Family Member 1) locus (**a**), the ELOVL3 (ELOVL Fatty Acid Elongase 3) locus (**b**), and the IDH1 (Isocitrate dehydrogenase 1) locus (**c**). Mean hydroxymethylation proportions based on WGBS/oxBS were displayed at a scale of 0 - 0.5, followed by hMeSeal data of differentiation of SGBS cells (score scale: 0 – 100, experiment 2). Next follow ChromHMM tracks of adipose-derived stem cells (ADS, E025) (Roadmap Epigenomics et al., 2015) and *in vitro* differentiated to mature adipocytes (Adipocytes, E023) (Roadmap Epigenomics et al., 2015). DHS and MED1 binding (Schmidt et al., 2015), as well as CEBPA and PPARG binding (Schmidt et al., 2015) of mature SGBS cells (day 10) are displayed. Color code of ChromHMM states as in Fig. 20. Experiment 2 was performed by LK. hMeSeal library preparation and data alignment performed by FJ, WGBS/oxBS library generation and downstream data analysis performed by myself (CFA). See Fig. 8 for experimental design. Modified from (Feuerstein-Akgoz, C. et al., *in preparation*).

4.4 Clustering of hydroxymethylation dynamics

As hMeSeal analyses were sensitive and produced highly reproducible data, I was able to investigate in more detail the dynamics of 5hmC during human adipogenesis. I performed Mfuzz clustering of hMeSeal peak scores and identified six distinct clusters, each representing a characteristic hydroxymethylation profile. The first hydroxymethylation cluster with “transient increase” was characterized by stable detection of hydroxymethylation during adipocyte differentiation, with a transient peak of elevated levels at day 1. The other clusters displayed no hydroxymethylation at day 0. However, levels started to increase from day 1 or day 7 (Fig. 18). In hydroxymethylation clusters “early-persistent“ and “intermediate-persistent“ I observed gain in hydroxymethylation at day 1 and 7, respectively, with stable elevated hydroxymethylation levels afterwards. In clusters “intermediate increase 1”, “intermediate increase 2” and “late increase“ hydroxymethylation levels continued to increase at day 11 and day 27 at different rates. To confirm that the hydroxymethylation dynamics are not resulting from artifacts of the enrichment-based method, I compared the hydroxymethylation levels of the hMeSeal data with the WGBS/oxBS-based hydroxymethylation data (Fig. 19).

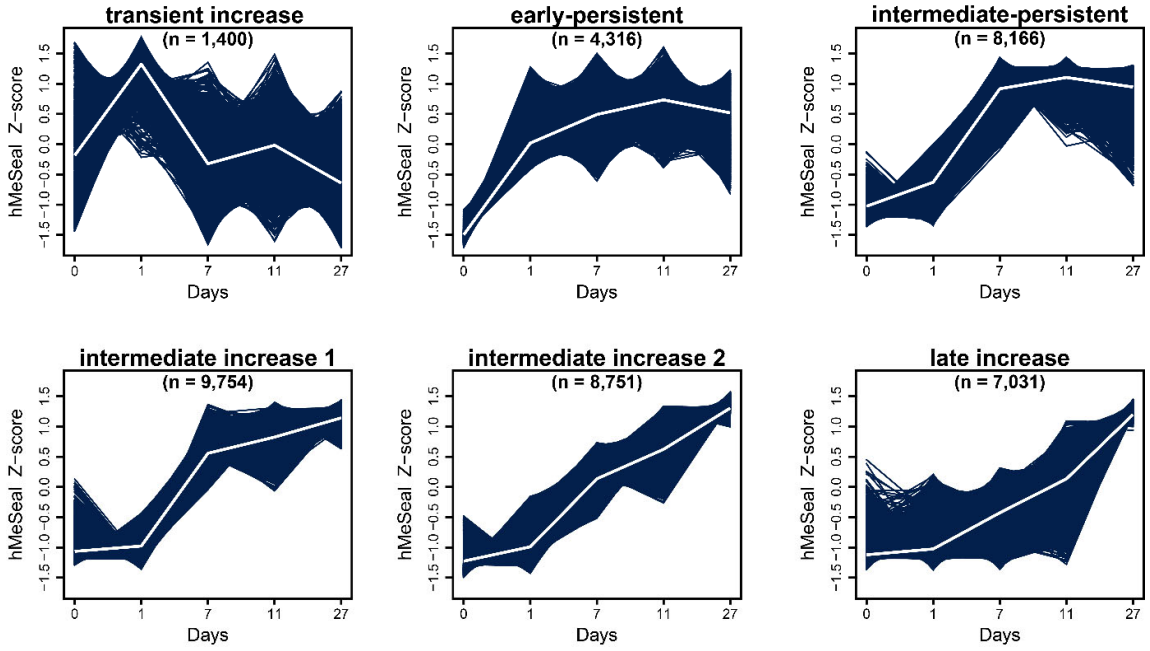

Fig. 18| Mfuzz clustering of hydroxymethylation dynamics. Mfuzz clustering of scaled hMeSeal scores identifying six hydroxymethylation clusters representing hydroxymethylation dynamics over day 0, 1, 7, 11, and 27 of SGBS adipogenesis (n = 3, except for day 27 (n = 2)). Cluster centers are displayed by white lines. Data in this figure are derived from experiment 2, performed by LK. hMeSeal library preparation and data alignment performed by FJ and downstream data analysis by myself (CFA). See Fig. 8 for experimental design. Modified from (Feuerstein-Akgoz, C. et al., *in preparation*).

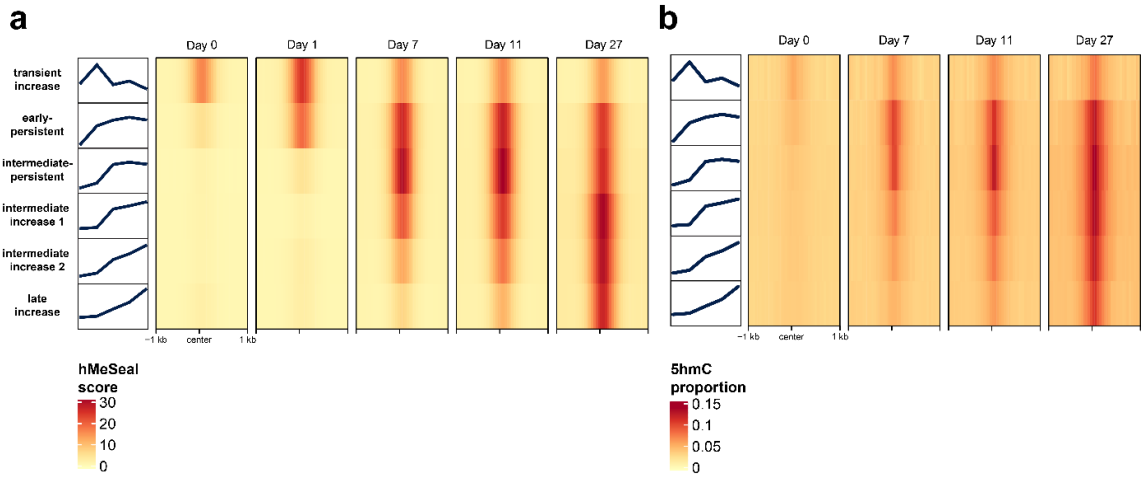

Fig. 19| Comparison of hydroxymethylation changes in hydroxymethylation clusters. a-b, Heatmaps depicting the average hMeSeal score for each hydroxymethylation cluster and time point (**a**) or hydroxymethylation proportions (WGBS/oxBS) ± 1 kb around hMeSeal peaks. Data in this figure are derived from experiment 2, performed by LK. hMeSeal library preparation and data alignment performed by FJ and WGBS/oxBS libraries and downstream data analysis performed by myself (CFA). See Fig. 8 for experimental design. Modified from (Feuerstein-Akgoz, C. et al., *in preparation*).

As timepoint day 1 is missing for the WGBS/oxBS-based hydroxymethylation data, I was not able to confirm the transient increase of hydroxymethylation at day 1 characteristic for the first cluster. However, the persistent presence of hydroxymethylation at the other time points was confirmed in the WGBS/oxBS-based hydroxymethylation data (Fig. 19b). Clusters “early-persistent” and “intermediate-persistent“ could not be distinguished in the WGBS/oxBS data, as the difference between these two clusters is the presence or absence of hydroxymethylation at day 1. The hydroxymethylation profiles of the last three clusters were confirmed by WGBS/oxBS. Overall, I observed broader peaks by hMeSeal, which were primarily defined by the fragmentation size of the DNA before library preparation (Fig. 19a). In contrast, for the WGBS/oxBS-based hydroxymethylation data, the peak width represents a high density of hydroxymethylated sites around the center (Fig. 19b).

As none of the clusters displayed loss, but rather an accumulation of hydroxymethylation, these data collectively suggest stalling of the demethylation process at the 5hmC mark in mature adipocytes.

4.5 Hydroxymethylation is enriched at adipocyte enhancer regions

For further characterization of hydroxymethylated sites, I investigated whether increase in hydroxymethylation was enriched in specific chromatin states of mature adipocytes (Roadmap Epigenomics et al., 2015). Chromatin states were defined by the ChromHMM algorithm using the combination of H3K4me3, H3K4me1, H3K36me3, H3K9me3, and H3K27ac ChIP-seq data of *in vitro* differentiated mature adipocytes (Fig. 20a). I observed a continuous increase in hydroxymethylation levels at ChromHMM states with H3K4me1 marks, such as regions flanking transcribed genes (TxFlnk), as well as at gene regulatory elements, such as regions flanking the active TSS (TssAFlnk) or enhancer regions (Enh/EnhG) (Fig. 20b). A weak increase in hydroxymethylation was also observed in bivalent regions (TssBiv/BivFlnk/EnhBiv). When stratifying according to the individual hydroxymethylation clusters, cluster “transient increase” displayed the lowest enrichment ratios (Fig. 20c). At the TxFlnk state, the enrichment increased with cluster number, and at bivalent enhancers, hydroxymethylation was only enriched in the last four clusters. Overall, enrichment was quite similar for the different hydroxymethylation clusters.

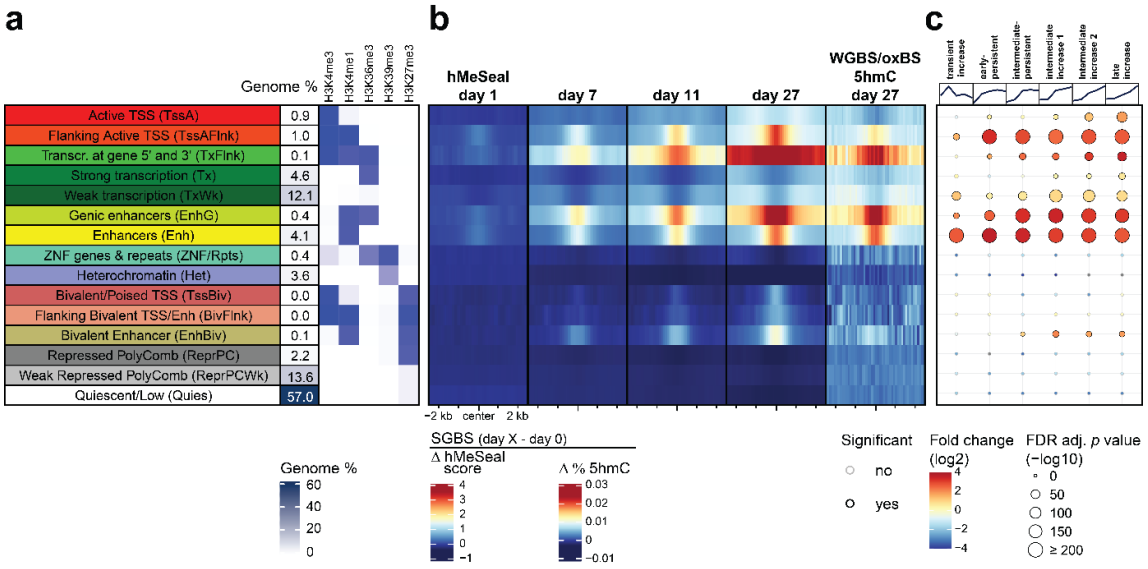

Fig. 20| Hydroxymethylation is enriched in enhancer regions. a, ChromHMM states of mature adipocytes differentiated from adipose-derived stem cells (ADS, E023) defined by H3K4me3, H3K4me1, H3K36me3, H3K9me3, and H3K27ac ChIP-seq data (figure modified from (Roadmap Epigenomics et al., 2015))**. b**, Mean difference in hMeSeal signal (day 1, 7, 11 and 27 vs day 0, n = 2 - 3) or hydroxymethylation proportions (day 27 vs day 0, n = 1) based on WGBS/oxBS data at chromatin regions defined by ChromHMM of mature adipocytes (E023). Displayed are regions in an interval of ± 2.5 kb around the center of the corresponding chromatin state (left panel). **c**, Enrichment analysis (right panel) of hydroxymethylation clusters in ChromHMM states of mature adipocytes (E023). Fisher's exact test was performed to define significant enrichment (Bonferroni-adjusted *p* value ≤ 0.05). Data in this figure are derived from experiment 2, performed by LK. hMeSeal library preparation and data alignment performed by FJ and WGBS/oxBS library preparation and downstream data analysis performed by myself (CFA). See Fig. 8 for experimental design. Modified from (Feuerstein-Akgoz, C. et al., *in preparation*).

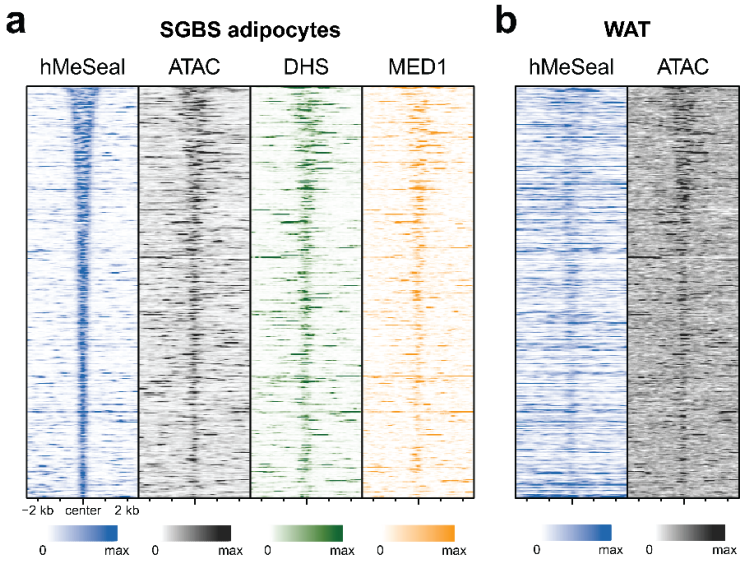

Fig. 21| Hydroxymethylation in chromatin accessible regions. a, Heatmap displays hydroxymethylation levels (hMeSeal score, day 27, n = 2, experiment 2), chromatin accessibility (ATAC) (Cannon et al., 2019), DNase I hypersensitivity (DHS), and MED1 binding in mature SGBS cells (Schmidt et al., 2015) ± 2.5 kb around hMeSeal peak centers of hydroxymethylation clusters. Peaks are ordered with decreasing peak width. **b**, hMeSeal (n = 5, PATHWAY-27 LIS) and ATAC-seq (n = 3) (Cannon et al., 2019) of human white adipose tissue samples are displayed for the same regions as in (**a**). Data in this figure are derived from experiment 2, performed by LK, WAT samples of the PATHWAY-27 LIS were collected by SG, MF, GU, GR, LR under coordination of AB, WAT tissue was pulverized by KK and AW, hMeSeal library generation and data alignment by FJ and downstream data analysis by myself. See Fig. 8 + 10 for experimental design. Modified from (Feuerstein-Akgoz, C. et al., *in preparation*). LIS: large intervention study.

I was also able to show that the hydroxymethylation peaks in hydroxymethylation clusters display characteristics of gene regulatory regions in mature SGBS cells. hMeSeal peaks overlapped with ATAC peaks (Cannon et al., 2019) and were enriched for DHS and MED1 binding regions (Schmidt et al., 2015), representing accessible DNA and promoter-enhancer interactions in SGBS cells, respectively (Fig. 21a). These regions also displayed enrichment of hydroxymethylation and ATAC peaks in WAT (Cannon et al., 2019), hinting towards *in vivo* relevance (Fig. 21b).

As a representative example, I visualized the gain in hMeSeal signal during adipocyte differentiation at the *PLIN1 (Perilipin 1)* locus. *PLIN1* is a gene encoding for a protein that coats the surface of lipid droplets in mature adipocytes (Lyu et al., 2015). During the adipocyte differentiation process, I detected multiple emerging hMeSeal peaks with reproducible detection levels starting from day 7 of adipocyte differentiation that were maintained until day 27, as well as in WAT. The hMeSeal peaks overlapped with gene regulatory regions characterized in mature SGBS by DHS with MED1, CEBPB, and/or PPARG binding (Fig. 22). A more precise characterization by the ChromHMM model defined these regions as genic and intergenic enhancers located upstream of *PLIN1*.

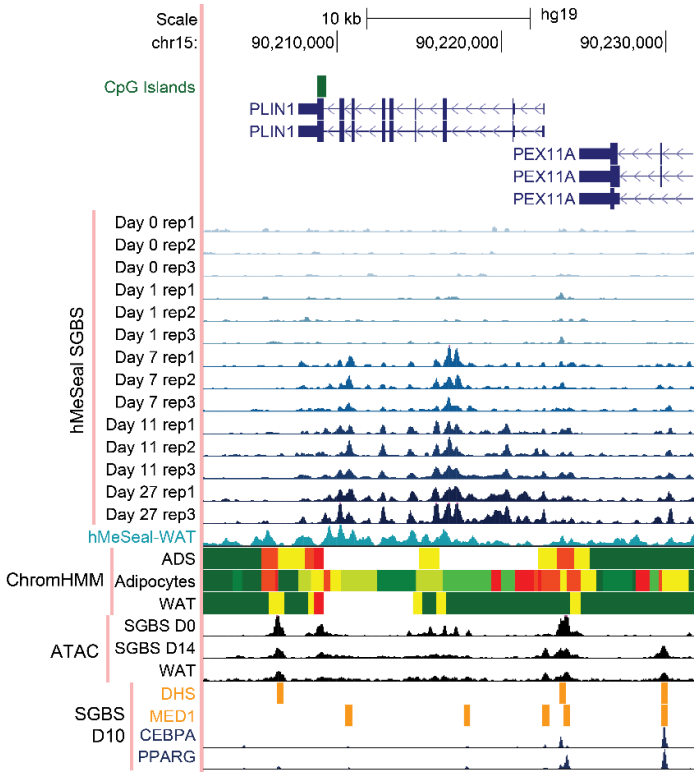

Fig. 22| UCSC genome browser track of hMeSeal signal at the PLIN1 locus. Visualization of hMeSeal signal emerging during SGBS differentiation. hMeSeal scores are displayed at a scale of 0 – 70 and color-coded in a color gradient from light to dark blue reflecting each a timepoint of differentiation (day 0, 1, 7, 11, 27, experiment 2). hMeSeal peaks overlap partially with hMeSeal peaks of human white adipose tissue (WAT, n = 5) as well as gene regulatory regions of mature adipocytes or WAT samples (ChromHMM MSC (E025), Adipocytes (E023) and Adipose tissue (E063) (Roadmap Epigenomics et al., 2015)). In mature SGBS cells, these regions overlap with chromatin accessibility (ATAC) (Cannon et al., 2019), DNase I hypersensitivity (DHS) and/or MED1 (Schmidt et al., 2015), CEBPA, and PPARG binding (Schmidt et al., 2011). For a description of ChromHMM states see Fig. 20. Experiment 2 was performed by LK, WAT samples were collected by SG, MF, GU, GR, LR under coordination of AB, WAT tissue was pulverized by KK and AW, hMeSeal library generation and data alignment by FJ and downstream data analysis by myself. See Fig. 8 + 10 for experimental design. Modified from (Feuerstein-Akgoz, C. et al., *in preparation*).

After identifying the different hydroxymethylation clusters with distinct dynamics, I wondered whether they showed differences regarding their functional role. Hydroxymethylated sites were located at gene regulatory regions and, therefore, they represent sites of potential TF binding. Therefore, I investigated whether the fragments with hydroxymethylated sites represented in the six hydroxymethylation clusters showed differences in TF binding motifs. All hydroxymethylation clusters displayed a strong enrichment in motifs of key adipogenic TFs (Fig. 23). The first cluster (transient increase) with hydroxymethylation detectable at all timepoints was enriched for motifs of the AP-1 transcription factor subunits JUN/FOS. I identified them as early response TFs, as they are involved in clonal expansion, a process occurring on the first day after the induction of the differentiation process (Johnson et al., 1996).

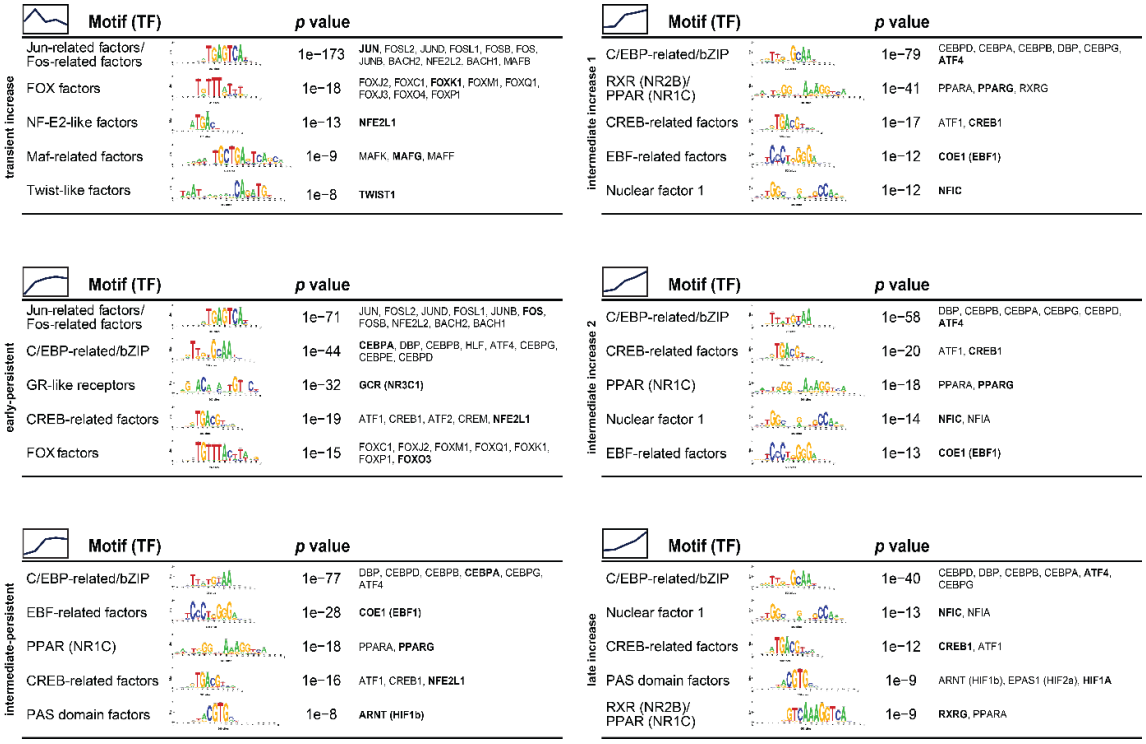

Fig. 23| Motifs of adipogenic transcription factors (TF) are enriched at hydroxymethylation clusters. For each hydroxymethylation cluster an individual transcription factor (TF) motif enrichment analysis was performed. To create TF families, hocomoco motifs were clustered by motif similarity. The motif and enrichment results of the best-enriched TF motifs within the TF family are displayed for the top 5 enriched TF families. For each TF family, all enriched and expressed motifs were displayed in order of enrichment and the highest expressed at the timepoint of highest hydroxymethylation was highlighted (for cluster “transient increase”: day1, “early-persistent” and “intermediate-persistent”: day 11, ”intermediate increase 1+2” and “late increase”: day 27). Data analysis based on data of experiment 2, performed by LK. hMeSeal library generation and data alignment performed by FJ and downstream data analysis by myself (CFA). See Fig. 8 for experimental design. Taken from (Feuerstein-Akgoz, C. et al., *in preparation*).

These TFs are engaged in the differentiation of adipocytes, but also of multiple other cell types, which is achieved by a selective combination of the AP-1 sub-units (Distel et al., 1987). Also, several TFs of the forkhead-box (FOX) TF motif family, such as FOXC2, FOXO1, and others, are known for their adipogenic potential (Gerin et al., 2009). More specifically, they are involved in the initiation of differentiation and metabolism. The early-persistent hydroxymethylation cluster, characterized by an early increase in hydroxymethylation at day 1, can be considered as an intermediate cluster. It shares enrichment of motifs with both “transient increase” and all other clusters. I identified similarly to cluster “transient increase” the two early response TF motif families JUN/FOS and FOX, and similarly to the last four clusters, the CEBP-related TFs, such as the early transcription factor CEBPB. CEBPA, however, is induced by CEBPB and is rather a late adipogenic TF, indicating the broad time range of action of the different CEBP-related TFs during adipogenesis. In addition, I also identified TF motifs only enriched in the last four clusters (intermediate-persistent, intermediate increase 1, intermediate increase 2, and late increase), representing clusters with later increases in hydroxymethylation. One

example is the enrichment of motifs of PPAR TFs and their heterodimer RXR (retinoid X receptor), suggesting binding of the late adipogenic TF PPARG. Further enriched TF motifs involved in adipogenesis include hypoxia inducible factor 1 subunit alpha (HIF1A) (Floyd et al., 2007) and TFs with a role in metabolic signaling pathways, such as activating transcription factor 1 (ATF1), CREB1, and EBF transcription factor 1 (EBF1) (Griffin et al., 2013; Zhang et al., 2004).

With the enrichment-based method hMeSeal, I was able to estimate the approximate location of the hydroxymethylation next to specific adipogenic TF motifs. For comparison, I used WGBS/oxBS-provided hydroxymethylation data at base-pair resolution to estimate the exact distance of 5hmC to the TF binding motifs (Fig. 24). The average distance of the 5hmC mark to the early TF binding motifs JUN and FOX, exemplarily represented by JUN and FOXJ2, was about ± 100 base pairs (bp). The distance to the late transcription factors such as the C/EBP TFs and PPAR/RXR TFs was even smaller, at about ± 50 bp. CEBPE displayed at the center of the binding motif the highest density of hydroxymethylated sites, which might reflect the fact that this TF is the only one that can harbor a CpG site within its binding motif (TTG**CG**CAATCTT).

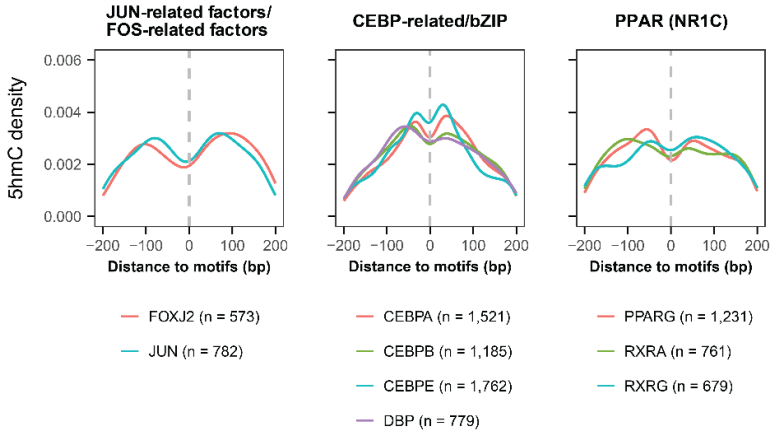

Fig. 24| Hydroxymethylation is enriched around the TF binding motifs. Density plot of hydroxymethylated sites (from WGBS/oxBS) depicted around hocomoco motifs within ± 200 bp overlapping with hMeSeal peaks of all hydroxymethylation clusters. Hydroxymethylated sites were defined as CpG sites with a hydroxymethylation proportion > 25 % at any time point of differentiation (day 0, 7, 11, and 27). N = Number of hocomoco TF motifs overlapping with hMeSeal peaks in all hydroxymethylation clusters. Data in this figure are derived from experiment 2, performed by LK. hMeSeal library generation and data alignment performed by FJ, WGBS/oxBS library preparation and downstream data analysis performed by myself (CFA). See Fig. 8 for experimental design. Modified from (Feuerstein-Akgoz, C. et al., *in preparation*).

4.5.1 5hmC at adipogenic TF binding

The presence of a binding motif is predictive, however, not the only decisive factor for TF binding. Therefore, I confirmed the enrichment of hydroxymethylation at experimentally determined TF binding sites in SGBS cells. I displayed hydroxymethylation levels (WGBS/oxBS data) of hydroxymethylated CpGs (> 0.25) ± 1,000 bp around CEBPA and PPARG binding (Schmidt et al., 2011) and detected the highest density of hydroxymethylation at ~ 80 - 100 bp around the TF binding (Fig. 25).

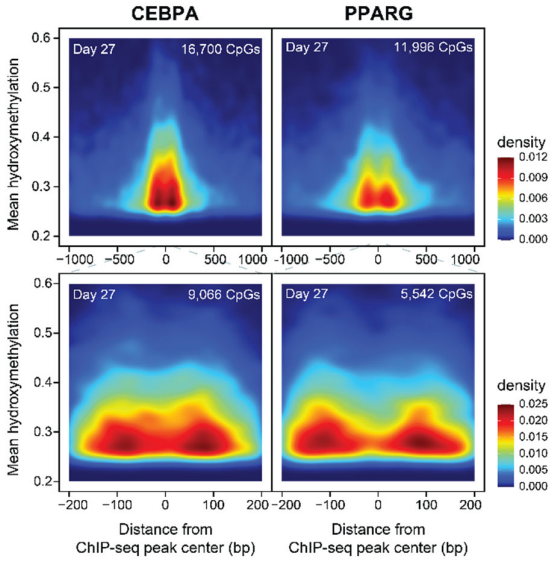

Fig. 25| Hydroxymethylation is enriched around CEBPA and PPARG binding. a, Density plots depicting hydroxymethylated sites at day 27 (from WGBS/oxBS, experiment 2) of CpGs located within ± 1 kb (upper panel) and ± 200 bp (lower panel) to CEBPA (left) or PPARG (right) ChIP-seq peaks of mature SGBS adipocytes (Schmidt et al., 2011). Hydroxymethylated sites were defined as CpG sites with a hydroxymethylation proportion > 0.25 at day 27. Experiment 2 was performed by LK, WGBS/oxBS library preparation, and downstream data analysis done by myself (CFA). See Fig. 8 for experimental design. Modified from (Feuerstein-Akgoz, C. et al., *in preparation*).

4.5.2 5hmC at CTCF binding

Dubois-Chevalier *et al.* have shown previously in 3T3-L1 cells as a murine adipogenesis model that hydroxymethylation levels increased at sites where the insulating factor CTCF is *de novo* recruited (Dubois-Chevalier et al., 2014). One of the functions of CTCF is to control gene expression through regulating the 3D structure of chromatin (Phillips and Corces, 2009; Wang et al., 2012a). CTCF is attractive in terms of hydroxymethylation as its motif contains one or two CpG sites, which influence CTCF DNA binding through their methylation status.

In our analyses, the CTCF binding motif did not appear to be enriched in the hydroxymethylation clusters. Therefore, I repeated the analysis and classified CTCF binding sites as constitutive or dynamic based on ChIP-seq data from confluent human adipose-derived stem cells (ADS) and mature adipocytes (Mikkelsen et al., 2010). In addition, I classified the CTCF binding sites based on their methylation level in SGBS preadipocytes (day 0), since unmethylated sites cannot gain hydroxymethylation. Interestingly, nearly half of the CTCF binding sites displayed a methylation level < 10 %, which I classified as unmethylated (Fig. 26a). The remaining CTCF binding sites displayed low methylation, with levels of at least 10 %. Most CTCF binding regions showed constitutive binding, with CTCF bound throughout

ADS differentiation. In these regions, I observed only low gain in hMeSeal signal in SGBS cells. Among the ~3,000 dynamic CTCF binding sites with *de novo* recruited CTCF binding in mature adipocytes, I detected the strongest enrichment in hydroxymethylation in mature SGBS cells (Fig. 26a + b). I also analyzed the distance of hydroxymethylated CpGs to the center of the CTCF binding motifs and, similarly to the above analyzed TFs, the distance was around ± 60 bp to the CTCF binding motif (Fig. 26c).

To sum up, our findings support the view of a highly regulated system resulting in gain in hydroxymethylation during adipogenesis, mostly at newly occupied enhancer regions that are essential for the transition of a preadipocyte to a mature adipocyte.

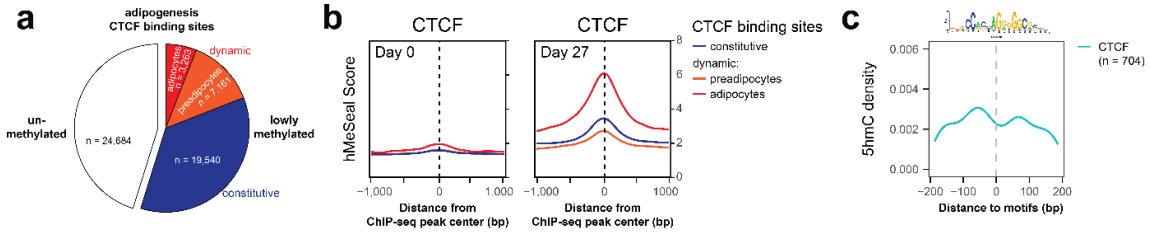

Fig. 26| Hydroxymethylation levels at CTCF binding sites. a, Venn diagram displaying the number of adipogenesis CTCF binding sites characterized by methylation status at ± 200 bp around the CTCF binding sites (unmethylated < 10 % methylation, lowly methylated > 10 % methylation, based on WGBS, experiment 2). The subset of lowly methylated CTCF binding sites was further classified into constitutive binding (in preadipocytes and adipocytes) or dynamic CTCF binding (in preadipocytes or adipocytes) (Mikkelsen et al., 2010). **b**, Density line plot of hydroxymethylation (hMeSeal score) at day 0 (left) and day 27 (right) at lowly methylated constitutive or dynamic CTCF binding sites at an interval of ± 1,000 bp **c**, Density plot of hydroxymethylated sites (from WGBS/oxBS, experiment 2) depicted around hocomoco CTCF motifs within ± 200 bp overlapping with hMeSeal peaks of all hydroxymethylation clusters. Hydroxymethylated sites were defined as CpG sites with a hydroxymethylation proportion > 25 % at any time point of differentiation (day 0, 7, 11, and 27). n = Number of hocomoco TF motifs overlapping with hMeSeal peaks in all hydroxymethylation clusters. Experiment 2 was performed by LK. hMeSeal library preparation and data alignment performed by FJ and WGBS/oxBS library generation and downstream data analysis done by myself (CFA). See Fig. 8 for experimental design. Modified from (Feuerstein-Akgoz, C. et al., *in preparation*).

4.6 Transcriptome changes during SGBS differentiation

The function of enhancer regions is to co-regulate the level of transcription of locally interacting target genes. As hydroxymethylation at enhancer regions might affect enhancer function, I next investigated transcriptional changes during the SGBS differentiation process and tested whether they can be linked to the hydroxymethylation dynamics.

4.6.1 Global transcriptome changes

To assess global transcriptional changes, we performed RNA sequencing during SGBS differentiation. Performing Mfuzz clustering of all expressed genes (Fig. 27), I identified five mRNA expression clusters (eCl) with distinct profiles. In eCl1, I observed an immediate transient decrease from day 0 to day 7 followed by increasing levels after day 7. In contrast, in eCl2, gene expression levels decreased from day1 to day 7 and were then persistent at low levels. eCl3 displayed a transient peak of elevated expression at day 1 followed by a drop in expression levels. Finally, eCl4 + 5 were characterized by increasing mRNA levels; eCl4 with a continuous raise in expression levels, and eCl5 with a sharp upregulation between day 1 and day 7 and persistent levels after day 7.

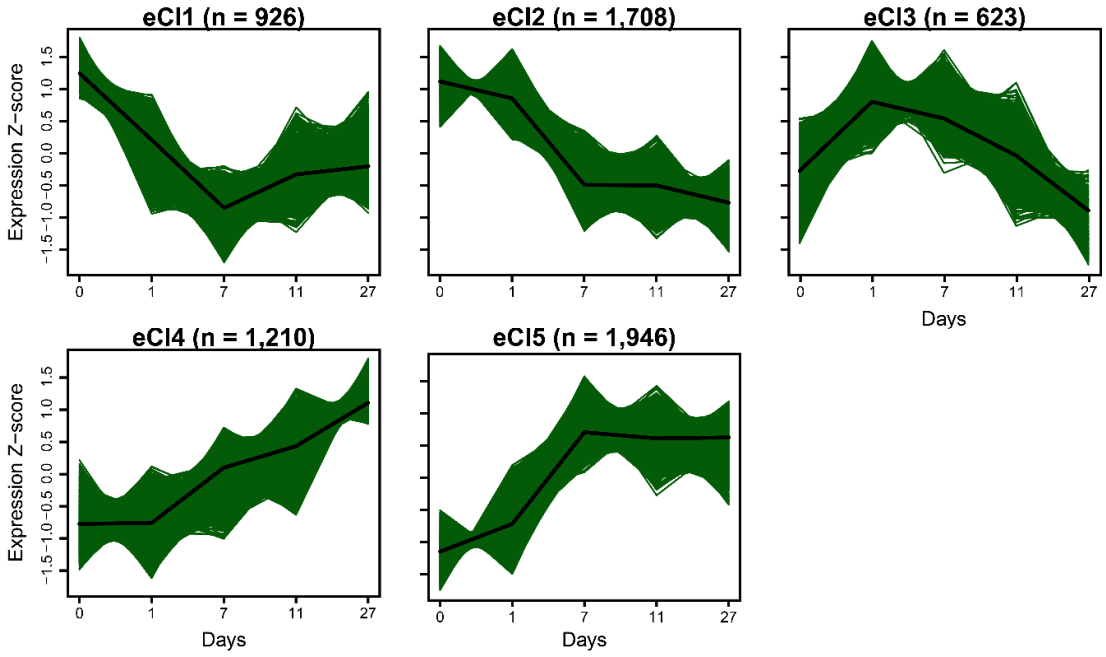

Fig. 27| Mfuzz clustering of transcriptional changes. Scaled gene expression data (RNA-seq) of SGBS differentiation at day 0, 1, 7, 11 and 27 (n = 3 per time point, except day 27 with n = 1) were clustered into 5 mRNA expression clusters (eCl) by Mfuzz. Black lines depict cluster centers. Data in this figure are derived from experiment 2, performed by LK, downstream data analysis were done by myself (CFA). See Fig. 8 for experimental design. Taken from (Feuerstein-Akgoz, C. et al., *in preparation*).

For each expression cluster, I performed KEGG pathway gene overrepresentation analysis (Fig. 28). Genes that were immediately downregulated after induction of differentiation (eCl1) were enriched for “Focal adhesion”, a pathway involved in the regulation of cell shape. This was consistent with the visual observation of morphological changes at about the same time (Fig. 11), namely a switch from a spindle-like cell structure to a rounded cell morphology starting directly after the induction of differentiation. Genes involved in “cell cycle regulation”, such as proliferating cell nuclear antigen (PCNA) and marker of proliferation Ki-67 (MKI67), were downregulated between day 1 and day 7. Also, expression of genes involved in DNA methylation maintenance, such as DNMT1 and UHRF1, was reduced. This reflects cell cycle arrest following the induction of clonal expansion by the differentiation medium and the subsequent reduced need of DNA methylation maintenance. In eCl3, genes upregulated at day 1 were involved in clonal expansion, namely 66 of 153 genes of the ribosome, necessary for the increased translation activity in proliferating cells. eCl4 was not enriched in any particular pathway. Upregulated genes clustered in eCl5 were enriched for multiple metabolic pathways, which represent the switch of preadipocytes to functional mature adipocytes. At the top of the hierarchy, I identified the “PPAR signaling pathway” that induces the expression of genes of multiple metabolic pathways. Downstream pathways that were enriched in eCl5

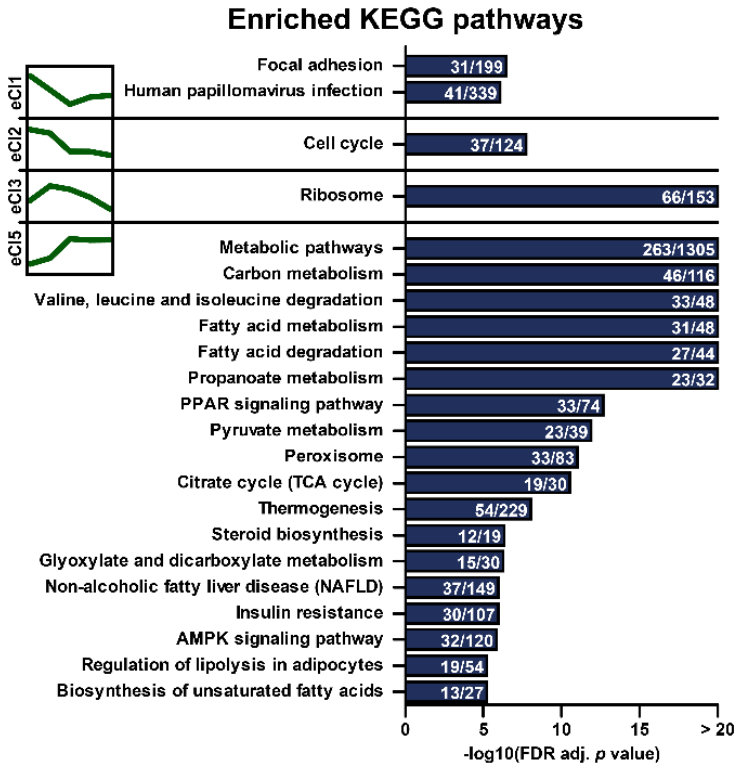

Fig. 28| KEGG overrepresentation analysis of eCls. KEGG overrepresentation analysis was performed with genes of 5 mRNA expression clusters (eCl) (FDR adj. *p* value < 1e-5). The matching/total number of genes within the pathway are listed in each bar. eCl4 displayed no significant enrichment. See expression dynamics of eCl of experiment 2 in Fig. 27. Experiment 2 was performed by LK, downstream data analysis by myself (CFA). See Fig. 8 for experimental design. Modified from (Feuerstein-Akgoz, C. et al., *in preparation*).

included “tricarboxylic acid cycle (TCA cycle)” and “pyruvate metabolism” to generate acetyl-CoA for the “biosynthesis of unsaturated fatty acids”. The KEGG pathway “degradation of valine, leucine, and isoleucine” is an additional pathway that provides metabolites for the biosynthesis of fatty acids in adipocytes. In addition, I identified pathways enriched such as the “AMPK pathway” and “fatty acid degradation (lipolysis)” that represent functions of normal adipocytes, but their pathological upregulation can result in insulin resistance and high levels of fatty acids in the blood, respectively, both observed in the metabolic syndrome. In line with the characterization of the clusters, also all markers of adipogenesis (*CEPBA, PPARG, sterol regulatory element binding transcription factor 1 (SREBF1), PLIN1, CFD, fatty acid synthase (FASN), FABP4)* were found in this last cluster.

Gene expression is a well established indicator of changes in cellular functions, however, gene activity is more precisely interpreted at the protein level. For comparative analyses, I received proteome data obtained by UPLC-MS analyses of tryptic digests of protein lysates collected during SGBS differentiation (Schaffert et al., 2021). As genes of eCl5 are responsible for the function of mature adipocytes, I wanted to confirm the mRNA expression changes at the protein level (Fig. 29). While some lowly or nuclear expressed proteins, including transcription factors such as PPARG, were technically not detectable, I was able to globally validate the transcriptional upregulation of these genes also at the protein level. Among the highlighted examples, I displayed the upregulation of *ACSL1* and *IDH1*, two genes for which I previously described an increase of hydroxymethylation (Fig. 17a + c).

To sum up, clustering of gene expression data based on gene expression dynamics allowed the identification of pathways that are de-/activated at specific time points, reflecting the different stages of the differentiation program, starting from clonal expansion and morphological changes followed by cell cycle arrest and finally activation of multiple metabolic pathways.

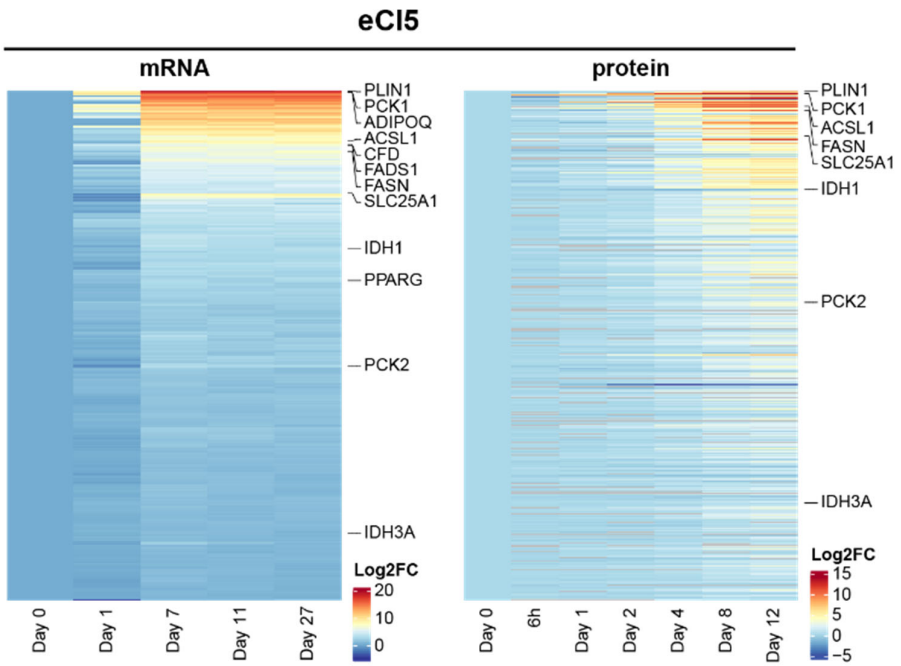

Fig. 29| Validation of mRNA expression changes of eCl5 at the protein level. Heatmaps depict changes in mRNA expression (left panel) and protein abundance (right panel) of genes clustered in mRNA expression cluster 5 (eCl5) during adipocyte differentiation. RNA-seq data (mean Log2FC) were plotted for experiment 2 (n = 3 per time point, except day 27 with n = 1) and expression of all detected proteins (mean Log2FC) was plotted for experiment 4 (n = 5). Heatmaps are both ordered by mRNA Log2FC expression levels. Proteins below the detection limit were depicted in grey. Experiment 2 was performed by LK, experiment 4 published by (Schaffert et al., 2021), downstream data analysis was done by myself (CFA). See Fig. 8 for experimental design. Modified from (Feuerstein-Akgoz, C. et al., *in preparation*).

4.6.2 Transcriptome changes linked to hydroxymethylation

After characterizing the activation and downregulation of transcriptional programs at specific timepoints, I wanted to investigate whether the changes in gene expression might be associated with the changes in hydroxymethylation at enhancer regions. For that purpose, I first matched hydroxymethylated regions within ± 100 kb to each TSS (to account for the fact that enhancer-promoter interaction can be long-ranged) and then performed an enrichment of hydroxymethylation of specific hydroxymethylation clusters at each mRNA expression cluster (eCl). I identified an enrichment of the first two hydroxymethylation clusters (“transient increase”, “early-persistent”) at the two eCls with downregulated genes (eCl1 + 2), mainly genes involved in cell cycle and cell morphology (Fig. 30). The hydroxymethylated peaks were present at early time points and were enriched for early transcription factors. The expression clusters eCl3+4 displayed no specific enrichment. However, for genes in expression cluster eCl5 that are induced between day 1 and 7 and are mainly involved in metabolic pathways, we identify in the vicinity an enrichment of hydroxymethylation gain between day 1 and 7 (last

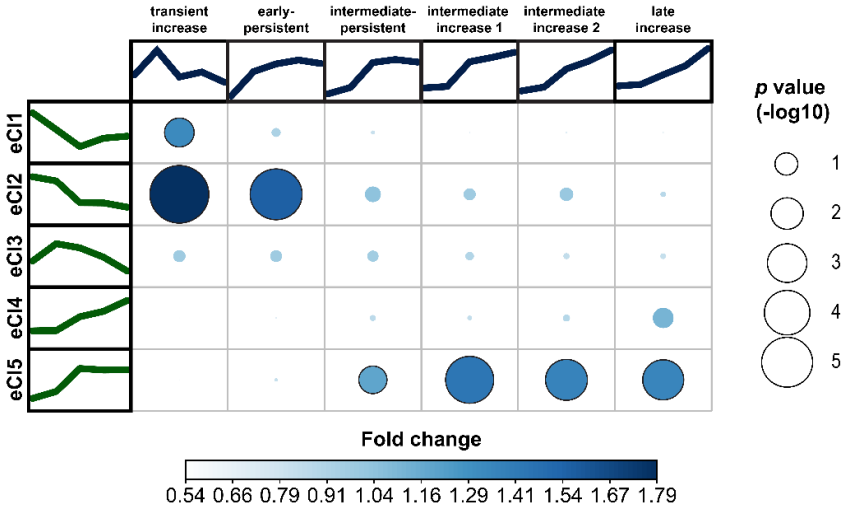

Fig. 30| Transcriptional changes linked to hydroxymethylation changes. Distance-based enrichment analysis of hydroxymethylation clusters within ± 100 kb of TSS of genes represented in mRNA expression clusters (eCl). Fisher's exact test was performed to define significant enrichment (Bonferroni-adjusted *p* value ≤ 0.05). Hydroxymethylation clusters were defined based on hMeSeal scores, see Fig. 18. eCls were defined based on RNA-seq data, see Fig. 27. Data in this figure are derived from experiment 2, performed by LK, downstream data analysis by myself (CFA). See Fig. 8 for experimental design. Modified from (Feuerstein-Akgoz, C. et al., *in preparation*).

four hydroxymethylation clusters). These hydroxymethylated regions surround enhancer regions bound by late adipogenic transcription factors such as PPARG and CEBPA.

In summary, hydroxymethylation at early time points was identified around enhancer regions with binding of early transcription factors, surrounding genes expressed at early time points. Analogously, we identified late gain in hydroxymethylation at late adipogenic transcription factor binding sites, surrounding genes of metabolic pathways induced at late time points of adipogenesis. “This suggests that gene expression is tightly controlled at enhancer regions and that hydroxymethylation might contribute to this process in regulating enhancer function during adipocyte differentiation.” (Feuerstein-Akgoz, C. et al., *in preparation*)

4.7 Metabolic changes

4.7.1 Integrated pathway analysis based on metabolites and associated proteins

Epigenetic gene regulation and the cellular metabolism are two closely interacting processes. On the one hand, epigenetic gene regulation controls the enzyme abundance affecting the throughput of metabolites. On the other hand, metabolites including some of the TCA cycle

(Boon et al., 2020; Haws et al., 2020; Martinez-Reyes and Chandel, 2020) can serve as substrates for epigenetic enzymes. One of the examples related to DNA hydroxymethylation, is the regulation of TET activity that can be controlled at the level of transcription, but also at the level of availability of the substrate αKG (Wu and Zhang, 2017). As I observed an upregulation of genes involved in various metabolic pathways during adipocyte differentiation, e.g. the TCA cycle, in eCl5, I also anticipated changes at the level of metabolite concentrations, which might affect the epigenetic regulation of gene expression.

To assess global changes in metabolites concentrations, I received from collaboration partners metabolite levels from an untargeted metabolomics analysis of SGBS adipocyte differentiation (experiment 3, Fig. 7, described in (Miehle et al., 2020)). As for the hydroxymethylation and gene expression data, I performed Mfuzz clustering on scaled metabolite intensities (Fig. 31). I identified in total three stable metabolite clusters (mCls), one with increasing concentrations (mCl1), one with transient up- followed by downregulation (mCl2), and one with decreasing metabolite concentrations (mCl3).

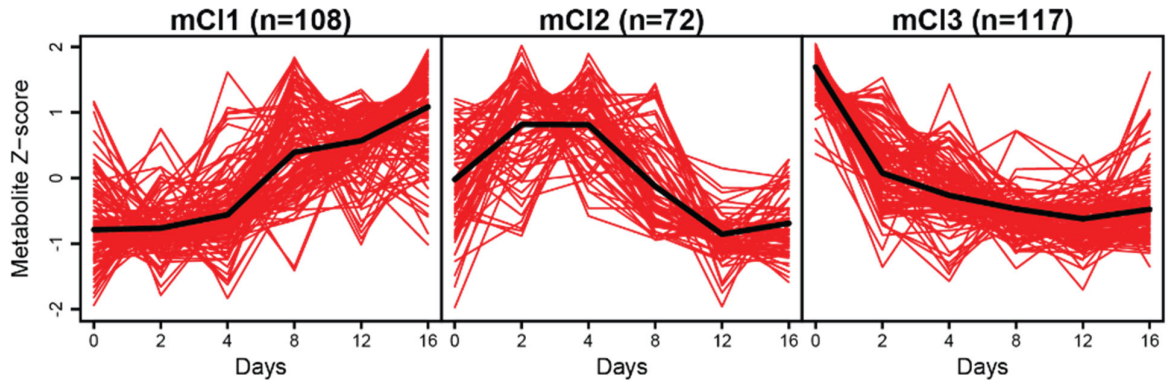

Fig. 31| Mfuzz clustering of metabolites. Clustering of scaled mean metabolite signal intensities of SGBS differentiation at day 0, 4, 8, 12, and 16 (n = 5 - 6) into 3 metabolite clusters (mCl) by Mfuzz. Black lines depict cluster centers. Data in this figure are derived from experiment 3, provided by FM (Miehle et al., 2020), downstream data analysis was performed by myself (CF). See Fig. 8 for the experimental design. Modified from (Feuerstein-Akgoz, C. et al., *in preparation*).

To perform integrated pathway analysis of proteins and metabolite dynamics, I matched to each detected metabolite the associated proteins. These proteins represent enzymes generating or using the metabolites in a chemical reaction. In Fig. 32a, the three metabolite clusters (mCls) and their associated proteins are sub-grouped by the protein dynamics into three upregulated (u-mCls) and three downregulated (d-mCls) clusters. For the clusters with declining protein levels (d-mCls), representing proteins with a predominant role in preadipocytes, I identified only a few enriched pathways. “Purine metabolism” represented proteins with reduced abundance during adipogenesis, associated with metabolites with

increasing levels, suggesting accumulation of purine metabolites, despite the global downregulation of the pathway. “Cysteine and methionine metabolism” represented a group of proteins and associated metabolites that were downregulated during adipogenesis. This pathway is involved in the generation of SAM, the methyl donor of DNA methyltransferases. We could not confirm decrease of SAM itself, as it was not detectable in the metabolomics analysis. Since differentiating cells are cell cylce arrested, both SAM and DNMTs might indeed be dispensable.

Among the clusters with increasing protein levels (u-mCls), I identified a large variety of enriched metabolic pathways. I observed pathways such as “TCA cycle”, “Pyruvate metabolism”, and “Valine, leucine, and isoleucine degradation” that were already identified at the mRNA level (Fig. 32b + 28). The majority of the pathways were enriched in at least two or even all three of the u-mCls, suggesting that although the vast majority of the metabolic proteins became upregulated by the adipogenic signaling cascade, the metabolite concentrations followed varying cellular steady-state dynamics due to complex networks of connected enzymatic reactions with distinct reaction kinetics.

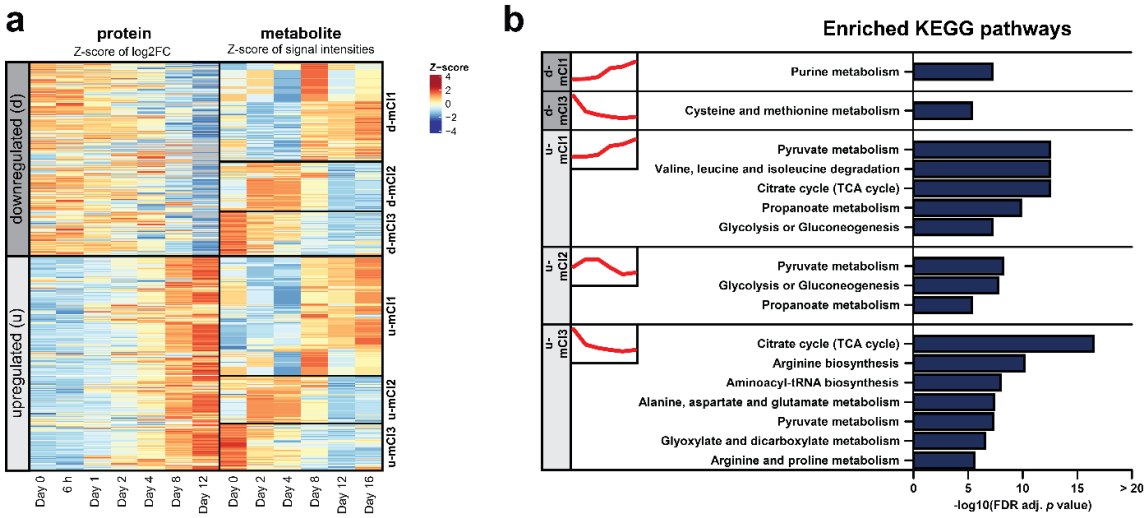

Fig. 32| Integrated KEGG pathway enrichment analysis of protein and metabolite dynamics. a, Heatmap displays all detected metabolites on the right side (experiment 3, n = 5 - 6) and the associated proteins on the left side (experiment 4, n = 5). Heatmap of the three metabolite clusters (mCls) sub-grouped based on the protein expression changes into d-(downregulated) and u-(upregulated) mCls. **c**, KEGG overrepresentation analysis was performed with proteins and metabolites of d-/u-mCls (FDR adj. *p* value < 1e-5). mCls are described in more detail in Fig. 31. Data of experiment 3 was generated by FM (Miehle et al., 2020) and of experiment 4 by AS and LK2 (Schaffert et al., 2021). Downstream data analysis performed by myself (CFA). See Fig. 8 for the experimental design. Modified from (Feuerstein-Akgoz, C. et al., *in preparation*).

4.7.2 TCA cycle and hydroxymethylation

Exemplarily, I want to highlight the TCA cycle and its potential link to DNA hydroxymethylation regulation. The TCA cycle functions in the mitochondria as a provider of energy-rich ATP, NADH, and FADH2 through oxidative decarboxylation. Protein levels of all detectable enzymes of the TCA cycle increased during adipogenesis (Fig. 33a), suggesting a continuous increase in the TCA cycle throughput. Concentrations of most TCA cycle metabolites, however, decreased during adipogenesis or remained unchanged. We determined increasing concentrations only for acetyl-CoA (Fig. 33b).

IDH1 decarboxylates isocitrate to α-ketoglutarate (αKG), the TET co-factor, and creates, therefore, a link between cell metabolism and epigenetics. As transcript (Fig. 34) and protein levels (Fig. 33a) of *IDH1* were upregulated during SGBS differentiation, I expected, in turn, increased αKG concentrations.

In contrast, we measured a continuous loss of cellular steady-state αKG levels. The precursor metabolite isocitrate was even below the detection limit, possibly due to a high turnover of the TCA cycle (Fig. 33b + 34). Also, in the reaction step before, when citrate is converted to isocitrate by the enzyme aconitase (ACO1), we observe reduced levels of citrate similarly to αKG. A high turnover is further suggested by the accumulation of acetyl-CoA. The metabolite

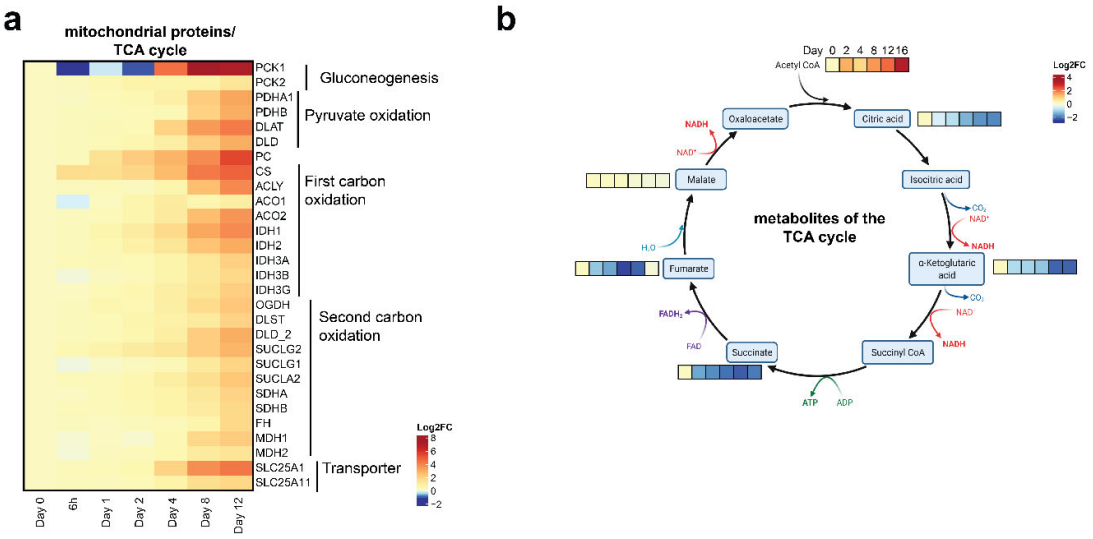

Fig. 33| Proteins of the TCA cycle are upregulated, but metabolites have distinct dynamics. a, Heatmap displays mean Log2FC of detectable proteins of the TCA cycle during SGBS adipogenesis (experiment 4, n = 5). **b**, Heatmaps of log2FC of detectable metabolites of the TCA cycle (experiment 3, n = 5 – 6, untargeted metabolomics). Data of experiment 3 was generated by (Miehle et al., 2020) and of experiment 4 published by (Schaffert et al., 2021). Downstream data analysis performed by myself (CFA). See Fig. 8 for the experimental design. Figure created with BioRender.com and modified from (Feuerstein-Akgoz, C. et al., *in preparation*).

acetyl-CoA is generated by the conversion of citrate by ATP citrate lyase (ACLY), which was upregulated at the protein and gene expression level (Fig. 33a+34). In addition, increasing lipid synthesis during adipogenesis by fatty acid synthases such as FASN from acetyl-CoA and NADPH would explain the increasing demand for acetyl-CoA and drain of citrate to acetyl-CoA synthesis.

To be available as substrates for epigenetic enzymes, αKG and citrate need to be exported from the mitochondria. Upregulation of both transporters *solute carrier family 25 member 11 (SLC25A11)* and *1* (*SLC25A1)* at the mRNA level would favor this export (Fig. 34). I also observed an upregulation of *L2HGDH (L-2-hydroxyglutarate dehydrogenase)* and *MDH1 (Malate Dehydrogenase 1)* mRNA levels, which encode for the enzymes catalyzing the oxidation/reduction of L-2-HG and αKG (Ye et al., 2018). As L-2-hydroxyglutarate is an inhibitor of TET activity, the declining steady-state concentrations during the differentiation process would suggest increased TET activity.

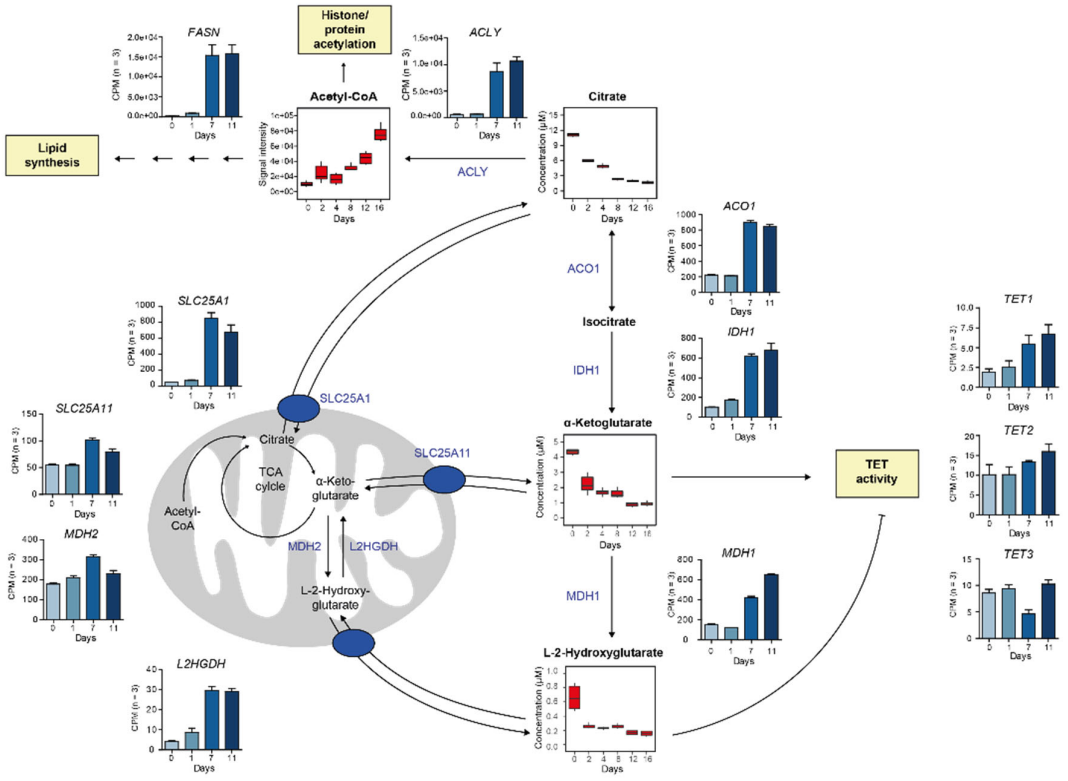

Fig. 34| TCA cycle displayed at the level of gene expression and metabolites. Barplot displays gene expression changes (CPM) of genes involved in the TCA cycle during adipogenesis (experiment 2, n = 3) and the abundance of the associated detectable metabolites displayed in µM (for targeted) or signal intensity (for untargeted) metabolomics, both of experiment 3, n = 5 - 6). Data of experiment 2 was generated by LK, of experiment 3 by (Miehle et al., 2020). Downstream data analysis performed by myself (CFA). See Fig. 8 for the experimental design. Figure modified from (Feuerstein-Akgoz, C. et al., *in preparation*).

To sum up, we identified decreased levels of the inhibitory substrate L-2-hydroxyglutarate, which would favor increased TET activity. However, as the concentrations of the substrate αKG, associated with the high turn-over of the TCA cycle, were also decreasing, our data suggest that during adipocyte differentiation changes in cells metabolism create an environment of an overall decreased TET activity.

4.8 Hydroxymethylation in white adipose tissue (WAT) – *in vivo* relevance

4.8.1 Hydroxymethylation at WAT enhancers

To confirm that gain in hydroxymethylation is not an artifact of the *in vitro* differentiation system, I wanted to investigate hydroxymethylation levels in human WAT. Therefore, we captured hydroxymethylated regions by hMeSeal in WAT biopsies of five volunteers. In parallel, we characterized the chromatin structure in WAT by ACT-seq for several activating (H3K4me3, H3K4me1, H3K27ac) and one repressive histone modification (H3K27me3) (Fig. 10). As an example, Fig. 35 depicts averaged tracks of all volunteers for the hMeSeal and ACT-seq signals at the adiponectin (*ADIPOQ)* locus in comparison to the hMeSeal signals in SGBS cells. With the ACT-seq tracks, I was able to recapitulate promoter regions (presence of H3K27ac and H3K4me3) and enhancer regions (presence of H3K27ac and H3K4me1 and absence of H3K4me3) as anticipated by ChromHMM from published WAT (Roadmap Epigenomics et al., 2015). It should be noted, however, that the WAT tracks represent an average of all cell types present in WAT. For example, *ADIPOQ* is only expressed in mature adipocytes (Uhlen et al., 2015). Therefore, the promoter mark H3K4me3 at this gene is as expected comparatively low, as other cell types in WAT will not exhibit this mark. In turn, I identified in the promoter region also the repressive mark H3K27me3, which is expected to be present in non-adipogenic cells. The hMeSeal peaks in WAT were more abundant in number and peak sizes were more homogeneous, compared to hMeSeal peaks in mature SGBS cells. This could be also a result of analyzing a mix of several cell types, where signals of different cell types are averaged out. At the *ADIPOQ* locus, hydroxymethylation overlapped with WAT enhancers, characterized by chromatin accessibility (ATAC-seq), H3K27ac, and H3K4me1 enhancer marks. In SGBS cells, these sites overlapped with DNase hypersensitivity, PPARG, and CEBPA-binding. In addition to hydroxymethylation at enhancer regions, I observed characteristic hydroxymethylation overlapping the gene body of *ADIPOQ*.

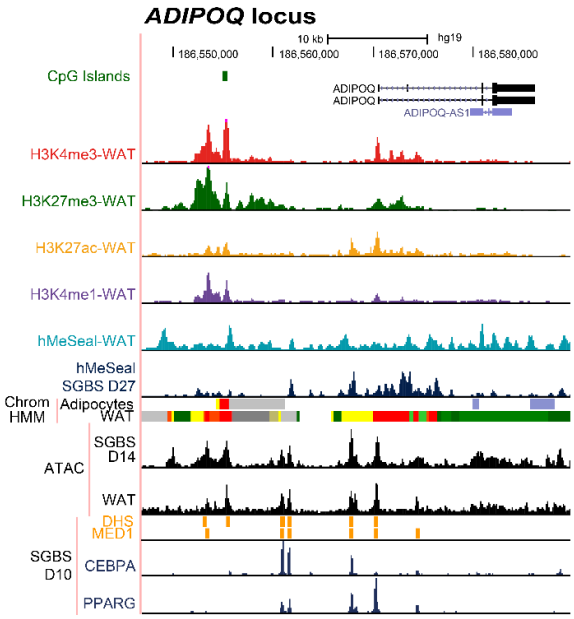

Fig. 35| UCSC track of hydroxymethylation and histone marks in WAT at the ADIPOQ locus. UCSC browser track of the adiponectin (ADIPOQ) locus. Average ACT-seq signals of histone modifications (n = 3 - 4) and hMeSeal in WAT (n = 5, PATHWAY-27 LIS) and mature SGBS adipocytes (experiment 2, n = 2) display hydroxymethylation at enhancer regions (yellow Enh/greenyellow EnhG state) and gene body of adiponectin. ChromHMM of adipocytes (E023) and adipose tissue (E063) are displayed (Roadmap Epigenomics et al., 2015). Next, ATAC data of mature SGBS cells and WAT are shown (Cannon et al., 2019), followed by DNase Hypersensitivity sites (DHS) and MED1 (Schmidt et al., 2015), CEBPA, and PPARG binding in mature SGBS cells (Schmidt et al., 2011). Description of ChromHMM states see in Fig. 20. Data of experiment 2 was generated by LK, WAT biopsies of PATHWAY-27 LIS were obtained by SG, MF, GU, GR, LR under coordination of AB. Tissue was pulverized by KK and AW, ACT-seq and hMeSeal libraries were prepared by KK, JH and FJ, respectively. All downstream analyses were performed by myself (CFA). See Fig. 10 for the experimental design. Modified from (Feuerstein-Akgoz, C. et al., *in preparation*). LIS: large intervention study.

After identifying the overlap of hydroxymethylation with enhancers in SGBS cells and at the *ADIPOQ* locus as an example in WAT, I performed a systematic analysis of hydroxymethylation at WAT enhancer regions. Displayed are all WAT enhancers ± 5 kb (n = 41,260), which were defined by the presence of H3K27ac and H3K4me1 and the absence of stringent H3K4me3 (Fig. 36). The enhancers overlapped with published chromatin accessibility (ATAC) data of WAT (Cannon et al., 2019). I identified in WAT an enrichment of hydroxymethylation at enhancer regions. However, comparison with SGBS adipocyte hydroxymethylation indicated that in WAT, hydroxymethylation was rather enriched at the enhancer boundaries with slightly decreased levels at the enhancer center. I performed a Spearman correlation analysis of hMeSeal signal with the histone marks and ATAC signal in WAT at 1 kb intervals within ± 5 kb around the enhancer center. I obtained correlation coefficients rho = 0.54 for the correlation of hMeSeal and H3K27ac and rho = 0.61 for the correlation of hMeSeal and H3K4me1 in enhancers (Fig. 36b). Similarly, in SGBS cells the strongest association of hydroxymethylation was found with H3K4me1 (Fig. 20).

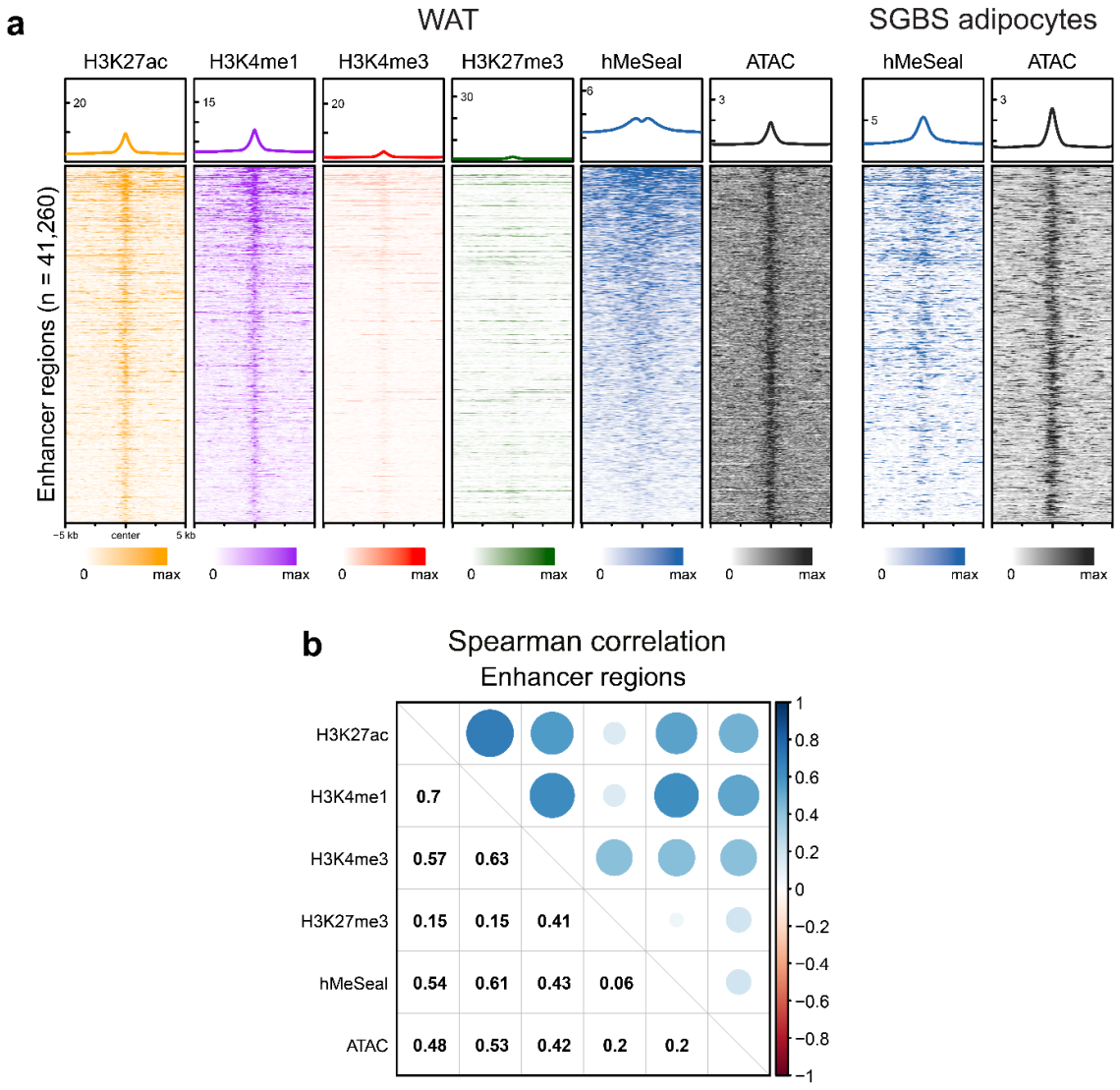

Fig. 36| Hydroxymethylation at WAT enhancer. a, Enrichedheatmap displays in the upper panel average intensity curves and in the lower panel heatmaps in a range of ± 5 kb around the center of enhancer regions. Enhancer regions were defined by H3K27ac binding (n = 3) overlapping with H3K4me (n = 3) and absence of stringent H3K4me3 (n = 4) binding in WAT samples (PATHWAY-27, LIS). Enhancer regions displayed no H3K27me3 (n = 3) chromatin marks and were enriched for hMeSeal signal (n = 5) (PATHWAY-27, LIS) and ATAC-seq in WAT (Cannon et al., 2019) and mature SGBS cells (experiment 2, day 27, n = 2) **b**, Spearman correlation analysis of read counts in 1 kb bins for four histone marks, ATAC-seq and hMeSeal in WAT enhancer regions ± 5 kb around the enhancer center. Data of experiment 2 was generated by LK, WAT biopsies of PATHWAY-27 LIS were obtained by SG, MF, GU, GR, LR under coordination of AB. Tissue was pulverized by KK and AW, ACT-seq and hMeSeal libraries were prepared by KK, JH and FJ, respectively. All downstream analyses were performed by myself (CFA). See Fig. 8 + 10 for experimental design. Modified from (Feuerstein-Akgoz, C. et al., *in preparation*). LIS: large intervention study.

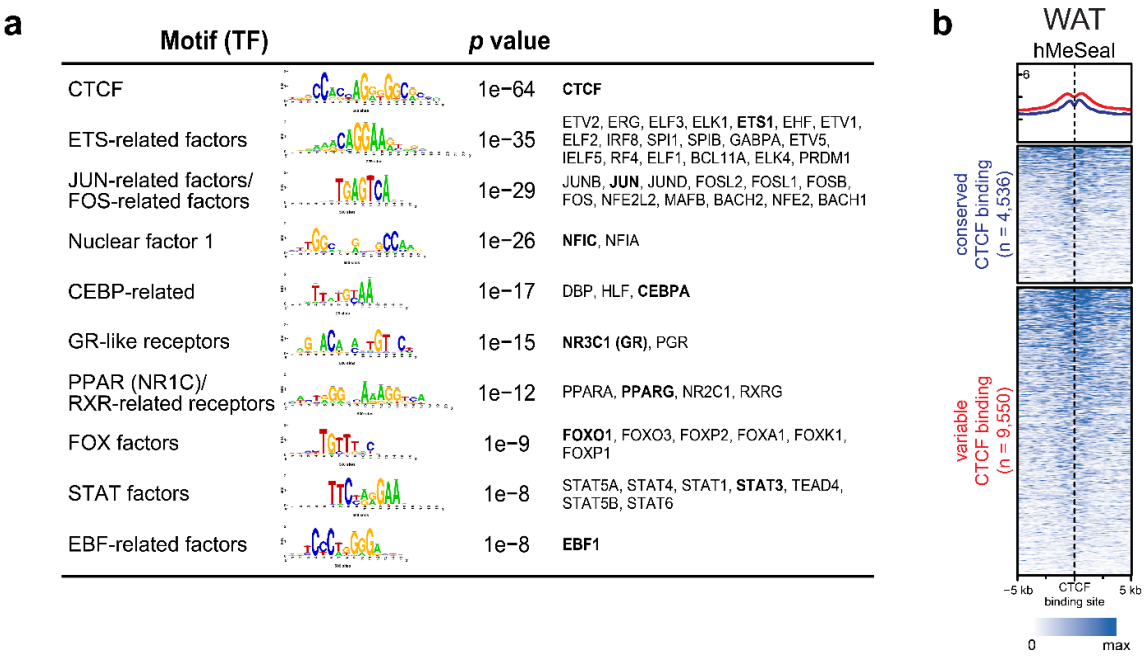

Fig. 37| Transcription factor motifs at WAT enhancer. a, The table displays the top 10 enriched transcription factor (TF) motif families in WAT enhancer. Hocomoco motifs are clustered by motif similarity and the motif with the strongest enrichment result of the TF motif family is displayed. Names of all enriched TF of the family are listed in the last column, the one with the strongest expression highlighted in bold. **b**, Hydroxymethylation EnrichedHeatmap displays in the upper panel average intensity curves and in the lower panel heatmaps of hMeSeal signal in a range of ± 5 kb around the center of enhancer regions (WAT of PATHWAY-27 LIS, n = 5). Enhancer regions were defined in WAT biopsies as described in Fig. 36. WAT biopsies of PATHWAY-27 LIS were obtained by SG, MF, GU, GR, LR under coordination of AB. Tissue was pulverized by KK and AW, ACT-seq and hMeSeal libraries were prepared by KK, JH and FJ, respectively. All downstream analyses were performed by myself (CFA). See Fig. 10 for the experimental design. Modified from (Feuerstein-Akgoz, C. et al., *in preparation*). LIS: large intervention study.

Next, I investigated which TF motifs are enriched in the above-mentioned WAT enhancers, surrounded by hydroxymethylation. I identified enrichment of early- and late-acting adipogenic TF motifs (Fig. 37a). Examples of early-acting TF included members of the ETS, JUN/FOS, and STAT transcription factor families, which are involved in adipose tissue development and physiology and were highly expressed in WAT (Birsoy et al., 2011; Lee et al., 2016; Richard and Stephens, 2014). In addition, they were described to induce the master TF CEBPA und PPARG. The nuclear factor I (NFI) TF family has been identified as essential for murine adipogenesis, and overexpression of NFIA was sufficient for induction of adipocyte differentiation in 3T3-L1 cells (Waki et al., 2011). In the *in vitro* differentiation, GR is an important TF and is activated by the synthetic GR ligand dexamethasone (Bauerle et al., 2018). FOXO1 regulates as an effector of the AKT signaling pathway proliferation and differentiation of adipocytes (Chen et al., 2019). As a top enriched TF motif, I identified CTCF. Similar to SGBS cells, I classified conserved CTCF binding sites with binding in ≥ 75 % of available cell types and variable CTCF binding sites (< 75 %). I identified hydroxymethylation around both, conserved and variable CTCF binding sites; however, hydroxymethylation levels at variable CTCF binding sites were stronger, as described by (Dubois-Chevalier et al., 2014) (Fig. 37b).

To sum up, I confirm that in SGBS and in WAT, I identified an accumulation and stable detection of hydroxymethylation. I was able to display the enrichment around cell-type-specific enhancer regions, which was anticipated by WGBS displaying the highest density of hydroxymethylation not at the TF binding motifs themselves, but ~ ± 70 – 100 bp around the binding motives.

4.8.2 Hydroxymethylation in WAT highly expressed genes

I extensively described hydroxymethylation in enhancer regions, but several previous studies had focused on gene body hydroxymethylation. In multiple tissues, hydroxymethylation overlapping the gene body has been associated with differences in gene expression (Cui et al., 2020). As WAT was not included among the tissue types, I performed a comparable analysis with gene body hydroxymethylation and gene expression in WAT. I first identified, using GTEx gene expression data, 225 genes that have a higher expression in WAT compared to other tissues (n = 27) (GTEx Consortium, 2020). As background, I selected genes that have similar expression levels but are expressed in several tissues. With these genes, I performed a correlation analysis of WAT gene body hydroxymethylation and gene expression. I identified for WAT-enhanced genes a positive correlation of R = 0.35 (Pearson) and rho = 0.32 (Spearman) comparable to the published correlations in other tissues (Cui et al., 2020), which was higher than for background genes (Fig. 38).

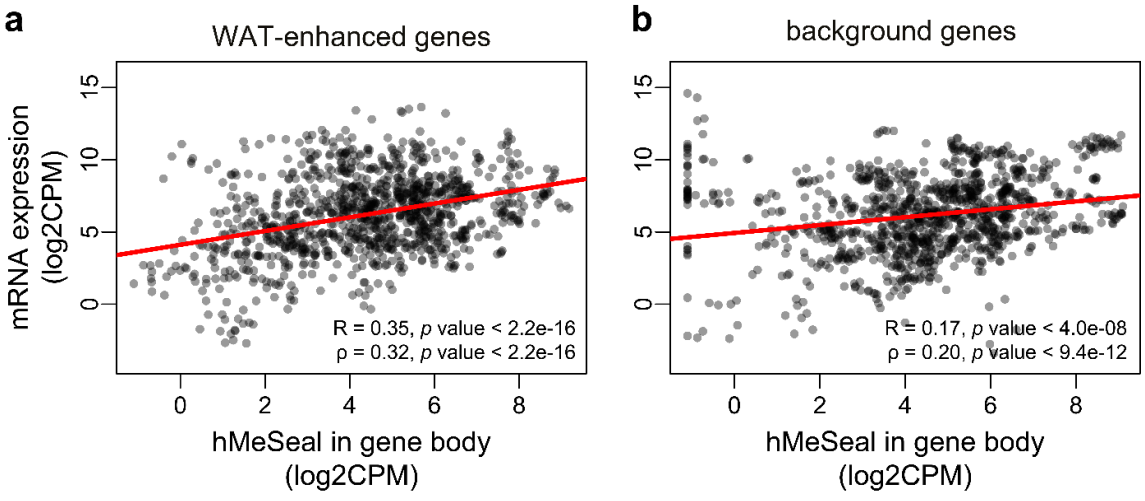

Fig. 38| Gene body hydroxymethylation in WAT enhances genes. a-b, Pearson (R) and Spearman (ρ) correlation between gene body hMeSeal (log2CPM) and gene expression (log2CPM) in WAT-enhanced and background genes. WAT biopsies of PATHWAY-27 LIS were obtained by SG, MF, GU, GR, LR under coordination of AB. Tissue was pulverized by KK and AW, hMeSeal libraries were prepared by FJ. All downstream analyses were performed by myself (CFA). See Fig. 10 for the experimental design. Modified from (Feuerstein-Akgoz, C. et al., *in preparation*). LIS: large intervention study.

4.9 Acetylated NEIL1 accumulates at adipogenic enhancers in white adipose tissue

NEIL1 is a member of the small Nei family of DNA repair enzymes involved in replication-associated base excision repair (BER) of oxidized DNA bases (Hegde et al., 2013; Pfeifer et al., 2019; Prakash et al., 2012; Rolseth et al., 2017). Several studies have linked knockout of *Neil1* in mice with increased susceptibility to obesity and hyperlipidemia (Rolseth et al., 2017; Sampath et al., 2011; Vartanian et al., 2006). This prompted us to investigate whether NEIL1 might be linked to maintenance of 5hmC and involved in regulating adipocyte function.

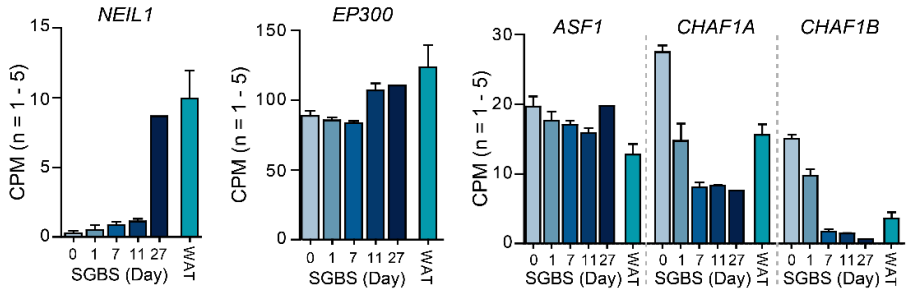

Fig. 39| Transcriptional changes of NEIL1 and interaction partners in adipogenesis and adipose tissue. a-c, mRNA expression of NEIL1 (**a**), EP300 (**b**) and histone chaperones (**c**) during SGBS adipogenesis (experiment 2, n = 3 or n = 1 for day 27) and in WAT (PATHWAY-27 LIS, n = 5). Experiment 2 was performed by LK, WAT biopsies of PATHWAY-27 LIS were obtained by SG, MF, GU, GR, LR under coordination of AB. Tissue was pulverized by KK and AW. All downstream analyses were performed by myself (CFA). See Fig. 8 for the experimental design. Modified from (Feuerstein-Akgoz, C. et al., *in preparation*). LIS: large intervention study.

NEIL1 mRNA expression was > 30-fold upregulated in mature SGBS cells at day 27 post differentiation compared to day 0. We confirmed similar transcript levels in WAT by RNA-seq (Fig. 39). Acetylation of NEIL1 by the histone acetyltransferase (HAT) p300 was previously found to stabilize its interaction with nucleosome remodeling histone chaperones (Sengupta et al., 2018). In differentiating SGBS cells and in WAT, transcript levels of p300 (*EP300*) were high and did not change during adipogenesis, facilitating NEIL1 acetylation in mature adipocytes. Transcript levels of the NEIL1 interaction partner ASF1A and CHAF1A/B, which were found to sequester and inhibit the BER complex in non-replicating chromatin (Yang et al., 2017), remained relatively constant or slightly declined during SGBS differentiation, respectively. These data collectively suggested that in mature non-replicating adipocytes, acetylated NEIL1 (acNEIL1) might be associated with chromatin and influence adipocyte function besides its role in BER.

To explore a potential epigenetic role in WAT, I analyzed chromatin binding of acNEIL1 in comparison to activating and repressive histone marks and 5hmC. I detected over 25,500 regions with acNEIL1 binding, with a mean size of about 780 bp (range 200 – 5,992 bp). acNEIL1 chromatin binding regions largely overlapped with the enhancer marks H3K27ac and

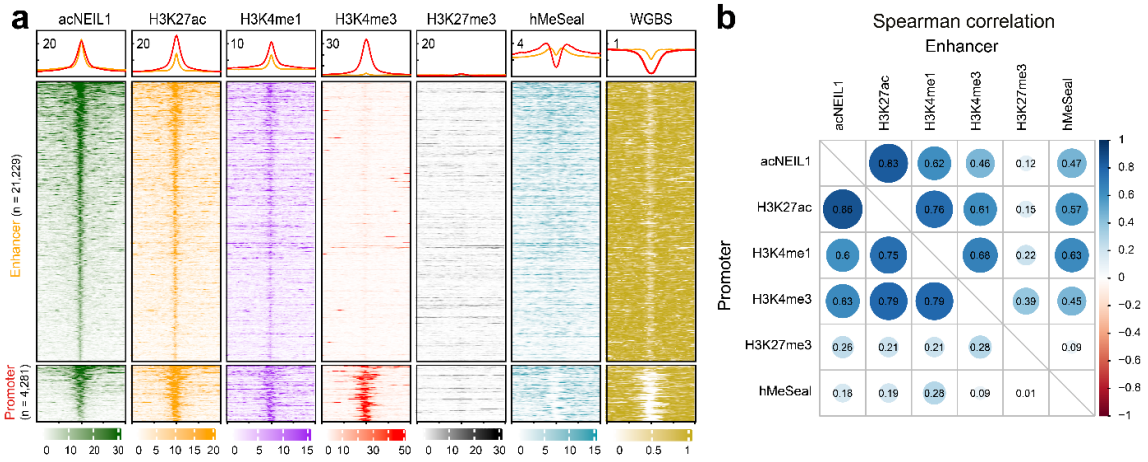

Fig. 40| The hydroxymethylation reader NEIL1 accumulates at enhancer regions in white adipose tissue. a, Average intensity curves (upper panel, smoothed average for WGBS) and heatmaps (lower two panels) in a range of ± 5 kb around the center of acNEIL1 binding (n = 3), H3K27ac (n = 3), H3K4me (n = 3), H3K4me3 (n = 4), H3K27me3 (n = 3) chromatin marks and hMeSeal (n = 5) in WAT (Pathway27 LIS). WGBS of adipose tissue from GSM1010983. **b**, Spearman correlation analysis of read counts in 1 kb bins for acNEIL1 and four histone marks in acNEIL1-bound regions ± 5 kb around the center. WAT biopsies of Pathway27 LIS were obtained by MF, GU, GR, LR under coordination of AB. Tissue was pulverized by KK and AW, ACT-seq and hMeSeal libraries were prepared by JH and FJ, respectively. All downstream analyses were performed by myself (CFA). See Fig. 10 for the experimental design. Modified from (Feuerstein-Akgoz, C. et al., *in preparation*). LIS: large intervention study.

H3K4me (Fig. 40a). This was confirmed by Spearman correlation analysis of binned read counts in a region of ± 5 kb around the center of acNEIL1 binding. I obtained correlation coefficients rho = 0.83/0.86 for the correlation of acNEIL1 and H3K27ac and rho = 0.62/0.60 for the correlation of acNEIL1 and H3K4me1 in enhancer (excluding the H3K4me3 mark) and promoter regions, respectively. acNEIL1 binding strongly overlapped with the promoter mark H3K4me3 in promoter regions (rho = 0.63), whereas binding to repressed regions indicated by H3K27me3 was negligible (Fig. 40a, b). Correlation of acNEIL1 signals with hMe-Seal peaks in WAT was higher at enhancer than at promoter regions (rho = 0.47/0.18). This could be explained by the fact that enhancer regions showed intermediate methylation levels (consistent with their characterization as LMRs (Stadler et al., 2011)), whereas promoter regions with acNEIL1 binding were generally unmethylated and therefore could not be hydroxymethylated (WGBS panel in Fig. 40a).

Exemplarily, we detected prominent acNEIL1-binding at the *PPARG* locus, overlapping with H3K27ac and H3K4me1 enhancer marks in WAT and DNase hypersensitivity, PPARG, and CEBPA-binding in mature SGBS cells (Fig. 41). In addition to hMeSeal peaks overlapping acNEIL1-binding, we observed characteristic gene body hydroxymethylation at the PPARG locus as a WAT-specific biomarker (Pfeifer and Szabo, 2018).

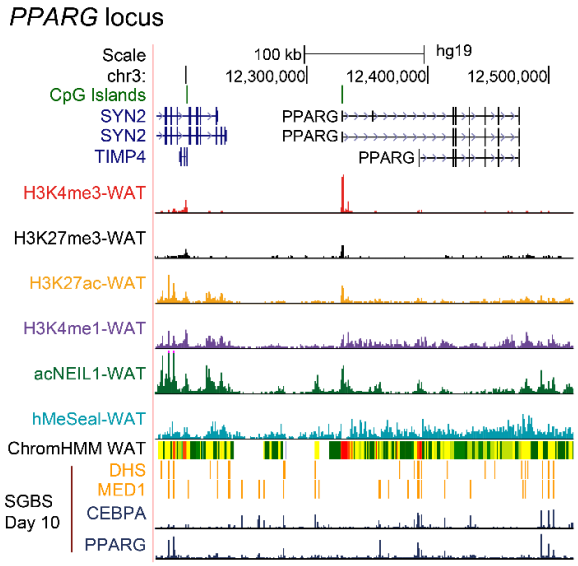

Fig. 41| UCSC brower track with NEIL1 binding at the PPARG locus. UCSC browser track of the *PPARG* locus. Average ACT-seq signals of acNEIL1 (n = 3), histone modifications (n = 3 - 4) and hMeSeal (n = 5) in WAT (PATHWAY-27 LIS) overlap enhancer regions (yellow Enh/greenyellow EnhG state, ChromHMM WAT Roadmap E063). For a description of the ChromHMM states see Fig. 20. ChromHMM track is followed by DNase Hypersensitivity sites and MED1 (Schmidt et al., 2015), CEBPA and PPARG binding in mature SGBS cells (Schmidt et al., 2011). (scale: H3K4me3: 0 - 80; H3K27me3: 0 - 25; H3K27ac: 0 - 75; H3K4me1: 0 - 25; acNEIL1: 0 - 60; hMeSeal: 0 - 25). WAT biopsies of PATHWAY-27 LIS were obtained by SG, MF, GU, GR, LR under coordination of AB. Tissue was pulverized by KK and AW, ACT-seq and hMeSeal libraries were prepared by KK, JH and FJ, respectively. All downstream analyses were performed by myself (CFA). See Fig. 10 for the experimental design. Modified from (Feuerstein-Akgoz, C. et al., *in preparation*). LIS: large intervention study.

Together, these data indicate that acNEIL1 binds to chromatin at adipogenic enhancers and promoters and this might enable and maintain functional WAT differentiation. Correlation analyses indicated a stronger association of acNEIL1 with H3K27ac than with hydroxymethylated regions, suggesting that the observed acNEIL1 binding at enhancer and promoter regions might rather be associated with its known role in BER to maintain genome integrity at gene regulatory regions, independent of an association with hydroxymethylation.

5 Discussion Part 1

In the first part of this thesis (chapter 4), I performed an epigenetic characterization of a human, non-transformed preadipocyte cell line, the SGBS cell line (Fischer-Posovszky et al., 2008). This study provides a map of hydroxymethylation changes during adipocyte differentiation at a base resolution level using WGBS/oxBS sequencing data. In addition, I validated these data by the 450k array technology (at base resolution) and at a non-base resolution level using hMeSeal data. Finally, I used RNA-sequencing data and published proteome (Schaffert et al., 2021) and metabolome data (Miehle et al., 2020) from collaboration partners for an integrated multi-ome analysis with the identified hydroxymethylation changes.

In my initial approach to identify adipocyte differentiation-induced alterations in DNA methylation, I observed only minor changes when analyzing data obtained from BS-treated DNA samples collected at day 0 and 11 of differentiation. However, when analyzing methylation data derived from BS and oxBS treatment combined, I identified thousands of sites displaying shifts from 5mC to 5hmC, which the BS method cannot distinguish (Fig. 13). Therefore, the current era of epigenomics, where BS treatment is considered the gold standard, might also be an era of neglected hydroxymethylation .

5.1 Hydroxymethylation at functional enhancer regions and gene body

During SGBS cell differentiation, I identified increasing 5hmC levels associated with time of differentiation, with highest levels in mature adipocytes (Fig. 16). Similarly, in a study of wild boar visceral adipose tissue, adipose nuclei sorted based on the expression PPARG alternative transcript 2 displayed the highest levels of 5hmC compared to adipocyte precursor cells or other tissue-resident cells (Yu et al., 2016). I identified 5hmC at the boundaries of LMRs of adipogenic genes, which I characterized as adipogenic enhancer regions (Fig. 14 + 20). These hydroxymethylated LMRs were enriched for adipogenic transcription factors, such as CEBPB, CEBPA, PPARG and RXR, and CTCF (Fig. 23 + 26) (Dubois-Chevalier et al., 2014; Schmidt et al., 2011; Serandour et al., 2012), where the TFs recruit TET enzymes to oxidize 5mC (Wu and Zhang, 2014). For *in vivo* validation, I found a significant overlap of 5hmC between SGBG and WAT samples at enhancer regions (Fig. 21).

Based on the enrichment analysis of hydroxymethylation clusters and gene expression clusters, I showed that hydroxymethylation accumulates very specifically in the neighborhood of cell-type specific upregulated genes, and not necessarily at highly expressed housekeeping

genes (Fig. 29), one reason why hydroxymethylation is suggested as a marker to identify a cell type (Ecsedi et al., 2018). Our data also confirm the specificity of hydroxymethylation, demonstrated by the differential 5hmC occupancy at CTCF binding sites (Fig. 23 + 35), where 5hmC is rather associated with dynamic CTCF binding with active cell-type specific enhancer function, in contrast to stable CTCF binding. This suggests active recruitment of TET enzymes at newly generated cell-type specific enhancer regions (Dubois-Chevalier et al., 2014). This specificity of hydroxymethylation is also observed regarding the selectivity of gene body hydroxymethylation. Based on correlation analysis, I identified a correlation between 5hmC levels and gene expression of adipocyte-specific genes (Fig. 38), an analysis previously performed in other tissues (Cui et al., 2020), while in housekeeping genes with similar expression levels, hydroxymethylation is detected at much lower levels (Pfeifer and Szabo, 2018). However, increased hydroxymethylation levels in the gene body might be partially also due to a higher number of tissue-specific intragenic enhancers and not only driven by its location in the gene body.

Finally, gain in 5hmC is not only relevant for human adipocyte differentiation but was previously also found during murine adipocyte differentiation (Serandour et al., 2012). In addition, gain in hydroxymethylation in the gene body and enhancer regions seems to be essential for various differentiation processes, as it was, for example, described in murine neural differentiation (Serandour et al., 2012), T cell maturation, and chondrocyte differentiation (Tsagaratou et al., 2014), demonstrating the importance of detecting this epigenetic mark during cell differentiation as stated in (Ecsedi et al., 2018).

5.2 Hydroxymethylation dynamics

With the characterization of the hydroxymethylation dynamics in the SGBS differentiation, I identified two distinct types of dynamics, a transient shift and a gradual accumulation of hydroxymethylation (Fig. 18). Transiently hydroxymethylated sites, with highest 5hmC levels at day 1, were enriched for enhancers with TF binding motifs of early adipogenic TFs (Fig. 23). On the other hand, the sites with gradual accumulation of hydroxymethylation until day 11, were enriched for enhancers with motifs of late adipogenic TFs. As observed with the transiently hydroxymethylated sites, 5hmC was previously often considered as an intermediate step during active demethylation and therefore neglected. Indeed, in a cell-free environment, TET2 can perform the 3-step oxidation of 5mC to 5caC in one encounter (Crawford et al., 2016). However, I detected increasing hydroxymethylation during adipocyte differentiation, suggesting that TET2 might lose its interaction with the 5hmC mark after the first oxidation

step. Ito *et al.* have shown that murine TET2 displays the highest affinity for 5mC, which could explain a temporal accumulation of 5hmC, where 5hmC competes for TET with other 5mC marks (Ito et al., 2011).

In vivo, the activity of TET might not only be regulated by substrate affinity but also by expression level, levels of co-substrates or inhibitors, posttranslational modifications of TET, or additional interaction proteins.

Most of the hydroxymethylated sites displayed a gradual accumulation during the differentiation process, completed at day 11 post induction. However, I wondered whether this might still be a transient process and demethylation might be completed at later time points. Therefore, we repeated the differentiation experiment and kept the mature adipocytes in culture until day 27 after induction of the differentiation process. Most hydroxymethylation marks were maintained, or hydroxymethylation levels even increased at sites with binding motifs of key adipogenesis transcription factors PPARG, CEBPA, and/or CREB1, supporting the fact that hydroxymethylation is a stable epigenetic mark that might have a specific function on its own (Fig. 16 + 23).

5.3 Regulation of hydroxymethylation dynamics

A stable hydroxymethylation mark can explain the constant hydroxymethylation levels, as described previously in two cancer cell lines, where the mark was even reestablished after cell division (Bachman et al., 2014). Another explanation would be a steady-state of dynamic demethylation and remethylation, as in embryonic stem cells. There, Ginno *et al.* described how dynamic demethylation and remethylation at the gene body is associated with high levels of transcription (Ginno et al., 2020). Similar events were described in transcriptionally active promoter regions (Métivier et al., 2008b). This can be tested by a perturbation of the steady-state by, e.g., inhibiting DNMTs. These described mechanisms were observed in embryonic stem cells with high TET expression levels (Wu et al., 2011) and/or in cycling cells; in contrast, preadipocytes enter after a clonal expansion into cell cycle arrest. Furthermore, in the SGBS cell line, reduced proliferation at later time points of differentiation was linked with a decrease in DNMT transcript levels (chapter 4.6.1). This would favor the model of a stable hydroxymethylation with reduced turnover, representing a cellular state which is less dependent on high DNMT expression for remethylation. Then the question arises, what is responsible for the low turnover of 5hmC. One possible explanation would be a reduced TET activity. Differentiation experiments in murine 3T3-L1 preadipocytes or human MCSs displayed that TET2 upregulated is essential for adipogenesis (Cakouros et al., 2019; Yoo et al., 2017).

In the SGBS cells, however, mRNA levels of TET2 enzymes were low in preadipocytes and mature adipocytes, with slightly higher expression in mature adipocytes (Fig. 34), while increase in TET1 expression was inconsistent between the different experiments (data not shown). As we did not observe a reduced expression, we considered it unlikely that in our SGBS model, accumulation in hydroxymethylation is regulated at the transcript level of TET enzymes.

5.3.1 Potential role of NEIL1 as 5hmC binding protein

In the search for additional explanations for the accumulation of hydroxymethylation, I wanted to investigate the involvement of DNA binding proteins, which might compete with TET for 5hmC binding. Various *in vitro* proteomics studies have identified 5hmC-interacting proteins (Pfeifer et al., 2019), which might contribute to the accumulation of 5hmC, including UHRF1/2, MECP2, MSH6, and NEIL1 (Iurlaro et al., 2013; Spruijt et al., 2013). UHRF2 has been shown earlier to enhance the processivity of TET enzymes (Spruijt et al., 2013; Wu and Zhang, 2017). Downregulation of UHRF2 during adipogenesis in our SGBS system could limit the step-wise oxidation of 5hmC to 5caC (chapter 4.6.1).

Different from the other putative 5hmC-interacting proteins, mRNA expression of the BER enzyme NEIL1 increased during SGBS adipogenesis (Fig. 39). A recent study suggested that DNA repair proteins often bind to genomic regions highly involved in genomic interactions, such as promoter-enhancer loops, to prevent DNA damage and rearrangements (Sobhy et al., 2019). Transcription of the NEIL1 inhibitory interaction partners ASF1A and CHAF1A/B, which regulate NEIL1 function as a BER enzyme, declined during differentiation. This suggested that in mature non-replicating adipocytes, acetylated NEIL1 (acNEIL1) might be associated with chromatin and influence adipocyte function with a different yet unknown function.

A potential influence of NEIL1 in maintaining adipose tissue function is supported by several *in vivo* knockout studies. Mice deficient in *Neil1* developed phenotypic symptoms associated with the metabolic syndrome, including spontaneous obesity, hepatic steatosis, hyperinsulinemia, and hyperleptinemia (Sampath et al., 2011; Vartanian et al., 2006), which might be linked to defective adipogenesis (Longo et al., 2019). I could demonstrate that in human WAT, acNEIL1 binds to chromatin preferentially at adipogenic enhancer and promoter regions, but it was less associated with hydroxymethylation (Fig. 40). Our data indicate that acNEIL1 has a role in maintaining enhancer function, but the methods were not specific or sensitive enough to exclude or support an additional role in 5hmC binding in WAT. The role of acNEIL1 in maintaining enhancer function in WAT could be explained by its known function as a repair protein of oxidative stress-induced DNA damage. Cells with high mitochondrial activity

have increased oxidative stress levels, typically affecting enhancer regions (Sobhy et al., 2019). My analyses indicate that acNEIL1 chromatin binding might reduce DNA damage at adipogenic enhancers and thereby maintain adipocyte differentiation capacity in WAT. Thus, acNEIL1 might contribute indirectly to adipocyte hyperplasia (increase in cell number) rather than hypertrophy (increase in cell size), which has been associated with metabolic complications in obesity (Longo et al., 2019).

5.3.2 Metabolism and TET activity

Cell metabolism represents a strong link between the cellular environment and epigenetic control of gene expression to induce cell differentiation or maintain cell identity (Dai et al., 2020). Conversely, defective cell metabolism can contribute to carcinogenesis via “non-mutational epigenetic reprogramming”, recently recognized as a hallmark of cancer (Hanahan, 2022).

5.3.2.1 The role of αKG and other factors

Recognizing the important influence of cell metabolism, I hypothesized that the abundance of cellular metabolites as substrates, co-substrates, or inhibitory substrates of TET enzymes might contribute to decreased 5hmC turnover during adipocyte differentiation. The availability of the co-substrate αKG, a TCA cycle intermediate, and the cofactor Fe(II) is elementary, while high pathological levels of inhibitory substrates lead to hypermethylation (Killian et al., 2013). However, metabolome studies of SGBS differentiation demonstrated that the levels of these metabolites did not increase in our differentiation model (Fig. 33+34).

Insulin-induced high import of glucose and an accumulation of acetyl-CoA suggest a high turnover of the TCA cycle. Nevertheless, I observed a low steady-state of αKG levels. αKG is involved in several cellular processes and is not only an intermediate metabolite of the TCA cycle to produce ATP. Although the subcellular concentrations of αKG are unknown to me, overall reduced cellular levels of αKG in late adipogenesis could be responsible for reduced TET activity. To maintain the pluripotent state in embryonic stem cells, αKG levels are pivotal for maintaining TET activity for sustaining high methylation and demethylation turnover (Carey et al., 2015; Shipony et al., 2014). Borkowska *et al*. found that aged adipose stem cells display increased 5hmC levels due to inefficient active demethylation due to reduced active (reduced TET activity) and passive demethylation (reduced proliferation) (Borkowska et al., 2020), while Tian *et al.*, reported lower circulating αKG levels in middle-aged mice (Tian et al., 2020). Similarly, in the first days of SGBS differentiation with high αKG levels, the generation of new

enhancer regions could be associated with complete demethylation due to high TET activity and proliferation-associated passive demethylation. In late differentiation, a reduced αKG pool would reduce TET activity and result in 5hmC stabilization due to cell cycle arrest. Similarly, Yang *et al.* showed that TET activity is associated with αKG levels by intraperitoneal injection of glucose or glutamine to mice. Increased levels of αKG in the bloodstream were associated with increased 5hmC levels in several tissues, linking αKG levels to TET activity in the first oxidation step of 5mC to 5hmC, while it remains unclear how further processing of 5hmC is regulated. The authors discussed that the decline of 5hmC levels seems to be independent of cell division (Yang et al., 2014). All in all, it seems clear that αKG levels are involved in controlling TET activity. However, it remains to be shown experimentally, whether a decline in αKG affects processivity of 5hmC or whether other yet unknown levels of regulation are involved.

5.3.2.2 Modulation of TET activity by posttranslational modifications

Metabolism affects TET activity not only by substrate availability but also by posttranslational modifications, such as acetylation, phosphorylation, and O-GlcNAcylation (Cao et al., 2019). Using the untargeted metabolome analysis, I was able to confirm the metabolic switch occurring during adipocyte differentiation by increased protein levels of enzymes involved in metabolic pathways (Fig. 26+31). However, the method was not sensitive enough to detect low abundant or nuclear proteins, such as TETs, and quantitatively estimate protein modifications. Opposing to Yang's observations, Wu *et al.* observed that high glucose levels resulted in reduced hydroxymethylation levels due to regulation of TET2 activity *via* the AMP-activated protein kinase (AMPK) pathway. Upon starvation, the increased AMP/ATP ratio activates the AMPK pathway, which leads to phosphorylation and stabilization of TET2. With high glucose levels, TET2 is rapidly degraded, leading to reduced hydroxymethylation levels, a phenomenon observed in obesity and cancer (Wu et al., 2018). Overall there are four known degradation pathways that affect TET2 levels, and each of them is regulated by different posttranslational modifications (Cong et al., 2021). Acetylation of TET2 in the N-terminal, e.g., prevents proteasomal degradation of TET2 during oxidative stress (Zhang et al., 2017). Due to the tight connection between the metabolic rate and the regulation of TET2 activity, TET2 is considered as an intracellular "sensor/regulator" of glucose levels (Ma and Kang, 2019). Hydroxymethylation was associated with obesity (Ali et al., 2021; Nicoletti et al., 2015), and is higher in VAT than in SAT, suggesting a regulation *via* cell metabolism (Rohde et al., 2015). While it seems clear that αKG levels, but also posttranslational modifications, are involved in regulating TET activity and are crucial for lineage specifications, less is known about the *in vivo* regulation dynamics of TET activity during adipocyte differentiation.

5.4 Function of hydroxymethylation as an epigenetic mark

Accumulation of hydroxymethylation seems to be a consequence of metabolic circumstances. However, the question remains whether hydroxymethylation is merely a consequence of the cellular metabolism or a ‘communication hub’ with relevant cellular signaling function (Juan et al., 2016). In recent years the perception of 5hmC has been changing from being an intermediate mark of demethylation to a mark with its own regulatory function. Still, possible roles are only based on educated guesses, while its exact role in epigenetic regulation remains unclear.

The fact that some 5hmC binding proteins, such as acNEIL1, have a higher binding affinity to 5hmC than to 5mC, suggests the existence of 5hmC ‘readers’ (Fig. 40). However, the indications are more substantial for the existence of 5hmC ‘anti-readers’, as several 5mC binding proteins lose their affinity to 5hmC (Pfeifer et al., 2019). In this case, it would be irrelevant whether 5hmC is further processed or not.

The most prominent binding protein is TET itself. TET enzymes are enriched at hydroxymethylated sites, e.g., in bivalent regions (Fig. 17). They are described to recruit repressive marks to prevent remethylation by DNMTs and, therefore, maintain cell plasticity (Wu et al., 2011). Also, at the boundaries of CpG islands, 5hmC could significantly prevent the remethylation of unmethylated ‘canyons’ (Pfeifer et al., 2019; Williams et al., 2011). However, it is not clear whether the function of 5hmC is to bind TET proteins and prevent DNMT action or whether 5hmC is sustained by high methylation and demethylation turnover as suggested by Wiehle *et al.* (Wiehle et al., 2016).

In brain tissue, Wen *et al.* demonstrated that 5hmC in the gene body is highly biased towards the sense strand, while the anti-sense strand is enriched for 5mC (Wen et al., 2014). It is discussed that 5hmC in the gene body could have a more substantial influence than 5mC in suppressing uncontrolled TSS in highly expressed genes (Fig. 38), as previously discussed by (Pfeifer and Szabo, 2018). Wen and colleagues, however, propose that 5hmC on the sense strand might be a consequence of increased accessibility for TET, while the anti-sense strand is needed during mRNA transcription. Biophysical studies suggest that 5hmC changes the forces needed for strand separation and could, therefore indeed, affect the accessibility of the transcriptional machinery to the DNA (Severin et al., 2013). This was also suggested by *in vitro* fluorescence resonance energy transfer (FRET) assays, showing that hydroxymethylation might facilitate incorporation of DNA into nucleosomes, but also generate a less compact nucleosomal state due to weaker interactions of the DNA with the nucleosomes, as it is needed for a transcriptionally active state (Mendonca et al., 2014).

6 Conclusion & Outlook Part 1

Based on our study, I have established a possible link between αKG decline and the maintenance of 5hmC levels during human adipocyte differentiation. One possibility to finally prove the stability of the hydroxymethylation mark would be to perform the SGBS differentiation experiment by feeding heavy L-methionine-(methyl-13C,d3) as methyl donor after clonal expansion to investigate whether there is still DNMT activity, which could be measured by the increased molecular weight of the newly generated 5mC and 5hmC by mass spectrometry (Bachman et al., 2014). If I indeed detect incomplete oxidation of 5mC after clonal expansion with an accumulation of the 5hmC mark without DNMT activity, then no accumulation of heavy 5hmC should be observed. On the other hand, a dynamic turnover would require the heavy methyl donor for DNMT action, and heavy 5mC and 5hmC should accumulate.

Bayliak *et al.* discuss that indeed the ratio of αKG and other TCA cycle intermediates such as succinate and fumarate could be imperative for a proper equilibrium of the methylation and demethylation machinery; an impaired equilibrium was observed during aging (Bayliak and Lushchak, 2020). In mice, the importance of αKG in brown adipogenesis was shown mechanistically by the need of αKG for DNA demethylation at the *PR/SET domain 16* (*Prdm16)* promoter (Yang et al., 2016). In aging mice, αKG levels could be restored by dietary supplementation and promoted beige adipogenesis, while supplementation had no effects in young mice with high αKG levels (Tian et al., 2020). As αKG also functions as mimetic of caloric restriction by activating AMPK (Bayliak and Lushchak, 2020), the dependency of brown adipogenesis to αKG could also be mediated *via* its dependency on high AMPK signaling, which in turn promotes DNA demethylation at the *Prdm16* promoter mainly *via* signal transduction. This idea is also supported by the fact that white adipocyte differentiation was not affected by lower αKG levels (Yang et al., 2016). Both differentiation processes are dependent on DNA demethylation, and high AMPK signaling will favor beige and brown adipogenesis and inhibit white adipogenesis (Ahmad et al., 2020; van der Vaart et al., 2021). This suggests that metabolite dependencies of epigenetic enzymes should be interpreted carefully, as for example αKG might affect DNA methylation not only by substrate availability, but also indirectly *via* signaling events.

With respect to analyzing the importance of cellular metabolism for epigenetic mechanisms including hydroxymethylation, our *in vitro* SGBS model might have limitations. An *in vitro* model represents a closed system without considering metabolite in- and outflux. Thus, the cellular metabolite concentrations including that of αKG determined during SGBS differentiation might not be representative of αKG levels in adipose tissue. To understand the molecular

dependencies on metabolites such as αKG, it might not be sufficient to detect cellular metabolites concentrations, as they present only a snapshot of the cellular steady-state. In contrast, it might be necessary to consider subcellular metabolite concentrations and require perturbation experiments to reveal metabolic dependencies and the substrate flow between metabolic processes across multiple cell types and organs.

Currently, I could not conclusively demonstrate a role of acNEIL1 for 5hmC stability during adipogenesis. A time-course experiment of acNEIL1 binding during SGBS differentiation would allow identifying associations of acNEIL1 binding and hydroxymethylation within one cell type, instead of within a mixture of different cells in a complex tissue. Also, NEIL1 expression could be manipulated in gain and loss of function experiments, to test whether this would influence hydroxymethylation stability and differentiation capacity of the SGBS cells.

Using the SGBS cells as a model of human adipocyte differentiation without known genetic aberrations allowed us to study the differentiation process in a setting similar to the *in vivo* situation. We identified a large overlap of the 5hmC mark in mature SGBS adipocytes and WAT. However, for a better comparison, nuclei of isolated mature adipocytes should be considered instead of WAT tissue, consisting of a mixture of different cell types. Furthermore, WAT samples were taken from humans at risk of metabolic syndrome. Thus, data on adipocyte size and numbers in their adipose tissue to characterize hyperplasia or hypertrophy would be informative help to assess whether these characteristics are associated with global or local differences in hydroxymethylation. Finally, SGBS differentiation is induced by strong chemical adipogenic inducers, like the PPARG agonist rosiglitazone, enabling *in vitro* differentiation independent of cellular, physical, metabolic, or signaling interactions in the niche of adipose tissue. Therefore, all findings generated *in vitro* can only be suggestive and should be carefully validated *in vivo*.

Considering the current expansion of the prevalence of obesity and the associated metabolic diseases, the better characterization of human adipocyte differentiation and, therefore, a better understanding of the molecular mechanisms are pivotal for developing strategies for healthy adipose tissue expansion.

7 Results Part 2
Effect of DHA on SGBS preadipocytes

7.1 Experimental design and treatment conditions

The aim of the second part of this thesis was to investigate the mode of action of the bioactives DHA, protocatechuic acid (PA) as the most abundant anthocyanin metabolite, and the beta-glucan metabolite propionate (PRO), for prevention of the metabolic syndrome. As DNA methylation is relatively stable in contrast to the more dynamic changes in chromatin accessibility and histone modifications, I focused on DNA methylation as “an epigenetic mark of cellular memory” (Kim and Costello, 2017). To investigate bioactive-induced methylation changes, I selected SGBS preadipocytes rather than mature SGBS cells. Mature adipocytes represent non-proliferating cells where we expected little changes in DNA methylation to occur after compound treatment.

To determine toxicity thresholds of the bioactives, I performed cytotoxicity assays with SGBS preadipocytes using sulforhodamin B (SRB) staining to determine cell counts (Skehan et al., 1990b). In initial experiments, I determined the optimal seeding density for SGBS cells in 96-well format, allowing for exponential growth for three days. To determine toxic effects, I then seeded 500 cells/well and treated the cells after 24 h once with PA or PRO in eight serial dilutions in a concentration range of 0.78 µM – 100 µM in three independent replicates, and with DHA in a range of 0.35 µM – 45 µM. After three days of incubation, the half-maximal inhibitory concentrations (IC_{50}) of PA and PRO were determined as > 100 µM. For DHA, I detected growth inhibitory effects on preadipocytes with a mean IC_{50} of 23.5 ± 5.1 µM (Fig. 42). For long-term treatment of the preadipocytes, I initially selected a concentration of 10 µM DHA and physiologically relevant concentrations of 20 µM PA and 70 µM PRO. When I performed cultivation experiments with the indicated concentrations at a more extended period of 4 weeks, I observed that 10 µM DHA still displayed toxic effects. Therefore, I performed another series of experiments using 5 µM DHA, which was tolerated by the SGBS preadipocytes and represented after three days of treatment ~ IC_5.

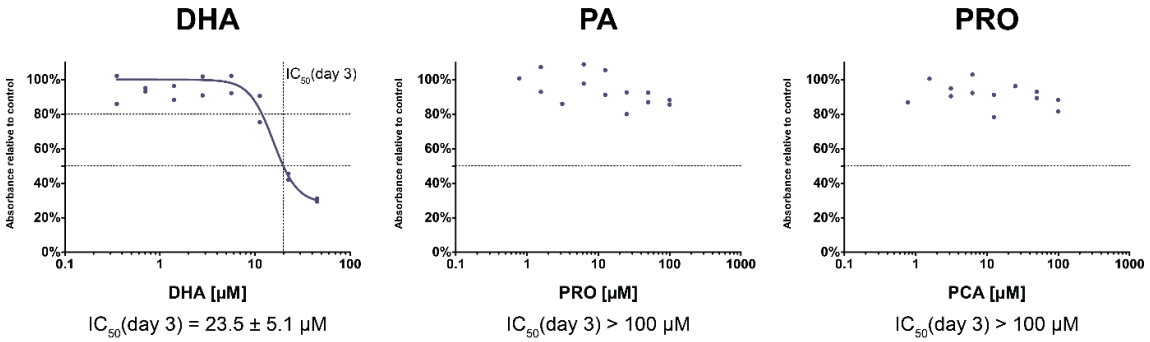

Fig. 42| Cytotoxicity experiments of docosahexaenoic acid (DHA), propionate (PRO), and protocatechuic acid (PA) using SRB staining. Cytotoxicity of the bioactive DHA was tested in SGBS preadipocytes in a range of 0.35 µM – 45 µM, and PRO and PA in a range of 0.78 µM – 100 µM in a 96-well format, n = 2 in 2 independent experiments (graph shows 1 experiment). Below each graph the mean IC_{50} of all experiments + SD is given. SD: standard deviation.

To provide the SGBS cells with DHA in a physiological manner, I complexed the free fatty acid to BSA under nitrogen conditions. This method protects the double bonds of the n-3 fatty acid from peroxidation through free radicals (Brown et al., 2004). PA and PRO were dissolved in DMSO and ethanol, respectively. Each treated sample obtained the solvents of all three bioactives. Twice a week, I passaged the SGBS cells and added again each time the bioactives alone or in combination. Samples treated with DHA or a combination with DHA (5 µM DHA, 5 µM DHA + 70 µM PRO, 5 µM DHA + 20 µM PA) are mentioned in the following as "**DHA"** samples. Sample without DHA-treatment, namely treated with 70 µM PRO, 20 µM PA, the solvent control, and a completely untreated sample were called "**nonDHA"** samples (Fig. 9). The concentrations of the bioactives and solvents were well tolerated by the cells. However, DHA-treated cells still displayed a slightly reduced proliferation rate (~ 80 – 90% of the nonDNA samples), so I compensated during passaging for the reduced number of cells.

7.2 Characterization of the SGBS methylome represented on the EPIC array

For methylation analysis, I submitted DNA of three independent biological replicates (rep I, III, and IV) at day 0 and after long-term cultivation for 3 - 4 weeks for methylation analysis of ~ 850,000 preselected CpG dinucleotides on the Infinium HumanMethylationEPIC BeadChip. After preprocessing and normalization steps using the RnBeads package (Assenov et al., 2014), ~ 726,000 CpG sites remained for further analyses.

Compared to WGBS data (Fig. 12), where I was able to deduce methylation data for about 20 million CpG sites with ≥ 10x coverage, the EPIC array covers only a fraction of all CpGs sites. Especially CpGs in fully methylated regions (FMR) and partially methylated domains (PMDs) are underrepresented on the EPIC array, as it was designed to mainly cover promoter (UMR) and enhancer regions (LMR). Genome-wide, most CpGs are located in FMRs and PMDs (Fig. 43a), and of those, less than 4 % are covered on the EPIC array (Fig. 43b). In contrast, of CpG sites located in UMR and LMR, approximately 13 % and 7 % are covered, respectively (**Error! Reference source not found.**b). Therefore, although most of the CpGs on the EPIC array are located in PMDs (Fig. 43c), PMDs are actually underrepresented.
I visualized the CpG sites covered on the EPIC array as well as in WGBS of our SGBS cells in the UCSC genome browser (first two methylation tracks) and compared them to the methylation levels of two published WGBS data sets of adipose-derived stem (ADS) cells (Lister et al., 2011) and (ADS, E025) (Roadmap Epigenomics et al., 2015) (Fig. 44). While the second ADS track ADS (E025) displayed almost no demethylation in PMDs (average methylation close to 1), in the first ADS track and SGBS cells, I observed extensive demethylation in these regions; the larger the domains, the lower the average methylation.

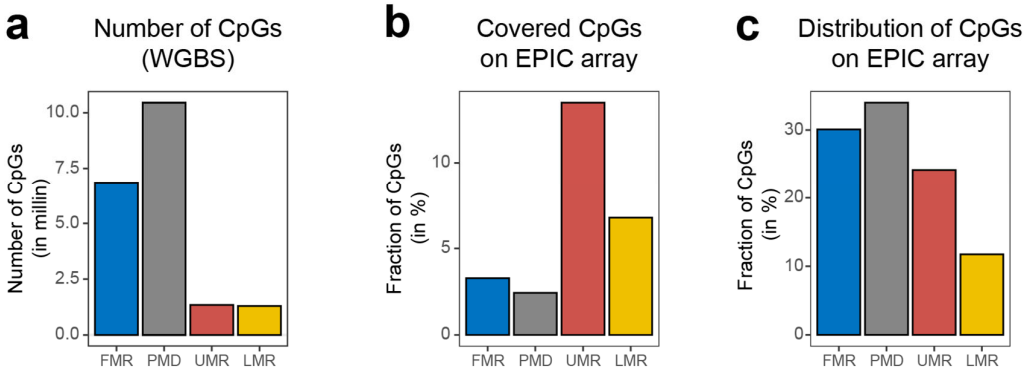

Fig. 43| Characterization of the SGBS methylome and its representation on the EPIC array. a, Bar plot depicting number of CpGs from WGBS data (coverage ≥ 10x) within fully methylated regions (FMR), partially methylated domains (PMD), defined using WGBS in SGBS data (experiment 2), unmethylated regions (UMRs) and lowly methylated regions (LMRs). **b**, Bar plot depicting the percentage of respective CpGs covered on the EPIC array (experiment 5). **c**, Bar plot depicting distribution of CpGs on the EPIC array representing FMR, PMD, UMR and LMR (experiment 5). Experiment 2 was performed by LK, experiment 5, WGBS/oxBS library generation and data analysis were performed by myself (CFA). See Fig. 8 and Fig. 9 for experimental design.

PMDs overlapped with the heterochromatin-associated histone mark H3K9me3, and the borders of the PMDs were marked with the facultative-heterochromatic mark H3K27me3 (Roadmap Epigenomics et al., 2015). Underrepresentation of CpG sites in PMDs on the EPIC arrays is also visible in the UCSC track. While the small PMDs on the right side are still relatively highly covered with CpGs, the CpG density in the large PMD in the center is low.

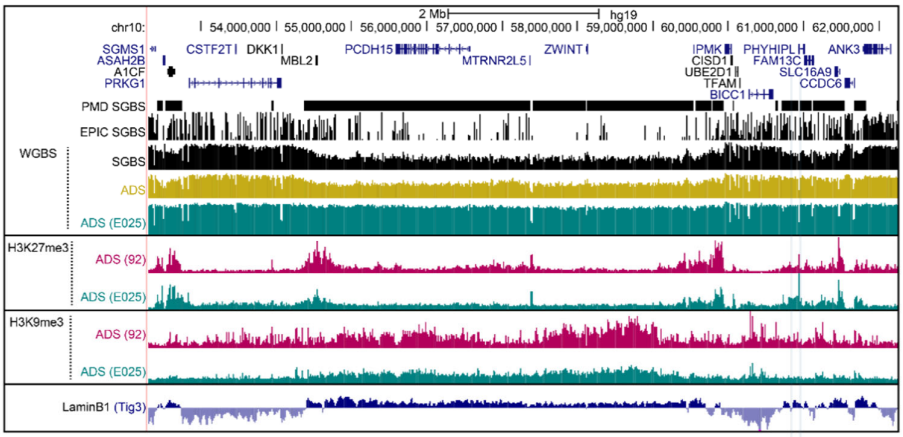

Fig. 44| Partially methylated domains are marked by H3K9me3 and flanked by H3K27me3. Visualization of a partially methylated domain (PMD) on chromosome 10. PMDs represent regions where at least 4 of 7 WGBS samples of SGBS cells display PMD characteristics (experiment 2). Below the PMD track, EPIC array and WGBS of SGBS preadipocytes tracks (experiment 2) are followed by WGBS data of cultured primary adipose-derived stem cells (ADS) (beige) (Lister et al., 2011) and (E025, green) (Roadmap Epigenomics et al., 2015), displayed in a methylation range between 0 and 1. Borders of PMDs overlap with H3K27me3 and the body of PMDs with H3K9me3 (Roadmap Epigenomics et al., 2015). The LaminB1 track in Tig3 cells represent log2-ratio scores between -2 and 2, a score for nuclear lamina-associated domains (Guelen et al., 2008). Experiment 2 was performed by LK. WGBS/oxBS library generation and data analysis performed by myself (CFA). See Fig. 7 for experimental design.

7.3 Global methylation changes during SGBS cultivation confound DHA-induced methylation changes

After obtaining an overview of the analyzed CpG sites, I performed a principal component analysis to visualize differences in methylation related to bioactive treatments in all three replicates compared to the cultured control samples and day 0 (Fig. 45). With the purpose of a better interpretation of the identified methylation changes, I included data of untreated control samples from studies of two other students (Student 2 and 3) in our division (LD & LK), who investigated the effects of long-term cultivation with other bioactives.

The strongest variability of the observed methylation changes was induced by long-term cell culture, both in samples treated with bioactives and in untreated samples (Fig. 45a). Day 0 of

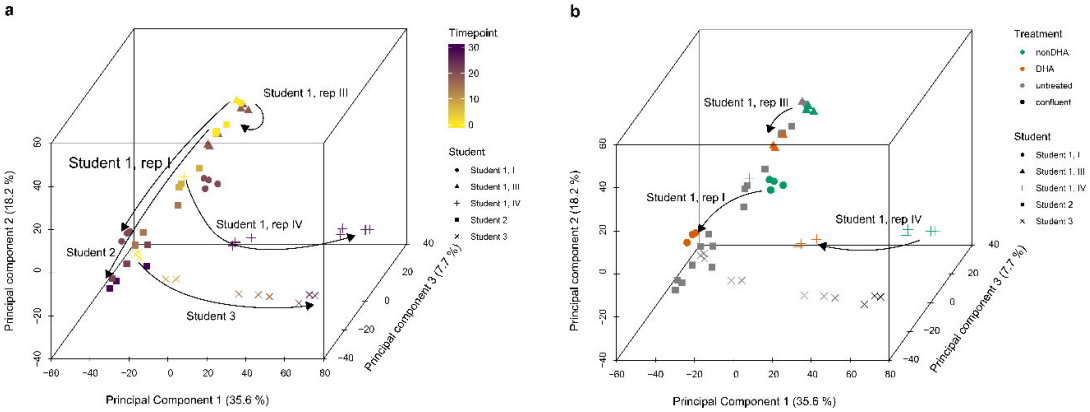

Fig. 45| Tri-dimensional PCA of methylation changes during SGBS cultivation and DHA long-term treatment. Principal component analysis based on methylation values of CpG sites covered on the EPIC array of cultured SGBS preadipocytes of three students, cultured for 18 to 29 days (experiment 5 - 7). Individual biological replicates are coded by shapes. Timepoints are color-coded by a gradient from yellow to purple (**a**) or treatment with DHA (orange) and nonDHA (green), respectively. Experiment 6 was performed by LD (Student 2), experiment 7 by LK (Student 3), experiment 5 and data analysis were performed by myself (CFA, Student 1). See Fig. 9 for experimental design.

cultivation in replicate I, III, and Student 2 was located in the upper part of the plot (yellow). With increasing cultivation time (color scale from yellow to purple), samples of these replicates dropped to the lower left front of the PCA. In contrast, day 0 of replicate IV started were samples of replicate I ended, and day 0 of Student 3 started, where samples of Student 2 ended. From there, time-dependent changes in replicate IV and Student 3 represented the first principal component and samples of these replicates ended on the right side of the PCA (follow the arrows in Fig. 45a).

In Fig. 45b, I visualized the samples of my experiments (rep I, III, IV) colored by DHA and nonDHA, since treatment with DHA alone and in combination demonstrated a reproducible effect compared to the nonDHA samples. DHA and nonDNA samples, respectively, in all three replicates grouped together. Therefore, we concluded that the effects of PRO and PA alone were negligible and both compounds did not have any significant additive or synergistic effect when combined with DHA (Fig. 45b).

Consequently, for the rest of the thesis, I focused on the impact of DHA. When inspecting the DHA effect in the context of the long-term cultivation, it became evident that DHA-associated methylation changes in rep I and III overlapped with the culture effects observed for Student 2 samples. In contrast, the effects on rep IV antagonized the culture effects of Student 3 samples.

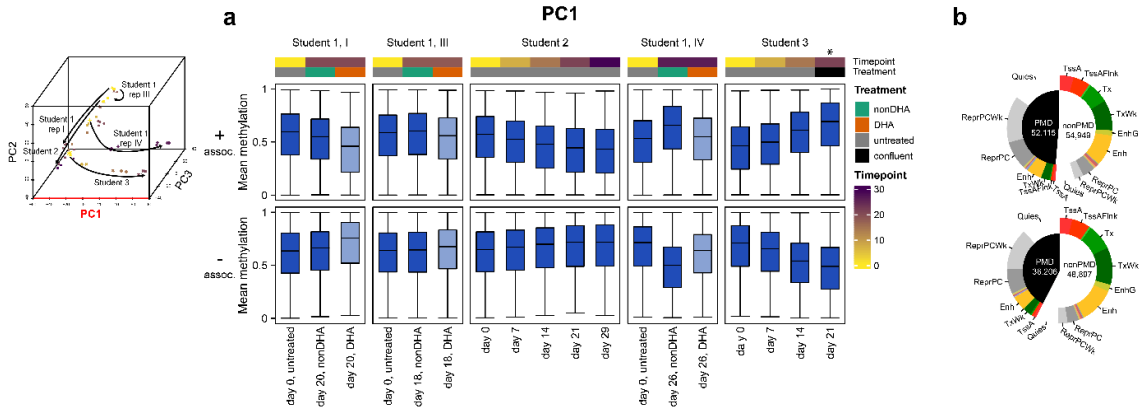

Fig. 46| Methylation changes associated with principal component 1. a, Boxplots of 107,064 CpG sites with a positive (upper panel) and 85,103 CpGs with negative (lower panel) association with principal component 1 (PC1) displaying a methylation range > 0.2 and a significant linear regression (FDR adj. *p* value < 0.005). Boxes display mean methylation values (n = 1 - 4, see Fig. 26) of control samples (dark blue) of Student 1 - 3 and DHA samples (light blue, Student 1). Boxplots show median (horizontal line), upper, and lower quartiles (boxes), and vertical lines extending to the 1.5× interquartile range. See Supplementary Fig. 3 with Heatmap of individual methylation values. **b**, Pie chart displays the ChromHMM annotation of adipose-derived stem cell (ADS, E025) (Roadmap Epigenomics et al., 2015) of the CpG sites displayed in Fig. 46a, grouped as PMD and nonPMD sites defined in SGBS cells. Experiment 6 was performed by LD (Student 2), experiment 7 by LK (Student 3), experiment 5 and data analysis were performed by myself (CFA, Student 1). See Fig. 9 for experimental design.

To understand the nature of methylation changes induced by long-term culturing SGBS cells, I next characterized the variability of the methylation changes in the first three principal components in more detail. I identified with a linear model all CpGs with a significant association (FDR adj. *p* value < 0.005) between PC1 and methylation levels (methylation range > 0.2) (Fig. 46a + Supplementary Fig. 3 to view the individual CpG sites). CpGs associated with PC1 displayed the most substantial methylation changes in Student 3 and replicate IV data due to cultivation. CpGs, with intermediate median methylation at day 0, and with positive (+) association with PC1 showed a gain in methylation during the cultivation time of about 23 % (median methylation at day 21 vs day 0) and the opposite effect, a loss in methylation, in replicate I and Student 2 data. In contrast, CpGs with a negative (-) association, which on average were higher methylated at day 0 than CpGs with positive association, displayed an extensive loss of about 21 % in replicate IV and Student 3 data, but only a minimal gain in methylation in replicate I and Student 2 data.

When considering the DHA effect on PC1-associated methylation chances, in replicate I and III, DHA treatment led to an extension of the culture effect. In contrast, in replicate IV, I observed attenuation of the culture effect in DHA samples compared to nonDHA samples. In both groups (with positive or negative associations), CgG sites located in PMDs and nonPMDs were about equally affected (Fig. 46b). NonPMD sites were annotated in adipose derived stem cells (E025) to gene regulatory (Tss and Enh), transcribed (Tx) and repressed regions (Roadmap Epigenomics et al., 2015).

Overall, the fact that I observed both gain and loss in methylation at CpG sites located both in PMDs (heterochromatin) or in gene regulatory regions (euchromatin), as well as opposing effects between students and experiments, argued against only one targeted mechanism underlying these methylation changes represented in PC1.

While PC1 covered opposing methylation changes in rep I, rep III, and Student 2 vs rep IV and Student 3, PC2 represented methylation changes associated with all experiments except samples of Student 3 (Fig. 47). Notably, median methylation levels of Student 3 samples were among the lowest for CpG sites with positive associations, and among the highest for sites with negative associations. For CpG sites with positive association, I observed a cultivation-associated loss in methylation affecting about 14 % of all CpG sites covered on the EPIC array (Fig. 47a). The majority of these sites was located in PMDs (~ 70 %) (Fig. 47b, see Supplementary Fig. 4 for visualization of the methylation of the individual CpG sites). In contrast, I identified ~ 40 k CpGs displaying culture-associated gains in methylation, depleted in PMDs, and represented rather CpGs located in gene regulatory or transcribed regions. These methylation changes might be associated with replication-associated loss in methylation in PMDs and with cultivation-associated silencing of genes due to promoter/enhancer hypermethylation (Antequera et al., 1990; Raghavan et al., 2021; Smiraglia et al., 2001). In rep I and III, DHA samples displayed a further loss or gain in methylation compared to the nonDHA samples, whereas in replicate IV, DHA had no additional effect on methylation.

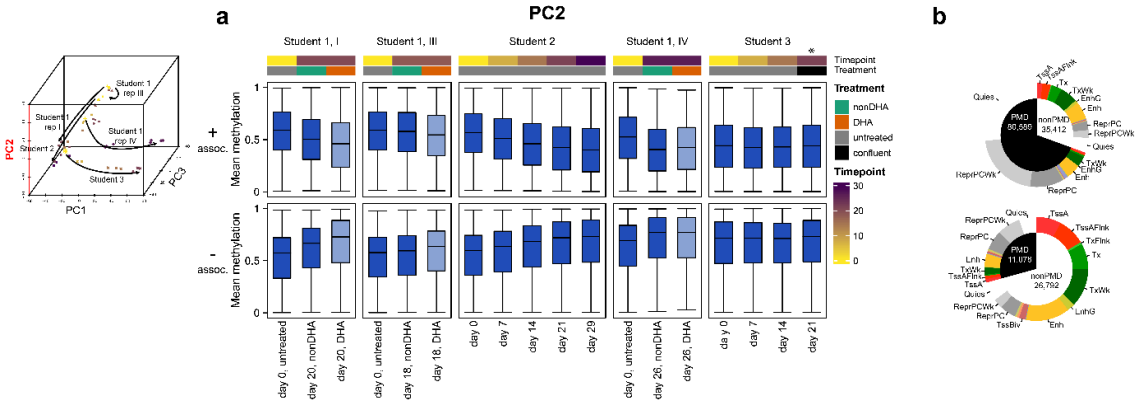

Fig. 47| Methylation changes associated with principal component 2. a, Boxplots of 116,001 CpG sites with a positive (upper panel) and 37,870 CpGs with negative (lower panel) association with principal component 2 (PC2) displaying a methylation range > 0.2 and a significant linear regression (FDR adj. *p* value < 0.005). Boxes display mean methylation values (n = 1 - 4, see Fig. 26) of control samples (dark blue) and DHA samples (light blue) of Student 1-3. Boxplots show median (horizontal line), upper, and lower quartiles (boxes), and vertical lines extending to the 1.5× interquartile range. See Supplementary Fig. 4 with Heatmap of individual methylation values. **b**, Pie chart displays the ChromHMM annotation of adipose-derived stem cell (ADS, E025) (Roadmap Epigenomics et al., 2015) of the CpG displayed in the upper or lower boxplots, grouped by PMDs and nonPMDs defined in SGBS cells. Experiment 6 was performed by LD (Student 2), experiment 7 by LK (Student 3), experiment 5 and data analysis were performed by myself (CFA, Student 1). See Fig. 9 for experimental design.

The third principal component PC3 represented methylation changes of roughly 38 k CpG sites associated explicitly with replicate IV and Student 3, with no alterations in methylation among the other experiments (Fig. 48). CpGs with positive association gained methylation during the cultivation in replicate IV and lost methylation in Student 3 data. The opposite effect was observed for CpG sites with a negative association. In the DHA sample of replicate IV, the methylation changes compared to day 0 were attenuated in both association groups. CpG sites located both in PMDs and nonPMDs were equally affected.

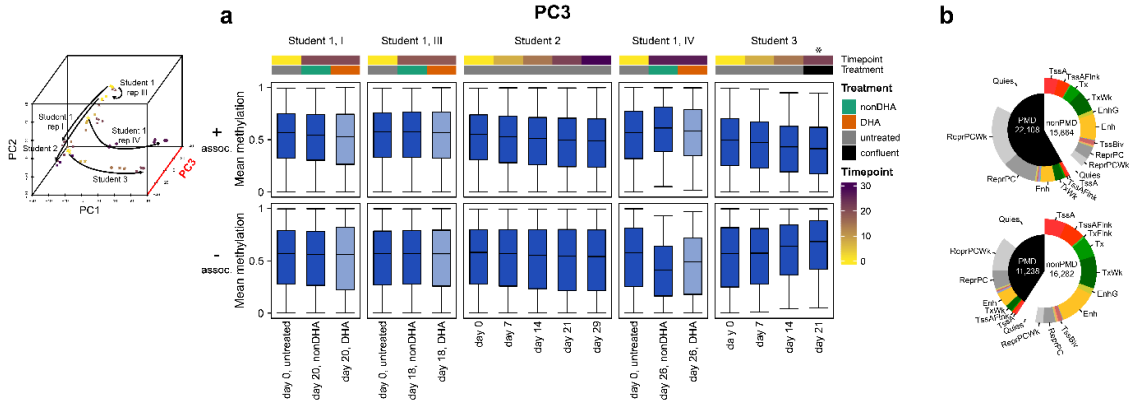

Fig. 48| Methylation changes associated with principal component 3. a, Boxplots of 37,972 CpG sites with a positive (upper panel) and 27,520 CpGs with negative association (lower panel) with principal component 3 (PC3) displaying a methylation range > 0.2 and a significant linear regression (FDR adj. *p* value < 0.005). Boxes display mean methylation values (n = 1 - 4, see Fig. 26) of control samples (dark blue) of Student 1 - 3 and DHA samples (light blue) of Student 1. Boxplots show median (horizontal line), upper, and lower quartiles (boxes), and vertical lines extending to the 1.5× interquartile range. See Supplementary Fig. 6 with Heatmap of individual methylation values. **b**, Pie chart displays the ChromHMM annotation of adipose-derived stem cells (ADS, E025) (Roadmap Epigenomics et al., 2015) of the CpG displayed in the upper or lower panels, grouped by PMDs and nonPMDs defined in SGBS cells. Experiment 6 was performed by LD (Student 2), experiment 7 by LK (Student 3), experiment 5 and data analysis were performed by myself (CFA, Student 1). See Fig. 9 for experimental design.

7.4 Gain of methylation in gene regulatory regions

After matching the CpGs to the three PC either by positive or negative association (linear model), I performed an enrichment analysis based on published ChromHMM states of adipose-derived stem cells (ADS) (Roadmap Epigenomics et al., 2015). CpGs with a positive association to all three PCs were enriched for states like heterochromatin and repressed or quiescent (no histone mark detected) regions. The strongest enrichments were found in PC2 (Fig. 49). These chromatin states are also associated with PMDs, mainly with larger PMDs (Supplementary Fig. 5) and therefore agree with the strong enrichment of PMDs seen in Fig. 47b. The negatively associated CpGs were enriched instead in gene regulatory and transcribed regions, with the exception of PC2, where I additionally identified enrichment for bivalent areas.

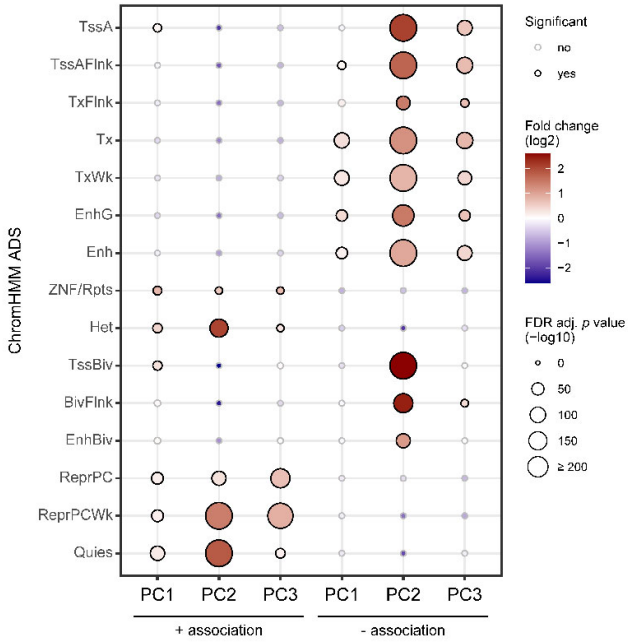

Fig. 49| Enrichment analysis of ChromHMM states. With each set of CpGs (positive or negative association with PC1 - 3), enrichment analysis for ChromHMM states of adipose-derived stem cells was performed (ChromHMM ADS: E025 (Roadmap Epigenomics et al., 2015)). Fisher's exact test was applied to define significant enrichment (Bonferroni-adjusted *p* value ≤ 0.05). The analysis is based on experiments 5 - 7. Experiment 6 was performed by LD (Student 2), experiment 7 by LK (Student 3), experiment 5, and data analysis were performed by myself (CFA, Student 1). See Fig. 9 for experimental design.

As CpGs with a negative association with PC2 were enriched at enhancer regions, these CpGs might reflect a gain in methylation to promote silencing of specific enhancers that became inactive during prolonged cell culture. Thus, I filtered for CpGs located in LMRs, which mark typically enhancer regions, and that I defined using WGBS-based methylation data in SGBS cells (Fig. 12 + 43) (Burger et al., 2013). The aim was to identify possible upstream regulators associated with the observed gain in methylation or enhancer silencing, respectively. With CpG sites negatively associated with PC2 and located in LMRs, I performed an enrichment analysis of TF binding motifs and visualized the top 10 enriched TF clusters (Fig. 50a). To further investigate a possible regulatory function of the TF, I performed a correlation analysis between methylation and gene expression to see whether a gain in methylation is associated with a reduced expression of the TF (negative Pearson's r (red)) (Fig. 50b). I identified motifs of several TFs involved in adipogenesis, such as PPARG, the glucocorticoid receptor (NR3C1), EBF transcription factor 1 (EBF1), and NFIC, all TFs previously identified in hydroxymethylated enhancers (Fig. 23). Also, zinc finger and BTB domain containing 7a (ZBTB7A) binding plays an essential role during adipogenesis and displayed the strongest negative correlation between methylation at LMRs and gene expression (Fig. 50b) (Laudes et al., 2004), indicating that reduced expression of ZBTB7A was associated with the methylation gain at ZBTB7A

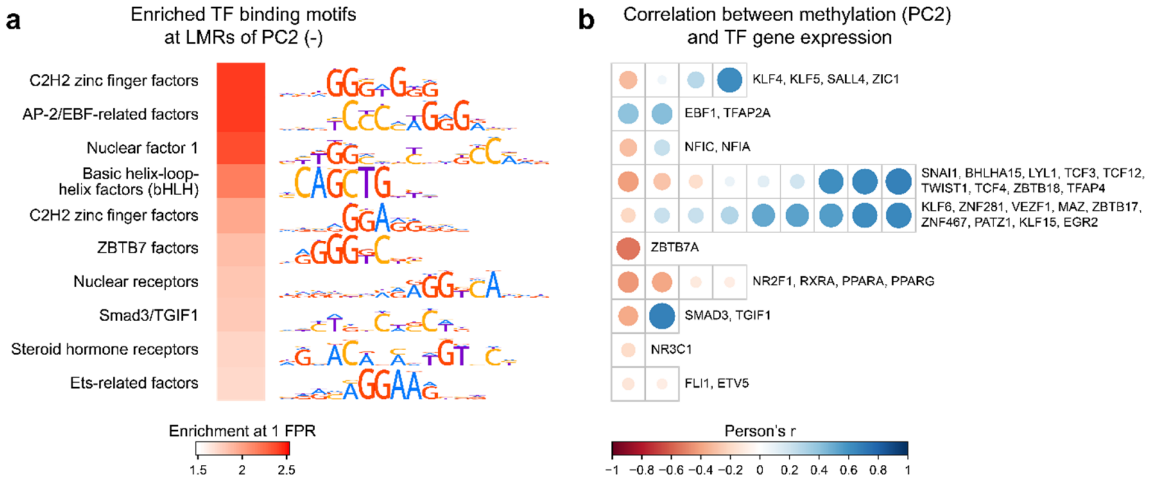

Fig. 50| Top10 enriched transcription factor motifs associates with Principal Component 2 (-). **a**, CpGs with a negative association with PC2 overlapping with lowly methylated regions (LMRs) were used for transcription factor (TF) motif enrichment. To create TF families, hocomoco motifs were clustered by motif similarity. The motif and enrichment of the best-enriched TF within the TF family are displayed for the top 10 enriched TF families. **b**, For each TF family, all enriched and expressed motifs were displayed in order of correlation between methylation and gene expression (Person's r). The analysis is based on experiments 5 - 7. Experiment 6 was performed by LD (Student 2), experiment 7 by LK (Student 3), experiment 5, and data analysis were performed by myself (CFA, Student 1). See Fig. 9 for experimental design. FPR: fraction of false positives or (1-specificity).

binding sites. KLF4 is a transcription factor associated with stemness and a critical regulator of adipogenesis, binding to the promoter of CEBPB (Birsoy et al., 2008) and snail family transcriptional repressor 1 (SNAIL1) is involved in stemness and inhibits adipogenesis (Peláez-García et al., 2015). These data suggested that certain gene regulatory elements that become nonessential during cultivation are being repressed via the methylation mark and possibly inhibit adipocyte differentiation, displayed by the associated reduced gene expression (Antequera et al., 1990). The cultivation of the samples of Student 3 started at a later passage. The methylation data suggest that these cells had acquired the gain in methylation already, but during further cultivation, these sites displayed a stabilized methylation pattern (Fig. 47).

The TF motif analysis was an attempt to shed light on the upstream or downstream effects of the methylation changes, possibly, e.g., by hypermethylation of gene-regulatory elements to shut down those that are considered currently as nonessential. However, it is essential to note that the majority of the methylation changes associated with PC2 were not occurring in LMRs, but in PMDs, and might be related to replication.

7.5 Epigenetic mitotic clocks in SGBS cells

To further investigate the considerable methylation changes occurring during cultivation especially in PMDs, I next investigated whether the methylation changes are associated with the number of cell divisions. I correlated the methylation-based PCs with the scores calculated by different methylation-based mitotic clocks, recently compared by Teschendorff (Teschendorff, 2020). The best correlation was identified between PC2 and 1-(EpiCMIT.hypo) with an $r^2 = 0.875$ (Fig. 51a). EpiCMIT describes Epigenetically-determined Cumulative MIToses. The EpiCMIT.hypo score decreases with mitotic cell divisions and is based on a selection of highly methylated CpGs located in inactive regions that lose methylation in B-cell samples with the highest vs the lowest proliferative history (Duran-Ferrer et al., 2020). Since the CpGs selected to construct the EpiCMIT.hypo score are located per definition in H3K9me3-marked heterochromatin and quiescent genomic regions, I concluded that the EpiCMIT.hypo score represents the demethylation process occurring in PMDs, mainly in my cultivation experiments (Student 1) in replicates I and IV, as well as in samples of Student 2. Samples of Student 3 already displayed low methylation levels at the beginning of the cultivation, which might associate with a high starting passage. However, the methylation in Student 3 samples did not further decrease during the cultivation process. A high correlation between PC2 and the 1-(EpiCMIT.hypo) score might represent the demethylation in PMDs, affecting ~ 81,000

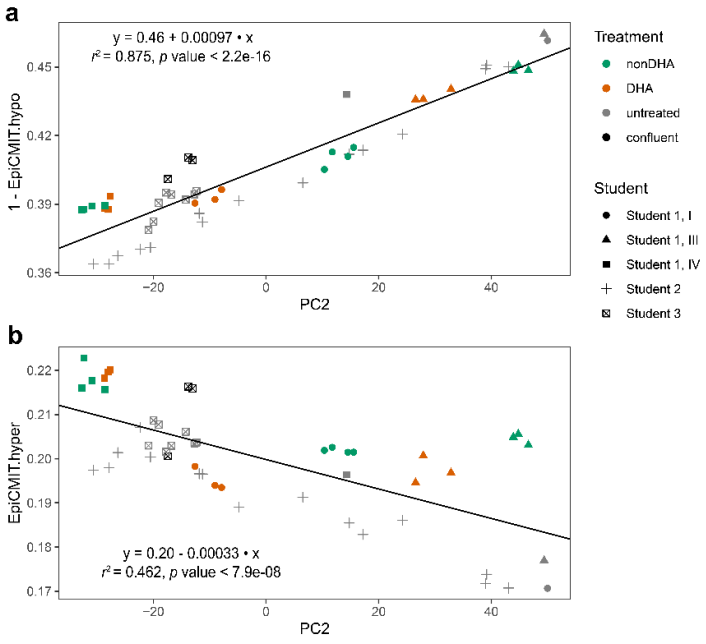

Fig. 51| Principal component 2 correlates best with mitotic clock EpiCMIT.hypo. a,b Dot plot shows linear regression between PC2 defined by variability within methylation data (see Fig. 45 + 47) and 1-EpiCMIT.hypo (a) score defined for each sample by a published selection of CpG sites mainly located in PMDs (Duran-Ferrer et al.) or EpiCMIT.hyper (b) mainly representing Polycomb-repressed CpGs. The figure includes data of experiments 5 - 7. Experiment 6 was performed by LD (Student 2), experiment 7 by LK (Student 3), experiment 5, and data analysis were performed by myself (CFA, Student 1). See Fig. 9 for experimental design.

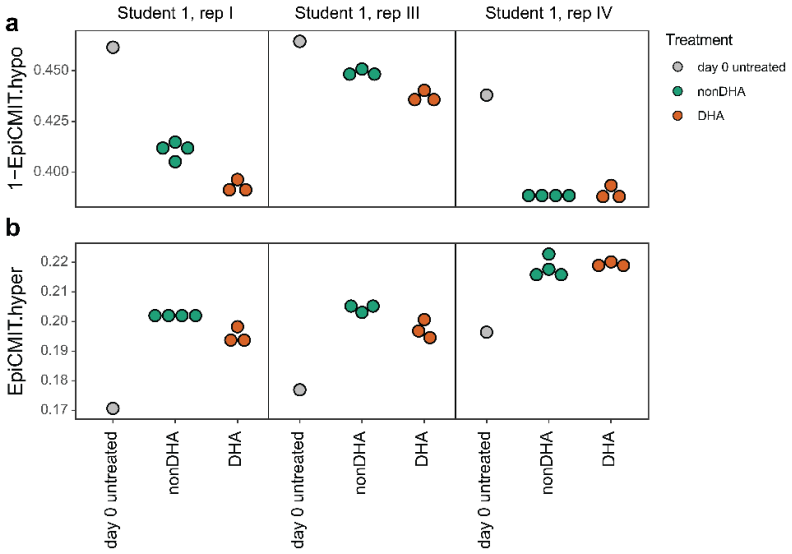

Fig. 52| DHA treatment effects on methylation-based mitotic clocks. a,b, Dot plot displaying two methylation-based mitotic scores, the-EpiCMIT.hypo (a) and EpiCMIT.hyper (b), at day 0 and after cultivation in nonDHA and DHA samples of replicates I, III and IV. The figure includes data of experiment 5. See Fig. 9 for experimental design.

CpG on the EPIC array. The EpiCMIT.hyper score is calculated from unmethylated CpGs located in H3K27me3-repressed regions or poised promoters, with increasing methylation during cell division. Correlation between PC2 and EpiCMIT.hyper score was albeit weaker (Fig. 51b).

The two scores also displayed differences in DHA-treated samples (Fig. 52). While the 1-(EpiCMIT.hypo) score shows that in DHA-treated samples PMD demethylation is enhanced during the cultivation time, compared to nonDHA samples, the EpiCMIT.hyper score showed that DHA samples display fewer mitotic cell divisions compared to nonDHA samples. This would be in line with the fact that DHA-treated samples grew slower than nonDHA samples and that the cell number had to be compensated for during passaging.

To sum up, I observe a close link between DHA-associated methylation changes and cultivation-associated methylation changes, such as the demethylation process in large PMDs, but also the regulation of the epigenome at gene regulatory regions. Therefore, DHA might affect cultivation-associated pathways that indirectly induce massive global methylation changes while overlaying and confounding possibly smaller direct DHA-specific methylation effects.

7.6 DHA-induced gene expression changes

In the hunt for direct DHA-mediated effects in SGBS cells, I next investigated DHA-associated changes at the gene expression level, which is affected by signal transduction processes and epigenetic regulation. I performed a principal component analysis with all expressed genes (mean expression of log2CPM > 0 in at least one group) using RNA-seq data of experiment 7, rep I, III, and IV. I identified differences in the first two principal components separating the replicates. Similar to methylation data, DHA samples always clustered separately from nonDHA samples (Fig. 53a). I identified an exclusive DHA effect on the third principal component describing 7.7 % of the variability, most pronounced in replicate IV (Fig. 53b).

To identify genes associated with PC3, I applied a linear model on gene expression levels and identified 575 DHA-induced and 581 DHA-downregulated genes with a log2CPM range > 1 and p value < 0.05 (Fig. 54). In addition, I found selected upregulated genes that link to methylation changes. For instance, I observed an upregulation of the transcription factor KLF4, which is involved in stemness (Fig. 54). Its motif was enriched in LMRs of methylation-associated PC2 (Fig. 50). The same was true for RXRA, a transcription factor that can be inhibited by DHA binding (Sampath and Ntambi, 2004). Also, transforming growth factor beta 1 (TGFB1) was upregulated by DHA treatment.

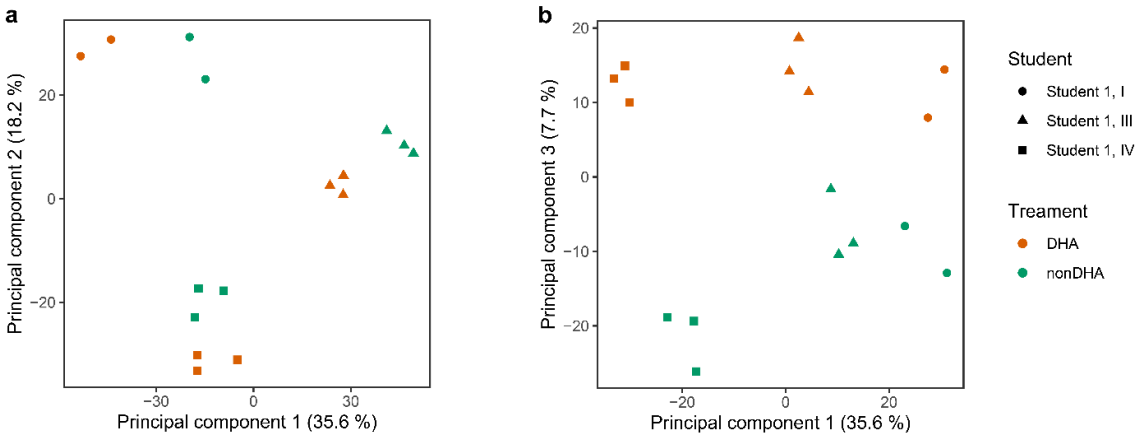

Fig. 53| DHA-associated gene expression changes in cultivated SGBS preadipocytes. Principal component analysis based on RNA-seq data (log2CPM) of cultured SGBS preadipocytes of three independent replicates. Individual biological replicates are coded by shapes and treatment with DHA (orange) and nonDHA (green). The figure includes data of experiment 5. See Fig. 9 for experimental design.

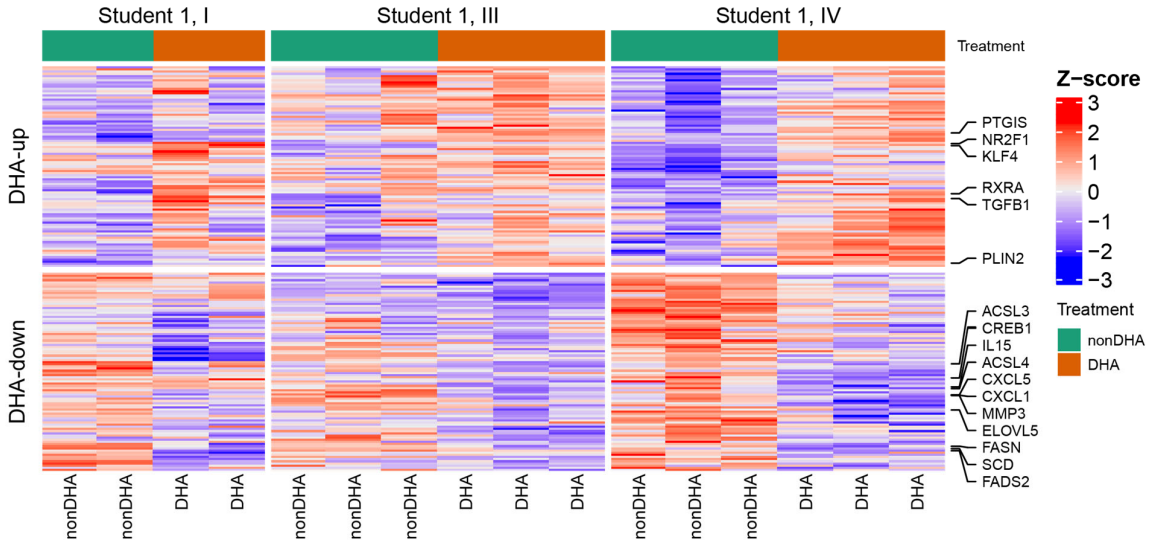

Fig. 54| Heatmap of DHA-regulated genes. Heatmap displays Z-scores of 575 genes downregulated and 581 upregulated by DHA treatment. Genes were selected by significant association with gene expression principal component 3 (PC3 visualized in Fig. 48), displaying a log2CPM range > 1 and a significant linear regression (*p* value < 0.05). The figure includes data of experiment 5. See Fig. 9 for experimental design.

No KEGG or WIKI pathway was overrepresented among the genes upregulated by DHA. However, among the downregulated genes, I identified several overrepresented pathways associated with fatty acid and cholesterol metabolism and SREBP signaling (Fig. 55). DHA treatment was also associated with an anti-inflammatory effect visualized by the downregulated genes of the TNF signaling pathway (Fig. 55a).

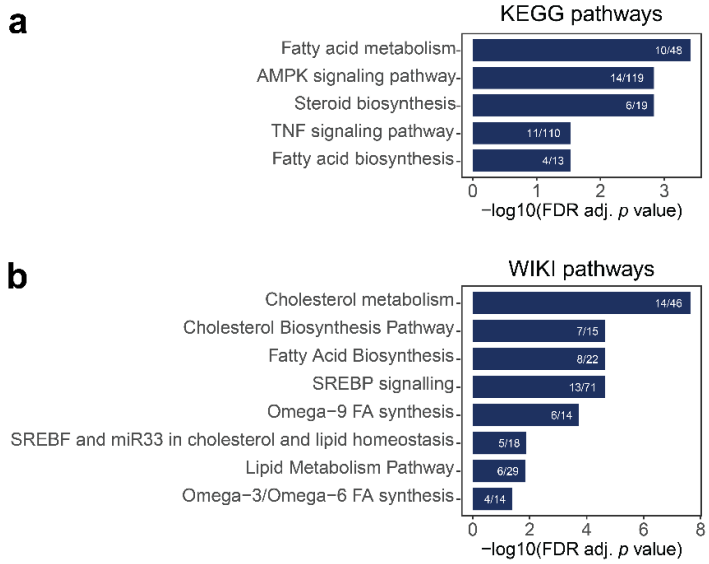

Fig. 55| Pathway overrepresentation analysis of DHA-induced downregulated genes. a-b, Barplot displays significantly overrepresented KEGG (**a**) or WIKI pathways (**b**) among the genes downregulated by DHA treatment. Downregulated genes with significant negative association with principal component 3 of the gene expression analysis (linear regression *p* value < 0.05) and log2CPM range > 1 were used for the pathway analyses. Enriched pathways with a significant overrepresentation of genes (FDR adj. *p* value < 0.05) are displayed. The matching/total number of genes within the pathway are listed in each bar. The analysis was performed on data of experiment 5. See Fig. 9 for experimental design.

I visualized changes in gene expression of all genes annotated to the cholesterol (WP4718) and SREBP signaling pathways (WP1982) that were expressed in SGBS cells (41 of 47 genes and 63 of 71 genes, respectively) and identified significant downregulation over all replicates (Fig. 56a,b).

SREBP binding motifs were not enriched in my methylation-based motif analysis (Fig. 50), suggesting reduced SREBP activity might not be due to increased methylation at the TF binding site, but by reduced *SREBF* transcript levels. Indeed, mRNA expression of both, *SREBF1* and *2,* was reduced in DHA-treated samples (Fig. 56c,d). I also performed an Ingenuity Pathway Analysis (IPA) on genes associated with principal component 3, and *SREBF1*/*2* were identified as central regulators involved in the downregulation of the pathway "metabolism of sterol" and "conversion of fatty acid" pathways (Fig. 56e).

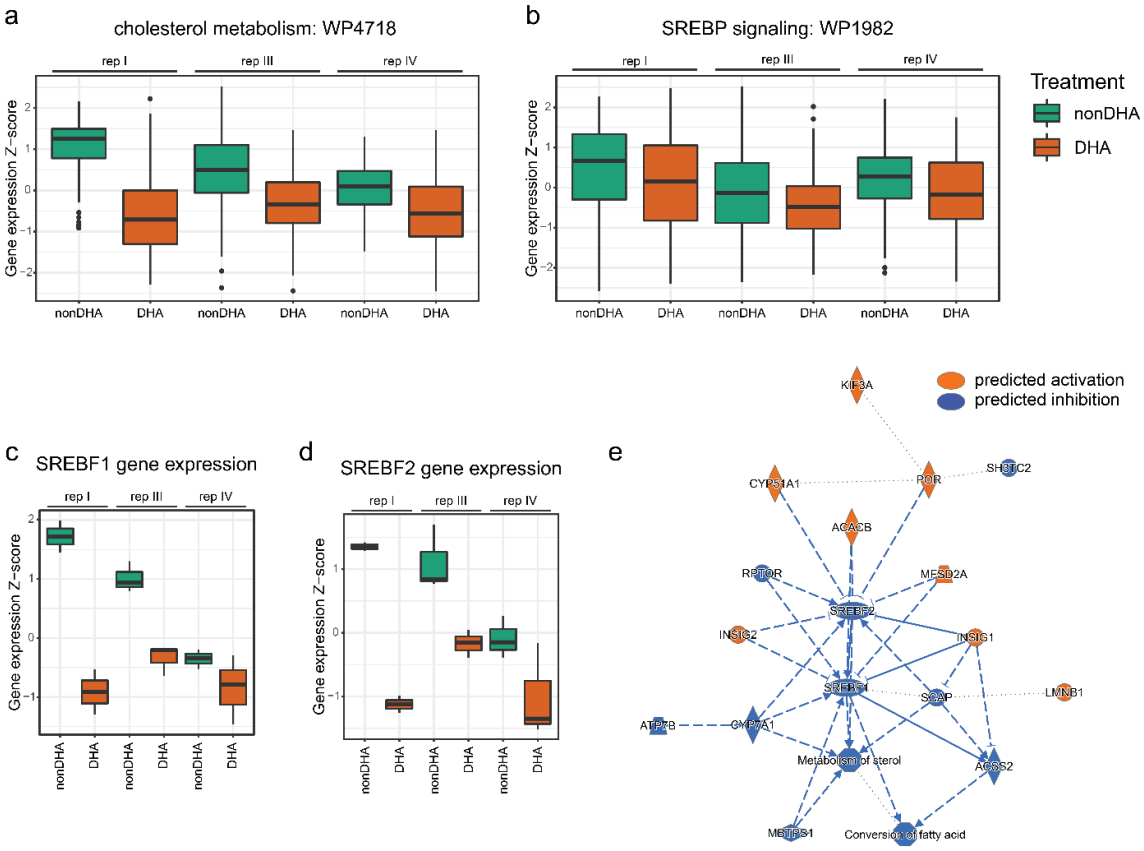

Fig. 56| DHA downregulates genes associated with Cholesterol metabolism and the SREBP signaling pathway. a+b, Boxplots of genes included in the Wikipathways "cholesterol metabolism" and "sterol regulatory element-binding protein (SREBP) signaling" (see Fig. 54). Boxplots display mean scaled gene expression of DHA and nonDHA treated samples in all three replicates (Student 1, replicates I, III, IV) of all expressed genes (n = 41 of 47 genes / n = 63 of 71 genes) of the respective pathways. **c + d**, Boxplot of scaled gene expression of *SREBF1* and *SREBF2* genes of DHA and nonDHA treated samples (n = 2 - 3) for each replicate (Student 1, replicates I, III, IV). **e**, Graphical summary of the Ingenuity Pathway Analysis of regulated genes significantly associated with principal component 3 (linear regression *p* value < 0.05) and log2CPM range > 1. The analyses were performed on data of experiment 5. See Fig. 9 for experimental design.

Insulin-induced gene 1 (INSIG1) and 2 are possible upstream regulators of SREBPs that are upregulated in DHA-treated samples and prevent the transport of SREBPs from the endoplasmic reticulum to the Golgi, where SREBPs are cleaved and released to enter the nucleus (Lee et al., 2006). To be able to investigate systematically the upstream regulators that might regulate DHA-induced transcriptional changes, I performed an Integrated System for Motif Activity Response analysis (ISMARA). The tool identifies the variability within the gene expression using RNA-seq data. Based on the TF binding motifs within the promoter regions of the affected genes, it identifies potential regulating upstream TFs (Balwierz et al., 2014). I

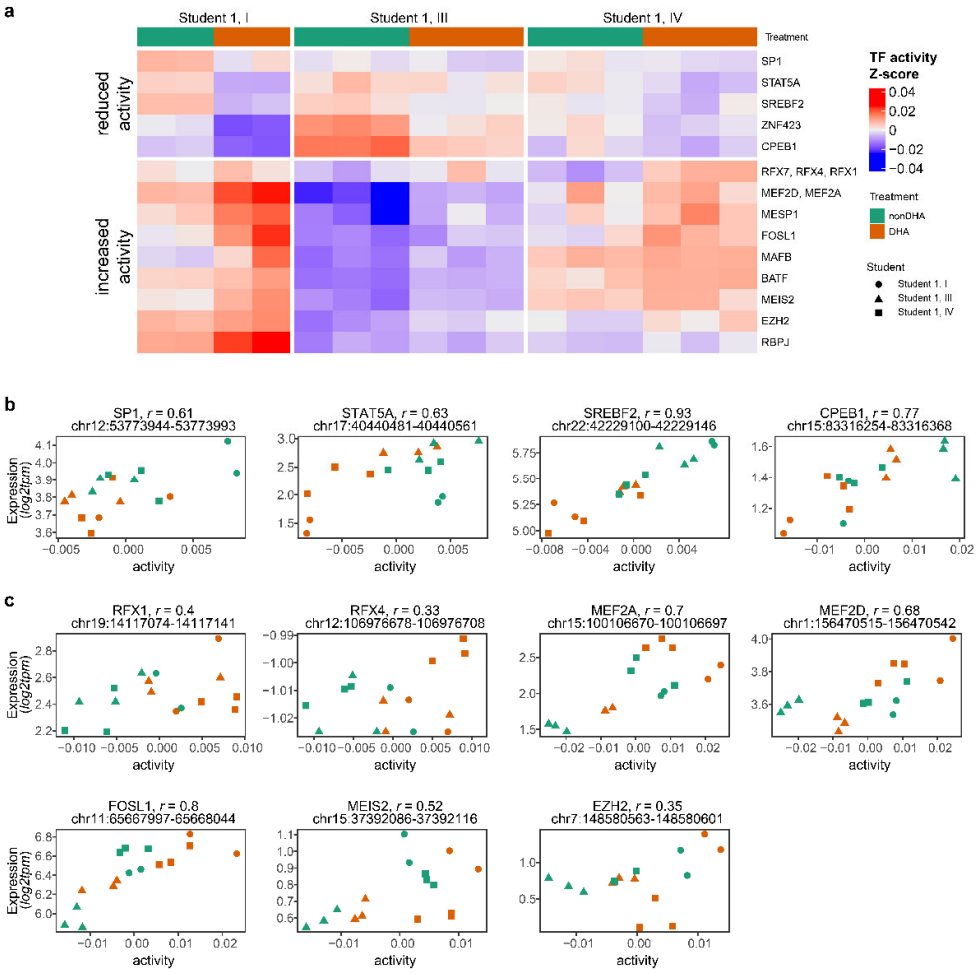

Fig. 57| Transcription factor activity associated with DHA treatment. Gene expression-based analysis of TF activity was performed with all DHA- and nonDHA-treated samples for each replicate individually (Exp. 7, rep. I, III, IV) using the ISMARA web tool (Balwierz et al., 2014). Displayed are all TF with a consistent increase or decrease in DHA-treatment associated transcription factor (TF) activity with a Z-value > 2.5 in at least one replicate and the others > 0.7. **a**, Heatmap of TF activity Z-scores over all replicates, grouped by replicates and treatment. **b - c**, Pearson correlation of TF activity (Z-score) and TF gene expression (*log2tpm*) of all TF with a significant increase (**b**) or decrease (**c**) and Pearson correlation coefficient $r > 0.3$. The location of the promoter of the corresponding transcript is given as chromosomal position in hg19. Individual biological replicates are coded by shapes and treatment with DHA (orange) and nonDHA (green). Figures display experiment 5. See Fig. 9 for experimental design

performed a grouped ISMARA analysis between DHA vs nonDHA samples in each replicate independently and selected for TFs that had a consistent DHA-associated effect in all three replicates (Z-value > 0.7 and > 2.5 in at least one replicate) (Fig. 57). TFs that were suppressed in DHA-treated samples were involved in cell proliferation (SP1, STAT5), and response to inflammatory signaling pathways (SP1, STAT5A, SREBF2). Transcription factors with increased activity were involved in stemness function (FOS like 1, FOSL1), mesoderm function (mesoderm posterior BHLH transcription factor 1, MESP1), and the developmental TF MEIS2 (meis homeobox 2). BATF (basic leucine zipper ATF-like transcription factor), an inhibitor of AP1, could be regulating the inhibition of proliferation. MAF BZIP transcription factor B (MAFB) is involved in the suppression of interferon signaling (Motohashi and Igarashi, 2010). RBPJ (recombination signal binding protein for immunoglobulin kappa J region) of the NOTCH signaling pathway is involved in proliferation and differentiation (Ali et al., 2016). Four of the five TFs with decreased TF activity displayed a significant correlation between TF expression and activity, with a Pearson correlation coefficient r > 0.3 (Fig. 57b). Among the TF with increased TF activity seven of nine TF displayed a significant Pearson correlation (Fig. 57c).

Taken together, my analysis of gene expression data suggests that DHA executes its cellular effects via regulation of the expression and activity of several transcription factors.

7.7 DHA affects TFs regulated in adipocyte differentiation

Promoting adipose tissue expansion *via* adipocyte differentiation (hyperplasia) might alleviate some of the metabolic complications in patients with metabolic syndrome. To investigate whether DHA could target this mechanism, I initiated adipocyte differentiation after long-term cultivation with DHA and nonDHA conditions to study adipocyte differentiation capacity. The differentiation capacity was drastically impaired in the DHA-treated samples, but as well in the control groups. Therefore, I suspect that the long-term cultivation-associated effects on the SGBS cells that I identified at the methylation but also gene expression level affected the differentiation capacity of the SGBS cells, making it difficult to investigate the effect of DHA on this process.

To identify possible DHA-induced early priming for adipocyte differentiation, I selected DHA-affected TFs, identified by ISMARA (Fig. 57), and displayed their activity during adipocyte differentiation (Fig. 58a). SREBP2 and SP1 are two TFs that were suppressed by DHA, but are activated during adipogenesis. SREBP2 activity is central for mature adipocytes, but the activity is not regulated at the expression level during adipogenesis (no positive correlation with gene expression), but at the level of proteolytic activation (Inoue et al., 2001). In contrast,

STAT5A and zinc finger protein 423 (ZNF423) are TFs that were suppressed by DHA but are essential at early timepoints of adipogenesis and are downregulated at later timepoints of adipogenesis (Behrmann et al., 2014; Siersbaek and Mandrup, 2011). Among the DHA-activated transcription factors, we identified MAFB (Pettersson et al., 2015) and the myogenic TF MEF2A as TFs that increase their activity during adipogenesis with increasing levels of TF gene expression. In contrast, regulatory factor X1 (RFX1), FOSL1 and EZH2 showed increased activity due to DHA treatment, and had decreased activity and expression during adipogenesis, with a significant correlation of TF activity and TF gene expression.

To sum up, all DHA-regulated TFs were also regulated during SGBS differentiation. Therefore, these TFs are possible candidates influencing the capacity of adipocyte differentiation after long-term DHA treatment, both positively and negatively.

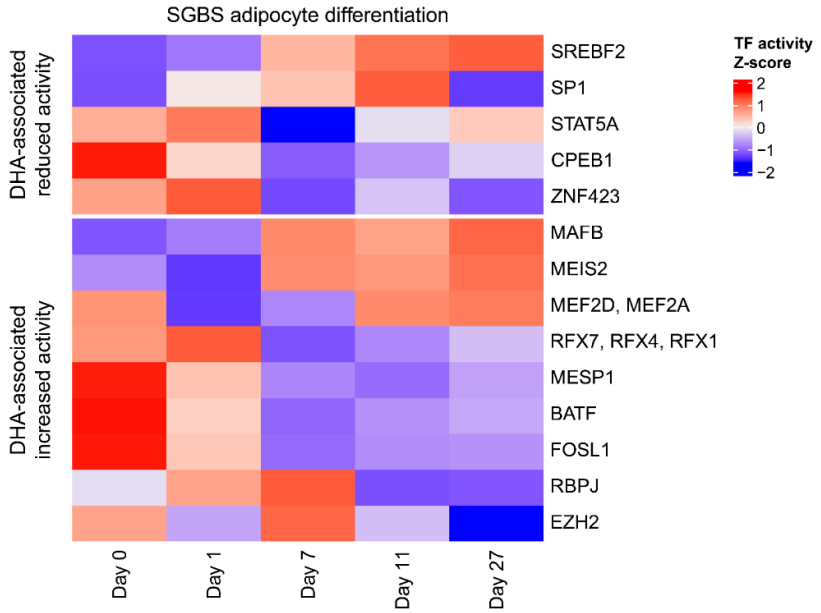

Fig. 58| DHA-associated TF in adipocyte differentiation. Heatmap of mean TF activity Z-scores over all timepoints of SGBS adipocyte differentiation (experiment 2) of DHA-associated TF (see Fig. 57). Gene expression-based analysis of TF activity was performed with all DHA- and nonDHA-treated samples for each replicate individually (Exp. 7, rep. I, III, IV) using the ISMARA web tool (Balwierz et al., 2014). Displayed are all TF with a consistent increase or decrease in DHA-treatment associated transcription factor (TF) activity with a Z-value > 2.5 in at least one replicate and the others > 0.7 (experiment 5). Experiment 2 was performed by LK, experiment 5, and data analysis performed by myself (CFA). See Fig. 8 + 9 for experimental design.

8 Discussion Part 2

Considering the current knowledge on anti-inflammatory, lipid-lowering, and insulin-sensitizing functions of DHA, I wanted to investigate the role of DHA in the prevention of metabolic syndrome as a modulator of adipogenic differentiation. Therefore, I studied the effect of DHA in SGBS preadipocytes after long-term cultivation with DHA vs nonDHA conditions. To characterize biological effects, I investigated DNA methylation using EPIC array technology, covering ~ 850,000 CpG sites, and gene expression using RNA-seq (chapter 7).

8.1 Cultivation-associated effect in SGBS preadipocytes

At the DNA methylation level and the gene expression level, I identified differences between DHA- and nonDHA-treated samples. However, in a principal component analysis, the first three principal components, explaining together about 60 % of the variability, represented differences between replicates rather than between treatment groups (Fig. 43). This was especially problematic for the interpretation of DHA-associated effects on DNA methylation, as DHA- and cultivation-associated effects were largely overlapping. Members of our laboratory had not observed such massive changes during cultivation using established (cancer) cell lines before. Therefore, I wanted to investigate possible sources for the cultivation-associated changes in the SGBS preadipocytes.

Due to the substantial changes in DNA methylation, I wondered whether I was observing the clonal expansion of one particular clone with a different methylation profile than the initial culture or a progressive, gradual change in methylation. Based on signal intensities on the EPIC array for the detection of copy number alterations (CNA) using the Conumee R package, I was not able to identify outgrow of genetic clones based on amplification or deletion of genomic regions (data not shown). The question remains whether I observed clonal outgrow of an epigenetic clone. However, the fact that I observed gradual methylation changes over time occurring in several technical replicates in parallel or even independently in the hands of different students, strongly argues for a progressive change in methylation due to culturing “environmental” conditions.

I also considered genetic causes that could explain the susceptibility of the SGBS cells toward environmental influences on DNA methylation. It is not known which mutation is responsible for the SGBS disease of the child from which the cell line was generated. The gene typically associated with SGBS (*GPC3*) was sequenced, and no mutation was found (Wabitsch et al.,

2001). When comparing WGBS sequencing data of SGBS cells with whole-genome sequencing (WGS) data of a male WAT tissue sample, I found no amplifications or deletions (data not shown). These findings confirmed the array-based CNA analysis and rather suggest an unidentified single point mutation or small insertion or deletion in the SGBS cell line, which was responsible for the SGBS disease and might also be associated with epigenetic vulnerability.

As in the SGBS preadipocytes, no genetic mutation was found yet that could be causal for the SGBS disease. Therefore, to identify possible disease-driving genetic aberrations, whole-genome sequencing of SGBS cells is being performed for an in-depth analysis. Identifying a point mutation might also help to find a cause for the susceptibility towards epigenetic destabilization.

8.1.1 DNA methylation and demethylation machinery

The SGBS preadipocyte cell line is characterized by substantially reduced methylation levels in late replicating regions, also named as PMDs (Fig. 42). These PMDs are often found in cancer and in established cancer cell lines, and only to a comparably little extent in healthy human tissue (Lister et al., 2009; Timp et al., 2014). During cultivation, I observed a substantial extent of PMD demethylation (Fig. 49a), as it is regularly observed during cancer progression or extensive cultivation of cancer cell lines (Timp et al., 2014). PMD demethylation is currently explained by the incapability of proper DNA maintenance, mostly in late (during G2) replicating domains due to DNMT infidelity, potentially resulting from high replicative stress (Teschendorff, 2020). However, in SGBS cells, there was an inconsistency between the extent of PMD demethylation, derived from the EpiCMIT.hypo score, and calculated mitotic cell divisions, derived from the EpiCMIT.hyper score, especially in DHA-treated samples (Fig. 50). DNA maintenance is accomplished by the PCNA/UHRF1/DNMT1/HDAC1/EHMT2 complex (Hervouet et al., 2018), where UHRF1 can recognize either H3K9me2/3 and/or hemimethylated DNA for recruitment of DNMTs (Liu et al., 2013). According to Salbhab *et al.*, in PMDs with extensive demethylation, the associated H3K9me3 mark is maintained or even increased, possibly due to a compensation mechanism (Salhab et al., 2018), providing a requirement for UHRF1 to recruit DNMT1. This indicates the involvement of other regulatory mechanisms on UHRF1 to regulate DNMT1 recruitment. I noticed that samples with the strongest PMD demethylation were associated with higher UHRF1 expression (Supplementary Fig. 7). This could be due to higher proliferation rates, or even take a causal role, as overexpression of UHRF1 in zebrafish was shown to induce DNA demethylation *via* destabilization and delocalization of DNMT1 (Mudbhary et al., 2014). This finding could be a

possible mechanism for PMD demethylation in cancer, where UHRF1 is often overexpressed. However, I cannot tell whether the increase of UHRF1 during SGBS cell cultivation would be sufficient for decreasing DNMT1 activity.

I also observed gradual gain in methylation in PMDs (Fig. 44), which has not yet been described as a common mechanism. As UHRF1 is not dependent on hemimethylated CpGs for DNA methylation maintenance (as H3K9me2/3 is enough for recruiting UHRF1 function), I could envision that PMD demethylation might be recovered if the cellular conditions for proper DNA maintenance are reestablished (Liu et al., 2013).

DNA methylation could be affected due to deregulated histone modifications, with an indirect effect on DNA methylation. For example, in tumors, overexpression of EZH2 *via* the mechanistic target of rapamycin (mTOR) pathway resulted in increased levels of the H3K27me3 mark (Harachi et al., 2020), which could result in increased DNA methylation levels (Cedar and Bergman, 2009). However, in all cultivation experiments, expression of EZH2 was associated with DNMT1 expression (Supplementary Fig. 7) and cell proliferation. As gain in repressive marks was also hypothesized as a compensation mechanism of reduced methylation in PMDs, I could also envision the opposite effect. Therefore, only the combined analysis of DNA methylation and histone modifications would give a better picture of the possible regulatory mechanism.

Finally, I observed not only PMD-associated methylation changes but also a substantial degree of gradual methylation changes in gene-regulatory regions (Fig. 47). TET activity plays an essential role in gene-regulatory regions, as TET competes with DNMTs for the methylation status at CpG islands and enhancer regions (Charlton et al., 2020). In the cultivation experiments, expression of TETs were highest in replicate I of Student 1, and TET2 was associated with DNMT1 expression, suggesting a competition between TET and DNMTs (Supplementary Fig. 7). Environmental factors can also regulate TET activity *via* posttranslational modifications (Bauer et al., 2015) and affect thereby global DNA methylation in cell-type specific enhancer regions. As enhancer-associated demethylation is also highly dependent on cellular signaling, I am not able to attribute changes in enhancer methylation directly to TET activity.

8.1.2 Metabolism and epigenetic regulation

Various mechanisms can mediate effects on the DNA methylation and demethylation machinery *via* metabolic alterations, which could be easily affected by changes in the cultivation medium. Cultivation of SGBS cells was associated with fast medium “consumption”,

and I observed a rapid drop in medium pH during cell culture, indicating the build-up of acidic metabolic metabolites or lactic acid.

Histone and DNA methylation depend on the availability of SAM, which is sustained through the diet or the cell culture medium by methyl donors, such as methionine (Dai et al., 2018; Maddocks et al., 2016; Raboni et al., 2021). In cancer, excessive DNA and histone methylation promote glycolysis, lipogenesis and inhibit gluconeogenesis, suggesting a feed-forward loop between metabolism and epigenetics (Fukano et al., 2021). During severe methyl donor deficiency, first histones are demethylated to maintain DNA methylation as long as possible, making it unlikely that medium fluctuations might have caused methylation changes due to methyl donor deficiency (Ye et al., 2019). The histone and DNA demethylation process is dependent on oxygen (van den Beucken et al., 2014; Prickaerts et al., 2016). Oxygen deficiency in the medium is affected by cell density and medium volume; however, considering the given variables and the environmental oxygen levels of ~ 21 %, it is unlikely that hypoxic levels were reached (Place et al., 2017).

Variabilities in the concentrations of nutrients in the medium by consumption could affect cellular choices of type of energy metabolism mediated *via* epigenetic reprogramming (Fukano et al., 2021). While mature SGBS cells have a high capacity of oxidative phosphorylation and are therefore metabolically flexible, SGBS preadipocytes have four-times decreased oxidative phosphorylation rate (only ~ 15 % of the ATP production), and are therefore depending highly on glycolysis (~ 85 %), resulting in reduced metabolic flexibility (Keuper, 2019). As in all experiments, cells were passaged in the same interval, every 3 - 4 days, all experiments should be affected similarly by fluctuations in nutrient and oxygen availability. However, I cannot exclude that temporal shifts in medium properties or the quality of utilized medium components might have affected the experiments differently.

8.1.3 Signaling-induced cellular identity

Signal transduction is an effective mechanism for reacting to extracellular signals. These extracellular signals act at receptors, leading to transduction by intracellular second messengers to generate a cellular response. Such cellular reactions are carried out by TFs inducing the transcription of target genes, involving DNA demethylation at enhancer regions to achieve a change in cellular identity. A cellular process that has previously been associated with massive changes in DNA methylation is the epithelial-to-mesenchymal transition (EMT) (Pistore et al., 2017). Methylation changes induced by conditioned medium of cancer-associated fibroblasts in a prostate cancer cell line were associated with reduced expression of DNMT1 and UHRF1, and antagonizing the EMT process reverted the methylation changes.

In SGBS cells, all preadipocytes displayed mesenchymal features. However, the samples revealed replicate-specific differences in EMT gene expression. Another more artificial model of EMT is the transition induced by transforming growth factor beta (TGFβ/TGFB1) (Cardenas et al., 2014).

Interestingly, my replicates displayed substantial differences in TGFβ signaling, positively associated with extracellular matrix (ECM) gene expression levels (data not shown) (Hinz, 2015). In ovarian cancer cell lines, TGFβ-induced EMT was also associated with changes in DNA methylation, however at a lower number of CpG sites and was associated with an increase in DNMT levels. Differences in the observed DNA methylation changes between these studies could be dependent on the type of the selected EMT model (conditioned medium vs TGFβ), the starting cell type (prostate vs. ovarian) but not on the detection method, as both used 450k array technology. Furthermore, sources of variability in the TGFβ signaling could be originated by different batches of FBS or differences in acquired cell density (Nallet-Staub et al., 2015). Finally, physical forces can release latent TGFβ from the ECM so that the splitting process could also affect TGFβ signaling.

TGFβ signaling is antagonized by FGF1. FGF1 signaling results in reduced collagen expression (ECM), reverts EMT, and counteracts profibrotic effects (Becerril et al., 1999; Ramos et al., 2006, 2010). As FGF1 is a protein that is added to the cultivation medium of SGBS preadipocyte, samples with high TGFβ signaling could have been cultivated with FGF1 affected by freeze-thaw processes (Jain et al., 2021). The quality of FGF1 protein is currently the best explanation of the observed differences in TGFβ-associated signaling differences and might be a source for the cultivation-associated methylation changes that should be tightly controlled in future experiments with the SGBS cell line.

8.1.4 Lessons learned from cultivating SGBS preadipocytes

With the careful interpretation of the cultivation-associated DNA methylation changes and gene expression differences, I identified methylation changes that might have been due to cell proliferation and or cell culture conditions related to the quality or delivery of FGF1 as an important growth factor for fibroblasts (including preadipocytes). I also identified and discussed culture-associated effects at the gene expression level; however, a systematic analysis is still pending. As DHA-associated methylation differences were nearly all overlapping with cultivation-associated differences, I found it challenging to isolate DHA-specific effects, as they seemed to be overlaid by DHA-indirect effects associated with cultivation. Therefore, it is pivotal to repeat experiments where FGF1 freeze-thaw-associated destabilization is reduced to a minimum. In replicates with functional FGF1 signal, I still observed massive changes in

DNA methylation, particularly in PMDs, suggesting that FGF1 is not the only source of variability. Therefore, a controlled repetition of the long-term cultivation experiments with controlled changes in nutrient supply could be helpful to investigate whether the discussed possible downstream effects on DNA methylation, histone marks, and gene expression can be reproduced experimentally. When DNA methylation stability can be achieved during long-term cultivation, the DHA treatment can be repeated to identify methylation-associated gene regulation and identify DHA-associated TF binding.

Our gene expression data were also affected by cell cultivation, however, to a smaller extent than the methylation data, so I could separate the DHA-associated impact on gene expression from culture effects, as discussed in the following chapters.

8.2 DHA-associated effects in SGBS preadipocytes

Some of the known roles of DHA in the context of metabolic syndrome are the anti-inflammatory and lipid-lowering effects (Albracht-Schulte et al., 2018; Li et al., 2021). DHA executes its bioactive function in several cell types of different organs, such as adipocytes and hepatocytes, though little is known of its role on preadipocytes.

8.2.1 DHA affects *in vitro* and *in vivo* adipocyte differentiation

The best-characterized effect of DHA on preadipocytes is related to its influence on adipocyte differentiation, however, with conflicting results. After long-term cultivation of SGBS preadipocytes with low DHA concentrations, I could not successfully differentiate them to mature adipocytes. Differentiation capacity was affected in the DHA-treated, but also the nonDHA-treated control cells. Increased TGFβ signaling might have inhibited adipocyte differentiation (Choy and Derynck, 2003). To estimate the adipogenic differentiation capacity in SGBS preadipocytes, I analyzed DHA-affected TF activity during adipogenesis and identified pro- and anti-adipogenic effects (Fig. 57).

In several previous studies, DHA was interpreted as an inhibitor of adipogenesis due to the induction of apoptosis (Hanada et al., 2011; Kim et al., 2006). In proliferating AML-1 cells, another human preadipocyte cell line, DHA was delivered at very high concentrations (250 µM) and in DMSO - a delivery system, which does not prevent oxidation of DHA (Hanada et al., 2011). In a different study using murine 3T3-L1 preadipocytes, DHA was delivered to confluent cells and applied during the whole differentiation process at a concentration of 50 and 200 µM,

complexed to BSA in a ratio of DHA:BSA of 4:1, thereby reducing the risk of oxidation (Kim et al., 2006). DHA treatment induced apoptosis and thereby inhibited clonal expansion in a dose-dependent way. As DHA was delivered during adipocyte differentiation – a multi-step process of dynamic chromatin remodeling – it is challenging to mechanistically investigate its effects in more detail, as it can act on several stages. Martins *et al.,* in contrast, delivered 50 µM DHA to confluent 3T3-L1 preadipocytes for 24 h and afterward initiated the differentiation (Martins et al., 2020). This approach resulted in inhibition of adipogenesis by downregulation of PPARG and CIDEC (cell death inducing DFFA like effector C). Similar results were obtained by delivery of DHA during 3T3-L1 differentiation, where adipocyte markers were reduced, accompanied by reduced lipid accumulation (Valli et al., 2018).

In contrast, Madsen *et al.* have shown that DHA increased differentiation of 3T3-L1 cells, and that this effect was dependent on lipoxygenase (LOX) enzymes, which generated DHA metabolites that can act as PPARG agonists (Madsen et al., 2003). By using the same cell line, Hilgendorf *et al*. have observed that preadipocytes possess a primary cilium similar to the *in vivo* situation, where the G protein-coupled receptor (GPCR) free fatty acid receptor 4 (FFAR4/GPR120) is located. DHA acts as a ligand and induces a local elevation of cAMP in the cilium, thereby inducing the adipogenic program (Hilgendorf et al., 2019). In their work, the authors tested the effect of DHA on adipogenesis by titrating the concentrations of insulin, DEX (a synthetic glucocorticoid), and IMBX (a cAMP-elevating agent). They observed that the proadipogenic effect was only visible when they decreased the dose of insulin, DEX, and/or IBMX. This suggests that the substances are partially redundant, e.g., in the function of elevating cAMP levels. The last two studies did not use a synthetic PPARG agonist (rosiglitazone), which could outperform the potential of DHA or its downstream metabolites as PPARG agonist, as rosiglitazone has an extremely high affinity to PPARG (Edvardsson et al., 1999).

In vivo, increased n-3 and n-6 fatty acid levels in SAT correlated with reduced size and an increased number of adipocytes (Garaulet et al., 2006), thereby contributing to improved insulin resistance in mature adipocytes. Todorčević *et al.* reviewed that in mice, most studies reported with the ingestion of n-3 fatty acids, a reduced total fat mass, with reduced adipocyte size and number. However, in this process, the main regulator might not be adipocyte differentiation but decreased hepatic lipogenesis, which creates a reduced flux of lipids to the adipose tissue (Todorčević and Hodson, 2015). Therefore, more studies are necessary to clarify the function of DHA on differentiation and adipocyte function in the contribution of metabolic health.

8.2.2 Anti-inflammatory effect of DHA in preadipocytes

DHA is a well-known anti-inflammatory agent (Djuricic and Calder, 2021; Liput et al., 2021). Accordingly, DHA reduced the expression of genes involved in the TNFα signaling (Fig. 53). In mature adipocytes and adipose tissue, DHA reduced the secretion of proinflammatory cytokines, such as IL-6, TNFα, and MCP-1 (Murumalla et al., 2012). It was shown that DHA acts as an extracellular ligand on FFAR4 to inhibit TNFα signaling (Oh et al., 2010) and therefore prevent TNFα-induced insulin resistance and suppression of adipogenic genes in mature adipocytes (Ruan et al., 2002). Not much is known about the DHA effect in preadipocytes. However, the role of preadipocytes in proinflammatory signaling has been studied. It was shown that the response towards LPS as a proinflammatory stimulus was much higher in preadipocytes than in mature adipocytes (Chung et al., 2006). Therefore, preadipocytes could be crucial contributors to proinflammatory signaling in adipose tissue. LPS activates NFκB and MAPK signaling, resulting in the secretion of MCP-1, which recruits macrophages. The secretion of other proinflammatory cytokines contributes to insulin resistance in mature adipocytes (Gao et al., 2014; Lagathu et al., 2006; Rotter et al., 2003).

In addition to acting on surrounding adipocytes, the reduction of proinflammatory cytokines could affect adipocyte differentiation capacity and display an additional and more indirect effect on differentiation. TNFα and interleukin 1 beta (IL-1b) were shown to inhibit adipogenesis (Gagnon et al., 2013; Isakson et al., 2009). However, conditioned medium of obese adipose tissue containing TNFα, IL-1b, and IL-6 induced adipogenesis in preadipocytes (Renovato-Martins et al., 2020).

Feeding mice with plankton oil rich in n-3 fatty acids reduced the *in vivo* macrophage infiltration in WAT, proinflammatory cytokine levels as well as adipocyte size (Höper et al., 2013). In humans with insulin resistance, dietary intervention with n-3 fatty acids resulted in a reduced number of macrophages in the adipose tissue. Similar to the observation in mice, it also decreased levels of proinflammatory cytokines in plasma (Spencer et al., 2013).

8.2.3 DHA-associated repression of SREBP signaling in preadipocytes

In my gene expression data, the most consistent effect of DHA treatment was the downregulation of SREBF1/2-associated pathways (Fig. 55 + 56). Upon glucose import, SREBP1s are involved in insulin-induced energy storage in form of TGs (lipogenesis), while SREBP2 is more strongly involved in cholesterol metabolism (Horton et al., 1998; Pai et al., 1998). SREBPs are lipid membrane-bound proteins, of which the N-terminus is proteolytically

cleaved and released to the nucleus for TF activity. During adipogenesis, SREBP1 expression highly increases, and enhanced SREBP2 activity is regulated by increased proteolytic activity (Inoue et al., 2001). SREBPs play a vital role in the development of insulin resistance. SREBP is still activated in insulin-resistant cells in the liver and further suppresses insulin signaling by repressing Insulin receptor substrate 2 (IRS-2) transcription (Ide et al., 2004). Also in myocytes, SREBP1c expression correlated with insulin resistance (Mingrone et al., 2003). SREBP2 is involved in hypertrophy of mature adipocytes (Bauer et al., 2011).

The molecular mechanisms of DHA action on SREBP activity have previously been mainly investigated in liver. In a liver cell line, PUFAs with high length and low saturation reduced SREBP1a/c mRNA expression and activity (Hannah et al., 2001). Reduced processing of SREBP1c is mediated by the extracellular binding of DHA to FFAR4. As a downstream effect, AMPK is activated and phosphorylates SREBP1c, which inhibits its proteolytic activation (Deng et al., 2015; Wang et al., 2017). In addition, the cleavage is inhibited by the mTOR pathway (Deng et al., 2015). A more recent study showed that when DHA is incorporated into the lipid membranes of hepatocytes, it can inhibit SREBP1 cleavage. This serves as a negative feedback mechanism, as it reduced PUFA synthesis (Hishikawa et al., 2020).

The contribution of DHA in preventing metabolic syndrome in preadipocytes and adipocytes *via* affecting SREBP TF activity is currently not so clear. Epididymal adipocytes of mice dramatically reduced their lipogenic potential in high fat diet-induced obesity (Sárvári et al., 2021). In adipocytes, PUFAs reduce nuclear SREBP and therefore further inhibit lipogenesis. The mechanism of action on SREBPs was described to be directly mediated by the fatty acid itself or indirectly *via* metabolites produced by cyclooxygenase (COX) enzymes (Madsen et al., 2005). On the one hand, reduced SREBP activity would result in smaller adipocytes and therefore a less hypotrophic phenotype, but also would decrease the energy storage capacity to prevent ectopic lipid accumulation. On the other hand, by reducing SREBP activity, reduced lipogenesis could create a switch from lipogenesis towards fatty acid oxidation and thereby improve the lipid profile and metabolism in adipocytes. One of the metabolic improvements could be increased insulin sensitivity (Albracht-Schulte et al., 2018).

While in adipocytes the function of SREBP and inhibition by DHA have been studied to some extent, even more studies will be needed in the future to understand the contribution of the DHA effect on preadipocytes in the prevention of the metabolic syndrome. Considering that DHA does not act only on a single organ, *in vivo* studies were not always able to clearly point out which tissues mediated the observed effects. Several metabolic effects of DHA could also be strongly modulated in the liver. Here, DHA prevents the activity of insulin-induced SREBP1c activity and thereby inhibits lipogenesis resulting in reducing plasma and hepatic triglycerides

(Deng et al., 2015). Therefore, the *in vivo* reduction of plasma TGs could be a strong confounding factor in increasing insulin sensitivity, as it could overlay the effects of DHA acting directly on the preadipocytes/adipocytes.

9 Conclusion & Outlook Part 2

The effect of DHA has been studied in recent years *in vitro* and *in vivo* in dietary interventions studies, such as in the PATHWAY-27 study. DHA is known to interfere with several layers of disease development, such as the modulation of the inflammatory response (Duan et al., 2021) and the reduction of TG levels in mice, as well as in humans (Martínez-Fernández et al., 2015). In murine studies, there are strong indications that DHA improves other obesity-associated complications such as aberrant glucose and insulin levels. However, there are still conflicting results regarding the effect on insulin sensitivity. The same is the case for findings in humans, where the studies might not have been large enough (Martínez-Fernández et al., 2015). Furthermore, there is high variability in the studies regarding dosage, and combination of n-3 fatty acids, so it is not always possible to precisely attribute the effects to DHA.

Estimations on conversion rates from ALA to DHA suggest that for an ideal supply, adults are dependent on the direct dietary supply of DHA, e.g., by fish oils (Gerster, 1998). However, these estimations have been challenged by questioning the accuracy of the used methods. Furthermore, animals that received a diet without DHA but with the precursor fatty acid ALA had normal DHA levels in the brain (Domenichiello et al., 2015). Similarly, there are indications that vegetarians and vegans with an ALA-rich diet can adapt to their diet and increase conversion rates (Welch et al., 2010). This shows that in healthy individuals conversion rates are highly variable (women have a higher conversion rate than men) but can be modulated to adapt to the biological needs. These adaptations might be inhibited in patients with metabolic syndrome, e.g., by the imbalance in the diet. In the era of diminished fish resources, studying the factors that modulate the conversion rate from ALA to DHA, but also the conversion rates to oxylipins is becoming even more critical. Also, exploring the effects of the DHA metabolites generated by COX, LOX, and CYP enzymes and how their balance affects the development of metabolic syndrome is a currently expanding research field that will help to mechanistically understand the effects of DHA and hopefully provide additional targets for disease modulation.

Metabolic syndrome is a disease with several involved organs and cell types, such as those of the adipose tissue, the liver, and the immune system. Therefore, DHA-associated *in vivo* effects might depend on the interplay of these metabolic organs and immune cells. To better recapitulate the DHA effects mechanistically, e.g., co-cultures between preadipocytes and

macrophages could represent a better model of the inflammatory signaling effects. The tight interconnection of the metabolism and epigenetics suggests that in further studies, in addition to DNA (hydroxy)methylation and gene expression data, the influence on histone marks should be considered, as DHA was shown to reduce the expression of the histone methyltransferase EZH2 in breast cancer cells (Dimri et al., 2010).

In times of COVID-19 pandemics, awareness of healthcare-related topics has fortunately been raised. However, the attention in another ongoing pandemic – obesity, has declined (Hepatology, 2021). Considering the dramatic impact of the COVID-19-associated restrictions on mental health and lifestyle, the expansion of the metabolic syndrome pandemic will continue. Therefore, knowledge on DHA and its function might help us understand how to reverse some of the adverse effects of obesity and its associated metabolic complications, showing us a path towards improved public health.

10 References

Adey, A., Morrison, H.G., Asan, Xun, X., Kitzman, J.O., Turner, E.H., Stackhouse, B., MacKenzie, A.P., Caruccio, N.C., Zhang, X., et al. (2010). Rapid, low-input, low-bias construction of shotgun fragment libraries by high-density in vitro transposition. Genome Biol *11*, R119.

Ahmad, B., Serpell, C.J., Fong, I.L., and Wong, E.H. (2020). Molecular Mechanisms of Adipogenesis: The Anti-adipogenic Role of AMP-Activated Protein Kinase. Front. Mol. Biosci. *7*.

Alberti, K.G.M.M., Zimmet, P., and Shaw, J. (2005). The metabolic syndrome—a new worldwide definition. The Lancet *366*, 1059–1062.

Alberti, K.G.M.M., Zimmet, P., Shaw, J., and Grundy, S.M. (2006). The IDF Consensus Worldwide Definition of the Metabolic Syndrom. https://www.idf.org/component/attachments/attachments.html?id=705&task=download, accessed January 2022.

Albracht-Schulte, K., Kalupahana, N.S., Ramalingam, L., Wang, S., Rahman, S.M., Robert-McComb, J., and Moustaid-Moussa, N. (2018). Omega-3 fatty acids in obesity and metabolic syndrome: a mechanistic update. J. Nutr. Biochem. *58*, 1–16.

Ali, M., Heyob, K., and Rogers, L.K. (2016). DHA Suppresses Primary Macrophage Inflammatory Responses via Notch 1/ Jagged 1 Signaling. Sci. Rep. *6*, 22276.

Ali, M.M., Hassan, C., Masrur, M., Bianco, F.M., Naquiallah, D., Mirza, I., Frederick, P., Fernandes, E.T., Giulianotti, C.P., Gangemi, A., et al. (2021). Adipose Tissue Hypoxia Correlates with Adipokine Hypomethylation and Vascular Dysfunction. Biomedicines *9*, 1034.

Ambele, M.A., Dhanraj, P., Giles, R., and Pepper, M.S. (2020). Adipogenesis: A Complex Interplay of Multiple Molecular Determinants and Pathways. Int. J. Mol. Sci. *21*, 4283.

Amemiya, H.M., Kundaje, A., and Boyle, A.P. (2019). The ENCODE Blacklist: Identification of Problematic Regions of the Genome. Sci Rep *9*, 9354.

Amstutz, P., Andeer, R., Chapman, B., Chilton, J., Crusoe, M.R., Valls Guimerà, R., Carrasco Hernandez, G., Ivkovic, S., Kartashov, A., Kern, J., et al. (2016). Common Workflow Language, draft 3. Figshare.

An, J., Rao, A., and Ko, M. (2017). TET family dioxygenases and DNA demethylation in stem cells and cancers. Exp. Mol. Med. *49*, e323.

Antequera, F., Boyes, J., and Bird, A. (1990). High levels of de novo methylation and altered chromatin structure at CpG islands in cell lines. Cell *62*, 503–514.

Arai, T., Kelly, V.P., Minowa, O., Noda, T., and Nishimura, S. (2006). The study using wild-type and Ogg1 knockout mice exposed to potassium bromate shows no tumor induction despite an extensive accumulation of 8-hydroxyguanine in kidney DNA. Toxicology *221*, 179–186.

Arner, P., Hellström, L., Wahrenberg, H., and Brönnegård, M. (1990). Beta-adrenoceptor expression in human fat cells from different regions. J. Clin. Invest. *86*, 1595–1600.

Assenov, Y., Muller, F., Lutsik, P., Walter, J., Lengauer, T., and Bock, C. (2014). Comprehensive analysis of DNA methylation data with RnBeads. Nat Methods *11*, 1138–1140.

Atlasi, Y., and Stunnenberg, H.G. (2017). The interplay of epigenetic marks during stem cell differentiation and development. Nat. Rev. Genet. *18*, 643–658.

Bachman, M., Uribe-Lewis, S., Yang, X., Williams, M., Murrell, A., and Balasubramanian, S. (2014). 5-Hydroxymethylcytosine is a predominantly stable DNA modification. Nat Chem *6*, 1049–1055.

Balwierz, P.J., Pachkov, M., Arnold, P., Gruber, A.J., Zavolan, M., and van Nimwegen, E. (2014). ISMARA: automated modeling of genomic signals as a democracy of regulatory motifs. Genome Res. *24*, 869–884.

Banani, S.F., Lee, H.O., Hyman, A.A., and Rosen, M.K. (2017). Biomolecular condensates: organizers of cellular biochemistry. Nat. Rev. Mol. Cell Biol. *18*, 285–298.

Bauer, C., Göbel, K., Nagaraj, N., Colantuoni, C., Wang, M., Müller, U., Kremmer, E., Rottach, A., and Leonhardt, H. (2015). Phosphorylation of TET proteins is regulated via O-GlcNAcylation by the O-linked N-acetylglucosamine transferase (OGT). J. Biol. Chem. *290*, 4801–4812.

Bauer, S., Wanninger, J., Schmidhofer, S., Weigert, J., Neumeier, M., Dorn, C., Hellerbrand, C., Zimara, N., Schäffler, A., Aslanidis, C., et al. (2011). Sterol Regulatory Element-Binding Protein 2 (SREBP2) Activation after Excess Triglyceride Storage Induces Chemerin in Hypertrophic Adipocytes. Endocrinology *152*, 26–35.

Bauerle, K.T., Hutson, I., Scheller, E.L., and Harris, C.A. (2018). Glucocorticoid Receptor Signaling Is Not Required for In Vivo Adipogenesis. Endocrinology *159*, 2050–2061.

Bayliak, M., and Lushchak, V. (2020). Pleiotropic effects of alpha-ketoglutarate as a potential anti-ageing agent. Ageing Res. Rev. *66*, 101237.

Becerril, C., Pardo, A., Montaño, M., Ramos, C., Ramírez, R., and Selman, M. (1999). Acidic fibroblast growth factor induces an antifibrogenic phenotype in human lung fibroblasts. Am. J. Respir. Cell Mol. Biol. *20*, 1020–1027.

Behrmann, L., Puller, A.-C., and Horstmann, M. (2014). ZNF423: Transcriptional modulation in development and cancer. Mol. Cell. Oncol. *1*.

Berry, R., Rodeheffer, M.S., Rosen, C.J., and Horowitz, M.C. (2015). Adipose Tissue-Residing Progenitors (Adipocyte Lineage Progenitors and Adipose-Derived Stem Cells (ADSC)). Curr. Mol. Biol. Rep. *1*, 101–109.

van den Beucken, T., Koch, E., Chu, K., Rupaimoole, R., Prickaerts, P., Adriaens, M., Voncken, J.W., Harris, A.L., Buffa, F.M., Haider, S., et al. (2014). Hypoxia promotes stem cell phenotypes and poor prognosis through epigenetic regulation of DICER. Nat. Commun. *5*, 5203.

Bibikova, M., Barnes, B., Tsan, C., Ho, V., Klotzle, B., Le, J.M., Delano, D., Zhang, L., Schroth, G.P., Gunderson, K.L., et al. (2011). High density DNA methylation array with single CpG site resolution. Genomics *98*, 288–295.

Birsoy, K., Chen, Z., and Friedman, J. (2008). Transcriptional regulation of adipogenesis by KLF4. Cell Metab. *7*, 339–347.

Birsoy, K., Berry, R., Wang, T., Ceyhan, O., Tavazoie, S., Friedman, J.M., and Rodeheffer, M.S. (2011). Analysis of gene networks in white adipose tissue development reveals a role for ETS2 in adipogenesis. Development *138*, 4709–4719.

Birsoy, K., Festuccia, W.T., and Laplante, M. (2013). A comparative perspective on lipid storage in animals. J. Cell Sci. *126*, 1541–1552.

Boden, G., and Shulman, G.I. (2002). Free fatty acids in obesity and type 2 diabetes: defining their role in the development of insulin resistance and beta-cell dysfunction. Eur. J. Clin. Invest. *32 Suppl 3*, 14–23.

Boon, R., Silveira, G.G., and Mostoslavsky, R. (2020). Nuclear metabolism and the regulation of the epigenome. Nat Metab.

Booth, M.J., Branco, M.R., Ficz, G., Oxley, D., Krueger, F., Reik, W., and Balasubramanian, S. (2012). Quantitative sequencing of 5-methylcytosine and 5-hydroxymethylcytosine at single-base resolution. Science *336*, 934–937.

Bordoni, A., Di Nunzio, M., Danesi, F., and Biagi, P.L. (2006). Polyunsaturated fatty acids: From diet to binding to ppars and other nuclear receptors. Genes Nutr. *1*, 95–106.

Bordoni, A., Boesch, C., Malpuech-Brugère, C., Orfila, C., and Tomás-Cobos, L. (2019). The role of bioactives in energy metabolism and metabolic syndrome. Proc. Nutr. Soc. *78*, 340–350.

Borkowska, J., Domaszewska-Szostek, A., Kolodziej, P., Wicik, Z., Polosak, J., Buyanovskaya, O., Charzewski, L., Stanczyk, M., Noszczyk, B., and Puzianowska-Kuznicka, M. (2020). Alterations in 5hmC level and genomic distribution in aging-related epigenetic drift in human adipose stem cells. Epigenomics *12*, 423–437.

Brenna, J.T., Salem, N., Sinclair, A.J., Cunnane, S.C., and International Society for the Study of Fatty Acids and Lipids, ISSFAL (2009). alpha-Linolenic acid supplementation and conversion to n-3 long-chain polyunsaturated fatty acids in humans. Prostaglandins Leukot. Essent. Fatty Acids *80*, 85–91.

Breuer, K., Assenov, Y., Lutsik, P., and Plass, C. (2020). Highly portable workflow suite based on the Common Workflow Language for processing of data generated by ChIP-seq, ChIPmentation, Cut&Run, and ACT-seq (Zenodo).

Brown, J.M., Boysen, M.S., Chung, S., Fabiyi, O., Morrison, R.F., Mandrup, S., and McIntosh, M.K. (2004). Conjugated linoleic acid induces human adipocyte delipidation: autocrine/paracrine regulation of MEK/ERK signaling by adipocytokines. J. Biol. Chem. *279*, 26735–26747.

Bruse, N., and Heeringen, S.J. van (2018). GimmeMotifs: an analysis framework for transcription factor motif analysis. BioRxiv 474403.

Buenrostro, J.D., Giresi, P.G., Zaba, L.C., Chang, H.Y., and Greenleaf, W.J. (2013). Transposition of native chromatin for fast and sensitive epigenomic profiling of open chromatin, DNA-binding proteins and nucleosome position. Nat Methods *10*, 1213–1218.

Buenrostro, J.D., Wu, B., Chang, H.Y., and Greenleaf, W.J. (2015). ATAC-seq: A Method for Assaying Chromatin Accessibility Genome-Wide. Curr Protoc Mol Biol *109*, 21 29 1-21 29 9.

Burdge, G. (2004). Alpha-linolenic acid metabolism in men and women: nutritional and biological implications. Curr. Opin. Clin. Nutr. Metab. Care *7*, 137–144.

Burger, L., Gaidatzis, D., Schubeler, D., and Stadler, M.B. (2013). Identification of active regulatory regions from DNA methylation data. Nucleic Acids Res *41*, e155.

Cakouros, D., Hemming, S., Gronthos, K., Liu, R., Zannettino, A., Shi, S., and Gronthos, S. (2019). Specific functions of TET1 and TET2 in regulating mesenchymal cell lineage determination. Epigenetics Chromatin *12*, 3.

Cannon, M.E., Currin, K.W., Young, K.L., Perrin, H.J., Vadlamudi, S., Safi, A., Song, L., Wu, Y., Wabitsch, M., Laakso, M., et al. (2019). Open Chromatin Profiling in Adipose Tissue Marks Genomic Regions with Functional Roles in Cardiometabolic Traits. G3 Bethesda *9*, 2521–2533.

Cao, J.Z., Hains, A.E., and Godley, L.A. (2019). Regulation of 5-Hydroxymethylcytosine Distribution by the TET Enzymes. In The DNA, RNA, and Histone Methylomes, S. Jurga, and J. Barciszewski, eds. (Cham: Springer International Publishing), pp. 229–263.

Cardenas, H., Vieth, E., Lee, J., Segar, M., Liu, Y., Nephew, K.P., and Matei, D. (2014). TGF-β induces global changes in DNA methylation during the epithelial-to-mesenchymal transition in ovarian cancer cells. Epigenetics *9*, 1461–1472.

Carey, B.W., Finley, L.W., Cross, J.R., Allis, C.D., and Thompson, C.B. (2015). Intracellular alpha-ketoglutarate maintains the pluripotency of embryonic stem cells. Nature *518*, 413–416.

Castro-Mondragon, J.A., Jaeger, S., Thieffry, D., Thomas-Chollier, M., and van Helden, J. (2017). RSAT matrix-clustering: dynamic exploration and redundancy reduction of transcription factor binding motif collections. Nucleic Acids Res *45*, e119.

Cedar, H., and Bergman, Y. (2009). Linking DNA methylation and histone modification: patterns and paradigms. Nat. Rev. Genet. *10*, 295–304.

Charlton, J., Jung, E.J., Mattei, A.L., Bailly, N., Liao, J., Martin, E.J., Giesselmann, P., Brändl, B., Stamenova, E.K., Müller, F.-J., et al. (2020). TETs compete with DNMT3 activity in pluripotent cells at thousands of methylated somatic enhancers. Nat. Genet. *52*, 819–827.

Chen, J., Lu, Y., Tian, M., and Huang, Q. (2019). Molecular mechanisms of FOXO1 in adipocyte differentiation. J Mol Endocrinol *62*, R239–R253.

Chen, Y.A., Lemire, M., Choufani, S., Butcher, D.T., Grafodatskaya, D., Zanke, B.W., Gallinger, S., Hudson, T.J., and Weksberg, R. (2013). Discovery of cross-reactive probes and polymorphic CpGs in the Illumina Infinium HumanMethylation450 microarray. Epigenetics *8*, 203–209.

Choy, L., and Derynck, R. (2003). Transforming growth factor-beta inhibits adipocyte differentiation by Smad3 interacting with CCAAT/enhancer-binding protein (C/EBP) and repressing C/EBP transactivation function. J. Biol. Chem. *278*, 9609–9619.

Chung, S., LaPoint, K., Martinez, K., Kennedy, A., Boysen Sandberg, M., and McIntosh, M.K. (2006). Preadipocytes Mediate Lipopolysaccharide-Induced Inflammation and Insulin Resistance in Primary Cultures of Newly Differentiated Human Adipocytes. Endocrinology *147*, 5340–5351.

Cong, B., Zhang, Q., and Cao, X. (2021). The function and regulation of TET2 in innate immunity and inflammation. Protein Cell *12*, 165–173.

Crawford, D.J., Liu, M.Y., Nabel, C.S., Cao, X.J., Garcia, B.A., and Kohli, R.M. (2016). Tet2 Catalyzes Stepwise 5-Methylcytosine Oxidation by an Iterative and de novo Mechanism. J Am Chem Soc *138*, 730–733.

Cristancho, A.G., and Lazar, M.A. (2011). Forming functional fat: a growing understanding of adipocyte differentiation. Nat Rev Mol Cell Biol *12*, 722–734.

Cui, X.L., Nie, J., Ku, J., Dougherty, U., West-Szymanski, D.C., Collin, F., Ellison, C.K., Sieh, L., Ning, Y., Deng, Z., et al. (2020). A human tissue map of 5-hydroxymethylcytosines exhibits tissue specificity through gene and enhancer modulation. Nat Commun *11*, 6161.

Dai, Z., Mentch, S.J., Gao, X., Nichenametla, S.N., and Locasale, J.W. (2018). Methionine metabolism influences genomic architecture and gene expression through H3K4me3 peak width. Nat. Commun. *9*, 1955.

Dai, Z., Ramesh, V., and Locasale, J.W. (2020). The evolving metabolic landscape of chromatin biology and epigenetics. Nat. Rev. Genet. *21*, 737–753.

Deichmann, U. (2016). Epigenetics: The origins and evolution of a fashionable topic. Dev. Biol. *416*, 249–254.

Deng, X., Dong, Q., Bridges, D., Raghow, R., Park, E.A., and Elam, M.B. (2015). Docosahexaenoic acid inhibits proteolytic processing of sterol regulatory element-binding protein-1c (SREBP-1c) via activation of AMP-activated kinase. Biochim. Biophys. Acta BBA - Mol. Cell Biol. Lipids *1851*, 1521–1529.

Di Conza, G., Tsai, C.-H., and Ho, P.-C. (2019). Fifty Shades of α-Ketoglutarate on Cellular Programming. Mol. Cell *76*, 1–3.

Dimri, M., Bommi, P.V., Sahasrabuddhe, A.A., Khandekar, J.D., and Dimri, G.P. (2010). Dietary omega-3 polyunsaturated fatty acids suppress expression of EZH2 in breast cancer cells. Carcinogenesis *31*, 489–495.

Distel, R.J., Ro, H.S., Rosen, B.S., Groves, D.L., and Spiegelman, B.M. (1987). Nucleoprotein complexes that regulate gene expression in adipocyte differentiation: direct participation of c-fos. Cell *49*, 835–844.

Djuricic, I., and Calder, P.C. (2021). Beneficial Outcomes of Omega-6 and Omega-3 Polyunsaturated Fatty Acids on Human Health: An Update for 2021. Nutrients *13*, 2421.

Domenichiello, A., Kitson, A., and Bazinet, R. (2015). Is DHA synthesis from ALA sufficient to supply the adult brain? Prog. Lipid Res. *127*.

Duan, J., Song, Y., Zhang, X., and Wang, C. (2021). Effect of ω-3 Polyunsaturated Fatty Acids-Derived Bioactive Lipids on Metabolic Disorders. Front. Physiol. *12*, 646491.

Dubois-Chevalier, J., Oger, F., Dehondt, H., Firmin, F.F., Gheeraert, C., Staels, B., Lefebvre, P., and Eeckhoute, J. (2014). A dynamic CTCF chromatin binding landscape promotes DNA hydroxymethylation and transcriptional induction of adipocyte differentiation. Nucleic Acids Res *42*, 10943–10959.

Duran-Ferrer, M., Clot, G., Nadeu, F., Beekman, R., Baumann, T., Nordlund, J., Marincevic-Zuniga, Y., Lönnerholm, G., Rivas-Delgado, A., Martin, S., et al. (2020). The proliferative history shapes the DNA methylome of B-cell tumors and predicts clinical outcome. Nat. Cancer *1*, 1066–1081.

Eckel, R.H., Grundy, S.M., and Zimmet, P.Z. (2005). The metabolic syndrome. Lancet Lond. Engl. *365*, 1415–1428.

Ecsedi, S., Rodríguez-Aguilera, J., and Hernandez-Vargas, H. (2018). 5-Hydroxymethylcytosine (5hmC), or How to Identify Your Favorite Cell. Epigenomes *2*, 3.

Edvardsson, U., Bergström, M., Alexandersson, M., Bamberg, K., Ljung, B., and Dahllöf, B. (1999). Rosiglitazone (BRL49653), a PPARγ-selective agonist, causes peroxisome proliferator-like liver effects in obese mice. J. Lipid Res. *40*, 1177–1184.

Enerbäck, S. (2010). Human Brown Adipose Tissue. Cell Metab. *11*, 248–252.

Ernst, J., and Kellis, M. (2012). ChromHMM: automating chromatin-state discovery and characterization. Nat Methods *9*, 215–216.

Esteve Ràfols, M. (2014). Adipose tissue: cell heterogeneity and functional diversity. Endocrinol. Nutr. Organo Soc. Espanola Endocrinol. Nutr. *61*, 100–112.

Ewels, P.A., Peltzer, A., Fillinger, S., Patel, H., Alneberg, J., Wilm, A., Garcia, M.U., Di Tommaso, P., and Nahnsen, S. (2020). The nf-core framework for community-curated bioinformatics pipelines. Nat Biotechnol *38*, 276–278.

Farmer, S.R. (2006). Transcriptional control of adipocyte formation. Cell Metab. *4*, 263–273.

Feldmann, H.M., Golozoubova, V., Cannon, B., and Nedergaard, J. (2009). UCP1 Ablation Induces Obesity and Abolishes Diet-Induced Thermogenesis in Mice Exempt from Thermal Stress by Living at Thermoneutrality. Cell Metab. *9*, 203–209.

Feuerstein-Akgoz, C., Janke, F., Heilmann, J., Kessler, L., Miehle, F., Artati, A., Weichenhan, D., Aviles-Huerta, D., Hey, J, Toth, R., et al. (*in preparation*). Metabolic changes during human adipocyte differentiation promote stable DNA hydroxymethylation and binding of acetylated NEIL1 to adipogenic enhancers.

Fischer-Posovszky, P., Newell, F.S., Wabitsch, M., and Tornqvist, H.E. (2008). Human SGBS cells - a unique tool for studies of human fat cell biology. Obes Facts *1*, 184–189.

Floyd, Z.E., Kilroy, G., Wu, X., and Gimble, J.M. (2007). Effects of prolyl hydroxylase inhibitors on adipogenesis and hypoxia inducible factor 1 alpha levels under normoxic conditions. J Cell Biochem *101*, 1545–1557.

Fujiki, K., Shinoda, A., Kano, F., Sato, R., Shirahige, K., and Murata, M. (2013). PPARgamma-induced PARylation promotes local DNA demethylation by production of 5-hydroxymethylcytosine. Nat Commun *4*, 2262.

Fukano, M., Park, M., and Deblois, G. (2021). Metabolic Flexibility Is a Determinant of Breast Cancer Heterogeneity and Progression. Cancers *13*, 4699.

Gagnon, A., Foster, C., Landry, A., and Sorisky, A. (2013). The role of interleukin 1β in the anti-adipogenic action of macrophages on human preadipocytes. J. Endocrinol. *217*, 197–206.

Gaidatzis, D., Burger, L., Murr, R., Lerch, A., Dessus-Babus, S., Schübeler, D., and Stadler, M.B. (2014). DNA sequence explains seemingly disordered methylation levels in partially methylated domains of Mammalian genomes. PLoS Genet. *10*, e1004143.

Gao, D., Madi, M., Ding, C., Fok, M., Steele, T., Ford, C., Hunter, L., and Bing, C. (2014). Interleukin-1β mediates macrophage-induced impairment of insulin signaling in human primary adipocytes. Am. J. Physiol. Endocrinol. Metab. *307*, E289-304.

Garaulet, M., Hernandez-Morante, J.J., Lujan, J., Tebar, F.J., and Zamora, S. (2006). Relationship between fat cell size and number and fatty acid composition in adipose tissue from different fat depots in overweight/obese humans. Int. J. Obes. *30*, 899–905.

Gerin, I., Bommer, G.T., Lidell, M.E., Cederberg, A., Enerback, S., and Macdougald, O.A. (2009). On the role of FOX transcription factors in adipocyte differentiation and insulin-stimulated glucose uptake. J Biol Chem *284*, 10755–10763.

Gerstein, M.B., Kundaje, A., Hariharan, M., Landt, S.G., Yan, K.K., Cheng, C., Mu, X.J., Khurana, E., Rozowsky, J., Alexander, R., et al. (2012). Architecture of the human regulatory network derived from ENCODE data. Nature *489*, 91–100.

Gerster, H. (1998). Can adults adequately convert alpha-linolenic acid (18:3n-3) to eicosapentaenoic acid (20:5n-3) and docosahexaenoic acid (22:6n-3)? Int. J. Vitam. Nutr. Res. Int. Z. Vitam.- Ernahrungsforschung J. Int. Vitaminol. Nutr. *68*, 159–173.

Ghaben, A.L., and Scherer, P.E. (2019). Adipogenesis and metabolic health. Nat Rev Mol Cell Biol *20*, 242–258.

Ginno, P.A., Gaidatzis, D., Feldmann, A., Hoerner, L., Imanci, D., Burger, L., Zilbermann, F., Peters, A., Edenhofer, F., Smallwood, S.A., et al. (2020). A genome-scale map of DNA methylation turnover identifies site-specific dependencies of DNMT and TET activity. Nat Commun *11*, 2680.

Gregoire, F.M., Smas, C.M., and Sul, H.S. (1998). Understanding Adipocyte Differentiation. Physiol. Rev. *78*, 783–809.

Griffin, M.J., Zhou, Y., Kang, S., Zhang, X., Mikkelsen, T.S., and Rosen, E.D. (2013). Early B-cell factor-1 (EBF1) is a key regulator of metabolic and inflammatory signaling pathways in mature adipocytes. J Biol Chem *288*, 35925–35939.

Gross, J.A., Pacis, A., Chen, G.G., Drupals, M., Lutz, P.E., Barreiro, L.B., and Turecki, G. (2017). Gene-body 5-hydroxymethylation is associated with gene expression changes in the prefrontal cortex of depressed individuals. Transl Psychiatry *7*, e1119.

GTEx Consortium (2020). The GTEx Consortium atlas of genetic regulatory effects across human tissues. Science *369*, 1318–1330.

Gu, Z., Gu, L., Eils, R., Schlesner, M., and Brors, B. (2014). circlize Implements and enhances circular visualization in R. Bioinformatics *30*, 2811–2812.

Gu, Z., Eils, R., and Schlesner, M. (2016). Complex heatmaps reveal patterns and correlations in multidimensional genomic data. Bioinforma. Oxf. Engl. *32*, 2847–2849.

Gu, Z., Eils, R., Schlesner, M., and Ishaque, N. (2018). EnrichedHeatmap: an R/Bioconductor package for comprehensive visualization of genomic signal associations. BMC Genomics *19*, 234.

Guelen, L., Pagie, L., Brasset, E., Meuleman, W., Faza, M.B., Talhout, W., Eussen, B.H., de Klein, A., Wessels, L., de Laat, W., et al. (2008). Domain organization of human chromosomes revealed by mapping of nuclear lamina interactions. Nature *453*, 948–951.

Gupta, R.K., Mepani, R.J., Kleiner, S., Lo, J.C., Khandekar, M.J., Cohen, P., Frontini, A., Bhowmick, D.C., Ye, L., Cinti, S., et al. (2012). Zfp423 Expression Identifies Committed Preadipocytes and Localizes to Adipose Endothelial and Perivascular Cells. Cell Metab. *15*, 230–239.

Hanada, H., Morikawa, K., Hirota, K., Nonaka, M., and Umehara, Y. (2011). Induction of apoptosis and lipogenesis in human preadipocyte cell line by n-3 PUFAs. Cell Biol. Int. *35*, 51–59.

Hanahan, D. (2022). Hallmarks of Cancer: New Dimensions. Cancer Discov. *12*, 31–46.

Hannah, V.C., Ou, J., Luong, A., Goldstein, J.L., and Brown, M.S. (2001). Unsaturated fatty acids down-regulate srebp isoforms 1a and 1c by two mechanisms in HEK-293 cells. J. Biol. Chem. *276*, 4365–4372.

Hansen, J.C., Maeshima, K., and Hendzel, M.J. (2021). The solid and liquid states of chromatin. Epigenetics Chromatin *14*, 50.

Harachi, M., Masui, K., Honda, H., Muragaki, Y., Kawamata, T., Cavenee, W.K., Mischel, P.S., and Shibata, N. (2020). Dual Regulation of Histone Methylation by mTOR Complexes Controls Glioblastoma Tumor Cell Growth via EZH2 and SAM. Mol. Cancer Res. MCR *18*, 1142–1152.

Haws, S.A., Leech, C.M., and Denu, J.M. (2020). Metabolism and the Epigenome: A Dynamic Relationship. Trends Biochem Sci *45*, 731–747.

Hegde, M.L., Hegde, P.M., Bellot, L.J., Mandal, S.M., Hazra, T.K., Li, G.M., Boldogh, I., Tomkinson, A.E., and Mitra, S. (2013). Prereplicative repair of oxidized bases in the human genome is mediated by NEIL1 DNA glycosylase together with replication proteins. Proc Natl Acad Sci U A *110*, E3090-9.

Hepatology, T.L.G.& (2021). Obesity: another ongoing pandemic. Lancet Gastroenterol. Hepatol. *6*, 411.

Hervouet, E., Peixoto, P., Delage-Mourroux, R., Boyer-Guittaut, M., and Cartron, P.-F. (2018). Specific or not specific recruitment of DNMTs for DNA methylation, an epigenetic dilemma. Clin. Epigenetics *10*, 17.

Hilgendorf, K.I., Johnson, C.T., Mezger, A., Rice, S.L., Norris, A.M., Demeter, J., Greenleaf, W.J., Reiter, J.F., Kopinke, D., and Jackson, P.K. (2019). Omega-3 Fatty Acids Activate Ciliary FFAR4 to Control Adipogenesis. Cell *179*, 1289-1305.e21.

Hinz, B. (2015). The extracellular matrix and transforming growth factor-β1: Tale of a strained relationship. Matrix Biol. *47*, 54–65.

Hishikawa, D., Yanagida, K., Nagata, K., Kanatani, A., Iizuka, Y., Hamano, F., Yasuda, M., Okamura, T., Shindou, H., and Shimizu, T. (2020). Hepatic Levels of DHA-Containing Phospholipids Instruct SREBP1-Mediated Synthesis and Systemic Delivery of Polyunsaturated Fatty Acids. IScience *23*, 101495.

Höper, A.C., Salma, W., Khalid, A.M., Hafstad, A.D., Sollie, S.J., Raa, J., Larsen, T.S., and Aasum, E. (2013). Oil from the marine zooplankton Calanus finmarchicus improves the cardiometabolic phenotype of diet-induced obese mice. Br. J. Nutr. *110*, 2186–2193.

Horton, J.D., Shimomura, I., Brown, M.S., Hammer, R.E., Goldstein, J.L., and Shimano, H. (1998). Activation of cholesterol synthesis in preference to fatty acid synthesis in liver and

adipose tissue of transgenic mice overproducing sterol regulatory element-binding protein-2. J. Clin. Invest. *101*, 2331–2339.

Huang, P.L. (2009). A comprehensive definition for metabolic syndrome. Dis. Model. Mech. *2*, 231–237.

Hudish, L.I., Reusch, J.E.B., and Sussel, L. (2019). β Cell dysfunction during progression of metabolic syndrome to type 2 diabetes. J. Clin. Invest. *129*, 4001–4008.

Ide, T., Shimano, H., Yahagi, N., Matsuzaka, T., Nakakuki, M., Yamamoto, T., Nakagawa, Y., Takahashi, A., Suzuki, H., Sone, H., et al. (2004). SREBPs suppress IRS-2-mediated insulin signalling in the liver. Nat. Cell Biol. *6*, 351–357.

Inoue, J., Kumagai, H., Terada, T., Maeda, M., Shimizu, M., and Sato, R. (2001). Proteolytic activation of SREBPs during adipocyte differentiation. Biochem. Biophys. Res. Commun. *283*, 1157–1161.

Isakson, P., Hammarstedt, A., Gustafson, B., and Smith, U. (2009). Impaired preadipocyte differentiation in human abdominal obesity: role of Wnt, tumor necrosis factor-alpha, and inflammation. Diabetes *58*, 1550–1557.

Ito, S., Shen, L., Dai, Q., Wu, S.C., Collins, L.B., Swenberg, J.A., He, C., and Zhang, Y. (2011). Tet proteins can convert 5-methylcytosine to 5-formylcytosine and 5-carboxylcytosine. Science *333*, 1300–1303.

Iurlaro, M., Ficz, G., Oxley, D., Raiber, E.A., Bachman, M., Booth, M.J., Andrews, S., Balasubramanian, S., and Reik, W. (2013). A screen for hydroxymethylcytosine and formylcytosine binding proteins suggests functions in transcription and chromatin regulation. Genome Biol *14*, R119.

Jain, K., Salamat-Miller, N., and Taylor, K. (2021). Freeze–thaw characterization process to minimize aggregation and enable drug product manufacturing of protein based therapeutics. Sci. Rep. *11*, 11332.

Janke, F. (2021). Genome-wide epigenomic analyses of cell-free DNA from anaplastic lymphoma kinase-rearranged non-small cell lung cancer patients [Unpublished doctoral dissertation]. University of Heidelberg.

Jensen, M.D. (2020). Visceral Fat. Endocrinol. Metab. Clin. North Am. *49*, 229–237.

Johnson, R., Spiegelman, B., Hanahan, D., and Wisdom, R. (1996). Cellular transformation and malignancy induced by ras require c-jun. Mol Cell Biol *16*, 4504–4511.

Juan, D., Perner, J., Pau, E.C.D., Marsili, S., Ochoa, D., Chung, H.R., Vingron, M., Rico, D., and Valencia, A. (2016). Epigenomic Co-localization and Co-evolution Reveal a Key Role for 5hmC as a Communication Hub in the Chromatin Network of ESCs. Cell Rep. *14*, 1246–1257.

Kangaspeska, S., Stride, B., Métivier, R., Polycarpou-Schwarz, M., Ibberson, D., Carmouche, R.P., Benes, V., Gannon, F., and Reid, G. (2008). Transient cyclical methylation of promoter DNA. Nature *452*, 112–115.

Katada, S., Imhof, A., and Sassone-Corsi, P. (2012). Connecting Threads: Epigenetics and Metabolism. Cell *148*, 24–28.

Kaya-Okur, H.S., Janssens, D.H., Henikoff, J.G., Ahmad, K., and Henikoff, S. (2020). Efficient low-cost chromatin profiling with CUT&Tag. Nat. Protoc. *15*, 3264–3283.

Kent, W.J., Sugnet, C.W., Furey, T.S., Roskin, K.M., Pringle, T.H., Zahler, A.M., and Haussler, D. (2002). The human genome browser at UCSC. Genome Res *12*, 996–1006.

Keuper, M. (2019). On the role of macrophages in the control of adipocyte energy metabolism. Endocr. Connect. *8*, R105–R121.

Kiihl, S.F., Martinez-Garrido, M.J., Domingo-Relloso, A., Bermudez, J., and Tellez-Plaza, M. (2019). MLML2R: an R package for maximum likelihood estimation of DNA methylation and hydroxymethylation proportions. Stat Appl Genet Mol Biol *18*.

Killian, J.K., Kim, S.Y., Miettinen, M., Smith, C., Merino, M., Tsokos, M., Quezado, M., Smith, W.I., Jahromi, M.S., Xekouki, P., et al. (2013). Succinate dehydrogenase mutation underlies global epigenomic divergence in gastrointestinal stromal tumor. Cancer Discov. *3*, 648–657.

Kim, M., and Costello, J. (2017). DNA methylation: an epigenetic mark of cellular memory. Exp. Mol. Med. *49*, e322–e322.

Kim, H.-K., Della-Fera, M., Lin, J., and Baile, C.A. (2006). Docosahexaenoic acid inhibits adipocyte differentiation and induces apoptosis in 3T3-L1 preadipocytes. J. Nutr. *136*, 2965–2969.

Klusóczki, Á., Veréb, Z., Vámos, A., Fischer-Posovszky, P., Wabitsch, M., Bacso, Z., Fésüs, L., and Kristóf, E. (2019). Differentiating SGBS adipocytes respond to PPARγ stimulation, irisin and BMP7 by functional browning and beige characteristics. Sci. Rep. *9*, 5823.

Kuda, O., Rossmeisl, M., and Kopecky, J. (2018). Omega-3 fatty acids and adipose tissue biology. Mol. Aspects Med. *64*, 147–160.

Kumar, L., and E. Futschik M (2007). Mfuzz: a software package for soft clustering of microarray data. Bioinformation *2*, 5–7.

Lafontan, M., and Girard, J. (2008). Impact of visceral adipose tissue on liver metabolism. Part I: heterogeneity of adipose tissue and functional properties of visceral adipose tissue. Diabetes Metab. *34*, 317–327.

Lagathu, C., Yvan-Charvet, L., Bastard, J.-P., Maachi, M., Quignard-Boulangé, A., Capeau, J., and Caron, M. (2006). Long-term treatment with interleukin-1beta induces insulin resistance in murine and human adipocytes. Diabetologia *49*, 2162–2173.

Langmead, B., and Salzberg, S.L. (2012). Fast gapped-read alignment with Bowtie 2. Nat Methods *9*, 357–359.

Laudes, M., Christodoulides, C., Sewter, C., Rochford, J.J., Considine, R.V., Sethi, J.K., Vidal-Puig, A., and O'Rahilly, S. (2004). Role of the POZ zinc finger transcription factor FBI-1 in human and murine adipogenesis. J. Biol. Chem. *279*, 11711–11718.

Lee, D.S., Choi, H., Han, B.S., Kim, W.K., Lee, S.C., Oh, K.J., and Bae, K.H. (2016). c-Jun regulates adipocyte differentiation via the KLF15-mediated mode. Biochem Biophys Res Commun *469*, 552–558.

Lee, J.N., Song, B., DeBose-Boyd, R.A., and Ye, J. (2006). Sterol-regulated Degradation of Insig-1 Mediated by the Membrane-bound Ubiquitin Ligase gp78*. J. Biol. Chem. *281*, 39308–39315.

Lemieux, I., Pascot, A., Couillard, C., Lamarche, B., Tchernof, A., Alméras, N., Bergeron, J., Gaudet, D., Tremblay, G., Prud'homme, D., et al. (2000). Hypertriglyceridemic waist: A marker

of the atherogenic metabolic triad (hyperinsulinemia; hyperapolipoprotein B; small, dense LDL) in men? Circulation *102*, 179–184.

Lenighan, Y.M., McNulty, B.A., and Roche, H.M. (2019). Dietary fat composition: replacement of saturated fatty acids with PUFA as a public health strategy, with an emphasis on α-linolenic acid. Proc. Nutr. Soc. *78*, 234–245.

Li, E., Bestor, T.H., and Jaenisch, R. (1992). Targeted mutation of the DNA methyltransferase gene results in embryonic lethality. Cell *69*, 915–926.

Li, G., Li, Y., Xiao, B., Cui, D., Lin, Y., Zeng, J., Li, J., Cao, M.-J., and Liu, J. (2021). Antioxidant Activity of Docosahexaenoic Acid (DHA) and Its Regulatory Roles in Mitochondria. J. Agric. Food Chem. *69*, 1647–1655.

Li, H., Handsaker, B., Wysoker, A., Fennell, T., Ruan, J., Homer, N., Marth, G., Abecasis, G., Durbin, R., and Genome Project Data Processing, S. (2009). The Sequence Alignment/Map format and SAMtools. Bioinformatics *25*, 2078–2079.

Liao, Y., Wang, J., Jaehnig, E.J., Shi, Z., and Zhang, B. (2019). WebGestalt 2019: gene set analysis toolkit with revamped UIs and APIs. Nucleic Acids Res. *47*, W199–W205.

Linton, M.F., Yancey, P.G., Davies, S.S., Jerome, W.G., Linton, E.F., Song, W.L., Doran, A.C., and Vickers, K.C. (2000). The Role of Lipids and Lipoproteins in Atherosclerosis. In Endotext, K.R. Feingold, B. Anawalt, A. Boyce, G. Chrousos, W.W. de Herder, K. Dhatariya, K. Dungan, A. Grossman, J.M. Hershman, J. Hofland, et al., eds. (South Dartmouth (MA): MDText.com, Inc.).

Liput, K.P., Lepczyński, A., Ogłuszka, M., Nawrocka, A., Poławska, E., Grzesiak, A., Ślaska, B., Pareek, C.S., Czarnik, U., and Pierzchała, M. (2021). Effects of Dietary n–3 and n–6 Polyunsaturated Fatty Acids in Inflammation and Cancerogenesis. Int. J. Mol. Sci. *22*, 6965.

Lister, R., Pelizzola, M., Dowen, R.H., Hawkins, R.D., Hon, G., Tonti-Filippini, J., Nery, J.R., Lee, L., Ye, Z., Ngo, Q.M., et al. (2009). Human DNA methylomes at base resolution show widespread epigenomic differences. Nature *462*, 315–322.

Lister, R., Pelizzola, M., Kida, Y.S., Hawkins, R.D., Nery, J.R., Hon, G., Antosiewicz-Bourget, J., O'Malley, R., Castanon, R., Klugman, S., et al. (2011). Hotspots of aberrant epigenomic reprogramming in human induced pluripotent stem cells. Nature *471*, 68–73.

Liu, C.-S., Toth, R., Bakr, A., Goyal, A., Islam, M.S., Breuer, K., Mayakonda, A., Lin, Y.-Y., Stepper, P., Jurkowski, T.P., et al. (2021). Epigenetic Modulation of Radiation-Induced Diacylglycerol Kinase Alpha Expression Prevents Pro-Fibrotic Fibroblast Response. Cancers *13*, 2455.

Liu, X., Gao, Q., Li, P., Zhao, Q., Zhang, J., Li, J., Koseki, H., and Wong, J. (2013). UHRF1 targets DNMT1 for DNA methylation through cooperative binding of hemi-methylated DNA and methylated H3K9. Nat. Commun. *4*, 1563.

Livak, K.J., and Schmittgen, T.D. (2001). Analysis of relative gene expression data using real-time quantitative PCR and the 2(-Delta Delta C(T)) Method. Methods *25*, 402–408.

Locke, W.J., Guanzon, D., Ma, C., Liew, Y.J., Duesing, K.R., Fung, K.Y.C., and Ross, J.P. (2019). DNA Methylation Cancer Biomarkers: Translation to the Clinic. Front. Genet. *10*.

Longo, M., Zatterale, F., Naderi, J., Parrillo, L., Formisano, P., Raciti, G.A., Beguinot, F., and Miele, C. (2019). Adipose Tissue Dysfunction as Determinant of Obesity-Associated Metabolic Complications. Int J Mol Sci *20*, 2358.

Lu, X., Zhao, B.S., and He, C. (2015). TET Family Proteins: Oxidation Activity, Interacting Molecules, and Functions in Diseases. Chem. Rev. *115*, 2225–2239.

Lun, A.T., and Smyth, G.K. (2016). csaw: a Bioconductor package for differential binding analysis of ChIP-seq data using sliding windows. Nucleic Acids Res *44*, e45.

Lyu, Y., Su, X., Deng, J., Liu, S., Zou, L., Zhao, X., Wei, S., Geng, B., and Xu, G. (2015). Defective differentiation of adipose precursor cells from lipodystrophic mice lacking perilipin 1. PLoS One *10*, e0117536.

Ma, X., and Kang, S. (2019). Functional Implications of DNA Methylation in Adipose Biology. Diabetes *68*, 871–878.

Macotela, Y., Emanuelli, B., Mori, M.A., Gesta, S., Schulz, T.J., Tseng, Y.-H., and Kahn, C.R. (2012). Intrinsic Differences in Adipocyte Precursor Cells From Different White Fat Depots. Diabetes *61*, 1691–1699.

Maddocks, O.D.K., Labuschagne, C.F., Adams, P.D., and Vousden, K.H. (2016). Serine Metabolism Supports the Methionine Cycle and DNA/RNA Methylation through De Novo ATP Synthesis in Cancer Cells. Mol. Cell *61*, 210–221.

Madsen, L., Petersen, R.K., Sørensen, M.B., Jørgensen, C., Hallenborg, P., Pridal, L., Fleckner, J., Amri, E.-Z., Krieg, P., Furstenberger, G., et al. (2003). Adipocyte differentiation of 3T3-L1 preadipocytes is dependent on lipoxygenase activity during the initial stages of the differentiation process. Biochem. J. *375*, 539–549.

Madsen, L., Petersen, R.K., and Kristiansen, K. (2005). Regulation of adipocyte differentiation and function by polyunsaturated fatty acids. Biochim. Biophys. Acta BBA - Mol. Basis Dis. *1740*, 266–286.

Markert, J., and Luger, K. (2021). Nucleosomes Meet Their Remodeler Match. Trends Biochem. Sci. *46*, 41–50.

Martin, M. (2011). Cutadapt removes adapter sequences from high-throughput sequencing reads. EMBnet.Journal *17*, 3.

Martínez-Fernández, L., Laiglesia, L.M., Huerta, A.E., Martínez, J.A., and Moreno-Aliaga, M.J. (2015). Omega-3 fatty acids and adipose tissue function in obesity and metabolic syndrome. Prostaglandins Other Lipid Mediat. *121*, 24–41.

Martinez-Reyes, I., and Chandel, N.S. (2020). Mitochondrial TCA cycle metabolites control physiology and disease. Nat Commun *11*, 102.

Martins, F.F., Aguila, M.B., and Mandarim-de-Lacerda, C.A. (2020). Eicosapentaenoic and docosapentaenoic acids lessen the expression of PPARγ/Cidec affecting adipogenesis in cultured 3T3-L1 adipocytes. Acta Histochem. *122*, 151504.

Mendonca, A., Chang, E.H., Liu, W., and Yuan, C. (2014). Hydroxymethylation of DNA influences nucleosomal conformation and stability in vitro. Biochim Biophys Acta *1839*, 1323–1329.

Métivier, R., Gallais, R., Tiffoche, C., Le Péron, C., Jurkowska, R.Z., Carmouche, R.P., Ibberson, D., Barath, P., Demay, F., Reid, G., et al. (2008a). Cyclical DNA methylation of a transcriptionally active promoter. Nature *452*, 45–50.

Métivier, R., Gallais, R., Tiffoche, C., Le Péron, C., Jurkowska, R.Z., Carmouche, R.P., Ibberson, D., Barath, P., Demay, F., Reid, G., et al. (2008b). Cyclical DNA methylation of a transcriptionally active promoter. Nature *452*, 45–50.

Miehle, F., Moller, G., Cecil, A., Lintelmann, J., Wabitsch, M., Tokarz, J., Adamski, J., and Haid, M. (2020). Lipidomic Phenotyping Reveals Extensive Lipid Remodeling during Adipogenesis in Human Adipocytes. Metabolites *10*, 217.

Mikkelsen, T.S., Xu, Z., Zhang, X., Wang, L., Gimble, J.M., Lander, E.S., and Rosen, E.D. (2010). Comparative epigenomic analysis of murine and human adipogenesis. Cell *143*, 156–169.

Mingrone, G., Rosa, G., Greco, A.V., Manco, M., Vega, N., Nanni, G., Castagneto, M., and Vidal, H. (2003). Intramyocitic lipid accumulation and SREBP-1c expression are related to insulin resistance and cardiovascular risk in morbid obesity. Atherosclerosis *170*, 155–161.

Miranda, P.J., DeFronzo, R.A., Califf, R.M., and Guyton, J.R. (2005). Metabolic syndrome: definition, pathophysiology, and mechanisms. Am. Heart J. *149*, 33–45.

Miranda, T.B., Cortez, C.C., Yoo, C.B., Liang, G., Abe, M., Kelly, T.K., Marquez, V.E., and Jones, P.A. (2009). DZNep is a global histone methylation inhibitor that reactivates developmental genes not silenced by DNA methylation. Mol. Cancer Ther. *8*, 1579–1588.

Moellmann, J., Klinkhammer, B.M., Droste, P., Kappel, B., Haj-Yehia, E., Maxeiner, S., Artati, A., Adamski, J., Boor, P., Schutt, K., et al. (2020). Empagliflozin improves left ventricular diastolic function of db/db mice. Biochim Biophys Acta Mol Basis Dis *1866*, 165807.

Morgan, M.A.J., and Shilatifard, A. (2020). Reevaluating the roles of histone-modifying enzymes and their associated chromatin modifications in transcriptional regulation. Nat. Genet. *52*, 1271–1281.

Morigny, P., Houssier, M., Mouisel, E., and Langin, D. (2016). Adipocyte lipolysis and insulin resistance. Biochimie *125*, 259–266.

Motohashi, H., and Igarashi, K. (2010). MafB as a type I interferon rheostat. Nat. Immunol. *11*, 695–696.

Mudbhary, R., Hoshida, Y., Chernyavskaya, Y., Jacob, V., Villanueva, A., Fiel, M.I., Chen, X., Kojima, K., Thung, S., Bronson, R.T., et al. (2014). UHRF1 Overexpression Drives DNA Hypomethylation and Hepatocellular Carcinoma. Cancer Cell *25*, 196–209.

Müller, U., Bauer, C., Siegl, M., Rottach, A., and Leonhardt, H. (2014). TET-mediated oxidation of methylcytosine causes TDG or NEIL glycosylase dependent gene reactivation. Nucleic Acids Res. *42*.

Murumalla, R.K., Gunasekaran, M.K., Padhan, J.K., Bencharif, K., Gence, L., Festy, F., Césari, M., Roche, R., and Hoareau, L. (2012). Fatty acids do not pay the toll: effect of SFA and PUFA on human adipose tissue and mature adipocytes inflammation. Lipids Health Dis. *11*, 175.

Nallet-Staub, F., Yin, X., Gilbert, C., Marsaud, V., Ben Mimoun, S., Javelaud, D., Leof, E.B., and Mauviel, A. (2015). Cell Density Sensing Alters TGF-β Signaling in a Cell-Type-Specific Manner, Independent from Hippo Pathway Activation. Dev. Cell *32*, 640–651.

Nanduri, R. (2021). Epigenetic Regulators of White Adipocyte Browning. Epigenomes *5*, 3.

Nicholls, D.G., and Locke, R.M. (1984). Thermogenic mechanisms in brown fat. Physiol. Rev. *64*, 1–64.

Nicoletti, C., Nonino, C., Oliveira, B., Pinhel, M., Mansego, M., Milagro, F., Zulet, M., and Alfredo, M. (2015). DNA Methylation and Hydroxymethylation Levels in Relation to Two Weight Loss Strategies: Energy-Restricted Diet or Bariatric Surgery. Obes. Surg. *26*.

Noer, A., Sørensen, A.L., Boquest, A.C., and Collas, P. (2006). Stable CpG hypomethylation of adipogenic promoters in freshly isolated, cultured, and differentiated mesenchymal stem cells from adipose tissue. Mol. Biol. Cell *17*, 3543–3556.

Oh, D.Y., Talukdar, S., Bae, E.J., Imamura, T., Morinaga, H., Fan, W., Li, P., Lu, W.J., Watkins, S.M., and Olefsky, J.M. (2010). GPR120 is an omega-3 fatty acid receptor mediating potent anti-inflammatory and insulin-sensitizing effects. Cell *142*, 687–698.

Okano, M., Bell, D.W., Haber, D.A., and Li, E. (1999). DNA methyltransferases Dnmt3a and Dnmt3b are essential for de novo methylation and mammalian development. Cell *99*, 247–257.

Ouwens, D.M., Sell, H., Greulich, S., and Eckel, J. (2010). The role of epicardial and perivascular adipose tissue in the pathophysiology of cardiovascular disease. J. Cell. Mol. Med. *14*, 2223–2234.

Pageaud, Y., Plass, C., and Assenov, Y. (2018). Enrichment analysis with EpiAnnotator. Bioinformatics *34*, 1781–1783.

Pai, J.T., Guryev, O., Brown, M.S., and Goldstein, J.L. (1998). Differential stimulation of cholesterol and unsaturated fatty acid biosynthesis in cells expressing individual nuclear sterol regulatory element-binding proteins. J. Biol. Chem. *273*, 26138–26148.

Peláez-García, A., Barderas, R., Batlle, R., Viñas-Castells, R., Bartolomé, R.A., Torres, S., Mendes, M., Lopez-Lucendo, M., Mazzolini, R., Bonilla, F., et al. (2015). A proteomic analysis reveals that Snail regulates the expression of the nuclear orphan receptor Nuclear Receptor Subfamily 2 Group F Member 6 (Nr2f6) and interleukin 17 (IL-17) to inhibit adipocyte differentiation. Mol. Cell. Proteomics MCP *14*, 303–315.

Pettersson, A.M.L., Acosta, J.R., Björk, C., Krätzel, J., Stenson, B., Blomqvist, L., Viguerie, N., Langin, D., Arner, P., and Laurencikiene, J. (2015). MAFB as a novel regulator of human adipose tissue inflammation. Diabetologia *58*, 2115–2123.

Pfeifer, G.P., and Szabo, P.E. (2018). Gene body profiles of 5-hydroxymethylcytosine: potential origin, function and use as a cancer biomarker. Epigenomics *10*, 1029–1032.

Pfeifer, G.P., Szabó, P.E., and Song, J. (2019). Protein Interactions at Oxidized 5-Methylcytosine Bases. J. Mol. Biol. S0022-2836(19)30501-7.

Phillips, J.E., and Corces, V.G. (2009). CTCF: master weaver of the genome. Cell *137*, 1194–1211.

Pistore, C., Giannoni, E., Colangelo, T., Rizzo, F., Magnani, E., Muccillo, L., Giurato, G., Mancini, M., Rizzo, S., Riccardi, M., et al. (2017). DNA methylation variations are required for epithelial-to-mesenchymal transition induced by cancer-associated fibroblasts in prostate cancer cells. Oncogene *36*, 5551–5566.

Place, T.L., Domann, F.E., and Case, A.J. (2017). Limitations of oxygen delivery to cells in culture: An underappreciated problem in basic and translational research. Free Radic. Biol. Med. *113*, 311–322.

Plourde, M., and Cunnane, S.C. (2007). Extremely limited synthesis of long chain polyunsaturates in adults: implications for their dietary essentiality and use as supplements. Appl. Physiol. Nutr. Metab. Physiol. Appl. Nutr. Metab. *32*, 619–634.

Prakash, A., Doublié, S., and Wallace, S.S. (2012). Chapter 4 - The Fpg/Nei Family of DNA Glycosylases: Substrates, Structures, and Search for Damage. In Progress in Molecular Biology and Translational Science, P.W. Doetsch, ed. (Academic Press), pp. 71–91.

Prickaerts, P., Adriaens, M.E., Beucken, T. van den, Koch, E., Dubois, L., Dahlmans, V.E.H., Gits, C., Evelo, C.T.A., Chan-Seng-Yue, M., Wouters, B.G., et al. (2016). Hypoxia increases genome-wide bivalent epigenetic marking by specific gain of H3K27me3. Epigenetics Chromatin *9*, 46.

Raboni, S., Montalbano, S., Stransky, S., Garcia, B.A., Buschini, A., Bettati, S., Sidoli, S., and Mozzarelli, A. (2021). A Key Silencing Histone Mark on Chromatin Is Lost When Colorectal Adenocarcinoma Cells Are Depleted of Methionine by Methionine γ-Lyase. Front. Mol. Biosci. *8*, 735303.

Raghavan, S., Winter, P.S., Navia, A.W., Williams, H.L., DenAdel, A., Lowder, K.E., Galvez-Reyes, J., Kalekar, R.L., Mulugeta, N., Kapner, K.S., et al. (2021). Microenvironment drives cell state, plasticity, and drug response in pancreatic cancer. Cell *184*, 6119-6137.e26.

Ramirez, F., Ryan, D.P., Gruning, B., Bhardwaj, V., Kilpert, F., Richter, A.S., Heyne, S., Dundar, F., and Manke, T. (2016). deepTools2: a next generation web server for deep-sequencing data analysis. Nucleic Acids Res *44*, W160-5.

Ramos, C., Montaño, M., Becerril, C., Cisneros-Lira, J., Barrera, L., Ruíz, V., Pardo, A., and Selman, M. (2006). Acidic fibroblast growth factor decreases alpha-smooth muscle actin expression and induces apoptosis in human normal lung fibroblasts. Am. J. Physiol. Lung Cell. Mol. Physiol. *291*, L871-879.

Ramos, C., Becerril, C., Montaño, M., García-De-Alba, C., Ramírez, R., Checa, M., Pardo, A., and Selman, M. (2010). FGF-1 reverts epithelial-mesenchymal transition induced by TGF-{beta}1 through MAPK/ERK kinase pathway. Am. J. Physiol. Lung Cell. Mol. Physiol. *299*, L222-231.

Rauch, A., Haakonsson, A.K., Madsen, J.G.S., Larsen, M., Forss, I., Madsen, M.R., Van Hauwaert, E.L., Wiwie, C., Jespersen, N.Z., Tencerova, M., et al. (2019). Osteogenesis depends on commissioning of a network of stem cell transcription factors that act as repressors of adipogenesis. Nat. Genet. *51*, 716–727.

Rausch, J., Gillespie, S., Orchard, T., Tan, A., and McDaniel, J.C. (2021). Systematic review of marine-derived omega-3 fatty acid supplementation effects on leptin, adiponectin, and the leptin-to-adiponectin ratio. Nutr. Res. *85*, 135–152.

Reik, W. (2007). Stability and flexibility of epigenetic gene regulation in mammalian development. Nature *447*, 425–432.

Reisinger, E., Genthner, L., Kerssemakers, J., Kensche, P., Borufka, S., Jugold, A., Kling, A., Prinz, M., Scholz, I., Zipprich, G., et al. (2017). OTP: An automatized system for managing and processing NGS data. J Biotechnol *261*, 53–62.

Renovato-Martins, M., Moreira-Nunes, C., Atella, G.C., Barja-Fidalgo, C., and de Moraes, J.A. (2020). Obese Adipose Tissue Secretion Induces Inflammation in Preadipocytes: Role of Toll-Like Receptor-4. Nutrients *12*, 2828.

Richard, A.J., and Stephens, J.M. (2014). The role of JAK-STAT signaling in adipose tissue function. Biochim. Biophys. Acta-Mol. Basis Dis. *1842*, 431–439.

Roadmap Epigenomics, C., Kundaje, A., Meuleman, W., Ernst, J., Bilenky, M., Yen, A., Heravi-Moussavi, A., Kheradpour, P., Zhang, Z., Wang, J., et al. (2015). Integrative analysis of 111 reference human epigenomes. Nature *518*, 317–330.

Robinson, M.D., McCarthy, D.J., and Smyth, G.K. (2010). edgeR: a Bioconductor package for differential expression analysis of digital gene expression data. Bioinformatics *26*, 139–140.

Rohde, K., Keller, M., Stumvoll, M., Dietrich, A., Blüher, M., and Böttcher, Y. (2015). DNA 5-hydroxymethylation in human adipose tissue differs between subcutaneous and visceral adipose tissue depots. Epigenomics *7*, 911–920.

Rolseth, V., Luna, L., Olsen, A.K., Suganthan, R., Scheffler, K., Neurauter, C.G., Esbensen, Y., Kusnierczyk, A., Hildrestrand, G.A., Graupner, A., et al. (2017). No cancer predisposition or increased spontaneous mutation frequencies in NEIL DNA glycosylases-deficient mice. Sci Rep *7*, 4384.

Rose, N.R., McDonough, M.A., King, O.N.F., Kawamura, A., and Schofield, C.J. (2011). Inhibition of 2-oxoglutarate dependent oxygenases. Chem. Soc. Rev. *40*, 4364–4397.

Rotter, V., Nagaev, I., and Smith, U. (2003). Interleukin-6 (IL-6) induces insulin resistance in 3T3-L1 adipocytes and is, like IL-8 and tumor necrosis factor-alpha, overexpressed in human fat cells from insulin-resistant subjects. J. Biol. Chem. *278*, 45777–45784.

Ruan, H., Hacohen, N., Golub, T.R., Van Parijs, L., and Lodish, H.F. (2002). Tumor necrosis factor-alpha suppresses adipocyte-specific genes and activates expression of preadipocyte genes in 3T3-L1 adipocytes: nuclear factor-kappaB activation by TNF-alpha is obligatory. Diabetes *51*, 1319–1336.

Salhab, A., Nordström, K., Gasparoni, G., Kattler, K., Ebert, P., Ramirez, F., Arrigoni, L., Müller, F., Polansky, J.K., Cadenas, C., et al. (2018). A comprehensive analysis of 195 DNA methylomes reveals shared and cell-specific features of partially methylated domains. Genome Biol. *19*, 150.

Sampath, H., and Ntambi, J.M. (2004). Polyunsaturated fatty acid regulation of gene expression. Nutr. Rev. *62*, 333–339.

Sampath, H., Batra, A.K., Vartanian, V., Carmical, J.R., Prusak, D., King, I.B., Lowell, B., Earley, L.F., Wood, T.G., Marks, D.L., et al. (2011). Variable penetrance of metabolic phenotypes and development of high-fat diet-induced adiposity in NEIL1-deficient mice. Am J Physiol Endocrinol Metab *300*, E724-34.

Sárvári, A.K., Van Hauwaert, E.L., Markussen, L.K., Gammelmark, E., Marcher, A.-B., Ebbesen, M.F., Nielsen, R., Brewer, J.R., Madsen, J.G.S., and Mandrup, S. (2021). Plasticity of Epididymal Adipose Tissue in Response to Diet-Induced Obesity at Single-Nucleus Resolution. Cell Metab. *33*, 437-453.e5.

Schaffert, A., Krieg, L., Weiner, J., Schlichting, R., Ueberham, E., Karkossa, I., Bauer, M., Landgraf, K., Junge, K.M., Wabitsch, M., et al. (2021). Alternatives for the worse: Molecular

insights into adverse effects of bisphenol a and substitutes during human adipocyte differentiation. Environ. Int. *156*, 106730.

Schmidt, S.F., Jorgensen, M., Chen, Y., Nielsen, R., Sandelin, A., and Mandrup, S. (2011). Cross species comparison of C/EBPalpha and PPARgamma profiles in mouse and human adipocytes reveals interdependent retention of binding sites. BMC Genomics *12*, 152.

Schmidt, S.F., Larsen, B.D., Loft, A., Nielsen, R., Madsen, J.G., and Mandrup, S. (2015). Acute TNF-induced repression of cell identity genes is mediated by NFkappaB-directed redistribution of cofactors from super-enhancers. Genome Res *25*, 1281–1294.

SeahorseBioscience (n.d.). Preparation of Bovine Serum Albumin-Palmitate conjugate for XF24 FAO Assays. http://www.wklab.org/wp-content/uploads/2016/02/Palmitate-BSA_Prep_SOP_v080624.pdf, accessed January 2022.

Sengupta, S., Yang, C., Hegde, M.L., Hegde, P.M., Mitra, J., Pandey, A., Dutta, A., Datarwala, A.T., Bhakat, K.K., and Mitra, S. (2018). Acetylation of oxidized base repair-initiating NEIL1 DNA glycosylase required for chromatin-bound repair complex formation in the human genome increases cellular resistance to oxidative stress. DNA Repair Amst *66–67*, 1–10.

Serandour, A.A., Avner, S., Oger, F., Bizot, M., Percevault, F., Lucchetti-Miganeh, C., Palierne, G., Gheeraert, C., Barloy-Hubler, F., Peron, C.L., et al. (2012). Dynamic hydroxymethylation of deoxyribonucleic acid marks differentiation-associated enhancers. Nucleic Acids Res *40*, 8255–8265.

Severin, P.M.D., Zou, X., Schulten, K., and Gaub, H.E. (2013). Effects of cytosine hydroxymethylation on DNA strand separation. Biophys. J. *104*, 208–215.

Shin, Y., and Brangwynne, C.P. (2017). Liquid phase condensation in cell physiology and disease. Science *357*, eaaf4382.

Shipony, Z., Mukamel, Z., Cohen, N.M., Landan, G., Chomsky, E., Zeliger, S.R., Fried, Y.C., Ainbinder, E., Friedman, N., and Tanay, A. (2014). Dynamic and static maintenance of epigenetic memory in pluripotent and somatic cells. Nature *513*, 115–119.

Siersbaek, R., and Mandrup, S. (2011). Transcriptional networks controlling adipocyte differentiation. Cold Spring Harb Symp Quant Biol *76*, 247–255.

Skehan, P., Storeng, R., Scudiero, D., Monks, A., McMahon, J., Vistica, D., Warren, J.T., Bokesch, H., Kenney, S., and Boyd, M.R. (1990a). New colorimetric cytotoxicity assay for anticancer-drug screening. J. Natl. Cancer Inst. *82*, 1107–1112.

Skehan, P.A., Storeng, R., Scudiero, D., Monks, A., McMahon, J., Vistica, D. ;J, Warren, J., Bokesch, H., Kenney, S., and Boyd, M. (1990b). New Colorimetric Cytotoxicity Assay for Anticancer-Drug Screening. J. Natl. Cancer Inst. *82*, 1107–1112.

Slenter, D.N., Kutmon, M., Hanspers, K., Riutta, A., Windsor, J., Nunes, N., Melius, J., Cirillo, E., Coort, S.L., Digles, D., et al. (2018). WikiPathways: a multifaceted pathway database bridging metabolomics to other omics research. Nucleic Acids Res *46*, D661–D667.

Slyvka, A., Mierzejewska, K., and Bochtler, M. (2017). Nei-like 1 (NEIL1) excises 5-carboxylcytosine directly and stimulates TDG-mediated 5-formyl and 5-carboxylcytosine excision. Sci Rep *7*, 9001.

Smiraglia, D.J., Rush, L.J., Frühwald, M.C., Dai, Z., Held, W.A., Costello, J.F., Lang, J.C., Eng, C., Li, B., Wright, F.A., et al. (2001). Excessive CpG island hypermethylation in cancer cell lines versus primary human malignancies. Hum. Mol. Genet. *10*, 1413–1419.

Sobhy, H., Kumar, R., Lewerentz, J., Lizana, L., and Stenberg, P. (2019). Highly interacting regions of the human genome are enriched with enhancers and bound by DNA repair proteins. Sci Rep *9*, 4577.

Song, C.X., Szulwach, K.E., Fu, Y., Dai, Q., Yi, C., Li, X., Li, Y., Chen, C.H., Zhang, W., Jian, X., et al. (2011). Selective chemical labeling reveals the genome-wide distribution of 5-hydroxymethylcytosine. Nat Biotechnol *29*, 68–72.

Song, C.X., Yin, S., Ma, L., Wheeler, A., Chen, Y., Zhang, Y., Liu, B., Xiong, J., Zhang, W., Hu, J., et al. (2017). 5-Hydroxymethylcytosine signatures in cell-free DNA provide information about tumor types and stages. Cell Res *27*, 1231–1242.

Spalding, K.L., Arner, E., Westermark, P.O., Bernard, S., Buchholz, B.A., Bergmann, O., Blomqvist, L., Hoffstedt, J., Näslund, E., Britton, T., et al. (2008). Dynamics of fat cell turnover in humans. Nature *453*, 783–787.

Spencer, M., Finlin, B.S., Unal, R., Zhu, B., Morris, A.J., Shipp, L.R., Lee, J., Walton, R.G., Adu, A., Erfani, R., et al. (2013). Omega-3 fatty acids reduce adipose tissue macrophages in human subjects with insulin resistance. Diabetes *62*, 1709–1717.

Spruijt, C.G., Gnerlich, F., Smits, A.H., Pfaffeneder, T., Jansen, P.W., Bauer, C., Munzel, M., Wagner, M., Muller, M., Khan, F., et al. (2013). Dynamic readers for 5-(hydroxy)methylcytosine and its oxidized derivatives. Cell *152*, 1146–1159.

Stadler, M.B., Murr, R., Burger, L., Ivanek, R., Lienert, F., Scholer, A., van Nimwegen, E., Wirbelauer, C., Oakeley, E.J., Gaidatzis, D., et al. (2011). DNA-binding factors shape the mouse methylome at distal regulatory regions. Nature *480*, 490–495.

Steger, D.J., and Lazar, M.A. (2011). Adipogenic hotspots: where the action is: Adipogenic hotspots. EMBO J. *30*, 1418–1419.

Sun, L., Zhang, H., and Gao, P. (2021). Metabolic reprogramming and epigenetic modifications on the path to cancer. Protein Cell.

Symonds, M.E. (2017). Adipose Tissue Biology (Springer).

Tahiliani, M., Koh, K.P., Shen, Y., Pastor, W.A., Bandukwala, H., Brudno, Y., Agarwal, S., Iyer, L.M., Liu, D.R., Aravind, L., et al. (2009). Conversion of 5-methylcytosine to 5-hydroxymethylcytosine in mammalian DNA by MLL partner TET1. Science *324*, 930–935.

Tan, C.Y., and Vidal-Puig, A. (2008). Adipose tissue expandability: the metabolic problems of obesity may arise from the inability to become more obese. Biochem. Soc. Trans. *36*, 935–940.

Tang, W., Zeve, D., Suh, J.M., Bosnakovski, D., Kyba, M., Hammer, R.E., Tallquist, M.D., and Graff, J.M. (2008). White fat progenitor cells reside in the adipose vasculature. Science *322*, 583–586.

Tchkonia, T., Giorgadze, N., Pirtskhalava, T., Thomou, T., DePonte, M., Koo, A., Forse, R.A., Chinnappan, D., Martin-Ruiz, C., Zglinicki, T. von, et al. (2006). Fat Depot–Specific Characteristics Are Retained in Strains Derived From Single Human Preadipocytes. Diabetes *55*, 2571–2578.

Teschendorff, A.E. (2020). A comparison of epigenetic mitotic-like clocks for cancer risk prediction. Genome Med. *12*, 56.

Teschendorff, A.E., Marabita, F., Lechner, M., Bartlett, T., Tegner, J., Gomez-Cabrero, D., and Beck, S. (2013). A beta-mixture quantile normalization method for correcting probe design bias in Illumina Infinium 450 k DNA methylation data. Bioinformatics *29*, 189–196.

Teven, C.M., Liu, X., Hu, N., Tang, N., Kim, S.H., Huang, E., Yang, K., Li, M., Gao, J.-L., Liu, H., et al. (2011). Epigenetic regulation of mesenchymal stem cells: a focus on osteogenic and adipogenic differentiation. Stem Cells Int. *2011*, 201371.

Tian, Q., Zhao, J., Yang, Q., Wang, B., Deavila, J.M., Zhu, M.J., and Du, M. (2020). Dietary alpha-ketoglutarate promotes beige adipogenesis and prevents obesity in middle-aged mice. Aging Cell *19*, e13059.

Timp, W., Bravo, H.C., McDonald, O.G., Goggins, M., Umbricht, C., Zeiger, M., Feinberg, A.P., and Irizarry, R.A. (2014). Large hypomethylated blocks as a universal defining epigenetic alteration in human solid tumors. Genome Med. *6*, 61.

Tiwari, U., and Cummins, E. (2011). Meta-analysis of the effect of β-glucan intake on blood cholesterol and glucose levels. Nutr. Burbank Los Angel. Cty. Calif *27*, 1008–1016.

Todorčević, M., and Hodson, L. (2015). The Effect of Marine Derived n-3 Fatty Acids on Adipose Tissue Metabolism and Function. J. Clin. Med. *5*, 3.

Tran, K.-V., Gealekman, O., Frontini, A., Zingaretti, M.C., Morroni, M., Giordano, A., Smorlesi, A., Perugini, J., De Matteis, R., Sbarbati, A., et al. (2012). The Vascular Endothelium of the Adipose Tissue Gives Rise to Both White and Brown Fat Cells. Cell Metab. *15*, 222–229.

Tsagaratou, A., Äijö, T., Lio, C.-W.J., Yue, X., Huang, Y., Jacobsen, S.E., Lähdesmäki, H., and Rao, A. (2014). Dissecting the dynamic changes of 5-hydroxymethylcytosine in T-cell development and differentiation. Proc. Natl. Acad. Sci. *111*, E3306–E3315.

Uhlen, M., Fagerberg, L., Hallstrom, B.M., Lindskog, C., Oksvold, P., Mardinoglu, A., Sivertsson, A., Kampf, C., Sjostedt, E., Asplund, A., et al. (2015). Proteomics. Tissue-based map of the human proteome. Science *347*, 1260419.

Unger, R.H. (2003). Lipid overload and overflow: metabolic trauma and the metabolic syndrome. Trends Endocrinol. Metab. TEM *14*, 398–403.

van der Vaart, J.I., Boon, M.R., and Houtkooper, R.H. (2021). The Role of AMPK Signaling in Brown Adipose Tissue Activation. Cells *10*, 1122.

Valli, V., Heilmann, K., Danesi, F., Bordoni, A., and Gerhäuser, C. (2018). Modulation of Adipocyte Differentiation and Proadipogenic Gene Expression by Sulforaphane, Genistein, and Docosahexaenoic Acid as a First Step to Counteract Obesity. Oxid. Med. Cell. Longev. *2018*, 1617202.

Vartanian, V., Lowell, B., Minko, I.G., Wood, T.G., Ceci, J.D., George, S., Ballinger, S.W., Corless, C.L., McCullough, A.K., and Lloyd, R.S. (2006). The metabolic syndrome resulting from a knockout of the NEIL1 DNA glycosylase. Proc Natl Acad Sci U A *103*, 1864–1869.

Vegiopoulos, A., Rohm, M., and Herzig, S. (2017). Adipose tissue: between the extremes. EMBO J. *36*, 1999–2017.

Verboven, K., Wouters, K., Gaens, K., Hansen, D., Bijnen, M., Wetzels, S., Stehouwer, C.D., Goossens, G.H., Schalkwijk, C.G., Blaak, E.E., et al. (2018). Abdominal subcutaneous and visceral adipocyte size, lipolysis and inflammation relate to insulin resistance in male obese humans. Sci. Rep. *8*, 4677.

Wabitsch, M., Brenner, R.E., Melzner, I., Braun, M., Moller, P., Heinze, E., Debatin, K.M., and Hauner, H. (2001). Characterization of a human preadipocyte cell strain with high capacity for adipose differentiation. Int J Obes Relat Metab Disord *25*, 8–15.

Waddington, C.H. (1942). The epigenotype. Int. J. Epidemiol. *18*.

Waki, H., Nakamura, M., Yamauchi, T., Wakabayashi, K., Yu, J., Hirose-Yotsuya, L., Take, K., Sun, W., Iwabu, M., Okada-Iwabu, M., et al. (2011). Global mapping of cell type-specific open chromatin by FAIRE-seq reveals the regulatory role of the NFI family in adipocyte differentiation. PLoS Genet *7*, e1002311.

Walker, G.E., Marzullo, P., Ricotti, R., Bona, G., and Prodam, F. (2014). The pathophysiology of abdominal adipose tissue depots in health and disease. Horm. Mol. Biol. Clin. Investig. *19*, 57–74.

Wang, H., Maurano, M.T., Qu, H., Varley, K.E., Gertz, J., Pauli, F., Lee, K., Canfield, T., Weaver, M., Sandstrom, R., et al. (2012a). Widespread plasticity in CTCF occupancy linked to DNA methylation. Genome Res. *22*, 1680–1688.

Wang, J., Zhuang, J., Iyer, S., Lin, X., Whitfield, T.W., Greven, M.C., Pierce, B.G., Dong, X., Kundaje, A., Cheng, Y., et al. (2012b). Sequence features and chromatin structure around the genomic regions bound by 119 human transcription factors. Genome Res *22*, 1798–1812.

Wang, J., Zhuang, J., Iyer, S., Lin, X.Y., Greven, M.C., Kim, B.H., Moore, J., Pierce, B.G., Dong, X., Virgil, D., et al. (2013). Factorbook.org: a Wiki-based database for transcription factor-binding data generated by the ENCODE consortium. Nucleic Acids Res *41*, D171-6.

Wang, M., Zhang, X., Ma, L.-J., Feng, R.-B., Yan, C., Su, H., He, C., Kang, J.X., Liu, B., and Wan, J.-B. (2017). Omega-3 polyunsaturated fatty acids ameliorate ethanol-induced adipose hyperlipolysis: A mechanism for hepatoprotective effect against alcoholic liver disease. Biochim. Biophys. Acta BBA - Mol. Basis Dis. *1863*, 3190–3201.

Welch, A.A., Shakya-Shrestha, S., Lentjes, M.A.H., Wareham, N.J., and Khaw, K.-T. (2010). Dietary intake and status of n-3 polyunsaturated fatty acids in a population of fish-eating and non-fish-eating meat-eaters, vegetarians, and vegans and the product-precursor ratio [corrected] of α-linolenic acid to long-chain n-3 polyunsaturated fatty acids: results from the EPIC-Norfolk cohort. Am. J. Clin. Nutr. *92*, 1040–1051.

Wen, L., Li, X., Tan, Y., li, R., Zhao, Y., Wang, Y., Xie, J., Zhang, Y., Song, C., Yu, M., et al. (2014). Whole-genome analysis of 5-hydroxymethylcytosine and 5-methylcytosine at base resolution in the human brain. Genome Biol. *15*, R49.

Wiehle, L., Raddatz, G., Musch, T., Dawlaty, M.M., Jaenisch, R., Lyko, F., and Breiling, A. (2016). Tet1 and Tet2 Protect DNA Methylation Canyons against Hypermethylation. Mol. Cell. Biol. *36*, 452–461.

Williams, K., Christensen, J., and Helin, K. (2011). DNA methylation: TET proteins-guardians of CpG islands? EMBO Rep. *13*, 28–35.

World Health Organization (2021). Obesity and overweight fact sheet. https://www.who.int/news-room/fact-sheets/detail/obesity-and-overweight, accessed January 2022

Wu, H., and Zhang, Y. (2014). Reversing DNA methylation: mechanisms, genomics, and biological functions. Cell *156*, 45–68.

Wu, X., and Zhang, Y. (2017). TET-mediated active DNA demethylation: mechanism, function and beyond. Nat Rev Genet *18*, 517–534.

Wu, D., Hu, D., Chen, H., Shi, G., Fetahu, I.S., Wu, F., Rabidou, K., Fang, R., Tan, L., Xu, S., et al. (2018). Glucose-regulated phosphorylation of TET2 by AMPK reveals a pathway linking diabetes to cancer. Nature *559*, 637–641.

Wu, H., D'Alessio, A.C., Ito, S., Xia, K., Wang, Z., Cui, K., Zhao, K., Sun, Y.E., and Zhang, Y. (2011). Dual functions of Tet1 in transcriptional regulation in mouse embryonic stem cells. Nature *473*, 389–393.

Xia, J., Psychogios, N., Young, N., and Wishart, D.S. (2009). MetaboAnalyst: a web server for metabolomic data analysis and interpretation. Nucleic Acids Res *37*, W652-60.

Yang, C., Sengupta, S., Hegde, P.M., Mitra, J., Jiang, S., Holey, B., Sarker, A.H., Tsai, M.S., Hegde, M.L., and Mitra, S. (2017). Regulation of oxidized base damage repair by chromatin assembly factor 1 subunit A. Nucleic Acids Res *45*, 739–748.

Yang, H., Lin, H., Xu, H., Zhang, L., Cheng, L., Wen, B., Shou, J., Guan, K., Xiong, Y., and Ye, D. (2014). TET-catalyzed 5-methylcytosine hydroxylation is dynamically regulated by metabolites. Cell Res. *24*, 1017–1020.

Yang, Q., Liang, X., Sun, X., Zhang, L., Fu, X., Rogers, C.J., Berim, A., Zhang, S., Wang, S., Wang, B., et al. (2016). AMPK/α-Ketoglutarate Axis Dynamically Mediates DNA Demethylation in the Prdm16 Promoter and Brown Adipogenesis. Cell Metab. *24*, 542–554.

Ye, C., Sutter, B.M., Wang, Y., Kuang, Z., Zhao, X., Yu, Y., and Tu, B.P. (2019). Demethylation of the Protein Phosphatase PP2A Promotes Demethylation of Histones to Enable Their Function as a Methyl Group Sink. Mol. Cell *73*, 1115-1126.e6.

Ye, D., Guan, K.L., and Xiong, Y. (2018). Metabolism, Activity, and Targeting of D- and L-2-Hydroxyglutarates. Trends Cancer *4*, 151–165.

Yeung, A.W.K., Tzvetkov, N.T., El-Tawil, O.S., Bungău, S.G., Abdel-Daim, M.M., and Atanasov, A.G. (2019). Antioxidants: Scientific Literature Landscape Analysis. Oxid. Med. Cell. Longev. *2019*, 8278454.

Yoo, Y., Park, J.H., Weigel, C., Liesenfeld, D.B., Weichenhan, D., Plass, C., Seo, D.G., Lindroth, A.M., and Park, Y.J. (2017). TET-mediated hydroxymethylcytosine at the Ppargamma locus is required for initiation of adipogenic differentiation. Int. J. Obes. *41*, 652–659.

Yu, P., Ji, L., Lee, K.J., Yu, M., He, C., Ambati, S., McKinney, E.C., Jackson, C., Baile, C.A., Schmitz, R.J., et al. (2016). Subsets of Visceral Adipose Tissue Nuclei with Distinct Levels of 5-Hydroxymethylcytosine. PLOS ONE *11*, e0154949.

Yuan, H., and Zhao, C. (2011). 3T3-L1 Cell Line Revealing Partially White Adipogenesis of Mice. Asian J. Anim. Vet. Adv. *6*, 482–487.

Zhang, J.W., Klemm, D.J., Vinson, C., and Lane, M.D. (2004). Role of CREB in transcriptional regulation of CCAAT/enhancer-binding protein beta gene during adipogenesis. J Biol Chem *279*, 4471–4478.

Zhang, Y., Liu, T., Meyer, C.A., Eeckhoute, J., Johnson, D.S., Bernstein, B.E., Nusbaum, C., Myers, R.M., Brown, M., Li, W., et al. (2008). Model-based analysis of ChIP-Seq (MACS). Genome Biol *9*, R137.

Zhang, Y.W., Wang, Z., Xie, W., Cai, Y., Xia, L., Easwaran, H., Luo, J., Yen, R.-W.C., Li, Y., and Baylin, S.B. (2017). Acetylation Enhances TET2 Function in Protecting against Abnormal DNA Methylation during Oxidative Stress. Mol. Cell *65*, 323–335.

Zhou, W., Triche, T.J., Laird, P.W., and Shen, H. (2018). SeSAMe: reducing artifactual detection of DNA methylation by Infinium BeadChips in genomic deletions. Nucleic Acids Res. *46*, e123.

Zhou, X., Lindsay, H., and Robinson, M.D. (2014). Robustly detecting differential expression in RNA sequencing data using observation weights. Nucleic Acids Res. *42*, e91.

Zwick, R.K., Guerrero-Juarez, C.F., Horsley, V., and Plikus, M.V. (2018). Anatomical, Physiological, and Functional Diversity of Adipose Tissue. Cell Metab. *27*, 68–83.

11 Appendix

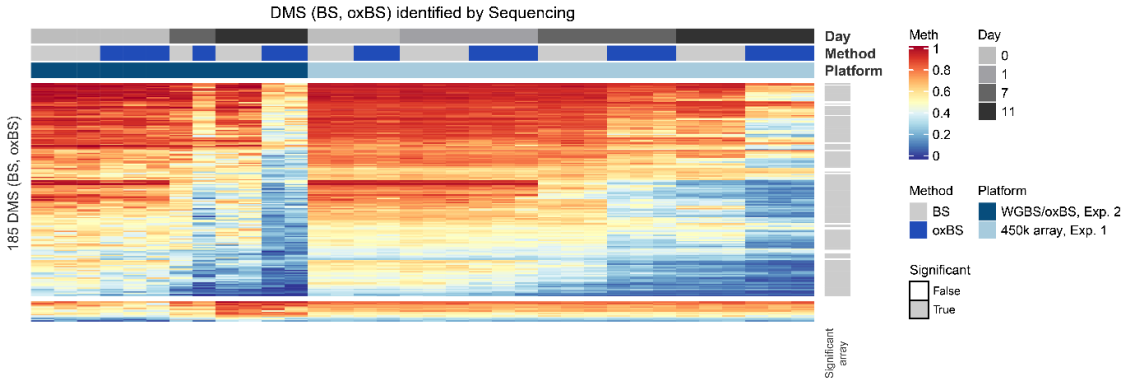

Supplementary Fig. 1| Validation of differentially methylated sites by 450k array. Heatmap depicts methylation proportions of differentially methylated sites (DMS) identified by whole-genome bisulfite (WGBS)/oxidative bisulfite (oxBS) sequencing in experiment 2 (mean methylation difference > 0.25, *p* value < 0.005, and difference between each sample to the mean of the other group > 0.15) that overlap with sites covered on 450k arrays in experiment 1. The last column at the right indicates in grey whether a CpG site was a DMS in BS/oxBS 450k analyses (mean proportion difference > 0.1 and the Mann-Whitney U (MWU) *p* value < 0.05). Experiment 2 was performed by LK, experiment 1, WGBS/oxBS library generation and data analysis performed by myself (CFA). See Fig. 7 for experimental design. Meth: methylation.

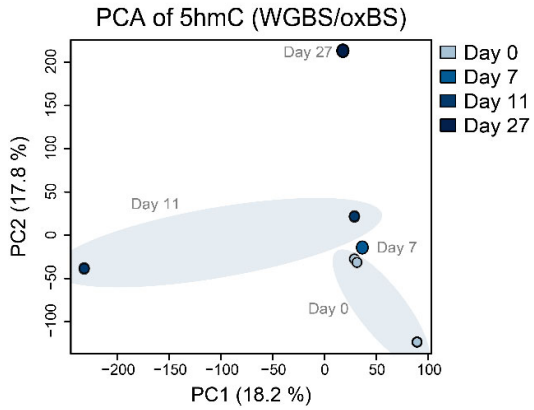

Supplementary Fig. 2| PCA of WGBS/oxBS-derived hydroxymethylation levels. Principal component analysis (PCA) of hydroxymethylation data calculated from whole-genome bisulfite (WGBS) and oxidative bisulfite (oxBS) sequencing data of experiment 2 at day 0 (n = 3), 7 (n = 1), 11 (n = 2) and 27 (n = 1). Experiment 2 was performed by LK, WGBS/oxBS library generation, and data analysis performed by myself (CFA). See Fig. 7 for experimental design. Meth: methylation

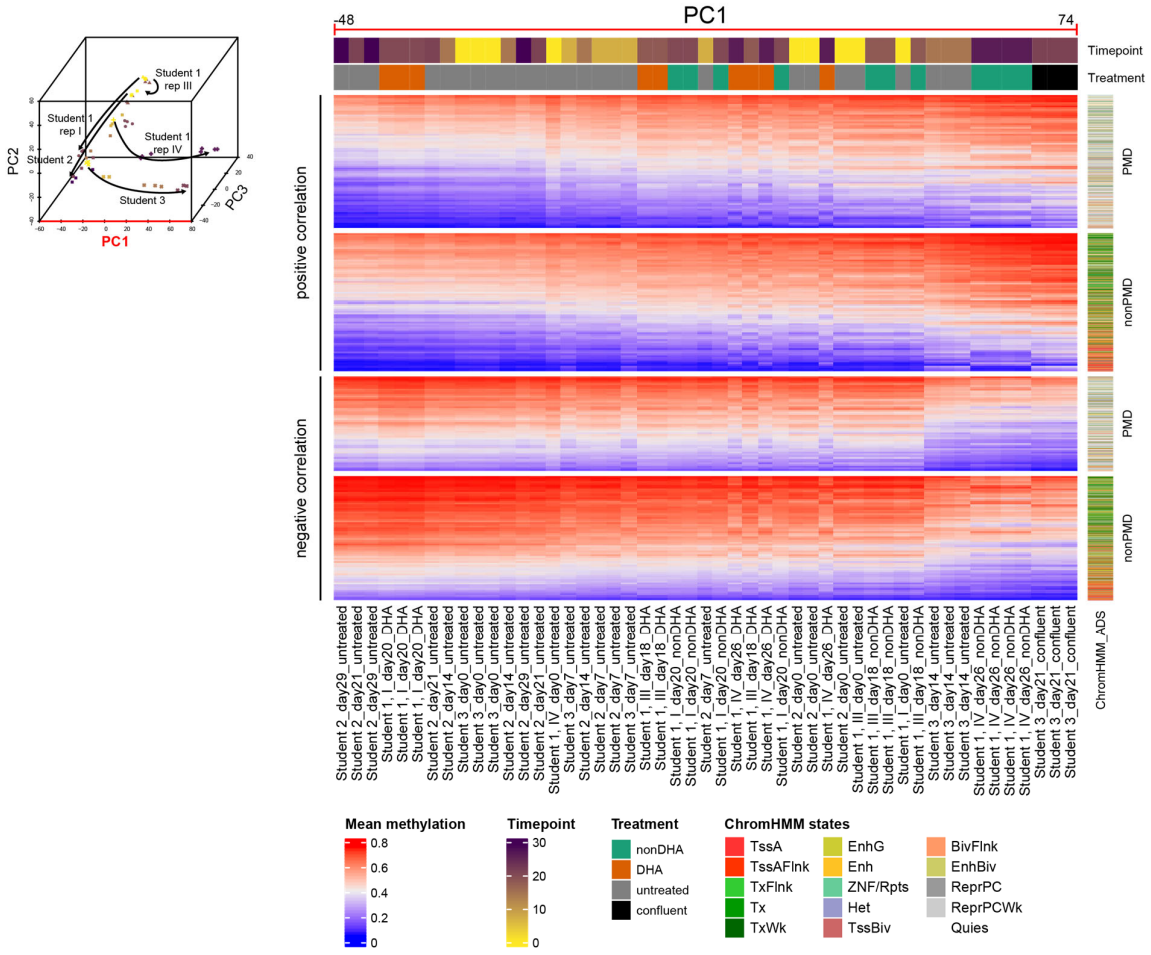

Supplementary Fig. 3| Heatmap of CpGs associated with PC1. Heatmap of methylation levels at 107,064 CpG sites with a positive (upper panel) and 85,103 CpGs with negative (lower panel) significant association with principal component 1 (PC1) of samples from experiment 5 - 7. Significance was defined by a significant linear regression (FDR adj. *p* value < 0.005) and methylation range > 0.2. CpG sites were annotated at the right side with ChromHMM states of adipose-derived stem cell (ADS, E025) (Roadmap Epigenomics et al., 2015) and further separated by PMDs and nonPMDs, defined by WGBS-seq (experiment 2). Experiment 6 was performed by LD (Student 2), experiment 2 + 7 by LK (Student 3), experiment 5, and data analysis were performed by myself (CFA, Student 1). See Fig. 9 for experimental design. WGBS-seq: whole-genome bisulfite sequencing.

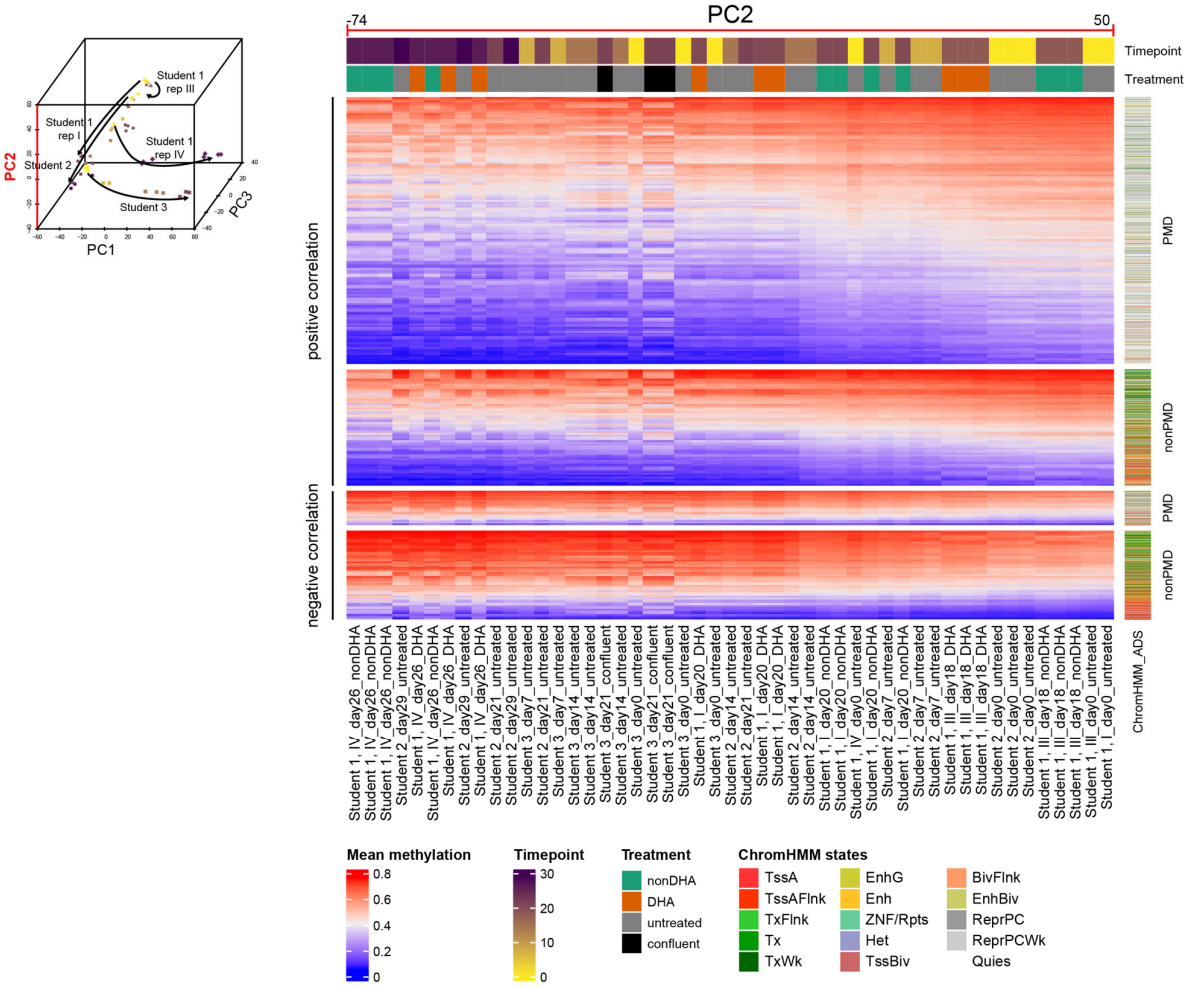

Supplementary Fig. 4| Heatmap of CpGs associated with PC2. Heatmap of methylation levels at 116,001 CpG sites with a positive (upper panel) and 37,870 CpGs with negative (lower panel) significant association with principal component 1 (PC1) of samples from experiment 5 - 7. Significance was defined by a significant linear regression (FDR adj. *p* value < 0.005) and methylation range > 0.2. CpG sites were annotated at the right side with ChromHMM states of adipose-derived stem cell (ADS, E025) (Roadmap Epigenomics et al., 2015) and further separated by PMDs and nonPMDs, defined by WGBS (experiment 2). Experiment 6 was performed by LD (Student 2), experiment 2 + 7 by LK (Student 3), experiment 5, and data analysis were performed by myself (CFA, Student 1). See Fig. 9 for experimental design. WGBS-seq: whole-genome bisulfite sequencing.

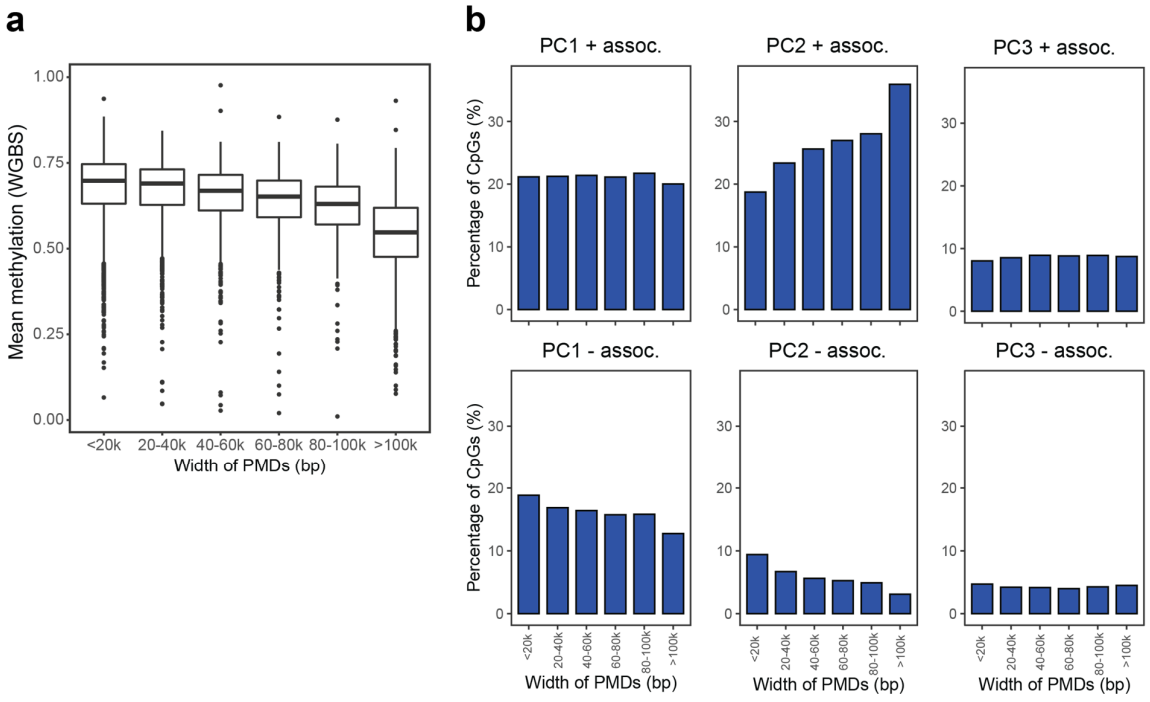

Supplementary Fig. 5| CpGs of PC2 (+ assoc.) are enriched for the largest PMDs with the strongest degree of demethylation. **a**, Boxplots display mean methylation of CpGs within a partially methylated domain (PMD), grouped by the width of the PMD (experiment 2). **b**, Barplots for each PC (+/- association) the percentage of CpGs located in PMDs, grouped by the width of the PMDs. PCs were defined by experiments 5 - 7 (see Fig. 46 - 48) and PMDs by WGBS (experiment 2). Experiment 6 was performed by LD (Student 2), experiment 2 + 7 by LK (Student 3), experiment 5, WGBS, and data analysis were performed by myself (CFA, Student 1). See Fig. 8 + 9 for experimental design. PC: principal component, WGBS-seq: whole-genome bisulfite sequencing.

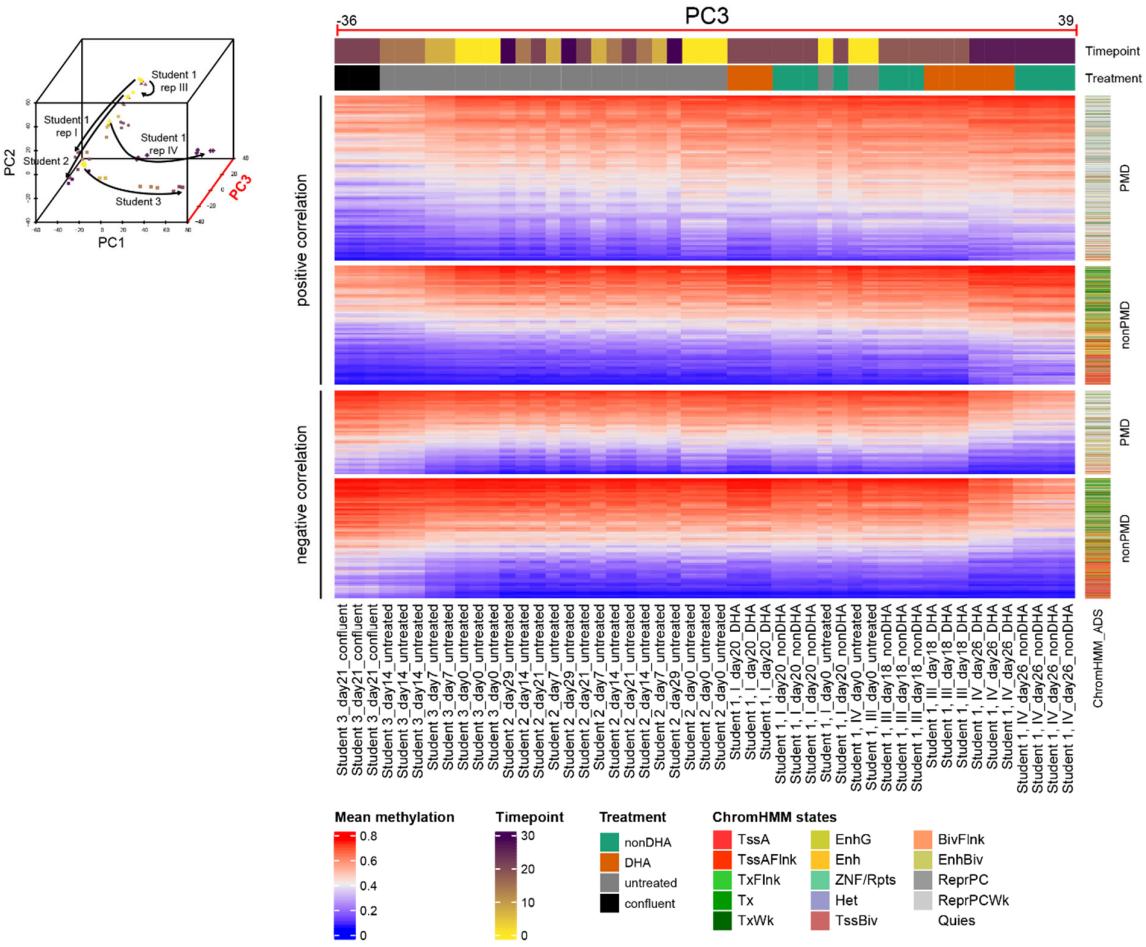

Supplementary Fig. 6| Heatmap of CpGs associated with PC3. Heatmap of methylation levels at 37,972 CpG sites with a positive (upper panel) and 27,520 CpGs with negative (lower panel) significant association with principal component 1 (PC1) of samples from experiment 5 - 7. Significance was defined by a significant linear regression (FDR adj. *p* value < 0.005) and methylation range > 0.2. CpG sites were annotated at the right side with ChromHMM states of adipose-derived stem cell (ADS, E025) (Roadmap Epigenomics et al., 2015) and further separated by PMDs and nonPMDs, defined by WGBS (experiment 2). Experiment 6 was performed by LD (Student 2), experiment 2 + 7 by LK (Student 3), experiment 5 and data analysis were performed by myself (CFA, Student 1). See Fig. 9 for experimental design, WGBS-seq: whole-genome bisulfite sequencing.

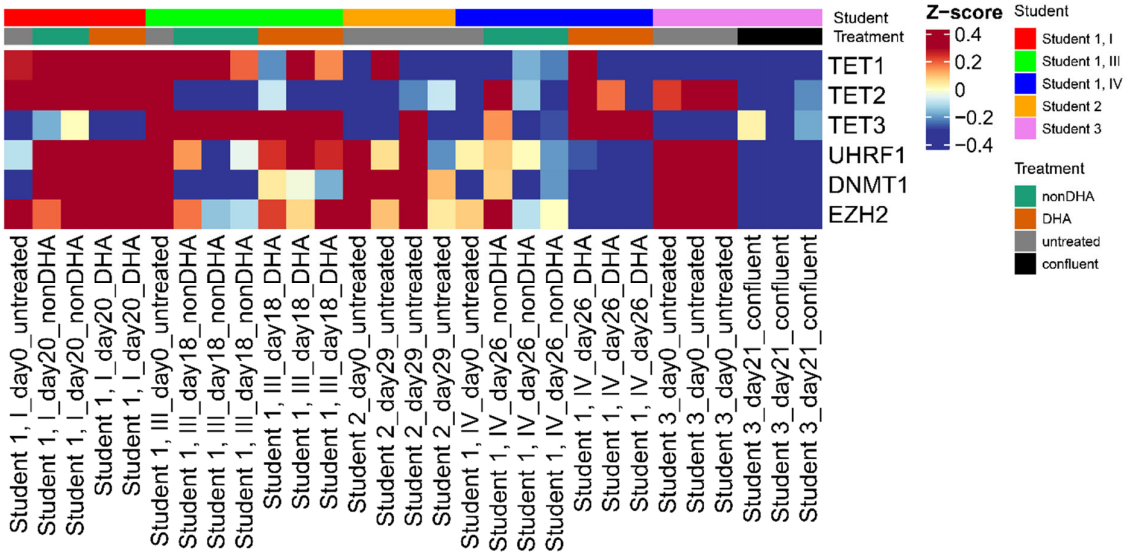

Supplementary Fig. 7| Expression of epigenetic genes during long-term cultivation. Heatmap of scaled (Z-score) log2CPM gene expression values of epigenetic genes. Experiment 6 was performed by LD (Student 2), experiment 7 by LK (Student 3), experiment 5 and data analysis were performed by myself (CFA, Student 1). See Fig. 9 for experimental design. log2CPM: log2 counts per million.

12 Publications and Presentations

12.1 Publications

Feuerstein-Akgoz C, Janke F, Heilmann J, Kessler L, Miehle F, Artati A, Weichenhan D, Aviles-Huerta D, Hey J, Toth R, Breuer K, Weninger A, Garelli S, Farnè M, Ugolini G, Rosati G, Ricciardiello L, Bordoni A, Assenov Y, Adamski J, Sültmann H, Plass C, Gerhauser C. **Integrated multi-ome dynamics of human adipocyte differentiation with focus on DNA hydroxymethylation** (manuscript in preparation)

Gerhauser C, Favero F, Risch T, Simon R, Feuerbach L, Assenov L, Heckmann D, Sidiropoulos N, Waszak SW, Hübschmann D, Urbanucci A, Girma EG, Kuryshev V, Klimczak LJ, Saini N, Stütz AM, Weichenhan D, Böttcher L, Toth R, Hendriksen JD, Koop C, Lutsik P, Matzk S, Warnatz H, Amstislavskiy V, Feuerstein C, Raeder B, Bogatyrova O, Schmitz E, Hube-Magg C, Kluth M, Huland H, Graefen M, Lawerenz C, Henry GH, Yamaguchi TN, Malewska A, Meiners J, Schilling D, Reisinger E, Eils R, Schlesner M, Strand DW, Bristow RG, Boutros PC, von Kalle C, Gordenin D, Sültmann H, Brors B, Sauter G, Plass C, Yaspo ML, Korbel JO, Schlomm T, Weischenfeldt J. **Molecular evolution of early onset prostate cancer identifies novel molecular risk markers and clinical trajectories.** Cancer Cell 2018, 34(6): 996-1011

12.2 PATHWAY-27 Project Reports

Gerhäuser C, Feuerstein C, Bordoni A, Ghini V, Tenori L. **PATHWAY-27 deliverable D6.4: Report on the mechanism/s of action of PATHWAY-27 bioactives and BEF identified in vitro (WP3) and in vivo (WP6).** (April 2018).

Capozzi F, Lucchini V, Ghini F, Tenori L, Picone G, Gerhäuser C, Feuerstein C, Nissen L, Ricciardiello L, Gianotti A, Luchinat C, Bordoni A. **PATHWAY-27 deliverable D6.3: Report summarizing the integrated analysis of WP6 results.** (April 2018).

Larsen B, Danesi F, Feuerstein C, Greve S, Gerhäuser C, Bordon A, Mandrup S, Luchinat C, Tenori L, Ghini V, Wilhelm U, Laurencikiene J, Ryden M, Arner P., Tomás L. **PATHWAY-27 deliverable D3.8: Final report on the integrated analysis of the mechanism/s of action of the selected bioactives.** (April 2018).

Gerhäuser C, Feuerstein C, Bordoni A, Ghini F, Tenori L, Nissen L, Gianotti A, Picone G, Lucchini V, Capozzi F. **PATHWAY-27 deliverable D6.2: Draft report on WP6 analysis to be used by WP3 as a guide for further analysis.** (March 2018).

Larsen B, Danesi F, Feuerstein C, Greve S, Gerhäuser C, Bordon A, Mandrup S. **PATHWAY-27 deliverable D3.7: Report on the molecular mechanism of selected bioactives in adipocytes and hepatocytes** (March 2018).

Larsen B, Feuerstein C, Nielsen R, Laurencikiene J, Björk C, Ryden M, Arner P, Gerhäuser C, Mandrup S. **PATHWAY-27 deliverable D3.6: Draft report on the effects of the selected bioactives on transcriptome in human adipocytes and hepatocytes** (December 2015).

12.3 Oral Presentations

Demo of: workflUX - the Workflow User eXperience: Chen M, Feuerstein-Akgoz C, Lutsik P; *ELIXIR Reproducible Research Workshop,* online (December 2021)

Docosahexaenoic acid (DHA) alters DNA methylation and gene expression in human preadipocyte. Feuerstein C, Klimo K, Weninger A, Toth R, Hey J, Assenov Y, Malpuech-Brugère C, Bub A, Orfila C, Ricciardiello C, Bordoni A, Gerhauser C, *AMPro Summer School 2019;* Garmisch-Partenkirchen, Germany (September 2019)

PATHWAY-27: Workpackage 3.4: In vitro Mechanistic Investigations. Gerhauser C Feuerstein C; *PATHWAY-27 final meeting;* Karlsruhe, Germany (March, 2017)

PATHWAY-27: Dynamic changes in DNA methylation during SGBS differentiation. Feuerstein C, Gerhauser C; *PATHWAY-27 3rd Annual Meeting;* Budapest, Hungary (May 2016)

12.4 Poster Presentations

Docosahexaenoic acid (DHA) alters DNA methylation and gene expression in human adipocytes and adipose tissue. Feuerstein C, Klimo K, Weninger A, Toth R, Hey J, Assenov Y and Gerhauser C. *International Graduate School for Cancer Research 2018 Ph.D. Poster Presentation;* Heidelberg, Germany (November 2018)

Docosahexaenoic acid (DHA) alters DNA methylation and gene expression in human adipocytes and adipose tissue. Feuerstein C, Klimo K, Weninger A, Toth R, Hey J, Assenov Y and Gerhauser C. *Chromatin and Metabolism Spetses Summer School;* Spetses, Greece (August 2018)
Awarded with travel grant

Effect of docosahexaenoic acid (DHA) on epigenetic gene regulation in adipocytes. Feuerstein C, Toth R, Hey J, Assenov Y, Gerhauser C. *FOODOMICS conference;* Bologna, Italy (January 2018)

Regulation of genes associated with Metabolic Syndrome by DNA methylation - A correlation analysis with clinical parameters. Feuerstein C, Larsen B, Toth C, Engelbert A, Bub A, Mandrup S, Gerhäuser C, *Epigenetics, Obesity and Metabolism Conference*, Cambridge, UK (October 2015)
Awarded with abcam travel grant

13 Acknowledgements

The work presented in my thesis was possible only due to the effort and support of many individuals, to whom I want to address my gratitude:

To my supervisor and group leader, Clarissa Gerhäuser, for bringing me into the team, believing in my potential, and supporting me throughout the time. Her dedication to the project and guidance during it were outstanding and I am grateful for the opportunity that I got for the smooth transition from wet-lab to bioinformatics. Thank you for always having an open door throughout the years, for your instructive advice, expertise, and ideas that always helped to advance the project. Also, a big thank you for helping me improve enormous amounts of presentations, posters, reports, and this thesis! More importantly, thank you also for the great atmosphere, the little acts of kindness, such as the Santa Clause surprises, and being so supportive during difficult times as well.

To Christoph Plass for providing the great scientific infrastructure in his division. To all members of the TAC committee, Odilia Popanda, Clarissa Gerhäuser, Achim Bub, and Alexandros Vegiopoulos, for productive discussions during the TAC meetings. And to all my examiners and members of the thesis committee, Odilia Popanda, Achim Bub, Benedikt Brors, and Michael Milsom, for your time.

To the collaboration partners involved in the preparation of the manuscript on hydroxymethylation, specially to Florian Janke (DKFZ, Heidelberg), Florian Miehle (TUM, Munich), and Kristin Schubert (UFZ, Leipzig) for your support in the study.

A thank you also to the collaboration partners of the PATHWAY-27 study. It was a great experience working on an EU project involving industry and different scientific institutions across Europe. It was great seeing the expertise in so many different fields coming together and experiencing the dynamics, and sometimes the necessary politics 😊. To Alessandra Bordoni (UNIBO, Italy), for her great coordination and dedication to the project.

To the core facilities at the DKFZ, particularly, the Genomics and Proteomics Core Facility (GPCF) and the Omics IT and Data Management Core Facility (ODCF), for providing excellent and reproducible work.

Thanks to the laboratory team –Karin Klimo, Annette Weninger, Jessica Heilmann – for all your experimental support and your energy.

To Reka Toth, Yassen Assenov, David Brocks, Joschka Hey, Anand Mayakonda, and Rajbir Batra, for your great bioinformatic support and in smoothening the transition to bioinformatics.

To all members of the lab, for the great time together. To my great office mates Sina Stäble and Jens Langstein. To the students in our group and for their support and time spend together: Anna-Lena Krug, Lisa Demoen, Nina Margot, Caroline Hausner (née Bossmann), and Linda Kessler. Also to all previous (Katharina Heilmann, Maria Pudenz) and current group members (Rajbir Batra, Kira Kornienko, Jessica Heilmann) for your scientific input in the group meetings, the coffee breaks and for just having a good time. Also a great thanks to all other fellow PhDs, Daniela Mancarella, Joschka Hey, Anand Mayakonda, Alexander Kühn, Yunhee Jeong, and Anna Riedel, for making the time at DKFZ a special one. To all members of the “lunch break community”, for the great talks and huge diversity on discussed topics, I miss you here in home office. And finally to Cornelia Jäkel, Caroline Hausner and Mariam Hakobyan for being my peer group, support system and for your friendship.

A big thanks goes to my friends supporting me specially throughout the last year from the distance with endless phone calls.

To my family, especially to my father, the most supportive father I can imagine and Junior, my “little” brother, who became a friend and wise mentor.

To Emin, for being my home and best friend. For making great sacrifices, enjoying the present and dreaming about the future with me.

Danke, muito obrigada, çok teşekkürler!